Modeling the metabolic response to oxidative stress : the role of regulations

Julien Hurbain

To cite this version:

Julien Hurbain. Modeling the metabolic response to oxidative stress : the role of regulations. Biological Physics [physics.bio-ph]. Université de Lille, 2022. English. NNT : 2022ULILR045 . tel-04012365

HAL Id: tel-04012365
https://theses.hal.science/tel-04012365
Submitted on 2 Mar 2023

Modeling the metabolic response to oxidative stress : the role of regulations

Université de Lille

Doctoral School : **ED SMRE**
Research Laboratory : **PhLAM**

Thesis presented by **Julien Hurbain**

Defended on **24th November, 2022**

In order to become **Doctor** in **Physics**
Specialty : Diluted Media and Fundamental Optics

Thesis supervised by :	Benjamin Pfeuty	Supervisor
	Quentin Thommen	Co-monitor
	François Anquez	Co-monitor

Committee members :

Referees	Geneviève Dupont	University of Brussels, Belgium	
	Hidde de Jong	Inria Grenoble, France	
Examiners	Marc Lefranc	University of Lille, France	Committee president
	Pierre Millard	University of Toulouse, France	
Thesis director	Benjamin Pfeuty	University of Lille, France	
Co-supervisors	Quentin Thommen	University of Lille, France	
	François Anquez	University of Lille, France	

Modélisation de la réponse métabolique à un stress oxydant : rôle des régulations

Université de Lille

Ecole Doctorale : **ED SMRE**

Laboratoire de Recherche : **PhLAM**

Thèse présentée par **Julien Hurbain**

Soutenue le **24 Novembre, 2022**

En vue de l'obtention du grade de **Docteur** en **Physique**

Spécialité : Milieux Dilués et Optique Fondamentale

Thèse encadrée par :	Benjamin Pfeuty	Directeur
	Quentin Thommen	Co-encadrant
	François Anquez	Co-encadrant

Membres du Jury

Rapporteurs	Geneviève Dupont	Université de Bruxelles, Belgique	
	Hidde de Jong	Inria Grenoble, France	
Examinateurs	Marc Lefranc	Université de Lille, France	Président du jury
	Pierre Millard	Université de Toulouse, France	
Directeur de thèse	Benjamin Pfeuty	Université de Lille, France	
Co-encadrants	Quentin Thommen	Université de Lille, France	
	François Anquez	Université de Lille, France	

Abstract

Living cells such as mammalian cells in particular, are continuously exposed to multiple and varied types of stress. These stresses can perturb the cellular homeostasis and induce damages on the cellular components which could induce several types of diseases. It is particularly the case for a change of cellular redox state called oxidative stress induced by an excessive production or insufficient consumption of reactive oxygen species such as hydrogen peroxide (H_2O_2).

Cells have developed efficient defence mechanisms against oxidative stress that involve anti-oxidant systems such as glutathiones which reduce the oxidizing molecules, but also metabolic pathways such as Pentose Phosphate Pathway (PPP) and glycolysis. These metabolic pathways are known to reroute the carbon flux resources from the glycolysis toward the PPP which induces high $NADPH$ recycling that is required for efficient detoxification rate of the anti-oxidant systems. It remains however unclear how regulatory mechanisms (i) contribute to such reallocation of metabolic flux resources during oxidative stress and (ii) give rise to observed adaptation profiles of intracellular H_2O_2 concentrations.

In the thesis, the role of regulations in the metabolic response to oxidative stress is addressed using a comprehensive kinetic modeling framework. First, a model is built from a set of metabolomics and ^{13}C labeling data, using conventional parameter estimation methods but also a novel metabolic flux analysis techniques based on a stochastic simulation algorithm. Systematic analysis of the model reveals that many metabolic inhibitions, especially on $G6PD$, PGI and $GAPD$, can favour flux rerouting for $NADPH$ production. In particular, we show that all these regulations work in a dose-dependent and complementary manner, which explains some paradoxes and controversies, and is consistent with observed adaptation phenotypes. A more phenomenological model has also been developed to show how such adaptation phenotype could contribute to cell-fate heterogeneity, such as fractional killing, as a long-term outcome of oxidative stress.

Keywords : Cell, oxidative stress, mathematical modeling, metabolic regulations, adaptation.

Résumé

Les cellules vivantes, telles que les cellules de mammifères en particulier, sont continuellement exposées à des types de stress multiples et variés. Ces stress peuvent perturber l'homéostasie cellulaire et induire des dégâts sur les composants cellulaires qui pourraient induire plusieurs types de maladies. C'est notamment le cas d'un changement d'état redox cellulaire appelé stress oxydatif induit par production excessive ou une consommation insuffisante d'espèces réactives de l'oxygène. L'une des espèces réactives de l'oxygène les plus importantes est le peroxyde d'hydrogène (H_2O_2).

Les cellules ont développé des mécanismes de défense efficaces contre le stress oxydatif qui impliquent des systèmes anti-oxydants tels que les glutathions qui réduisent les molécules oxydantes, mais aussi des voies métaboliques telles que la voie des Pentoses Phosphates (PPP) et la glycolyse. Ces voies métaboliques sont connues pour rediriger les ressources de flux de carbone de la glycolyse vers le PPP, ce qui induit un recyclage élevé du $NADPH$ nécessaire à un taux de détoxification efficace des systèmes anti-oxydants. Il n'est cependant pas clair comment les mécanismes de régulation (i) contribuent à une telle réallocation des ressources de flux métaboliques pendant le stress oxydatif et (ii) donnent lieu aux profils d'adaptation observés des concentrations intracellulaires de H_2O_2.

Dans la thèse, le rôle des régulations dans la réponse métabolique au stress oxydatif est abordé à l'aide d'un cadre de modélisation cinétique. Tout d'abord, un modèle est construit à partir d'un ensemble de données métabolomiques et de marquage ^{13}C, en utilisant des méthodes classiques d'estimation de paramètre mais aussi une nouvelle technique d'analyse des flux métaboliques basée sur un algorithme de simulation stochastique. L'analyse systématique du modèle révèle que de nombreuses inhibitions métaboliques, notamment sur $G6PD$, PGI et $GAPD$, peuvent favoriser la redirection des flux pour la production de $NADPH$. En particulier, nous montrons que toutes ces régulations fonctionnent de manière dose-dépendante et complémentaire, ce qui explique certains paradoxes et controverses, et est cohérent avec les phénotypes d'adaptation observés. Un modèle plus phénoménologique a également été développé pour montrer comment un tel phénotype d'adaptation pourrait contribuer à l'hétérogénéité du destin cellulaire, comme la mort fractionnée, en tant que résultat à long terme du stress oxydatif.

Mots clés : Cellule, stress oxydatif, modélisation mathématique, regulations métabolique, adaptation.

Remerciements

Tout d'abord, je tiens à remercier les membres du jury d'avoir accepté de faire partie de ce comité. Je remercie Geneviève Dupont et Hidde de Jong pour avoir accepté de rapporter mon travail, puis également Pierre Millard et Marc Lefranc pour avoir accepté de l'examiner. Je vous remercie pour tous les commentaires que vous avez pour faire sur mon travail. Je remercie l'école doctorale SMRE et la région Haut de France pour avoir co-financé cette thèse.
Je remercie ensuite mon directeur de thèse Benjamin Pfeuty ainsi que mes co-encadrants Quentin Thommen et François Anquez pour m'avoir fait confiance depuis de nombreuses années remontant bien avant le cadre de cette thèse. Je suis très reconnaissant d'avoir travaillé avec vous pour votre apport conséquent et complémentaire sur bien des domaines.

Benjamin, je n'oublierais jamais ce que tu as fait pour moi. Ta très grande implication et disponibilité dans ma thèse m'ont permis d'apprendre énormément scientifiquement et ont aidé à faire avancer le projet sur lequel nous avons travaillé jusqu'au toute dernière étapes de cette thèse. Je te remercie pour ta gentillesse et ta patience indéfectible. Je suis fier de t'avoir eu tant que directeur au vu de tout ce que tu m'as appris que ce soit scientifiquement, ou humainement.

Quentin, tout a commencé par toi quand je t'ai rencontré il y a maintenant 8 ans. Tu m'as permis de découvrir qu'il existait un monde entre la physique et la biologie notamment en me faisant confiance pour un simple stage pour enfin finir avec une thèse et pour ça, je t'en suis grandement reconnaissant. Je te remercie également pour ton expertise et tes idées originales que tu nous as apporté de nombreuses fois.

François, tu as contribué au scientifique que je suis devenu. J'ai particulièrement apprécié les nombreuses discussions, souvent spontanée mais toujours très intéressantes. Merci d'avoir accepté de se lancer dans le projet expérimental me permettant presque de devenir un *Expérimentaliste*.

Je remercie tous les membres du Biocal que j'ai pu côtoyer. Darka, I thank you for your involvement in my thesis and much more. I'm very glad to have met you. Pauline, Alan, Michael, Pierre, mon vécu dans le labo et surtout dans le Biocal aurait été bien différent sans vous. J'attend toujours la prochaine session de Mario Kart ! Pauline, je vérifierai que tu n'aies pas acheté le prochain Zelda avant d'avoir rendu ta thèse. Alan, j'attend toujours mes chocolats. Michael, nos débats me manquent déjà. Pierre, encore un peu et je serais également tombé dans la tentation des pauses café/thé. Merci également à Raoul et à Mathilde de m'avoir supporté dans la partie expérimentale. J'ai apprécié travailler avec vous, même pour une courte durée.

Merci à toi Corentin, tu as été pour moi un acolyte pendant cette thèse et bien au delà. Je suis très heureux de t'avoir eu à mes côtés pendant tous les évènements de ces dernières années. Petite dédicace à Camille, tu ne me battras pas à Catan ! Merci aux thésards Jordan, Martin et Alexandre qui eux, font de "la vrai science". Je sais que ce n'est que de la biologie, mais il n'est pas trop tard pour vous y mettre !

Benoit, Valentin, toutes ces années d'études aurait été bien tristes sans vous. Vous êtes pour moi des amis essentiels depuis maintenant tellement d'années. Faites que nos soirées sur les jeux PC, jeux de société durent éternellement. A quand le retour d'une nouvelle LAN ?

Je te remercie, Ponce, pour m'avoir accompagné avec tes lives qui sont devenus une réelle habitude quotidienne. Sache que tu as été un fond sonore très agréable qui a possiblement dégradé ma productivité de temps en temps mais il est sûr que tu as contribué à ce travail à ta façon.

Comment faire des remerciements sans citer la famille ! Papa, Maman, merci de m'avoir encouragé pendant toutes ces années d'études, me laissant faire ce que je voulais. Sans vous cela n'aurait, pour sûr, pas été possible, Merci pour tout ! Sébastien, Élodie, nous n'avons pas forcément la même façon de penser sur certain sujet, mais vous me supportez encore et encore quoiqu'il arrive, Merci ! Petite pensée à Guillaume et Marie qui ont aussi contribué à leur manière. Papy, Mamie, je suis content de vous avoir à mes côtés pendant ces évènements, et ça y est, je ne suis plus à l'école ! Merci à la belle-famille m'ayant également soutenue. Merci notamment à mes beaux-parents qui ont su me faire de plus en plus confiance au fil des années. Illona, peut-être ce sera bientôt ton tour ?

Enfin, la dernière mais pas des moindres, Victoria, ma femme, ma meilleure-amie, tu as été pour moi les fondations sur lesquelles se reposer à chaque instant. Je ne saurais comment te remercier pour tout ce que tu fais pour moi, notamment pour la confiance et le soutien quotidien et inconditionnel dont tu me fais preuve, mais surtout pour les papouilles et les bons repas. Je n'aurais pas pu y arriver sans toi. C'est bon, ton investissement durant toutes ces années va enfin pouvoir porter ces fruits !

Les espèces qui survivent ne sont pas les espèces les plus fortes, ni les plus intelligentes, mais celles qui s'adaptent le mieux aux changements.

Charles Darwin

Mais vous savez, moi je ne crois pas qu'il y ait de bonnes ou de mauvaises situations. Moi, si je devais résumer ma vie, aujourd'hui avec vous, je dirais que c'est d'abord des rencontres, des gens qui m'ont tendu la main peut-être à un moment où je ne pouvais pas, où j'étais seul chez moi.

Otis/Edouard Baer, *Astérix & Obélix : Mission Cléopâtre*

Contents

General introduction

Living cells are often exposed to different types of perturbations which come from diverse sources such as heat, pressure or chemical compounds etc... Oxidative stress is a perturbation of the redox state induced by excessive production on consumption of reactive oxygen species (ROS). Superoxide radicals ($O_2^{\bullet -}$), hydrogen peroxide (H_2O_2) and hydroxyl radicals ($^{\bullet}OH$) are well known ROS that induce oxidative stress. The ROS sources are varied and can be endogenous, i.e. coming from inside cells due to a disruption of their cellular mechanisms or exogenous, i.e. coming from external perturbations such as alcohols, smokes, pollutants. They transfer their oxidation to cellular molecules such as proteins, lipids inducing change of activity or loss of function. It has for consequences to induce damages on cellular components such as membrane or DNA. It can induce different cell fates such as programmed or, in extreme cases, non-programmed cell death or diseases such as cancer, Alzheimer's disease, Parkinson's disease etc... To avoid such fates, it exists diverse anti-oxidant molecules that capture and remove the oxidation of cells. The most famous anti-oxidants are glutathiones, peroxiredoxins/thioredoxins and catalase. It is know that these first two are the most efficient to detoxify the cellular compounds and also to remove directly the ROS. They are known to be recycled by $NADPH$ metabolism in order to highly respond to the stress.

Metabolism is all chemical reactions in cells to maintain them alive. In non-perturbation conditions, it allows to produce cellular energy needed to make happen most of the chemical reaction in cells or biomass needed to reproduce and divide. However, another function of the metabolism is the defence against perturbation such as the oxidative stress response. When cells are perturbed, metabolism is highly regulated to reallocate the resources in order to respond to the stress. Regulations can act in long time scale, for instance on the transcriptional regulation, or in short term by inducing direct change in enzyme activity. The Pentose Phosphate Pathway (PPP) combined to glycolysis are known to be highly regulated in order to reroute the input carbon flux to highly produce $NADPH$ molecules during oxidative stress response.

Despite evidences of numerous metabolic regulations, their role and cooperation during stress are still not clear. Indeed, an important issue is to understand how regulations are involved individually but also together in the flux rerouting, how does it induce adaptation to stress and how does it depend of the perturbation level. The aim of this thesis is to study the resources allocation orchestrated by metabolic regulations of the PPP and glycolysis during fast oxidative stress response using a mathematical model approach.

In **chapter 1**, the biological context of the oxidative stress is introduced. The source of oxidative stress and their consequences will be detailed. The mechanisms of anti-oxidant molecules are explained in order to understand the main use of glutathiones in the mathematical model. Then, all the metabolic pathways linked to the consumption or production of $NADPH$ is introduced. These metabolic pathways are using glucose molecules as source, react and spread the carbons atoms in the network. Efficiency of the PPP directly linked to glycolysis to reroute carbon flux will be highlighted. Finally, regulations of the metabolism allowing high oxidative stress response are shown.

In **chapter 2** is introduced the methods used in this thesis. It comprises the procedure to express mathematically the ordinary differential equations representing the metabolite concentration changes during oxidative stress. Then, theoretical analysis methods used in complement of the model such as flux balance analysis or metabolic control analysis are presented. Moreover, methods of data-driven estimation of model parameters comprising optimisation algorithms such as Monte Carlo Markov chain and genetic algorithm are used in this work to build the mathematical model in order to reproduce experimental behaviours and are also presented here. Finally, metabolic flux analysis will be used to convert labeling data into flux state data. Its framework will also be introduced here.

In **chapter 3**, a first analysis of the oxidative stress response is made by using a coarse-grained mathematical model of the PPP and glycolysis. It displays adaptation phenotype which would reveal a well established resources reallocation with a compromise between fast regulation with high metabolic cost and slow response regulation which would induce potential cellular damages before the adaptation.

In **chapter 4**, the metabolic flux management is analysed by first using flux balance analysis showing elementary modes. Their dedicated utilities correspond to the main objective of cellular metabolism and a highly efficient mode of carbons cycling allowing high $NADPH$ production. Analysis of experimental carbons labeling data by a new ^{13}C-based Metabolic Flux Analysis (^{13}C-MFA) algorithm based on Stochastic Simulation Algorithm (SSA) [1] allows to estimate fluxes during non-perturbed and perturbed states showing a carbon flux rerouting during oxidative stress response. This new algorithm is simple to implement and is also highly efficient to proceed to complex MFA such as non-stationary MFA or dynamic MFA.

In **chapter 5**, the reactions rates of the mathematical model are expressed as a function of the metabolite concentrations and parameters. Monte Carlo Markov chain and genetic algorithm are used to data-driven estimate distribution of model parameters. It creates an ensemble of models that reproduces experimental data of concentration fold change between non-stressed and stressed states, and fluxes previously estimated in **chapter 4**. Then, the temporal dynamics display biphasic time-course confirming a metabolic reaction. Dose response analyses show detoxification saturation but also input flux rerouting during oxidative stress allowing to increase $NADPH$ production. In complement, both temporal dynamics and dose responses are compared to experimental data in order to validate the model construction.

In **chapter 6**, regulations of the metabolic pathways are studied using numerical simulation of the model ensemble. Regulation parameters and enzyme activity parameters are used to analyse the effect of regulation on the carbon resource affectation during the oxidative stress response. Modifying experimentally a regulation efficiency on an enzyme without changing the enzyme activity would need extremely advanced techniques. However, modifying theoretically regulation parameters allows to investigate their efficiency showing a dose-dependent and synergistic work during oxidative stress response. Moreover, similarly to most of biological experimental work on this topic, enzyme activity can be modified. By changing the corresponding parameters of the key PPP enzymes, a non-linear response of 6-phosphogluconate dehydrogenase ($6PGD$) can be found confirming the regulation importance in oxidative stress response. A complementary theoretical study of the regulations is performed with the metabolic control analysis showing flux sensitivities to regulations during oxidative stress detoxification.

Previous works study response of the metabolism during oxidative stress and show the need of regulations to efficiently detoxify ROS. The impact of stress adaptation on cellular fate has also been investigated in Hurbain et al. 2020 [2]. In **chapter 7** will be an introduction of this theoretical study which shows that the presence of adaptation phenotype can affect the cell-fate heterogeneity, such as fractional killing, via the used of a mathematical model combining an adaptation module and an apoptosis initiation model.

Most of the results presented from **chapter 4** to **chapter 6** have been published in Hurbain et al. 2022 [3]. In this thesis, all used algorithms have been written by myself and are publicly available [3]. All simulations have been made using Matlab2018a/b. The stochastic simulation algorithm used in this paper is presented in Thommen et al. [1]. All published paper are given in **Chapter Publication**. A bit less of two years of my thesis has been spent in these theoretical studies. The last 6 months of my thesis have been used in experiments trying to reproduce theoretical prediction of oxidative stress detoxification during $6PGD$ enzyme activity modification. They consists in capturing the fluorescence of a reduction-oxidation sensitive green fluorescent protein 2 ($roGFP2$) tagged to an anti-oxidant enzyme (i.e. GRx) during oxidative stress and during a decrease of $6PGD$ enzyme activity by the specific inhibitor physcion. This work is still in progress and is not presented here. Finally, the abbreviations and mathematical symbols of the entire thesis are provided at the end of the document in **Chapter Abbreviations** and in **Chapter Mathematical symbols**.

Chapter 1

Biological context

Living cells are often exposed to perturbation of their environment inducing signaling and regulatory mechanisms. Reactive oxygen species are a group of unstable molecules that contains oxygen and tends to react easily. A higher or lower concentration of these molecules can induce oxidative stress. This perturbation has high impact for instance on cellular proteins or lipids. It is source of many phenotypes such as cell aging, or diseases such as cancer, Alzheimer's or Parkinson's diseases. To avoid such fates, cells have metabolic pathways that are regulated in order to adapt to oxidative stress. In this chapter will be presented the biological mechanisms of how reactive oxygen species can induce cellular oxidative stress and the metabolic pathways resources present in cells that can be used to adapt to perturbations.

1.1 Free radicals and reactive oxygen species

A free radical is an entity that has an unpaired electron which makes it very unstable and reactive [4]. It can be molecules or atoms which tend to accept or give an electron. Thus, they are often parts of redox reactions as oxidants or reductants. In cell, free radicals are produced by a lot of different biological processes such as enzymatic and non-enzymatic reactions. Reactive oxygen species (ROS) are a subgroup of the free radicals comprising oxygen. The most common ROS are superoxide radicals ($O_2^{\bullet -}$), hydrogen peroxide (H_2O_2), hydroxyl radicals ($^{\bullet}OH$), and singlet oxygen ($_1O^2$) [5, 6]. These molecules are maintained at low levels for chemical processes such as protein phosphorylation, activation of several transcriptional factors. A change of ROS production or consumption can lead to other biological processes such as apoptosis. It has been shown that enzymatic reactions that produce ROS are involved for instance in respiratory chain or phagocytosis [7, 6]. On the

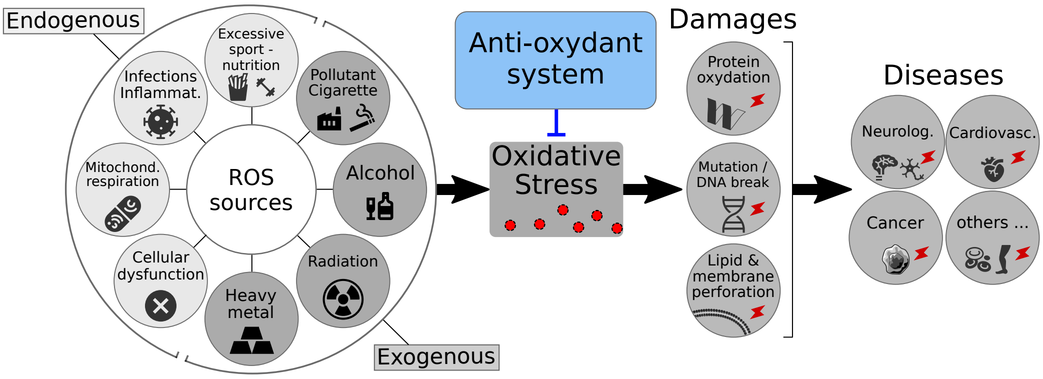

Figure 1.1: Causes and consequences of reactive oxygen species. Different sources produce reactive oxygen species symbolized by the red circle inside the cell which can induce oxidative stress. This perturbation can induce cellular damages which can themselves induce diseases in an organism. In order to avoid the damages or diseases, cells can uses defence mechanisms where ones of the first are the anti-oxidant systems.

---

other side, non-enzymatic reactions produce free radicals in mitochondrial respiration [6].

Free radicals or more precisely ROS are produced by endogenous and exogenous sources [7, 8, 6] (Figure 1.1) :

Endogenous : Processes inside cells are responsible of ROS production such as mitochondrial respiration, immune cell activation, inflammation, ischemia, infection, cancer, excessive exercise and aging. It has been shown that $NADPH$ oxidase is an important source of superoxide radicals ($O_2^{\bullet -}$) and hydrogen peroxide (H_2O_2) [9]. Moreover, one the most present ROS is hydrogen peroxide.;

Exogenous : External components can penetrate inside cells and can be degraded which induce ROS production. It can come from environmental pollutants, heavy metals, certain drugs, cooking (smoked meat or fat), cigarette smoke, alcohol, and radiations.

ROS are maintained at low concentrations. In this condition, they can be beneficial for the cells. Indeed, they can be used as a defence system against several pathogens. Phagocytes can store free radicals and release them to destroy pathogenic microbes [10]. Free radicals are also used in several signaling pathways [10]. Indeed, they can play important role of in signaling cascades in fibroblast, endothelial cells, cardiac myocytes or thyroid tissue [10]. In conclusion, when ROS are maintained at low levels, they can play important role in maintaining the cellular homeostasis which is the internal conditions (i.e. physical and chemical conditions) at steady state to keep themself alive.

1.2 Oxidative stress

Free radicals are present in cells and are maintained at low concentrations to be used in several cellular processes. However, an excess of free radicals or ROS due to production or consumption disorder can induce a perturbation of cellular redox state which is called oxidative stress (Figure 1.1). This perturbation is known to have negative impact on a lot of cellular structures such as membranes, lipids, proteins, lipoproteins, and deoxyribonucleic acid (DNA) [7, 8, 10]. Indeed, excess of ROS can lead for instance to lipid perforation which induces cell membrane damages ; DNA lesions, base and sugar lesions, DNA-protein cross-links, strand breaks, and base-free sites which could induces mutation, loss of epigenetic information [8]. When these modifications on cellular components are not repaired, it could induce several diseases or cell death in extreme cases, i.e. when damages are to important. It has been shown that oxidative stress is involved, for instance, in the onset of cancer with tobacco smoking or environmental pollutants as sources [7] ; cardiovascular diseases due to hypercholesterolaemia, hypertension, smoking habit, diabetes, unbalanced diet, and sedentary life [8]. It can also cause neurological diseases such as Alzheimer's disease, Parkinson's disease or others such as vitiligo, rheumatoid arthritis [6, 8, 10] etc...

Oxidative stress can induce a lot of different diseases or cell deaths. Before arriving to extreme fates, cells use mechanisms such as metabolic pathways made of particular molecules which are known to their specific utilities against ROS. For instance, a transcription factor called nuclear factor erythroid-derived 2-related factor 2 ($Nrf2$) induces regulation of anti-oxidative stress genes or the transcription factor $p53$ which is link to apoptosis cell death, cell cycle [7]. Moreover, anti-oxidant molecules are major actors in the oxidative stress defence.

1.3 Anti-oxidants

Anti-oxidants are molecules that tend to minimise oxidation induced by ROS (Figure 1.1). Thus, anti-oxidant molecules allow cells to defend against oxidative stress by reducing it. These molecules are of major importance in keeping

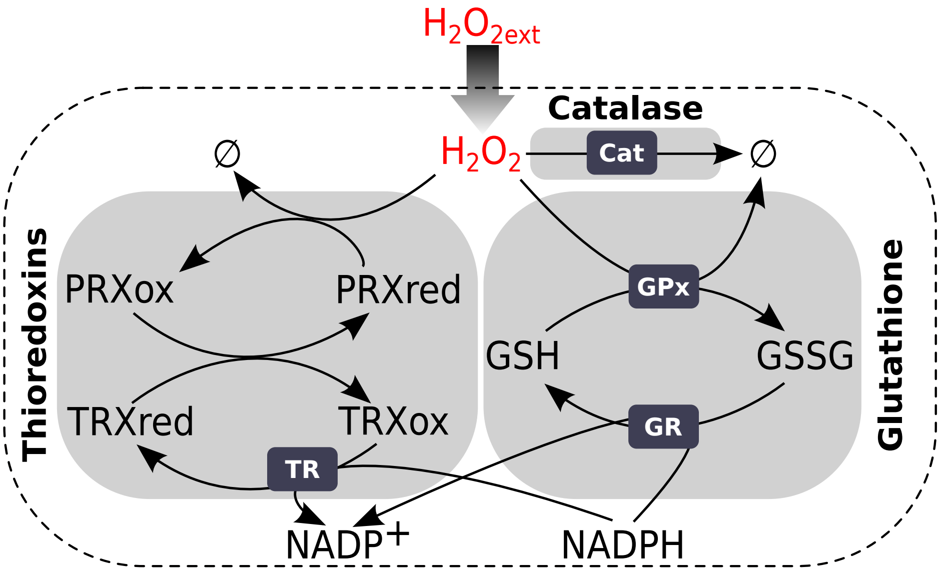

Figure 1.2: ***H_2O_2* detoxification pathways.** Hydrogen peroxide H_2O_2 is produced inside cells or can come from outside. The systems of H_2O_2 removing are made by glutathiones GSH and $GSSG$, peroxiredoxins/thioredoxins (PRX/TRX) and catalase (Cat). Enzymes are displayed with black rectangles.

ROS at a low concentration. One the most present ROS is hydrogen peroxide (H_2O_2). It has been shown that glutathiones (GSH in reduced state and glutathione disulfide $GSSG$ in oxidized state), peroxiredoxins/thioredoxins (PRX/TRX) or catalase (Cat) are major anti-oxidant used by cells to remove ROS such as hydrogen peroxide (Figure 1.2) [6, 10, 11]. Even if oxidative stress is known as negative effect, regulating the anti-oxidants could to act against several diseases as therapy [8].

- Glutathiones are anti-oxidant molecules that can be found in many cellular types. It plays a major role in the oxidative stress response by reducing free radicals that are oxidized during a perturbation [10, 6]. Indeed, GSH can capture the oxidation of a molecule by the following reaction :

  $$2GSH + 2R \rightarrow \; GSSG + 2R{-}H \tag{1.1}$$

  where R is a free radical. It is important to note that glutathione disulfide $GSSG$ is composed from 2 GSH molecules linked by an internal disulfide bridge on a cysteine site [10]. Moreover, glutathiones are known to be efficient in the detoxification of H_2O_2 stress. Indeed, catalysed by the enzyme glutathione peroxidase (GPx), 2 molecules of GSH can reduce hydrogen peroxide H_2O_2 into water H_2O by the following reaction :

$$2\ GSH + H_2O_2 \xrightarrow{\text{GPx}} GSSG + 2\ H_2O \tag{1.2}$$

Once free radicals and reactive oxygen species are reduced, 2 molecules of GSH are oxidised into $GSSG$ which can be reduced itself. Indeed, oxidation can be removed by recycling glutathiones using coenzyme nicotinamide adenine dinucleotide phosphate $NADP$ with $NADPH$ in reduced state and $NADP^+$ in oxidized state [12]. This reaction is catalysed by the glutathione reductase (GR) enzyme :

$$NADPH + GSSG \xrightarrow{\text{GR}} NADP^+ + 2\ GSH \tag{1.3}$$

- Peroxiredoxins (PRX) are anti-oxidant enzymes that reduce peroxides such as hydrogen peroxide [10]. They are very widely present inside cells and are combined to thioredoxins (TRX) which are key molecules to maintain the cellular redox state as well as $GSH/GSSG$. In hydrogen peroxide stresses, PRX can capture oxidation. Then, TRX enzyme reduces the oxidized PRX and in turn become oxidized itself and form an internal disulfide bridge. As well as glutathiones, TRX enzyme reacts with the coenzyme $NADPH$ to transmit the oxidation thanks to thioredoxin reductases (TR) enzyme. All these steps are detailed by the following reactions :

$$PRXred + H_2O_2 \rightarrow PRXox + 2\ H_2O \tag{1.4}$$
$$PRXox + TRXred \rightarrow TRXox + PRXred \tag{1.5}$$
$$TRXox + NADPH \xrightarrow{\text{TR}} NADP^+ + TRXred \tag{1.6}$$

- Catalase (Cat) [10, 6] are enzymes mostly stored in peroxisomes that catalyse direct reduction of hydrogen peroxide following the reactions :

$$2\ H_2O_2 \xrightarrow{\text{Cat}} O_2 + 2\ H_2O \tag{1.7}$$

All these reactions are important in oxidative stress detoxification allowing to remove H_2O_2 and ROS inside cells by transferring the oxidation mediated by few reactions. These 3 anti-oxidant processes have different behaviours and efficiencies. Catalase is one of the first enzyme that reduces hydrogen peroxide into water. Its activity is very high which makes this enzyme efficient to remove hydrogen peroxide. However, they are mainly located in the peroxisomes which limits the area of effect [11]. This anti-oxidant process is made by one reaction. In the other hand, glutathiones and thioredoxins are anti-oxidant molecules that reduce hydrogen peroxide via several enzymatic reactions. They are both very abundant in cytosol, nuclei and mitochondria. They are considered to be the most useful anti-oxidant molecules due to their omnipresence in cells, specifically for glutathiones that are in much higher concentration making it the most abundant small thiol molecules : $\approx 1 - 5mM$ [13] compared to few tens of μM for thioredoxins and catalase. They are both known to reduce oxidative damages present in cells with overlapping behaviours [11] but it has been shown that existing cell compartments have their own effect such as apoptosis for thioredoxins and deglutathionylation of actin which are important in neuronal cells ; cellular aging or fibroblast post-mitotic phenotype for glutathiones [11, 13]. Finally, they both see their oxidized molecules being reduced by $NADPH$-dependent enzyme such as glutathione reductase or thioredoxins reductase by transferring the oxidation. However, this reductase enzymes need reduced $NADP$, i.e. $NADPH$ to continue their action clearly revealing a high need of $NADPH$ production.

1.4 Role of metabolism in oxidative stress

1.4.1 NADPH metabolism

Oxidative stress is a cellular redox state perturbation made by ROS. It can induce damages to proteins, diseases or even cell death in extreme cases where ROS are not enough eliminated. In order to defend against, cells use anti-oxidant molecules that counteract oxidative stress by reacting with ROS, where most of them are catalysed by enzymes. The most present and efficient are glutathiones, thioredoxins combined to peroxiredoxins and catalase. Glutathiones and thioredoxins are catalysed by enzymes such as glutathione reductase and thioredoxin reductase which are $NADPH$-dependent enzymes. nicotinamide adenine dinucleotide phosphate ($NADP$) are either in reduced state ($NADPH$) or in oxidized state ($NADP^+$) [12]. Anti-oxidant enzymes need to have enough reduced $NADP$ to continue their actions and to be efficient. Thus, it is important to focus on the $NADPH/NADP^+$ metabolism to understand what are their sources of production and consumption in order to study oxidative stress response.

Understanding $NADPH$ metabolism is of major importance to analyse oxidative stress response. $NADP$ molecules are cofactors in a lot of metabolic

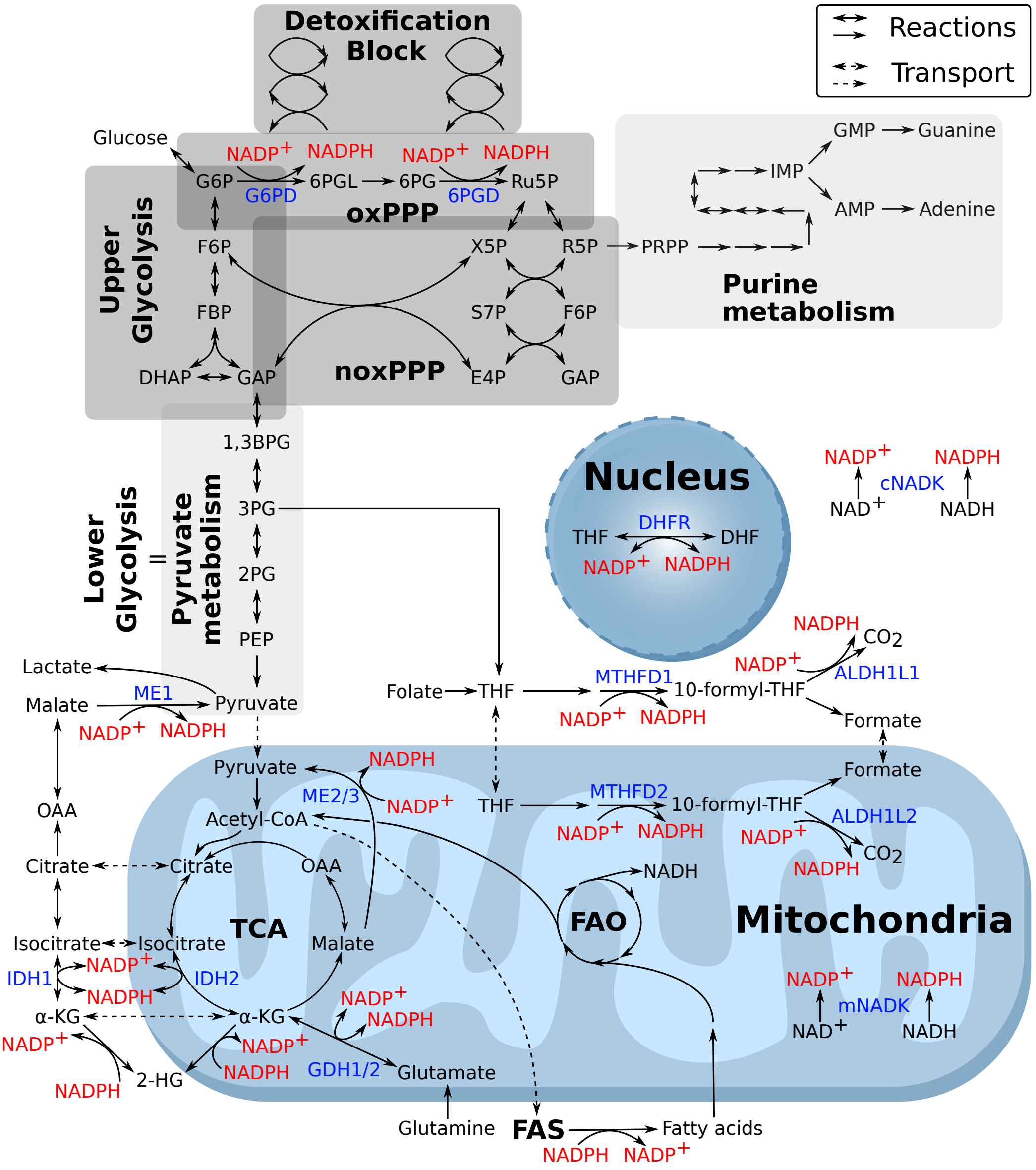

Figure 1.3: ***NADPH* metabolism.** Reduced and oxidized Nicotinamide adenine dinucleotide phosphate ($NADPH$ and $NADP^+$) molecules are shown in red using the corresponding enzymes shown in blue. The main production and consumption pathways of $NADPH$ are shown in the figure (i.e., oxPPP, folate metabolism, malic enzymes, fatty acid metabolism). Reactions are represented by solid arrows and transports are represented by dashed arrows. Major metabolic pathways of interest in this thesis are represented by darker grey block. Secondary metabolic pathways of interest in this thesis are represented by lighter grey block. oxPPP and noxPPP corresponds to respectively oxidative non-oxidative PPP. Acronyms are listed in the Abbreviation section. Inspired by Ju et al. 2020 [14].

pathways. In the cellular cytosol, the PPP contributes to $NADPH$ production about $\approx 30 - 50\%$, while the remaining part is produced, in cytosol or mitochondria, through folate cycle, malic enzymes and IDH1 (Figure 1.3) [14, 15, 16]. In turn, consumption of $NADPH$ is mainly related to fatty acid synthesis [15], besides antioxidant activities. In the context of oxidative stress response, the PPP (PPP) seems to be the metabolic pathways the most quickly and significantly upregulated upon oxidative stress. In the oxidative part of PPP, there is indeed a very high production of $NADPH$ due to glucose flux rerouting [14, 15, 17, 18, 19].

1.4.2 Pentose phosphate pathway (PPP)

The PPP is a metabolic pathway which starts at the early beginning of the glycolysis. It takes glucose molecules as input. This pathway can be splitted in two parts : oxidative (oxPPP) and non-oxidative (noxPPP) PPP [20].

- The oxPPP is made of chain of irreversible reactions catalysed by enzymes. Two of them are of major interest in the context of oxidative stress, and are the reason of the name of this first part. They correspond to $G6PD$ and $6PGD$ which catalyse the conversion of respectively $G6P$ and $6PG$ into $6PGL$ and ribulose-5-phosphate $Ru5P$ where both use $NADP^+$ to produce $NADPH$. These two enzymes are highly studied due to their capacities to produce $NADPH$ [15, 17, 18, 19, 21]. It has been shown that $G6PD$ has an increased activity in several types of cancers such as bladder, breast, prostate or gastric cancers. In the other hand, $6PGD$ enzyme activity is also very high and impact tumour growth. Changing $G6PD$ enzyme activity by for instance depleting it, decreases drastically $NADPH$ concentration which minimizes the oxidative stress defence [22]. However, in the case of $6PGD$ enzyme regulation, the results are contradictory with decreased level of $NADPH$ [23] or low/no change of $NADPH$ level [24, 25]. It is to note that, during $6PGD$ enzymatic reaction, a carbon is lost to produce a molecule of CO_2 which is of importance in terms of metabolic flux responses.

- The noxPPP is the non-oxidative part due to the non-interaction with $NADPH$. However, this branch is linked to the purine metabolism allowing to produce nucleotides, e.g. DNA replication, via $PRPPs$ enzyme. It is also linked to glycolysis at the level of GAP and $F6P$ metabolites. It is important to note that all reactions inside noxPPP are reversible such that the direction of metabolic flux can be in the two directions. In some cases associated to active cell cycle, a fraction of the metabolic flux goes from glycolysis through noxPPP toward the purine metabolism [24, 26, 27]. In the context of oxidative stress, the metabolic flux through noxPPP is rather expected to be recycled from oxPPP toward glycolysis to eventually return back to oxPPP [28].

1.4.3 Glycolysis

The glycolysis is a major metabolic pathway that is coupled to the PPP and that consumes glucose molecule to produce pyruvate metabolites through a linear chain of metabolic reactions. This metabolic pathway is commonly splitted into two parts [20] :

- The upper part of the glycolysis is made of enzymatic reactions from phosphoglucose isomerase (PGI) to glyceraldehyde 3-phosphate dehydrogenase ($GAPD$) where molecules that come out are mainly composed of 3 carbons. Because it is half the carbons quantity that enter into the glycolysis, the flux is also doubled. The enzymes are mainly reversible expect for phosphofructokinase-1 (PFK) which catalyses the reaction of fructose-6-phosphate ($F6P$) into Fructose 1,6-bisphosphate (FBP). However, it has the homologous enzyme which catalyses the reverse reaction called Fructose 1,6-bisphosphatase ($FBPase$). This part of the glycolysis is very interesting in the context of oxidative stress, because it is directly linked to both the oxPPP and noxPPP which allows to reuse glucose molecules that were reacting in the PPP [17, 18]. Indeed, glucose flux can be rerouted from the glycolysis to the oxPPP which then can be directed to the noxPPP and finally come back to the oxPPP by using the reverse glycolysis called gluconeogenesis. The more molecules that are reused, the more cyclical the flux, the greater the production of $NADPH$, the higher the oxidative stress defence.

- The lower part of the glycolysis corresponds to the pyruvate metabolism. It starts from $GAPD$ enzymatic reaction and allows to produce adenosine triphosphate (ATP) specifically during reactions catalysed by enzymes phosphoglycerate kinase (PGK) and pyruvate kinase (PK) which are the first and last enzyme of the lower glycolysis. ATP can be seen as cellular energy [29, 30]. Moreover, the pyruvate molecules can be used in different pathway : aerobic such as citric acid cycle and for electron transport and anaerobic in alcoholic fermentation to produce alcohol in yeast and several bacteria or homolactic fermentation to produce lactate in for instance several bacteria, muscle or red blood cells.

A lot of modeling studies of carbohydrate metabolism considers the entire glycolysis [31, 32]. However, in the context of oxidative stress response, it is reasonable to focus on the upper part of glycolysis that is the only part coupled to the PPP via $G6P$, $F6P$ and GAP metabolites. The lower glycolysis will be taken as an output flux which corresponds toward pyruvate production and eventually mitochondrial respiration. It is known that this pathway consumes around 90% of glucose without stress [17, 18, 33, 34], but it is significantly decreased during oxidative stress due to several regulations [18, 35, 36]. It is to note however that the link between lower part of glycolysis and oxidative stress has also been postulated through the oxidative regulation of pyruvate kinase [37, 19] and whether the fate outcome of pyruvate is to be consumed through mitochondrial respiration which generates ROS, or to wastefully produce excreted metabolites such as lactate, ethanol, acetate, even in presence of oxygen. This important issue relates to what is called the overflow metabolism, also known as Crabtree's effect or Warburg effect [38, 39]. It has been hypothesized that overflow metabolism could be somehow connected to oxidative stress and interpreted as an attempt to reduce the generation of reactive oxygen species [40], among many other hypothesis [41].

1.4.4 Purine metabolism

The purine metabolism is a pathway in continuity of the oxidative PPP. Even if it has not direct link in the $NADPH$ production or consumption, it consumes $R5P$ which comes from glucose molecules and are favoured to repair DNA damages induced by oxidative stress. This pathway is made of chain reactions in order to produce purine molecules :

$$R5P \xrightarrow{\text{PRPPs}} PRPP \rightarrow \rightarrow \rightarrow\ IMP \rightarrow GMP \text{ or } AMP \rightarrow Guanine \text{ or } Adenine \tag{1.8}$$

Guanine and adenine are purines used as nucleic base to produce nucleotide for DNA and are produced from Inosine Monophosphate (IMP). This pathway is then seen as a biomass production pathway. It has been shown that purine metabolism is essential during oxidative stress, in addition to serving as building blocks for DNA [42, 43]. Indeed, it allows to favour cell proliferation and survivability during oxidative stress [42]. Moreover, uric acid are produced at the end of purine metabolism and would serve as anti-oxidant. Thus, more glucose molecules are rerouted toward the purine metabolism during oxidative stress. In the context of the thesis, this pathway will be used as output flux via phosphoribosylpyrophosphate ($PRPP$) synthase ($PRPPs$).

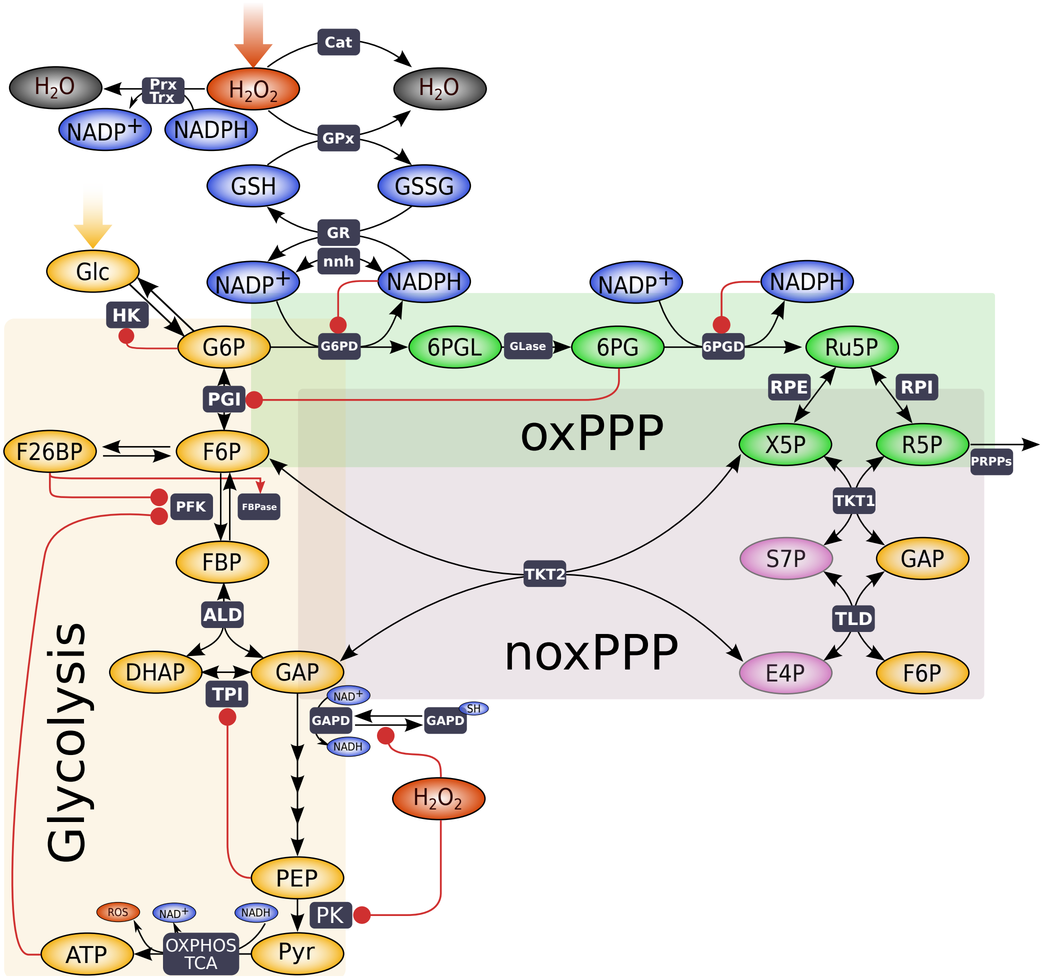

Figure 1.4: Metabolic regulations of PPP and glycolysis. Ellipses represent metabolites. Black arrows are the reactions and black rectangles are the corresponding enzymes. Red arrows correspond to regulations. Metabolic pathways are organized around (i) the anti-oxidant system (blue metabolites), (ii) the oxidative and non-oxidative pentose phosphate pathway (green and violet metabolites) and (iii) the glycolytic pathway (yellow metabolites).

1.5 Regulation of the metabolic response to oxidative stress

Metabolic pathways are regulated in order to satisfy different cellular needs such as proliferation, repair and energy or redox homeostasis, as function of the context, especially the presence of nutrients, stress or cell-to-cell communication (Figure 1.4). Indeed, enzyme activities can be regulated through a variety of mechanisms inducing either rapid changes of their activity or slow change of their expression. The expression of most enzymes of the glycolysis and the PPP are indeed known to be highly regulated through transcriptional, post-translational and allosteric mechanisms. Because this thesis study focuses on the adaptation dynamics occurring at early time from seconds to tenth minutes, we will restricted our focus to a specific set of regulatory mechanisms where metabolites directly interact to enzymes to modify their activities at such timescale. In the context of oxidative stress, it has been shown that $NADPH$ inhibition on $G6PD$ and $6PGD$ decrease during oxidation [44, 45, 34]. Hydrogen peroxide is one of major reactive oxygen species and inhibits several nodes of the glycolysis such as on $GAPD$ [36, 35, 46] or PK [37, 19] which directly links them to oxidative stress. However, other inhibitions or activations of the metabolic pathways are present such as on PGI [17, 47, 48], PFK and $FBPase$ [49, 50, 51], TPI [52, 53].

These regulations can be implemented by different types of mechanisms : Competitive, allosteric and oxidative inhibitions (Figure 1.5).

- Competitive inhibition is a regulation where an inhibitor binds to an enzyme at the active site of a substrate. Thus, the reactant cannot bind to the enzyme preventing the reaction to happen. $NADPH$ is known to competitively inhibiting $G6PD$ and $6PGD$ [44, 45, 34].

- Allosteric inhibition is a regulation where an inhibitor binds to an enzyme, modifying the active site, avoiding substrate to bind. This is the case for example when $6PG$ and $G6P$ is inhibiting respectively PGI [17, 48] and HK [54].

- Oxidative inhibition is a regulation where reactive oxygen species oxidise a sulfur linked to a cysteine of an enzyme. Oxidations of these atoms will induce creation of a disulfide bond making the enzyme inactive [55]. Once the enzyme is inactivated, the active site is then modified which prevents the reaction to happen. This is the case for example when H_2O_2 inhibits $GAPD$ [36, 35, 46].

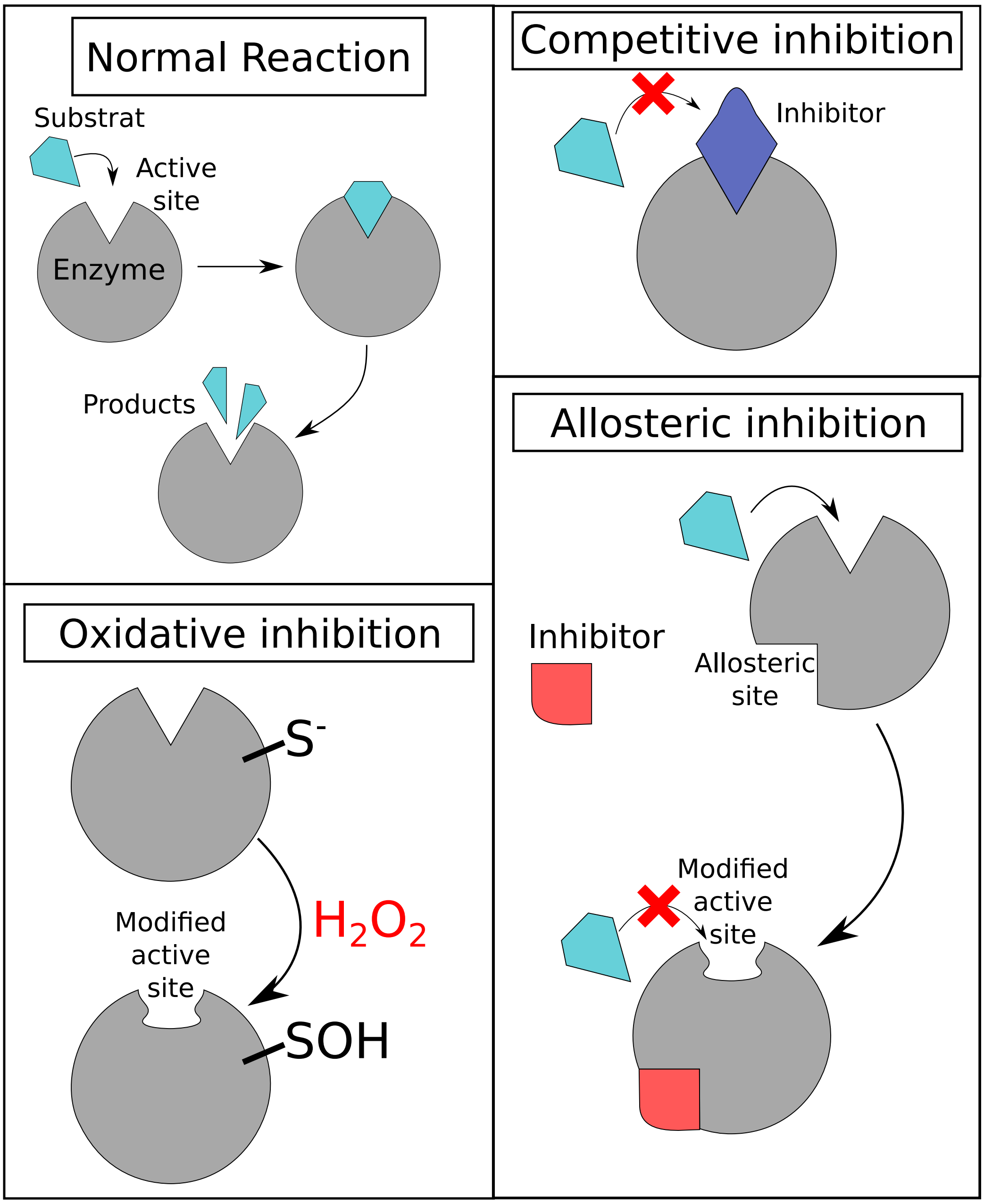

Figure 1.5: Control of enzymatic activity. Schematic representation of enzymatic reaction, competitive, allosteric, and oxidative inhibitions. Grey circle corresponds to an enzyme. Light blue is a substrate molecule. Darker blue and red are inhibitory molecules in respectively competitive and allosteric inhibition.

At longer timescale, stress-sensitive transcription factors such as $Nrf2$ and $p53$ are known to significantly contribute to the regulation of metabolic response to oxidative stress. Nuclear factor erythroid-derived 2-related factor 2 ($Nrf2$) is a transcription factor that highly transcriptionally regulates anti-oxidants genes such as glutathiones and thioredoxins anti-oxidants systems [56]. It also controls the expression of most enzymes in the PPP [57]. Another example is the tumour protein $p53$ that regulates directly or indirectly the transcription of several enzymes including $G6PD$ and PFK [58, 59, 60].

1.6 Adaptation dynamic during oxidative stress

Homeostasis is all chemical reactions in cells used to maintain themselves alive. However, during a perturbation, the cellular state is rapidly changed and can induce damages or diseases. Metabolic pathways are regulated in

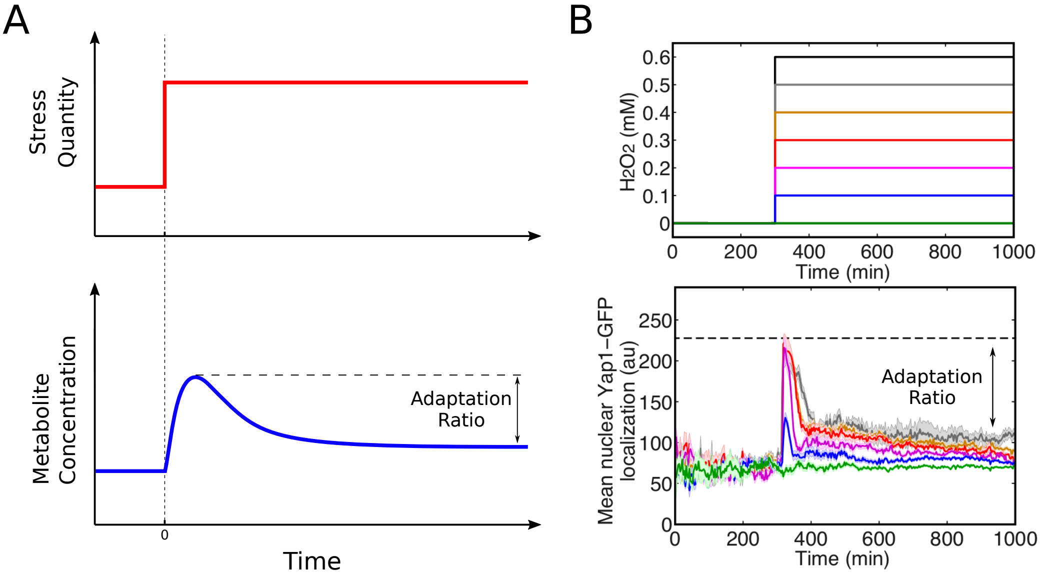

Figure 1.6: Temporal adaptation during stress perturbation. (A) Top : The stress (Red) is applied at $t_0 = 0$ (arbitrary unit). Bottom : A metabolite concentration (blue) displays an adaptation characterised by the ratio between maximum and steady state values called adaptation ratio. (B) Example of experimental result extracted from Goulev et al. 2017 [61]. Top : Temporal dynamics of oxidative stress profiles. Different levels of external hydrogen peroxide H_2O_2 concentrations are applied to yeast cells. Bottom : Temporal dynamics of mean nuclear transcription factor Yap1-GFP displaying adaptation as a function of the H_2O_2 level.

order to react and counteract the changes. When regulations are sufficiently efficient, cells can come back close to their initial state. This phenotype is called adaptation (Figure 1.6-A). Thus, it is a phenotype of a rapid and significant change due to the perturbation and then a relaxation due to the effects of regulations. When the final steady state is similar or close to the initial state, then the adaptation is respectively perfect or near-perfect [62, 63, 64]. It is often observed when metabolic pathways are composed of a negative feedback loop [64].

A strong adaptation means that the metabolism is sufficiently regulated to react and counteract the changes. However, the absence of an adaptation phenotype does not means an absence of regulation because a very fast regulation would induce instantaneous changes. Thus, the response to a perturbation is a compromise between rapid regulation allowing to minimize changes but with high metabolic cost and slow regulation which could imply high changes and potential damages in short term. This compromise can be captured by the presence of the adaptation phenotype. In the case of oxidative stress, adaptation has been observed in yeast by Goulev et al. 2017 [61] (Figure 1.6-B) or also in mammalian cell by Simiuc et al. 2020 [65]. Indeed, under hydrogen peroxide perturbation, the transcription factor Yap1 is relocated into the nucleus in yeast cells. However, the PPP and glycolysis are known to be highly regulated in order to highly produce $NADPH$ inducing decreasing nucleus Yap1 localisation. It then means that the rapid regulations of this specific carbons metabolism have important impacts in the oxidative stress detoxification.

Chapter 2

Methods

Oxidative stress is a perturbation of cellular redox state inducing potential damages, cell death or diseases. Regulation of the metabolism allows to drastically increase the $NADPH$ production in order to favour the stress response. A theoretical analysis of the oxidative stress response will be made in this thesis via a mathematical model. It will represent the temporal variation of metabolite of the PPP and glycolysis in response to a hydrogen peroxide perturbation. In this chapter, we introduce the modeling framework and tools that are used to construct a kinetic model of metabolic pathways, ranging from biochemical kinetics, data analysis, optimization procedure such as Monte Carlo Markov chain (MCMC) or genetic algorithm (GA). In addition, conventional methods to analyse the behaviour of metabolic network such as flux balance analysis (FBA) and metabolic control analysis (MCA) will be also introduced. All these methods are standard in the context of models of metabolism [66, 67].

2.1 Metabolic network modeling

A mathematical model made of ordinary differential equations (ODE) links metabolite concentration variations to reaction rates. In this section will be recall the procedure to generate ODEs corresponding to a metabolic network and to express their reaction rates as function of metabolite concentrations and parameters by using chemical laws (Figure 2.1).

2.1.1 Kinetic modeling of metabolism

Theoretical analysis is often useful to obtain complementary informations to experimental measurements or to make new predictions which could be

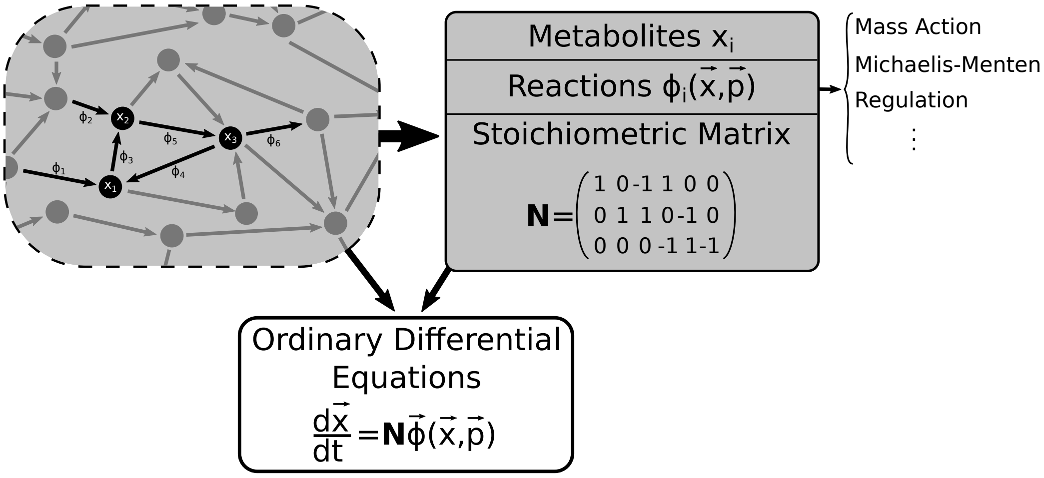

Figure 2.1: Mathematical modeling scheme of a metabolic network. A metabolic network of interest is modeled by using ordinary differential equations and link variations of metabolite concentrations $\vec{x}$ to reaction rates $\vec{\phi}$ with the stoichiometric matrix $\mathbf{N}$. Expression of reaction rates can be made by chemical laws.

---

verified experimentally. In this thesis will be addressed a theoretical analysis of the network made of PPP, glycolysis and anti-oxidant pathways using a mathematical model. A kinetic model of metabolic pathways can typically be formulated as a set of ordinary differential equations (ODE) describing temporal evolution of variables as a function of time [68] :

$$\frac{d\vec{x}}{dt} = \mathbf{N}\vec{\phi}(\vec{x},\vec{p}) \tag{2.1}$$

where $\mathbf{N}$ is the stoichiometric matrix. Each element is a stoichiometric coefficient of the corresponding reaction. $\vec{x}$ is the metabolic concentrations vector and the variation of metabolite concentrations is represented by $\frac{d\vec{x}}{dt}$. Thus, $\vec{\phi}(\vec{x},\vec{p})$ is the reaction rates vector which will depend as a function of the metabolite concentrations and the chemical parameters. They can be kinetic, regulation (i.e. inhibition or activation) or saturation parameters. At steady state (i.e. $\frac{d\vec{X}}{dt} = 0$), the vector of metabolite concentrations and flux rates are written with capitalized $\vec{X}$ and $\vec{\Phi}$. It exists a lot of mathematical formalisms to express the reaction rates [69]. In the context of this thesis, the following chemical laws will be used : Mass action laws and Michaelis-Menten equations.

2.1.2 Reaction kinetics

A metabolic network is made of chemical reactions such as the general reversible reaction :

$$\sum_j a_j S_j \underset{k_-}{\overset{k_+}{\rightleftharpoons}} \sum_j b_j P_j \tag{2.2}$$

where S and P are respectively the reactants and products. a and b are the stoichiometric coefficients. Parameters k_+ and k_- are the kinetic constants respectively for the forward and backward reactions corresponding to their reaction rates ϕ^+ and ϕ^-. For irreversible reactions, k_- is equal to 0. In most chemical reactions, one or two molecules are consumed for a reaction. Such reactions can then be expressed using chemical laws.

Mass action law

Mass action law is a chemical law which allows to mathematically express chemical reactions $\vec{\phi}(\vec{x}, \vec{p})$ as a function of the metabolite concentrations $\vec{x}$ and kinetic parameters $\vec{p}$ [68]. It assumes that rates of reactions are proportional, at a certain order, to reactant concentrations which are molecules reacting and consumed to generate products. It means that the higher reactant concentration, the higher the rate. When reactant concentrations are infinite, then the reaction rate will also increase to infinite. To a better understanding of the implication of this law, mass action law is implemented for the general reversible reaction (eq 2.2). The total rate ϕ can then be written which will be the difference between reaction rates of each direction (forward/positive ϕ^+ and backward/negative ϕ^-) :

$$\phi \;=\; \phi^+ \;-\; \phi^- \;=\; k_+ \prod_j [S_j]^{a_j} - k_- \prod_j [P_j]^{b_j} \tag{2.3}$$

where S and P are respectively the reactant and product. a and b are called orders of the mass action law. In the further studies, only the linear cases (i.e. first order) will be used due to stoichiometric coefficients (i.e. order parameter a and b) equal to 1.

Biochemical reactions are governed by thermodynamic principles. Reactions consist of transferring energy from a molecule to another. The relevant measure of this quantity at constant pressure and temperature is the Gibbs free energy G. Thus, during a reaction, the variation of energy will be quantified by $\Delta G = \sum_j G_{P_j} - \sum_j G_{S_j}$ where G_S and G_P are the Gibbs free energy of respectively the reactants and products. If $\Delta G < 0$, then the reaction will occurs spontaneously forward. If $\Delta G > 0$, then the reaction will not occur spontaneously. Equilibrium means $\Delta G = 0$ and allows to express the standard Gibbs free energy ΔG° which is ΔG at standard condition :

$$\Delta G^\circ = -RT \ln(Keq) \tag{2.4}$$

where R is the universal gas constant and T the temperature. Keq is the equilibrium constant which is the ratio of reactants and products concentrations at equilibrium. During the model construction, experimental measurement of the Gibbs free energy [32, 70] are used to determine equilibrium constant of the model and are made at $T = 310.15K$.

Concerning the mass action law, because the positive and negative reaction rates are equal at equilibrium, the equilibrium constant Keq will be expressed as :

$$\Phi = 0 \iff Keq = \frac{k_+}{k_-} = \frac{\prod_j [P_j]^*}{\prod_j [S_j]^*} \tag{2.5}$$

where $[x]^*$ is the concentration of the molecule x at equilibrium. The total reaction rate can then be written as function of the equilibrium constant :

$$\phi = k_+(\prod_j [S_j] - \frac{k_-}{k_+} \prod_j [P_j]) = k_+(\prod_j [S_j] - \frac{\prod_j [P_j]}{Keq}) \tag{2.6}$$

With this expression, the reaction rate will be positive meaning forward reaction when $\prod_j [S_j] > \frac{\prod_j [P_j]}{Keq}$. Thus, the higher the equilibrium constant, the more difficult it is to reverse the direction of reaction called backward reactions by modifying the concentration of the reactants and products. When the equilibrium constant is infinite, the reaction is irreversible.

Michaelis-Menten kinetics

In glycolysis and PPP, reactions are catalysed by enzymes. When an enzyme is involved in a chemical reaction, the corresponding rate can be expressed using Michaelis-Menten formalism [68] instead of mass action law. To derive the Michaelis-Menten kinetic law, an enzymatic reaction has to take into consideration intermediate reactions described in Figure 1.5 of Section 1.5 which can be written as :

$$E \ + \ S \underset{k_{-1}}{\overset{k_1}{\rightleftharpoons}} ES \xrightarrow{k_2} E \ + \ P \tag{2.7}$$

where S is a substrate, i.e. the reactant, E is the enzyme that catalyses the reaction, and P is the product. During chemical interactions, enzyme binds to the substrate and forms a complex ES before changing its conformation to release the product. Each reaction has their corresponding reaction rate constants k_1, k_{-1} and k_2. By applying the mass action law, each reaction rate can be mathematically expressed. Then, the Michaelis-Menten reaction rate can be written as :

$$\phi = \frac{V_{max,i}[S]}{[S] + Km_i} = \frac{k_i[S]}{1 + \frac{[S]}{Km_i}} \tag{2.8}$$

where $V_{max,i}$ is the maximum reaction speed and Km_i is the Michaelis-Menten constant for an enzyme $E = i$. In this thesis will be used the second expression of the reaction rate using $k_i = V_{max,i}/Km_i$ to easily relate with mass action kinetic for $Km \to \infty$. With this final expression, the reaction rate does not increase linearly but behaves as the hyperbolic curve (Figure 2.2). Then, maximum reaction speed V_{max} is the maximum value that can reach the reaction only if substrate concentration tends to infinity. Michaelis-Menten constant K_m is a concentration value that substrate S can reach to have a reaction rate equal to half the maximum rate. It is important to note that maximum reaction rate V_{max} is proportional to enzyme concentration in this formalism. If it changes as a function of time or changes from a cell to another, V_{max} will also vary. As oxidative stress will be studied during short time scale response, enzyme concentration and thus V_{max} also can be considered as constant.

A generalization of the uni-uni Michaelis-Menten equation can also be used for irreversible and reversible uni/bi-substrate reaction kinetics [71] :

$$\phi([S],[P],k_i,Keq_i,Km_i) = \frac{k_i \prod_j [S_j]}{\prod_j (1+[S_j]/Km_{Sj,i})} \tag{2.9}$$

$$\phi([S],[P],k_i,Keq_i,Km_i) = \frac{k_i\left(\prod_j [S_j]-(Keq_i)^{-1}\prod_j [P_j]\right)}{\prod_j\left(1+[S_j]/Km_{Sj,i}+[P_j]/Km_{Pj,i}\right)} \tag{2.10}$$

where $j = 1$ for unisubstrate reactions and $j = 1;2$ for bisubstrate reactions, and where the denominator contains numerous terms for each substrates and products. The assumption that $[S_i]$ or $[P_i] \ll Km_i$ can be made so as to reducing to a mass action dynamic allowing to reduce the number of terms and parameter in denominator.

Metabolic regulation of enzyme activity

Examples of metabolic regulations involved during oxidative stress have been presented in Section 1.5. To implement mathematically this type of metabolite-enzyme interaction, a similar formalism as Michaelis-Menten dynamic can be used but instead of saturating as a function of the substrate, reaction rate

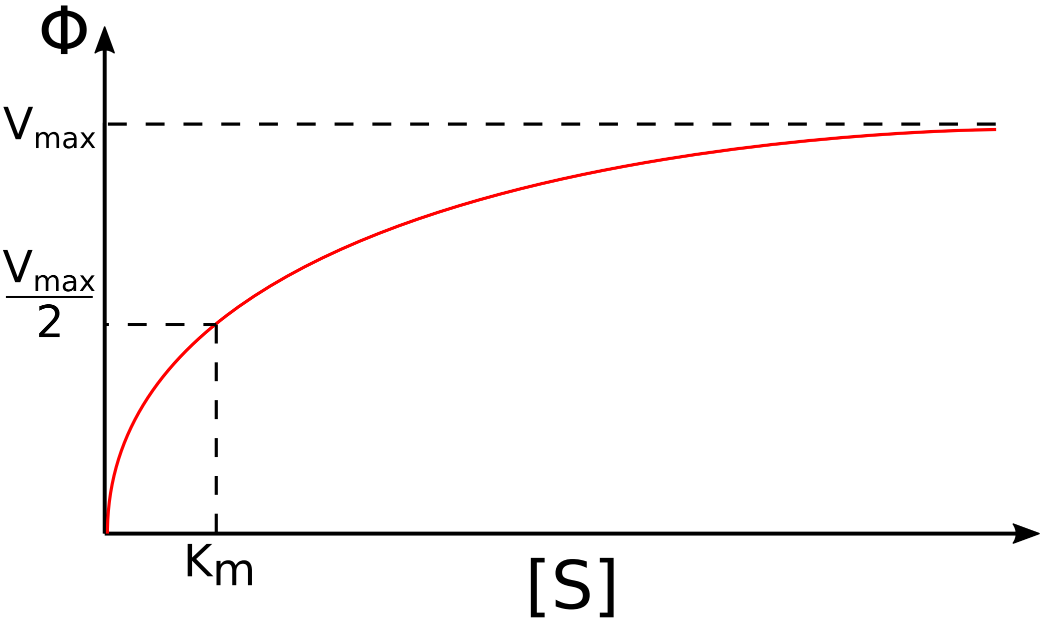

Figure 2.2: Michaelis-Menten reaction rate ϕ curve as function of substrate concentration $[S]$. K_m represents the Michaelis-Menten constant which is the value that $[S]$ can take to reach half the maximum rate V_{max}.

---

will decrease as a function of inhibitor concentration (Figure 2.3) depending on an inhibition constant Ki_i.

Thus, in the case of negligible Michaelian saturation, a general reversible reaction i that consumes the reactant S to produce P and inhibited by the inhibitor I can have a rate expressed mathematically by a generalized mass action law as :

$$\phi([S],[P],[I],k_i,Keq_i,Ki_i) = k_i \left(\prod_{j=1,m} [S_j] - (Keq_i)^{-1} \prod_{j=1,n} [P_j] \right) (1+[I]/Ki_i)^{-1} \tag{2.11}$$

where m and n are the number of substrates and products. ϕ is a reaction rate, and k_i, Ki_i, Keq_i are respectively maximum speed, inhibition and equilibrium constant. Note that the same maximum speed constant as generalised Michaelis-Menten dynamic is used in this case to keep the same formalism. When two behaviours, i.e. saturation and inhibition, are non negligible for the same reaction, both terms in the denominator are kept inducing two possible ways to decrease the maximum speed : as function of the substrate or inhibitor concentrations. Thus, the reaction rate expression will depend as

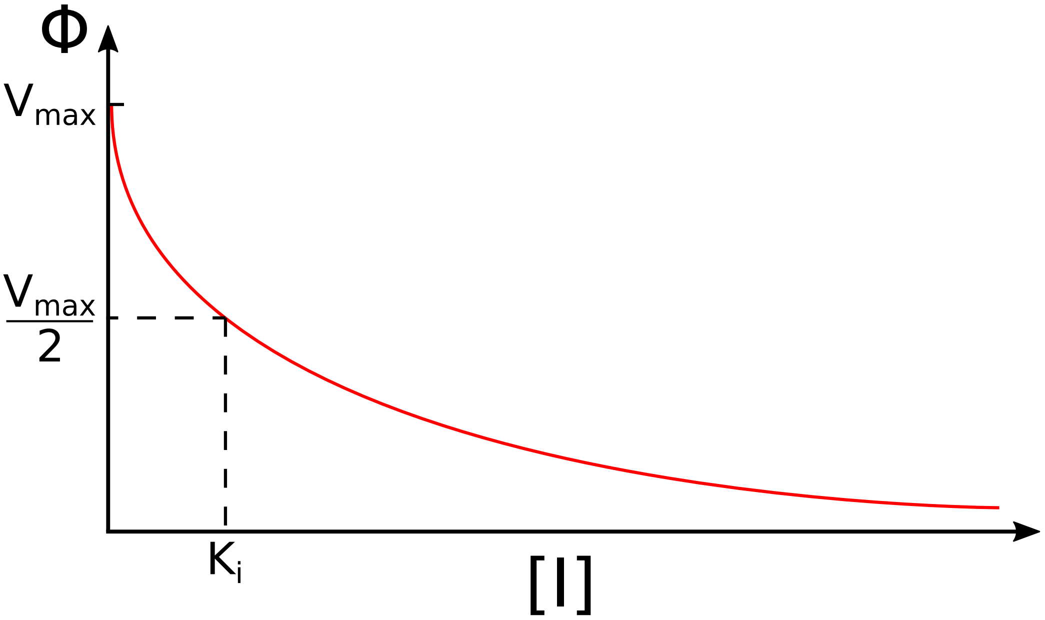

Figure 2.3: Reaction rate ϕ curve as function of inhibitor concentration I. K_i represents the inhibition constant which is the value that $[I]$ can take to reach half the maximum rate V_{max}.

---

a function of the regulation type [72]. For instance, a rate with competitive CI and non-competitive nCI inhibition and taking into account saturation can be expressed as :

$$\phi^{CI}([S],[P],[I],k_i,Keq_i,Km_i,Ki_i) = \frac{k_i\left(\prod_j [S_j] - (Keq_i)^{-1}\prod_j [P_j]\right)}{\prod_j\left(1+[S_j]/Km_{Sj,i}+[P_j]/Km_{Pj,i}+[I]/Ki_i\right)} \tag{2.12}$$

$$\phi^{nCI}([S],[P],[I],k_i,Keq_i,Km_i,Ki_i) = \frac{k_i\left(\prod_j [S_j] - (Keq_i)^{-1}\prod_j [P_j]\right)}{\prod_j\left(1+[S_j]/Km_{Sj,i}+[P_j]/Km_{Pj,i}\right)\left(1+[I]/Ki_i\right)} \tag{2.13}$$

In the context of this thesis, only the formalism using competitive inhibition will be used to model PPP and glycolysis inhibition during oxidative stress response.

2.2 Steady state analysis

A mathematical model made of ordinary differential equations allows to obtain temporal dynamics of metabolites in the context of a metabolic network.

A lot of studies are based on steady state solution, i.e. $d\vec{X}/dt = 0$ which allows to obtain a lot of informations, before entering in complex analysis such as numerical simulations providing temporal dynamics. Specific methods have been developed to analyse metabolic pathways at steady state (i) to study metabolic flux state via flux balance analysis or (ii) to study metabolic sensitivity to a small perturbation via metabolic control analysis.

2.2.1 Flux balance analysis

Flux Balance Analysis (FBA) is a mathematical method used to represent the steady state solution space of stoichiometric models supplemented with a set of constraints [73, 74, 68, 72, 75, 76]. FBA is particularly useful to identify the main cellular objectives and constraints that determine the metabolic flux state in various environmental conditions [77]. FBA framework can also be used, just to determine the allowable flux solution space and to represent the flux state in such space as a combination of elementary modes.

Explained in section 2.1, a metabolic network can be modeled by ordinary differential equations of metabolite concentrations $\vec{x}$ variations as a function of time which is equal to the corresponding reaction rates $\vec{\phi}$. At steady state, the metabolite concentration variation is equal to zero, thus equation (2.1) becomes the balance equation :

$$0 = \mathbf{N}\vec{\Phi}(\vec{X}, \vec{p}) \tag{2.14}$$

where capitalized $\vec{X}$ and $\vec{\Phi}$ represent steady-state concentration and flux vectors. $\mathbf{N}$ is the stoichiometric matrix $m \times n$ which has m rows equal to the number of variables, and n columns equal to the number of reaction rates. Then, the rank of the stoichiometric matrix can be defined with the rank–nullity theorem :

$$\mathrm{Rank}(\mathbf{N}) + \mathrm{Nullity}(\mathbf{N}) = n \tag{2.15}$$

where Nullity($\mathbf{N}$) equal to the Kernel dimension (dim(Ker($\mathbf{N}$))). When the mathematical model takes into account only independent variables, the dimension of the rank is equal to the number of metabolite concentrations m, inducing [78] :

$$\dim(\mathrm{Ker}(\mathbf{N})) = n - \mathrm{Rank}(\mathbf{N}) = n - m \tag{2.16}$$

The kernel dimension of the matrix $\mathbf{N}$ is equal to the number of modes that can be found by solving the matrix equation 2.14. The corresponding result is a basis of vectors that will reflect the pathways which can be found in the network. It does not exist unique solution, however, in this thesis, vectors with the maximum numbers of zeros and integer values will be kept to capture the essence of a minimal pathway that can take a network [79]. Then, more realistic modes can be found by combining these vectors in order to create a new basis. Finally a biological flux state $\vec{\Phi}$ will be a combination of elementary modes $\vec{V_i}$:

$$\vec{\Phi} = \sum_i \lambda_i \vec{V_i} \tag{2.17}$$

where λ_i is the component of the elementary mode $\vec{V_i}$. To find these modes, it is enough to know the structure of the network. Indeed, this method does not need to express reaction rates using chemical laws such as mass action law or Michaelis-Menten formalism.

2.2.2 Metabolic control analysis

Metabolic Control Analysis (MCA) is a mathematical framework used to analyse metabolic pathways by describing the sensitivity at equilibrium of metabolites concentrations or fluxes to a variation of enzyme activity, i.e. flux rate [80, 68, 81, 72, 82] (Figure 2.4). It can be extended to sensitivity to variation of other chemical parameters such as saturation or regulation parameters. After building an oxidative stress response model, sensitivity of the variables and reaction rates can be analysed via a change of parameters which are directly proportional to enzyme activity or regulation parameters. MCA allows to study these sensitivities thanks to properties called control coefficients, response coefficients and elasticities.

MCA is applied at equilibrium, thus changing a rate parameter will modify the steady state concentrations or fluxes curve. In Figure 2.4, the system is at equilibrium when rates are equal : $\Phi_1 = \Phi_2$, meaning steady state rates take their values when curves are crossing each others. Changing one of these enzyme activities (i.e. rate parameters) will change the corresponding reaction rates which will induce modification of the crossing point. It has for consequence to change other reaction rates but also metabolite concentrations.

$\vec{X}$ denotes the metabolite concentrations and $\vec{\Phi}$ (written $\vec{J}$ in this study) denotes the fluxes rates, both at equilibrium. Concentration and flux control coefficients $C^{X_j}_{\Phi_i}$ and $C^{J_j}_{\Phi_i}$ can be defined as relative steady state variation of respectively a metabolite concentration or flux as function of a small variation of a flux rate induced by modifying the corresponding parameter. It can be

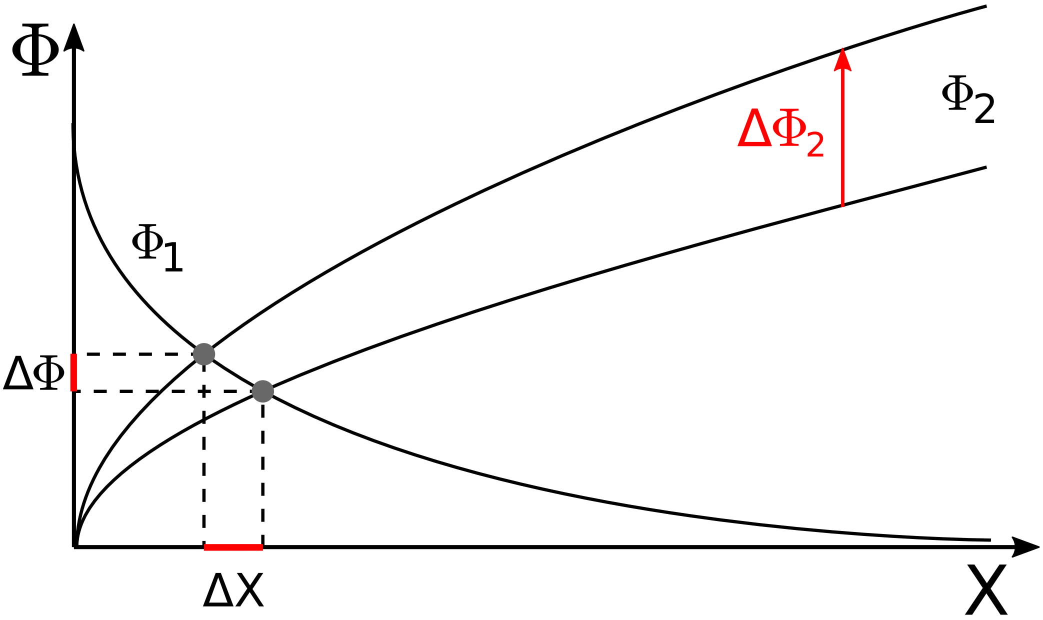

Figure 2.4: Principle of metabolic control analysis. X is metabolite concentration, Φ the reaction rate. $\Phi_1 = \Phi_2$ corresponds to steady state. ΔX is the variation of a quantity X to a variation of a flux rate $\Delta\Phi$.

---

written mathematically by the following respective derivative :

$$C_{\Phi_i}^{X_j} = \frac{dX_j}{d\Phi_i}.\frac{\Phi_i}{X_j} = \frac{d\ln(X_j)}{d\ln(\Phi_i)} \tag{2.18}$$

$$C_{\Phi_i}^{J_j} = \frac{dJ_j}{d\Phi_i}.\frac{\Phi_i}{J_j} = \frac{d\ln(J_j)}{d\ln(\Phi_i)} \tag{2.19}$$

These coefficients are positive when the concentrations/fluxes increase when the enzyme activity increases and reversibly. It has no effect when coefficient is equal to zero. Thus, it will be an important tool to estimate whether an enzyme has a positive or negative effect on the oxidative stress detoxification meaning hydrogen peroxide concentration removing. Reversely, It allows to estimate whether a change of oxidative stress parameters implies a positive or negative effect on metabolite concentrations or fluxes. The metabolite concentration control coefficients can be linked to fluxes control coefficients with the elasticities matrix $\boldsymbol{\epsilon}_X^J$ by :

$$\vec{C}_{\Phi_i}^{\vec{J}} = \vec{\Pi}_{\Phi_i} + \boldsymbol{\epsilon}_{\vec{X}}^{\vec{J}} \vec{C}_{\Phi_i}^{\vec{X}} \tag{2.20}$$

where $\vec{C}$ are control coefficient vectors to the corresponding $\vec{J}$ and $\vec{X}$ which are fluxes and metabolite concentrations vectors of the entire system at steady state for a specific enzyme perturbation i. $\vec{\Pi}$ is a unitary vector in the direction of Φ_i. $\boldsymbol{\epsilon}_{\vec{X}}^{\vec{J}}$ is the matrix of elasticities $\epsilon_{X_i}^{J_j} = \frac{\partial \ln(J_j)}{\partial \ln(X_i)}$ which represents the variations of fluxes with respect to variation of concentration at steady state.

It exists similar coefficients called response coefficients for modification of different parameters of enzyme activity :

$$R_{p_i}^{X_j} = \frac{\partial \ln X_j}{\partial \ln p_i} \tag{2.21}$$

$$R_{p_i}^{J_j} = \frac{\partial \ln J_j}{\partial \ln p_i} \tag{2.22}$$

They are often used to estimate the importance of metabolic interactions such as allosteric regulations. A variation of the response coefficients after a modification of a regulation parameter would reveal the importance of this regulation on a specific metabolic concentration or flux. Thus, a measure on the response coefficient of hydrogen peroxide production would show whether the regulation favours oxidative stress detoxification.

2.3 Stochastic modeling of metabolism

The metabolism is all chemical reactions in cells that maintain them alive by achieving specific functions such as production of energy, biomass or the stress defence. A reaction involves molecules which are discrete entities. When they are present in large quantities such as in the metabolism, discrete production or consumption of molecules do not have high impact on the properties of the system. Indeed, in general, the typical concentration of a metabolite is between the micromolar and millimolar which is equivalent to $\approx [10^5 - 10^8]$ molecules depending of the cellular volume which is typically $\approx 2000\mu m^3$. However, when this number is smaller, the stochasticity becomes much more important, impacting the properties of the system which is typically the case for instance with DNA molecules. Moreover, each cellular components can interact between each others which can add noise. Fluctuations in single component are also present impacting the performance of the network. The stochasticity is then an important feature that can be modeled. In this section will be presented the three main types of stochastic modeling of biochemical pathways.

2.3.1 Chemical master equation

The Chemical Master Equation (CME) describes the temporal dynamic of the probability to be in a certain state for each variable of the system. To mathematically follow the probabilities to be in each possible state, the equations do not describe the global concentration of the chemical compounds described in the deterministic ODE but follow the number of molecules. Thus, a possible state of the stochastic system is written as $\vec{\omega}$. The probability to be in the state $\vec{\omega}$ at time t can be written as $P(\vec{\omega}, t)$. This probability is changing as a function of time due to the chemical reactions which allow to swap from state to another. The transitions are captured by the chemical master equation [83, 84] :

$$\frac{dP(\vec{\omega}, t)}{dt} = \sum_j \left[\eta_j(\vec{\omega} - \vec{N}_j) P(\vec{\omega} - \vec{N}_j, t) - \eta_j(\vec{\omega}) P(\vec{\omega}, t) \right] \tag{2.23}$$

where $\eta(\vec{\omega})$ are the reaction propensities which are the probability of a reaction to reach a state $\vec{\omega}$. $\vec{N}_j$ is the stoichiometric coefficient vector of the corresponding reactions. Thus, the sum over j is the sum of all reactions that consume and produce a molecule which can occur in the network. The two terms of the equation are therefore the reactions rates which increase or decrease respectively the probability to be in the state $\vec{\omega}$.

2.3.2 Stochastic simulation algorithm

The stochastic simulation algorithm (SSA) is an algorithm that can reproduce the randomness and discrete behaviour of a system dynamic [85, 86]. When the stochasticity cannot be neglected, the use of stochastic algorithm is well justified to compute biological phenomena [87, 88]. It has been shown that stochastic simulation algorithms can be splitted in different smaller groups such as direct method, the first reaction method, the next reaction method and the rejection-based SSA in the exact stochastic simulation group, whereas the τ-leaping method [89, 90] and the chemical Langevin method are part of the approximate stochastic simulations which follow the Gillespie algorithm [91]. In this thesis will be presented a new ^{13}C-MFA algorithm based on SSA and also a stochastic study of cellular decision making using a model made by Langevin equations [2].

Two famous stochastic simulation algorithm are Gillespie algorithm introduced in 1976 and the next reaction method [92] which simulate a stochastic system of equation using chemical master equation [93]. This algorithm makes iterations to discretely reproduce the reactions that can occur in cells. In this thesis will be used a modified next reaction method which follows the general steps [92, 94] :

(i) generate the time necessary to make happen the reaction, and the corresponding propensities ;

(ii) determine which reaction that will occurs, and execute the reaction by changing the molecules numbers and by increasing the time value ;

(iii) recompute the new time value and propensities.

These steps allow to make happen chemical reactions. This algorithm is efficient because it uses small computational resources for instance by using only one random number per simulation loop, and with a calculation time proportional to logarithm of the reactions number.

2.3.3 Langevin equation

The chemical master equation can be approximated to the Langevin equation which is a stochastic differential equation representing a system undergoing fluctuations. It can be applied to a biochemical reaction network :

$$\frac{dX_i}{dt} = \sum_j N_{ij}\eta_j(t) + \sum_j N_{ij}\sqrt{\eta_j(t)}\zeta_j(t) \tag{2.24}$$

$$< \zeta_j(t)\zeta_{j'}(t') > = \frac{1}{\Omega}\delta_{j,j'}\delta(t-t') \tag{2.25}$$

where $\delta(t)$ is the Dirac delta function. $\vec{X}$ represents the system variables which are subjected to uncorrelated, statistically independent gaussian white noises $\zeta(t)$ inversely proportional to the system size Ω. The variation of these variables are given as a function of the reactions j associated to the propensities $\eta_j(t)$ and the stoichiometric values N_{ij}. The propensities can depend as a function of a perturbation such as during oxidative stress.

2.4 Data-driven model construction

A mathematical model of a metabolic network consists of describing the variation of the metabolite concentrations as a function of time. They depend directly to the model parameters which are constant quantities that influence directly the output, the prediction of the model. The entire parameter space, which can be seen as a genotype, encodes all the possible results of the model, corresponding to the phenotype. In the context of metabolic pathways, model depends of the reactions which can be mathematically expressed by chemical laws linking variables to parameters. It exists different classes of parameters such as kinetic, saturation or regulation (i.e. inhibition or activation) parameters (Section 2.1), which all can be determined by

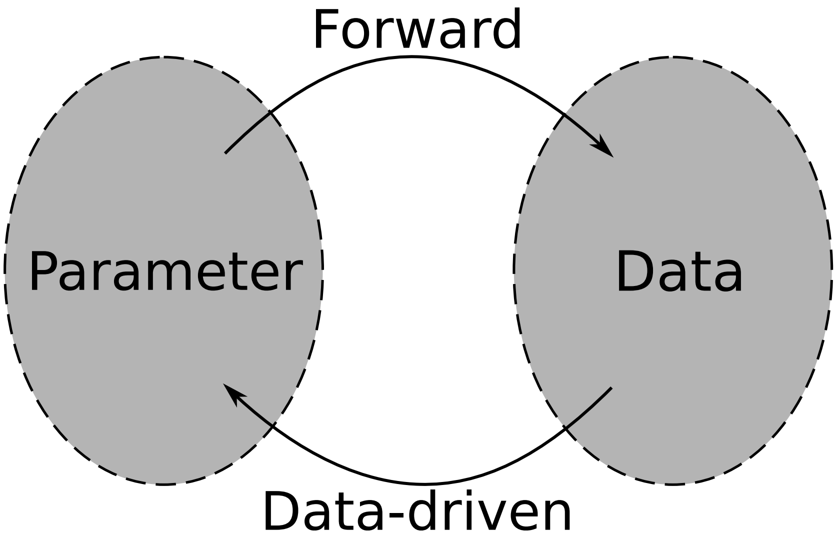

Figure 2.5: Forward and data-driven problem scheme. Left and right ellipses represent respectively the parameter and data space.

---

the experimental measurement. However, due to technical limitations, direct in-vivo measurement of those parameters during experiments is often a challenge. Thus, a specific procedure is necessary to assess parameter values that are consistent to a given dataset.

A score function represents the gap between experimental data X_{exp} and simulation results X_{sim} such as Root Mean Square Error (RMSE) :

$$RMSE(\vec{p_j}) = \sqrt{\frac{1}{\mathcal{N}_d} \sum_{i=1,\mathcal{N}_d} (X_{i,exp} - X_{i,sim}(\vec{p_j}))^2} \tag{2.26}$$

where $\mathcal{N}_d$ is the number of fitted data and $\vec{p_j}$ a parameter vector j which can be the model parameters. A low RMSE value induces small gap between experimental data X_{exp} and simulation results X_{sim} obtained with the set of parameters $\vec{p_j}$. A threshold value needs to be fixed to be able to say if the parameters allow to well reproduce the experimental data which is often arbitrary and corresponds to the Cauchy's criterion for convergence. The RMSE can be normalised by the experimental error where, in this case, the threshold value will be 1 meaning that $nRMSE < 1$, the gap between experimental and estimated values will be lower than experimental uncertainties. Contrary to the forward problem where the parameters are used to directly produce data via numerical simulation, the parameters can be estimated by minimizing a score function such as RMSE, corresponding to the inverse problem (Figure 2.5). The method allows to fit the experimental data in order to build a realistic mathematical model and is made by the use of dedicated algorithms. It exists different types of measurements that can be used to estimate parameters such as metabolomic, fluxomic data which will be used in the thesis or such as high throughput genomic data which are not used in this work.

To minimise the gap between experimental data and simulated results, it is necessary to travel through the parameter space in order to find the best set of parameters which can be done by dedicated algorithms such as Monte Carlo Markov chain (MCMC) [95, 96, 97] and genetic algorithms (GA) [98, 99, 100]. Finding the best set of parameters reproducing experimental data is finding the minimum of this score function called the global minimum. However, the parameter space dimension grows as a function of the estimated parameters number which tends to make complex space. Therefore, it will exist a huge number of hills and valleys creating a lot of local minimums in the score function. These are regions in the space that are locally the minimum but not the general minimum of the space. MCMC and GA are both stochastic algorithms that minimize a score function by travelling into score function space via stochastic moves into the parameter space without being stuck in a local minimum. Because it is long to find the global minimum, the algorithms try to find the best local minimum as a function of the computation time. An infinite computation time with an infinite number of iteration would guaranty the convergence to the global minimum. It exists many stochastic algorithm for mathematical optimisation but only these two have been used in this thesis. It also exists optimisation algorithm such as, for instance, gradient descent algorithm or conjugate gradient method [101, 102] that use a gradient method which consists in going down in the space following the corresponding gradient. These methods are robust to find a near local minimum but are often stuck into it and do not widely travel into the space avoiding to find a potential better solution. For this reason, they have often lower computational cost and time.

2.4.1 Genetic algorithm

Genetic algorithm (GA) is a class of algorithm to find a solution of an optimisation. It is inspired by natural selection by mimicking biological mechanisms such as mutation, crossover or selection [98, 100]. In our interesting case, it will be used to optimize a set of elements which will be set of parameters corresponding to kinetic, saturation and regulation parameters of the oxidative stress response model. GA are used due to its efficiency which is often higher than classic algorithms [103, 104].

GA is used to optimise a score function by minimizing it with processes close to biological natural selection. To decrease a score function ξ that represents the gap between simulated and experimental data, the algorithm will implement several parameter sets called a family where each set is an individual and will travel into the parameter space by applying modifications called mutations on copy of randomly chosen individuals (Figure 2.6). Original individuals are the parents and mutated individuals are the offspring. Finally, the algorithm applies selection by keeping the best individual between all parents and offspring :

> **Initialization** : Start from an arbitrary parent to which corresponds a score value xi. Create the first family of N_f individuals by applying N_f different mutations of the original individual which will be the N_f first parents linked to their score.
>
> **Step 1** : Apply mutations by modifying a small number of parameters on a copy of randomly chosen group of N_f parents to create the offspring. Each offspring has his corresponding score. A new family of $2N_f$ individuals is now made of the parents and offspring.
>
> **Step 2** : Select the N_f best individuals by keeping the N_f best scores to come back to a family of N_f individuals.
>
> and iterate to Step 1.

By generating a family twice its size, the algorithm can quickly travel in the parameter space. It keeps the best individuals corresponding to the best scores which allows to stay with a family of the same size. Because it always keeps the same number of individuals, bad score individual can be also kept with a certain probability. Thus, the algorithm avoids to be stuck in local minimum of score function space.

2.4.2 Monte Carlo Markov chain - Metropolis Hastings

Monte Carlo Markov chain (MCMC) method is a class of algorithm that computes a sample from a desired distribution. One of the existing algorithm is Metropolis Hastings algorithm which can also be used to minimize a function. In this thesis, such algorithm has been used to estimate a distribution of parameters by minimizing a function representing the gap between simulated and experimental values [95, 96, 97].

Basically, MCMC or more specifically Metropolis Hastings algorithm [105] consists in randomly and iteratively travel via small steps through the sample

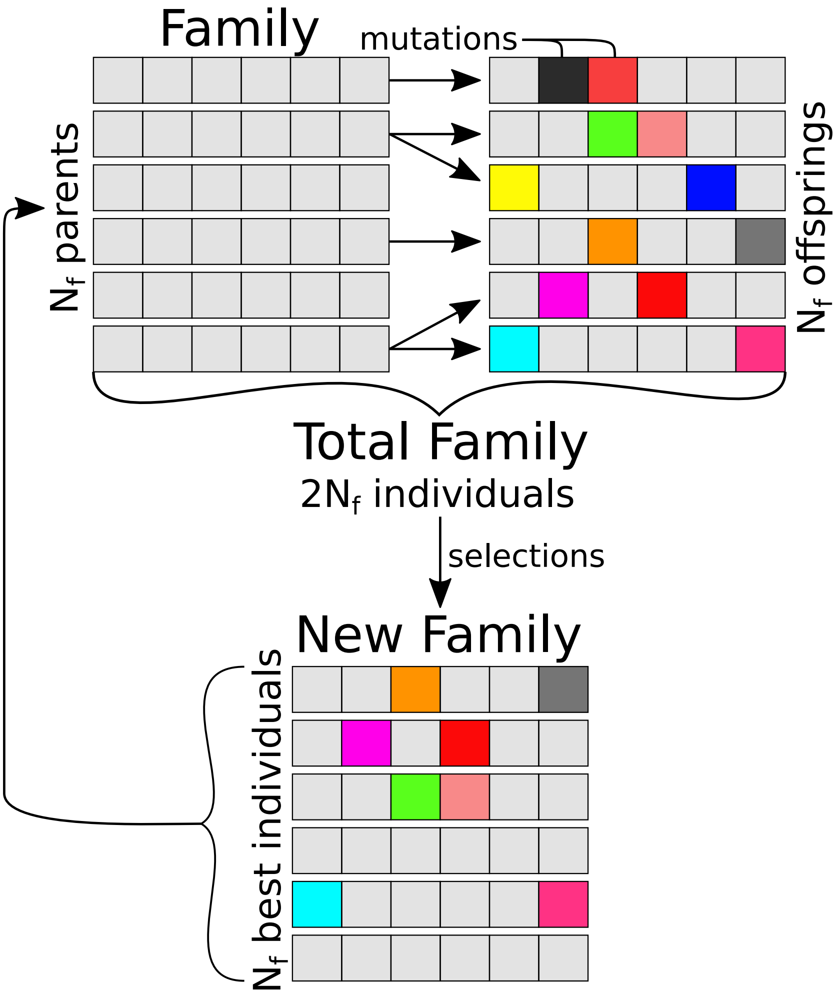

Figure 2.6: Genetic algorithm scheme. Starting from a family of N_f individuals, genetic algorithm applies mutations to each. By sorting them as a function of their score, the N_f best individuals are selected to generate a family of N_f individuals. Repeating these steps allows to minimize a score function and to find an optimal set of parameters.

---

space to find an acceptable region in this space (Figure 2.7-A). A move will be kept with a certain probability of acceptance α otherwise the algorithm stays in the same region. Let call a set of parameters $\vec{p}$ which is the element that needs to be optimized. This set of parameters is linked to a score function ξ which says if the set of parameters is far from the solution or not. The smaller the value of the function, the closer the parameters are to the solution. Thus, the algorithm can be defined as the several steps :

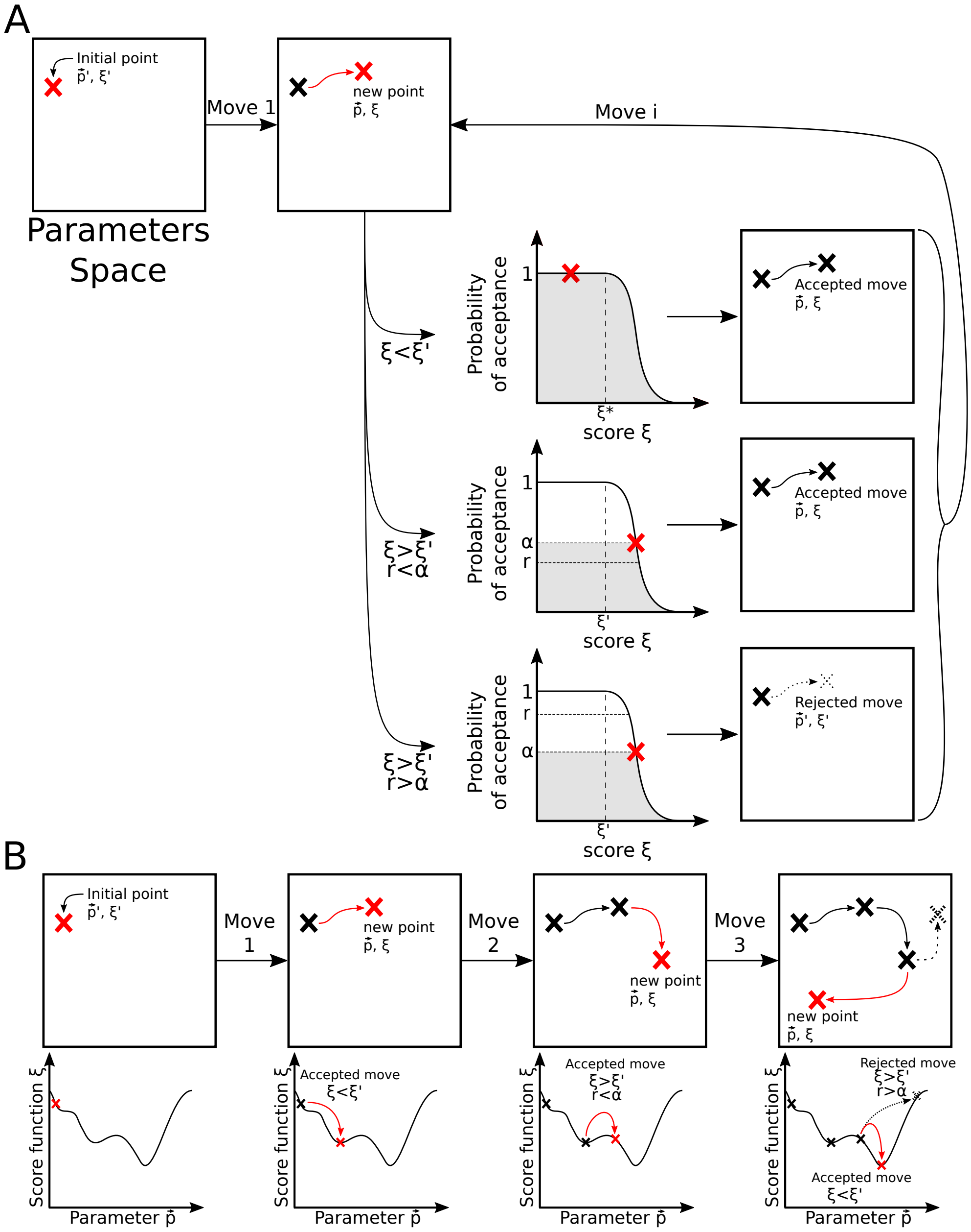

Figure 2.7: Monte Carlo Markov chain algorithm scheme. (A) Algorithm steps that show how to move in parameters space by accepting or rejecting moves depending on a probability of acceptance. (B) Algorithm steps that show how it can be used to minimize a score function by exploring the parameters space.

Initialization : Starts from an arbitrary point $\vec{p'}$ to which corresponds a score value ξ';

Step 1 : Creates a new point $\vec{p}$ by applying a random in the sample space to which corresponds a new score value ξ; $\mathcal{V}$

Step 2 : Calculates the probability of acceptance $\alpha = e^{(-\frac{\xi^2-\xi'^2}{2\mathcal{V}^2})}$ with $\mathcal{V} = \frac{\xi_{top}}{|\mathcal{N}_{fit}-\mathcal{N}_p|}$ where ξ_{top} is the minimum possible score value, $\mathcal{N}_{fit}$ are the number of fitted points and $\mathcal{N}_p$ is the size of a point in the sample space.

Step 3 : Chooses randomly a r value between 0 and 1. If $r \leq \alpha$ then accept the move, $\vec{p'} = \vec{p}$ and $\xi' = \xi$ otherwise keep the same point $\vec{p'}$ to which corresponds to ξ'.

and iterate to Step 1.

These repeated three steps allow to decrease a score function previously defined (Figure 2.7-B). It keeps the score lower than the previous one. However, when a score ξ is higher than the reference score ξ' reflecting a bad move, the probability of acceptance is not 0 meaning that few bad scores can be kept. It is important to have this criteria of acceptance to avoid being stuck in a local minimum, which might make think the algorithm has found the global solution. It is important to note that when the number of parameter is high, the space to scan is so large that MCMC algorithm won't be able to converge to a solution. Moreover, the MCMC algorithm is presented here in an optimisation algorithm but can also be used to find probabilities likelihood distributions. To conclude, MCMC is an algorithm that aims to create samples of a parameter space. It can be used to minimize a score function by exploring step-by-step this space [106].

2.5 13C-Metabolic flux analysis

Metabolic flux state is an important information to understand the biological function of metabolic networks. While experimental measurements often concern metabolite concentrations due to facilities in the experimental procedure [17, 61, 16], the reaction rates cannot be measured directly. Methods have been developed to proceed to metabolic flux analysis (MFA) [107] using stable isotopes [108] such as ^{13}C labeling experiments [109, 110]. Then, a specific procedure is now becoming a certain routine in order to estimate fluxes in a metabolic pathway [111].

Labeling experiments in MFA consist in modifying atoms of molecules to produce isotope isomers (isotopomers). Multiple atoms and different types of atoms can be labeled at the same time. This is typically the case for ^{13}C-based metabolic flux analysis (^{13}C-MFA) where 12 carbons are replaced by 13 carbons called labeled carbons. Because they differ by a single neutron, by measuring the mass of new molecules, a shift of neutron elementary mass will be detected into metabolic pathway as a function of the fluxes. Thus, a molecule of mass m with n labeled carbon by a ^{13}C induces a shift of n elementary mass. A workflow of ^{13}C labeling is described in Figure 2.8.

First, a labeling experiment consists in modifying ^{12}C into ^{13}C on molecules making this new molecule an isotopomer. Different information will be deduced as a function of positions of the labeled carbons. It is often beneficial to multiply the labeling positions to have full information of the metabolic flux state. Different molecules can be labeled but glucose (Glc) molecules can be useful to label in the context of oxidative stress response because it is the entering molecules of the glycolysis and the PPP. Labeled glucose molecules are converted to other metabolites through metabolic reactions which spread the labeled carbons [17] due to the chemical reaction rearrangement. The labeling of atoms implies a shift in the mass of molecules which can be measured at different nodes of the metabolic pathways using gas chromatography and mass spectroscopy or other methods [112, 113, 114]. The proportion of each labeling condition can be represented by the mass isotopomer distribution (MID) $m + n$ which can be computed as a function of the number of labeled carbon n per molecules. Obviously, the isotopomer distribution without labeling experiment is 100% at $m + 0$.

Once the isotopomer distribution are calculated after mass measurement, the fluxes can be estimated using dedicated algorithms combined to implementation of the metabolic pathways. Algorithms allow to estimate MID from a flux state corresponding to the forward problem. MFA consists in the flux state estimation from measured isotopomer distribution corresponding to the inverse problem, i.e. data-driven estimation with a score function minimisation, which is made by an algorithm that iteratively solve the forward problem with an updated flux state. Algorithms or software, such as Metran [115], COBRA [116, 117] or INCA [118] are based on decomposition methods such as cumulative isotopomers (cumomers) [119] or Elementary Metabolic Units (EMU) [120]. The current standard method is the EMUs decomposition which identifies the minimal number of system variables necessary to deterministically solve the balanced equation system of the isotopic labeling within a reaction network. In other words, it decomposes the system in smaller units forming a new basis to generate a new system of equations

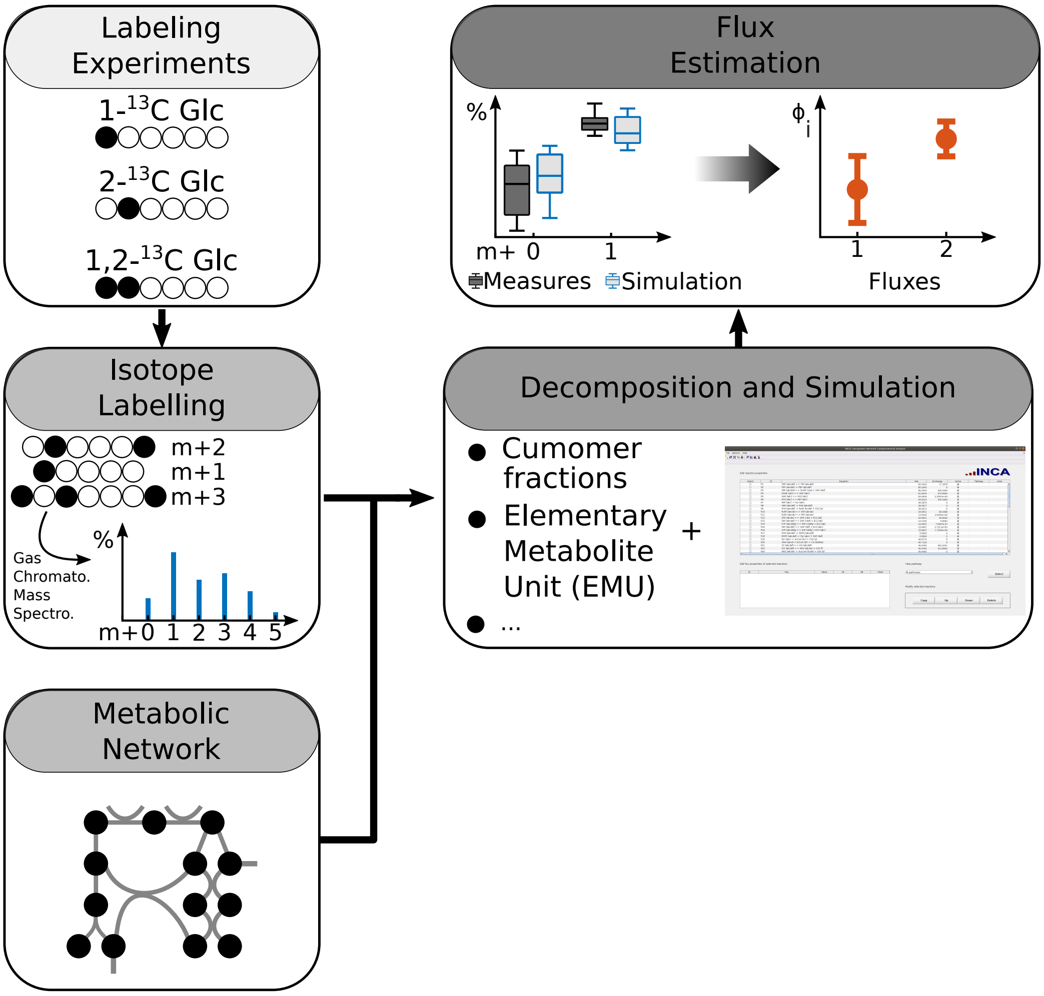

Figure 2.8: ^{13}**C-MFA method.** Workflow of a typical ^{13}C labeling experiment in order to estimate fluxes of a metabolic network. Labeled carbons are represented by black circles and non-labeled to empty circles. Labeling experiments consist of changing ^{12}C by ^{13}C. gas chromatography and mass spectroscopy are methods to measure the mass isotopomer distribution corresponding to the shift of mass $m+i$. Flux estimation of a specific metabolic network is made by using software or algorithm. Statistical analysis allows to compare simulated results to experimental data in the inverse problem allowing to find the final results.

linking isotopomers to fluxes. An EMU is a subset of all isotopomers of a molecule going to a maximum of $2^N - 1$ EMUs for a N-atoms molecules. However, in general, a small fraction of this number is necessary to solve the balanced equation system of the isotope labeling. The EMU decomposition is a very efficient method inducing from 10 to 100 times less variables than the total number of isotopomer. However, this number can still become high in large network and labeling conditions. Information needed for the decomposition are the reaction network stoichiometry, the atoms transitions for all reactions and the list of metabolite.

Most of the classical ^{13}C-MFA algorithms are restricted to the requirement of steady state conditions. However, advanced algorithms have been developed counteracting this problem with non-stationary MFA (^{13}C-NMFA or ^{13}C-instMFA) [121] or dynamic MFA (DMFA) [122] and ^{13}C dynamic MFA methods (^{13}C-DMFA) [109]. The classical MFA need metabolic isotopic steady state and stationary flux state. However, non-stationary MFA (instMFA or DMFA) can be used when the isotopic labeling is not constant in time and instMFA is implemented for instance in INCA software with an EMU decomposition while dynamic MFA allows to estimate non-stationary metabolic fluxes. No highly efficient software implements DMFA favouring the use of instMFA algorithm when the change of flux state can be neglected compared to isotopic labeling change as first approximation [123].

Chapter 3

Adaptation dynamics in response to oxidative stress

A stress induces drastic perturbations in cellular component which can induce damages or cell death. Adaptation dynamic corresponds to the cellular modifications made in order to avoid such fate. This cellular response is often accompanied by an overshoot [63]. In response to a step exposure of H_2O_2, such overshoot has been observed in yeast [61] or cancer cells [65]. In this chapter, a basic scheme of metabolic regulation of glycolysis and PPP fluxes will be studied to investigate how it could induce an overshoot adaptation response. A reduced model of H_2O_2 detoxification through flux rerouting into PPP will be used to identify the requirements to obtain an adaptation time course, more or less close to perfect adaptation. It will be concluded that effective delays into the PPP induces a significant adaptation response. This coarse-grained model provides preliminary insights for more advanced analyses of detailed stoichiometric and kinetic models.

3.1 Coarse-grained model

Oxidative stress response is induced by a sharp increase of external hydrogen peroxide H, detoxified by the glycolysis and PPP. These metabolic pathways are an ensemble of biochemical reactions catalysed by enzymes. Variation of molecules concentration as a function of time will be characterized by a system of ordinary differential equations (Section 2.1). To avoid complexity of the entire system, these metabolic pathways can be modeled with the principal nodes, namely $G6P$, $R5P$ and GAP (Figure 3.1). In addition to these metabolites, $NADPH$ will be used to recycle anti-oxidant molecules glutathiones GSH which remove internal H_2O_2. Moreover, glycolysis and

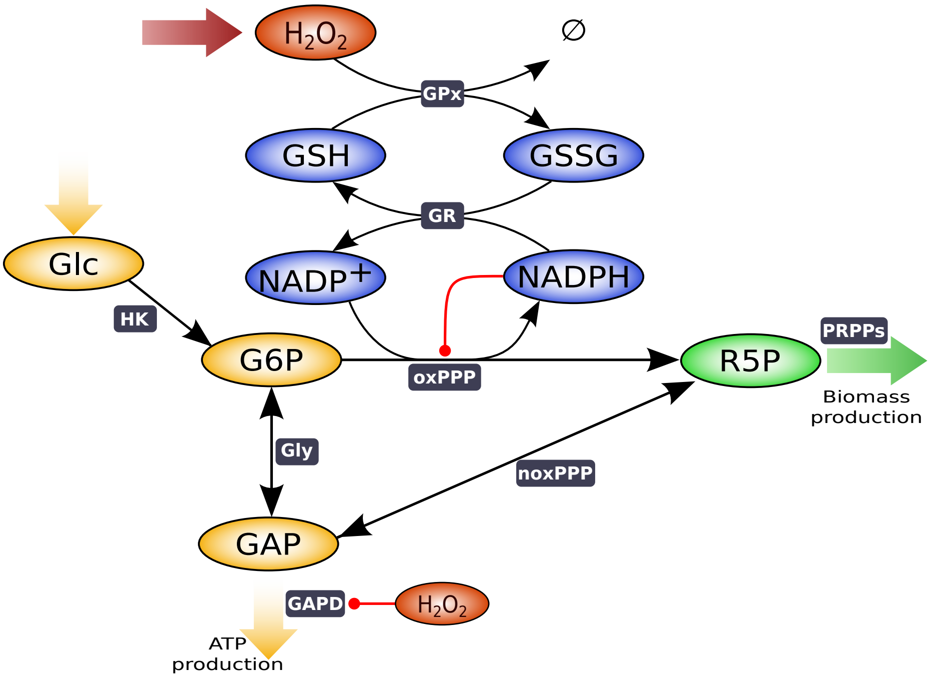

Figure 3.1: Coarse-grained model. Metabolites are represented by ellipses. Yellow, green and blue ellipses are metabolites of respectively glycolysis, PPP and detoxification pathways (i.e. glutathiones). Fluxes are represented by arrows. Black squares represent the names of fluxes in this reduced model. Red arrows correspond to inhibitions.

PPP are fuelled by incoming glucose molecules used as input flux. Reactions that consume and produce the system variable are first modeled with linear mass action law. Non-linearity made by regulations are then added in order to potentially obtain an adaptation phenotype during oxidative stress response. Concerning the anti-oxidant pathway, it can be modeled following expression of Benfeitas et al. 2014 [124]. Thus, the system can be modeled by the following equations as a function of the reaction rates :

$$\frac{d[H_2O_2]}{dt} = \phi_{H_2O_2} - \phi_{CAT} - \phi_{GPx} \tag{3.1}$$

$$\frac{d[GSH]}{dt} = 2\phi_{GR} - 2\phi_{GPx} \tag{3.2}$$

$$\frac{d[NADPH]}{dt} = \phi_{oxPPP} - \phi_{GR} \tag{3.3}$$

$$\frac{d[G6P]}{dt} = \phi_{HK} - (\phi_{gly} + \phi_{oxPPP}) \tag{3.4}$$

$$\frac{d[R5P]}{dt} = \phi_{oxPPP} - 6/5\phi_{noxPPP} - \phi_{PRPPs} \tag{3.5}$$

$$\frac{d[GAP]}{dt} = \phi_{gly} + \phi_{noxPPP} - \phi_{GAPD} \tag{3.6}$$

$$\frac{d[Glc]}{dt} = \phi_{GLU} - \phi_{HK} \tag{3.7}$$

where the reaction rates are :

$$\phi_{H_2O_2} = k_{H_2O_2} + k_{diff}(H - [H_2O_2]) \tag{3.8}$$

$$\phi_{CAT} = k_{CAT}[H_2O_2] \tag{3.9}$$

$$\phi_{GPx} = \frac{k_{GPx}[H_2O_2][GSH]}{\frac{[H_2O_2]}{KmH_{GPx}} + \frac{[GSH]}{KmG_{GPx}}} \tag{3.10}$$

$$\phi_{GR} = \frac{k_{GR}[NADPH][GSSG]}{1 + \frac{[NADPH]}{KmN_{GR}} + \frac{[GSSG]}{KmG_{GR}}} \tag{3.11}$$

$$\phi_{oxPPP} = \frac{k_{oxPPP}[G6P]}{1 + \frac{[NADPH]}{Ki_{oxPPP}}} \tag{3.12}$$

$$\phi_{noxPPP} = k_{noxPPP}(5/6[R5P] - [GAP]/Keq_{noxPPP}) \tag{3.13}$$

$$\phi_{PRPPs} = k_{PRPPs}[R5P] \tag{3.14}$$

$$\phi_{GAPD} = \frac{k_{GAPD}[GAPD]}{1 + \frac{[H_2O_2]}{Ki_{GAPD}}} \tag{3.15}$$

$$\phi_{gly} = k_{gly}([G6P] - [GAP]/Keq_{gly}) \tag{3.16}$$

$$\phi_{HK} = k_{HK}[Glc] \tag{3.17}$$

Regulations of the PPP and glycolysis during oxidative stress have been studied in the past years [17, 34, 36, 52, 125]. However, to meet the criteria of a minimal set of mechanistic features, only regulations on $G6PD$ and $GAPD$ are kept due to their potential high effect on flux rerouting which could induce adaptation to oxidative stress [18, 17, 36, 34]. Reactions of the PPP are modeled as one irreversible reaction. Similar approximation is made for the glycolysis and noxPPP but with a reversible reaction. However, because the noxPPP changes the conformation of the molecules due to the loss a carbon by consuming molecules with 5 carbons to produce with 6, it exists a stoichiometry of 5/6 from $R5P$ to GAP and vice-versa. $DHAP$ which is normally present inside the glycolysis is combined in the concentration of GAP. Because these molecules are made of 3 carbons, the total number of carbon is conserved.

To be able to simulate the coarse-grained model, it is necessary to set values to model parameter. A first set of value can be determined by solving the ordinary differential equations at steady state, i.e. $d\vec{X}/dt = 0$, in basal condition without external perturbation. Because there are 7 equations, it will fix 7 parameter values. It is important to note that parameter expressions found after this problem solving are dependent on the variable concentrations in basal condition. These concentrations are taken from experimental measurements or previous mathematical models [124, 126, 127, 32]. More parameters could be fixed by solving the system of equations at steady state in stress condition. However, in order to correspond to experimental phenotypes, the remaining parameters are fixed by direct experimental measurements, for instance regulation parameters can be directly extracted in Kuehne et al. 2015 [17], Peralta et al. 2015 [36]. Moreover, it is known that the incoming glucose flux is mainly glycolytic at around 90% in basal condition inducing $\Phi_{gly} = 0.90\Phi_{GLU}$ and therefore $\Phi_{oxPPP} = 0.10\Phi_{GLU}$. All the model parameters are listed in the table 3.1 :

Parameter	Expression	Value	References
Φ_{GLU}		40μM/s	
$k_{H_2O_2}$	$1.001\Phi_{oxPPP}$		
k_{diff}		1s^{-1}	[124]
k_{CAT}	$(k_{H_2O_2} - \Phi_{oxPPP})/H_2O_2$		[70]
k_{GPx}		1s^{-1}	[124]
KmH_{GPx}		0.04μM	[124]
KmG_{GPx}		9.72μM	[124]
k_{GR}		49s^{-1}	[124]
KmN_{GR}		8.5μM	[124]
KmG_{GR}		65μM	[124]
k_{oxPPP}	$\frac{\Phi_{oxPPP}(1+[NADPH]/Ki_{oxPPP})}{[GAP][NADP^{+}]}$		
Ki_{oxPPP}		10μM	[45, 17]
k_{noxPPP}	$\frac{\Phi_{noxPPP}}{(5/6[R5P]-[GAP]/Keq_{noxPPP})}$		
Keq_{noxPPP}		15μM	[70]

k_{PRPPs}	$(\Phi_{oxPPP} - 6/5\Phi_{noxPPP})/[R5P]$	
k_{GAPD}	$(\Phi_{gly} + \Phi_{oxPPP})\frac{(1+[H_2O_2]/Ki_{GAPD})}{[GAP]}$	
Ki_{GAPD}	1μM	[36, 35]
k_{gly}	$\Phi_{gly}/([G6P] - [GAP]/Keq_{gly})$	
Keq_{gly}	1.2μM	[70]
k_{HK}	$\Phi_{GLU}/[Glc]$	

Table 3.1: Parameter expressions and values. Parameter expressions correspond to solution of the system equations at steady state.

It is important to note that, because this model is a first investigation of oxidative stress response, a single value is given for the fixed parameters. However, to be more realistic, it would be necessary to consider a range of flexibility du to experimental uncertainties. A statistical analysis of the parameter range would be preferable instead of choosing one set of parameter.

3.2 Adaptation via flux reprogramming

Oxidative stress response is simulated through numerical integration of the mathematical model to compute the temporal dynamics of metabolite concentrations (Figure 3.2-A) under a concentration step of external hydrogen peroxide from $0\mu M$ to $100\mu M$. Some metabolite concentration show a response in two steps in second time scale. Indeed, $G6P$ and GAP is fastly decreasing which corresponds to the time scale of the $NADPH$ decrease to 0. This is followed by a slow increase phase. These two steps can correspond to first a consumption of the molecules reservoir shown by the drop of $NADPH$ concentration and then a slower reaction of the metabolic pathway inducing slow relaxation to the steady state. It is specifically visible for the variations of H_2O_2 and $G6P$ concentration as a function of time (Figure 3.2-B&C). Indeed, H_2O_2 shows a maximum value several seconds after the start of the oxidative stress which is followed by a slow relaxation to lower steady state which is called adaptation. This is probably du to the reaction of the network inducing increase of $G6P$ concentration. It then increases the oxPPP flux inducing higher $NADPH$ recycling in order to increase oxidative stress detoxification. The fast increase of PPP flux is probably to the decrease of $NADPH$ concentration inducing a decrease of PPP inhibition.

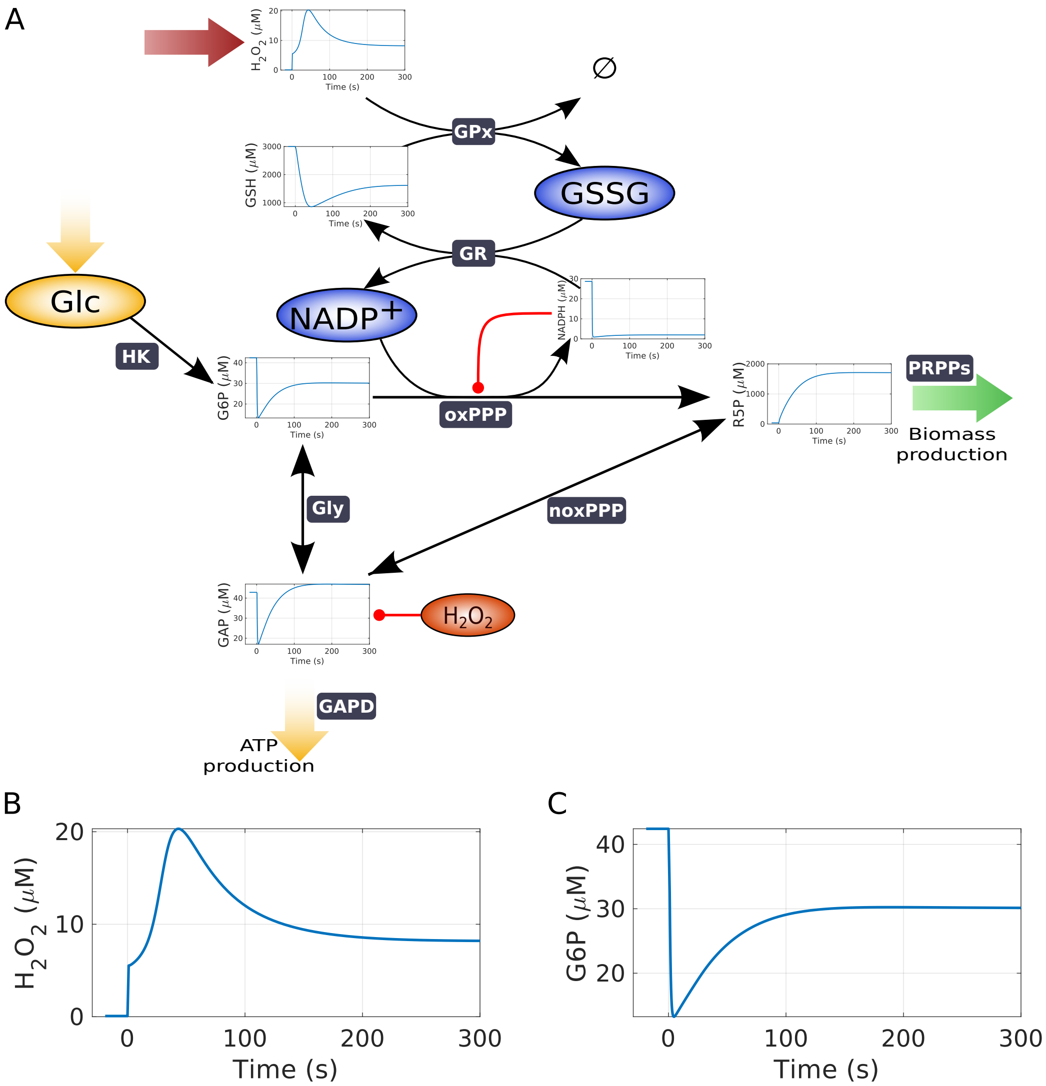

Figure 3.2: Transient dynamics of stress-induced metabolic responses in the reduced model. Temporal dynamic in the reduced model under oxidative stress made by a step of $100\mu M$ of H_2O_2. (A) Each metabolite concentration has its temporal dynamic represented in the reduced metabolic scheme at their corresponding place. (B-C) Temporal dynamics of H_2O_2 (B) and $G6P$ (C).

Simulating the metabolic response as function of different external hydrogen peroxide H level allows to identify the range of detoxification efficiency and the limits of this detoxification (Figure 3.3). It appears that the ratio between steady state concentration of internal and external hydrogen peroxide is very small for stresses lower than $\approx 100\mu M$ (Figure 3.3-A). After that level of stress, the ratio is highly increasing to finally saturate close to 1 showing that the metabolic pathway does not succeed to detoxify higher stresses. It is supplemented by the fact that $NADPH$ is falling to very small concentration which induces saturation of the oxidative stress detoxification

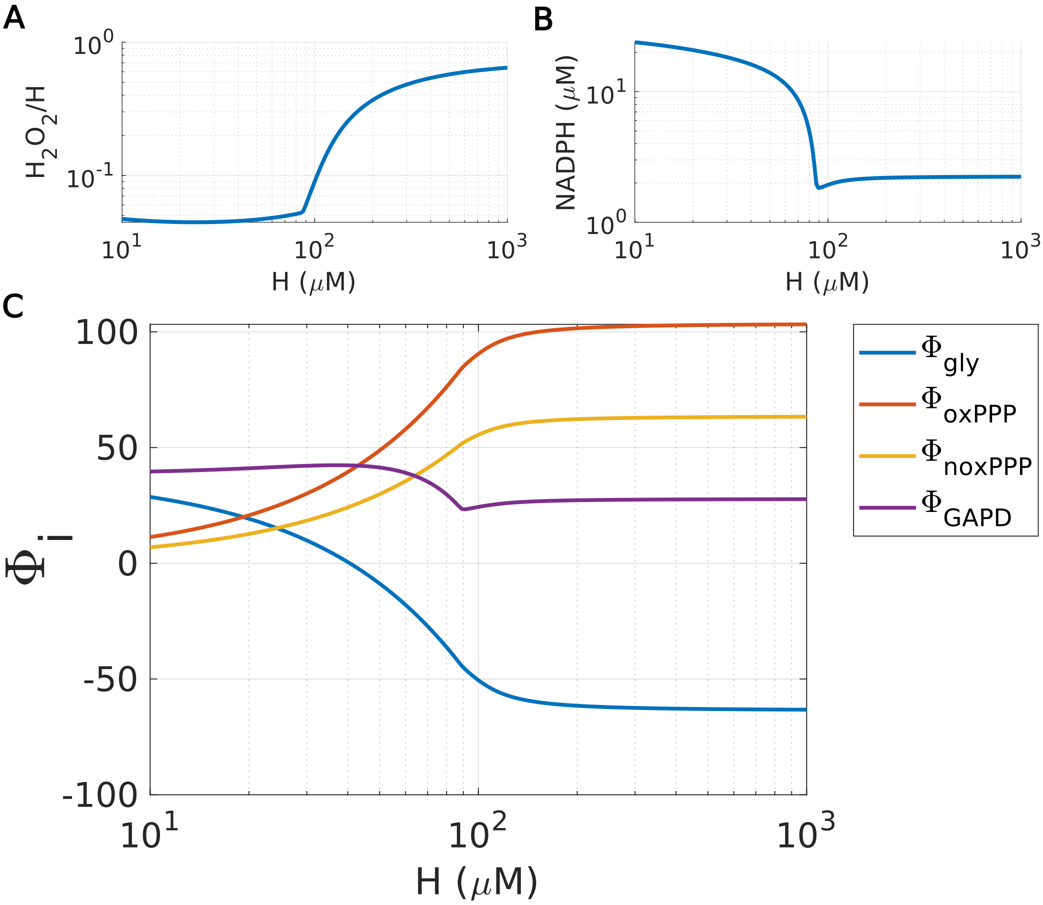

Figure 3.3: Dose-dependent profile of stress-induced metabolic response in the reduced model. Response to varying level of external hydrogen peroxide H at 5min. (A) Ratio of internal and external H_2O_2 and (B) $NADPH$ metabolite concentration as a function of H. (C) flux rates of the glycolysis Φ_{gly}, oxPPP and noxPPP respectively Φ_{oxPPP} and Φ_{noxPPP}, output flux $GAPD$ as a function of H.

(Figure 3.3-B). Finally, all these phenotypes can be understood by the flux state of the network as a function of H (Figure 3.3-C). Indeed, for small level of stress, the incoming glucose flux is mainly directed toward the glycolysis inducing high output flux through $GAPD$ toward ATP production. When the stress level is increasing, the incoming glucose flux is rerouted toward first the oxidative and then the non-oxidative PPP. Moreover, the PPP flux is sufficiently increasing to be higher than the incoming glucose flux set at $40\mu M/s$ meaning that there is cycling flux. Indeed, the reverse glycolysis allows carbons flux coming from the noxPPP to come back to oxPPP which highly increases the $NADPH$ recycling and therefore the stress detoxification. In cycling condition, the flux is going through the reverse glycolysis instead of going out through the output flux $GAPD$ as it is during small level of stress. It is probably because the lower glycolytic flux is inhibited by H_2O_2 which increases during oxidative stress.

To summarise, the coarse-grained model with a specific parameter set (without adjustment to experimental data) shows that the combination of an oxidative stress that shifts the redox state $NADP/NADPH$ and the regulation of lower glycolysis is qualitatively sufficient (i) to reroute the flux toward PPP and (ii) to generate an adaptation response.

3.3 Role of delay in adaptation

Adaptation profile has been observed experimentally for the H_2O_2 temporal dynamic in different cell types [61, 65] and also in the coarse-grained model previously presented in response to oxidative stress. It is characterized by an overshoot of the concentration during the metabolic response. In the case of oxidative stress, the final steady state is still not close enough to the initial state to call it perfect or near-perfect adaptation [64]. However, the presence of an adaptative phenotype describes a compromise between fast response inducing high metabolic cost and low response inducing damages. Regulations are important mechanisms in the metabolic response and would take part of the presence of the adaptative phenotype. A rapid effect of the regulatory mechanisms would lead to high metabolic response and would not allow concentration to sufficiently change to observe an adaptative phenotype. Thus, a response delay would be necessary to make appear such phenotype. Using the coarse-grained model of the PPP and glycolysis, artificial delay will be added in order to study the impact of the presence of adaptation phenotype.

An adaptation ratio (AR) can be defined as :

$$AR = \frac{[H_2O_2]^{max}}{[H_2O_2]^*} \tag{3.18}$$

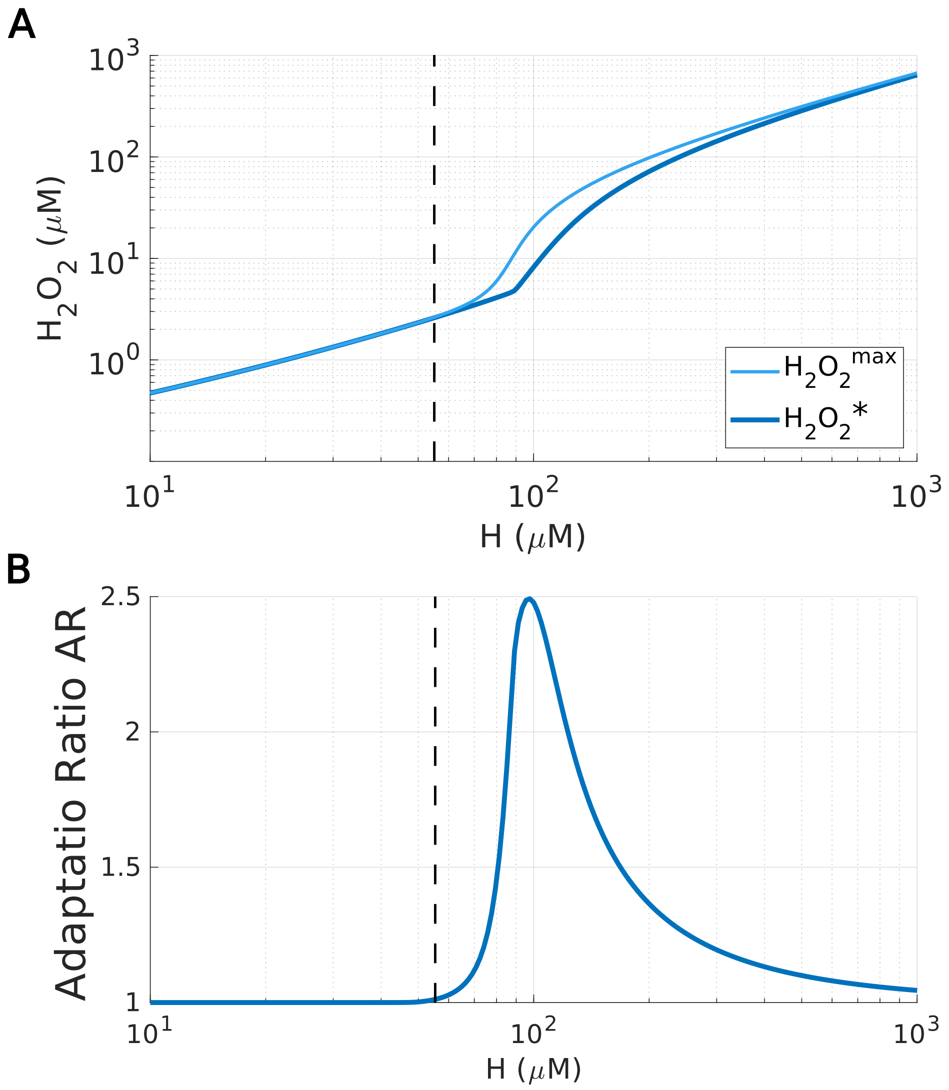

Figure 3.4: Adaptation ratio during oxidative stress. Simulations are made using mathematical model. (A) Internal H_2O_2 as a function of external hydrogen peroxide H. The maximum of H_2O_2 curve ($H_2O_2^{max}$) in temporal dynamic is shown in light blue curve. Steady steady H_2O_2 ($[H_2O_2]^*$) is dark blue curve. (B) Adaptation ratio is $AR = \frac{[H_2O_2]^{max}}{[H_2O_2]^*}$ using $[H_2O_2]^{max}$ and $[H_2O_2]^*$ from (A) and shown as a function of external hydrogen peroxide H. (A)-(B) The black dashed line corresponds to the dose to delimit the area of presence of an adaptation phenotype.

where $[H_2O_2]^{max}$ and $[H_2O_2]^*$ are respectively the maximum value and the steady state of the temporal dynamic of H_2O_2 concentration under oxidative stress. High AR would lead to a maximum value much higher than the steady state which could lead to extreme transient concentration and then to cell death. An AR equal to 1 induces maximum and steady state value equal meaning that either the metabolic response is too fast to see an adaptation or there is totally no response. This ratio will characterize how the adaptation phenotype is strong during the oxidative stress response.

In the previous section, the temporal dynamic has been studied to investigate a first oxidative stress response 3.2. It shows clearly a non-perfect adaptation profile with a maximum at a minute time scale and then a slow relaxation to lower steady state. This oxidative stress has been made with a step from $0\mu M$ to $100\mu M$ of H_2O_2 and leads to an $AR = 2.48$. Thus, AR is calculated for different level of stress (Figure 3.4-A&B). It shows that there is an adaptation for dose between $70\mu M$ and $300\mu M$ which is the range that the system is acting by changing its flux state (Figure 3.3). Before this range, the system is able to remove the stress efficiently and after, the network is not able to detoxify the stress anymore.

To confirm that the phenotype of adaptation is due to the activation time of the metabolic response, the same simulations are made with a modified mathematical model. Indeed, to increase the response time, several variables are added in chain in the model following the equations :

$$\frac{dx_i}{dt} = k_{i-1}(x_{i-1} - x_i/Keq_{i-1}) - k_i(x_i - x_{i+1}/Keq_i) \tag{3.19}$$

where x_i is the i-th metabolite, k_i and Keq_i are respectively the reaction rate constant and equilibrium constant of the i-th reaction which are all taken the same as the noxPPP parameters. These intermediate metabolites are added in the noxPPP. Adding several steps inside the PPP will bring closer to the completely detailed metabolic pathway and will favour the delay of response. It is important to note that inducing artificially delay does not modify the steady state concentration but only the adaptation ratio. Eight intermediate variables are added to compensate the number of metabolite in the detailed metabolic pathways. The dose-response of this new model displays higher adaptation ratio compared to the normal model (Figure 3.5). This AR increase is visible from $50\mu M$ to $200\mu M$. Thus, adding a delay in the metabolic response increases the adaptation ratio but also increases the region of doses where the adaptation can be observed. Indeed, it appears for lower doses where adaptation was not present yet. For even lower doses, the ratio is not modified probably because the network is still able to highly detoxify this level of stress. For higher dose than $200\mu M$, adding delay does

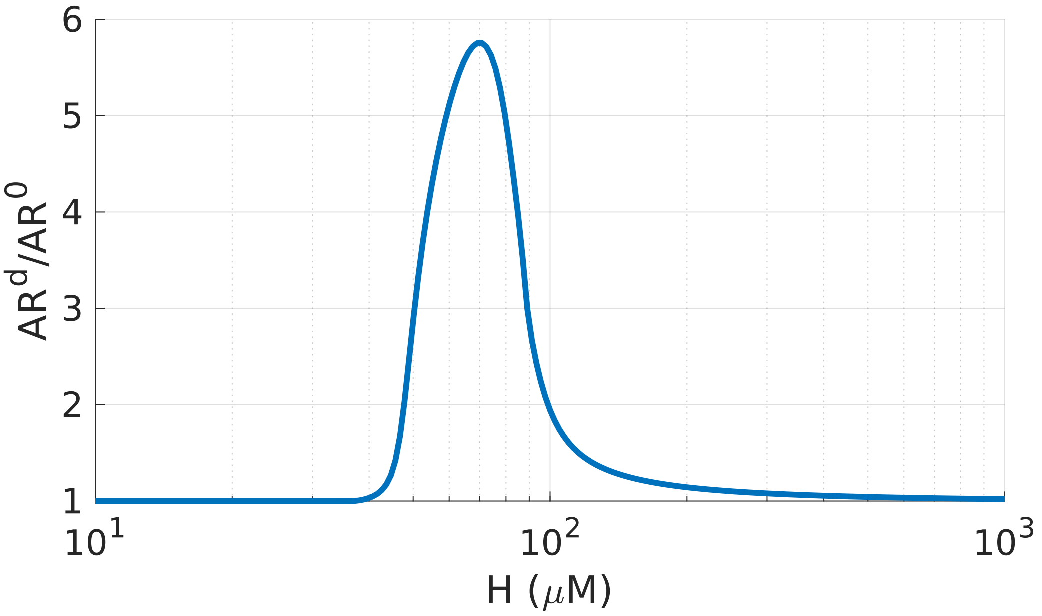

Figure 3.5: Adaptation ratio variation using delayed model during oxidative stress. Adaptation ratio AR is $AR = \frac{[H_2O_2]^{max}}{[H_2O_2]^*}$. Delayed model AR^d normalised by control model AR^0 is shown as a function of the external hydrogen peroxide H.

not modify the AR because the detoxification is already saturated. Thus, adding a delay impacts the transient metabolic response.

In conclusion, the system can display temporal adaptation dynamic, which is (ii) caused here by the inhibition of $GAPD$, (ii) enhanced by the presence of delays through intermediate reactions in non-oxidative pathways of PPP and (iii) the most significant for intermediate doses of stress. In the next studies, the link between regulation, flux rerouting and adaptation will be investigated via a model of the detailed metabolic pathways considering experimental data.

Chapter 4

Stoichiometric model of PPP

The metabolic fluxes are an important source of information allowing to understand the physiological state of a cell. Understanding the change in fluxes during a response to genetic or environmental perturbation can help to clarify metabolic pathway functions, such as the metabolic regulations in the context of this thesis [128, 129, 130]. In this chapter will be studied the metabolic fluxes of the PPP and glycolysis. Flux balance analysis is a theoretical method that will first be applied. Then, a new ^{13}C-MFA algorithm will be presented in order to employ it to data-driven estimate fluxes using experimental mass isotopomer measurements. It quantifies the rerouting flux pattern from a glycolytic mode to a oxPPP mode during oxidative stress.

4.1 Description and assumptions of the metabolic model

Metabolic concentration variations can be described by ordinary differential equations $\frac{d\vec{x}}{dt} = \mathbf{N}\vec{\phi}$ (eq 2.1). Structure of the equations are constrained by the structure of the metabolic pathways. Thus, a network comprising PPP, glycolysis and detoxification pathways shown in Figure 4.1 can be expressed by the following equations :

$$\begin{aligned}
d[H_2O_2]/dt &= \phi_{OX} - \phi_{CAT} - \phi_{GPx} && (4.1)\\
d[GSH]/dt &= 2\phi_{GR} - 2\phi_{GPx} && (4.2)\\
d[NADPH]/dt &= \phi_{G6PD} + \phi_{6PGD} + \phi_{NHN} - \phi_{NNH} - \phi_{GR} && (4.3)\\
d[G6P]/dt &= \phi_{HK} - \phi_{G6PD} - \phi_{PGI} && (4.4)\\
d[6PGL]/dt &= \phi_{G6PD} - \phi_{6PGL} && (4.5)\\
d[6PG]/dt &= \phi_{6PGL} - \phi_{6PGD} && (4.6)\\
d[Ru5P]/dt &= \phi_{6PGD} - \phi_{RPI} - \phi_{RPE} && (4.7)\\
d[X5P]/dt &= \phi_{RPE} - \phi_{TKT1} - \phi_{TKT2} && (4.8)\\
d[R5P]/dt &= \phi_{RPI} - \phi_{TKT1} - \phi_{PRPP} && (4.9)\\
d[S7P]/dt &= \phi_{TKT1} - \phi_{TLD} && (4.10)\\
d[E4P]/dt &= \phi_{TLD} - \phi_{TKT2} && (4.11)\\
d[Glc]/dt &= \phi_{GLU} - \phi_{HK} && (4.12)\\
d[F6P]/dt &= \phi_{PGI} - \phi_{PFK} + \phi_{TAL} + \phi_{TKT2} && (4.13)\\
d[FBP]/dt &= \phi_{PFK} - \phi_{ALD} && (4.14)\\
d[DHAP]/dt &= \phi_{ALD} - \phi_{TPI} && (4.15)\\
d[GAP]/dt &= \phi_{ALD} + \phi_{TKT1} - \phi_{TAL} + \phi_{TKT2} + \phi_{TPI} - \phi_{GAPD} && (4.16)
\end{aligned}$$

where ϕ_{ENZ} represents an enzymatic flux rate (i.e. reaction rate). The model will be built in order to reproduce fast oxidative stress response which is incompatible with long time scale modifications such as gene regulations or dilution induced by cell volume change. Despite this, other elements are not taken into account in the model :

- Lower glycolysis, tricarboxylic acid cycle, purine synthesis and other metabolic pathways are not of major interest in this work due to lack of available data during oxidative stress response.

- Most of the organic or inorganic cofactors are not taken into account in the model because their variations are assumed to be negligible compared to the rest of the metabolites. Indeed, it is the case of ATP, $Mg2+$ and $NAD+$ species which have been sometimes included in other mathematical models [31].

- Fructose 2,6-bisphosphate ($F26BP$) is a molecule in parallel of the glycolysis often integrated in mathematical models [31]. It is produced from fructose-6-Phosphate ($F6P$) by phosphofructokinase-2 ($PFK2$) enzyme. The reverse reaction is catalysed by the enzyme fructose

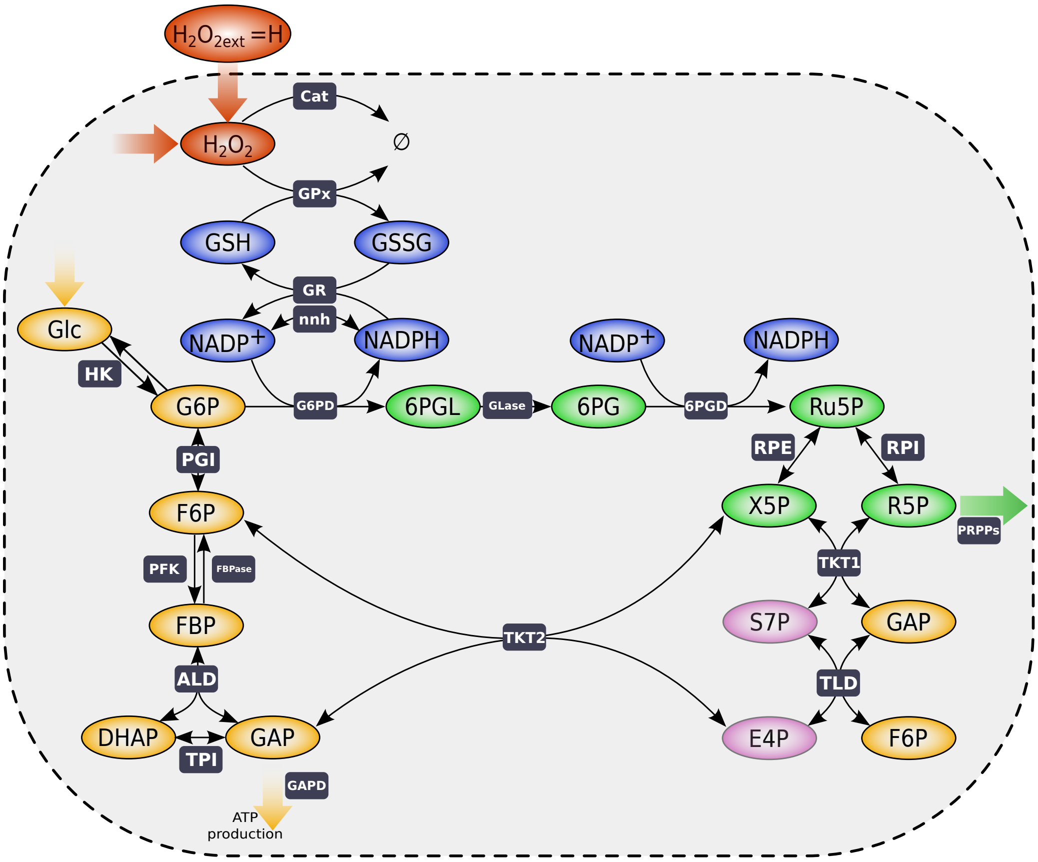

Figure 4.1: Metabolic pathways used in the stoichiometric model. From Hurbain et al. 2022 [3]. Schematic representation of the network comprising the metabolites shown by coloured ellipses, chemical reactions shown by black arrows with their corresponding enzymes in black squares. OxPPP is in green, non-oxidative in pink, glycolysis in yellow, anti-oxidant system in blue and oxidant molecules in red. Input and output fluxes are represented by big arrows.

---

bisphosphatase-2 ($FBPase2$). $F26BP$ is an activator of PFK enzyme which converts $F6P$ into FBP and also an inhibitor of $FBPase$ which produces the reverse reaction. During oxidative stress response, this activation and inhibition would reverse glycolysis allowing to favour glucose flux cycling to increase the detoxification. It is not included in the stoichiometric model because of the lack of metabolomics data for such metabolite.

- Direct hydrogen peroxide detoxification is made by glutathiones which consume $NADPH$ which is itself recycled via PPP reactions. It exists other reactions that consume and produce $NADPH$ (e.g., malic enzyme, IDH, fatty acid synthase, folate cycle) [15, 16] but are condensed in two effective reactions called NNH and NHN respectively.

- It exists different anti-oxidant molecules (catalase, glutathione and thioredoxins (TRX)/Peroxiredoxins (PRX)) involved during oxidative stress response to degrade H_2O_2. Each of them display a specific role, but most of them need $NADPH$ as electron donor. For simplicity, only catalase and glutathiones are included in the model.

The system is acting in cytoplasm thus the model takes into account only one compartment. Except H_2O_2 which diffuses from outside to inside the cell, metabolites of the system do not diffuse.

4.2 Elementary modes in the PPP

Flux balance analysis (FBA) is a mathematical method that analyses the allowable flux states for a given stoichiometric matrix. In this thesis, metabolic response to oxidative stress can be first investigated in term of change of flux pattern associated to a stress perturbation. It is known that the metabolic pathway displays a flux rerouting under oxidative stress in order to increase production of $NADPH$ and detoxification of H_2O_2 [18, 17]. FBA allows to identify the elementary flux modes and to represent functional flux states in term of combination of the elementary modes.

For FBA, the steady state equation 2.1 can be rewritten as $\frac{d\vec{x}}{dt} = \mathbf{N}\vec{\phi} = 0$ $\mathbf{N}$ is the stoichiometric matrix and its dimension is $n \times m$ where n is the number of concentration variable which is here equal to 16 and m the number of flux equal to 21. The metabolite vector can be defined as $\vec{x}$ following the order of the equations 4.1-4.16 and the fluxes vector is $\vec{\phi}$ shown in equation 4.17. In this theoretical study, absence of passive production and degradation induces conservation of the total number of glutathiones and $NADP$ allowing to remove equations of $GSSG$ and $NADP^+$. Moreover, it also allows to express fluxes of the flux state vector $\vec{\phi}$ directly as a function of the only input flux, i.e. incoming glucose flux Φ_{GLU}.

There are 16 equations that can be solved at steady state as a function of 21 fluxes. Then, the flux vector can be expressed as a function of 5 of them.

By injecting these relations, the fluxes vector $\vec{\Phi}$ can be decomposed as :

$$\vec{\Phi} = \begin{pmatrix} \Phi_{OX} \\ \Phi_{CAT} \\ \Phi_{GPx} \\ \Phi_{GR} \\ \Phi_{NNH/NHN} \\ \Phi_{G6PD} \\ \Phi_{6PGL} \\ \Phi_{6PGD} \\ \Phi_{RPI} \\ \Phi_{RPE} \\ \Phi_{PRPPs} \\ \Phi_{TKT1} \\ \Phi_{TLD} \\ \Phi_{TKT2} \\ \Phi_{GLU} \\ \Phi_{HK} \\ \Phi_{PGI} \\ \Phi_{PFK} \\ \Phi_{ALD} \\ \Phi_{TPI} \\ \Phi_{GAPD} \end{pmatrix} \Phi_{OX} \begin{pmatrix} 1 \\ 0 \\ 1 \\ 1 \\ 1 \\ 0 \\ 0 \\ 0 \\ 0 \\ 0 \\ 0 \\ 0 \\ 0 \\ 0 \\ 0 \\ 0 \\ 0 \\ 0 \\ 0 \\ 0 \\ 0 \end{pmatrix} + \Phi_{CAT} \begin{pmatrix} 0 \\ 1 \\ -1 \\ -1 \\ -1 \\ 0 \\ 0 \\ 0 \\ 0 \\ 0 \\ 0 \\ 0 \\ 0 \\ 0 \\ 0 \\ 0 \\ 0 \\ 0 \\ 0 \\ 0 \\ 0 \end{pmatrix} + \Phi_{GAPD} \begin{pmatrix} 0 \\ 0 \\ 0 \\ 0 \\ 0 \\ 0 \\ 0 \\ 0 \\ 0 \\ 0 \\ 0 \\ 0 \\ 0 \\ 0 \\ 3/6 \\ 3/6 \\ 3/6 \\ 3/6 \\ 3/6 \\ 3/6 \\ 1 \end{pmatrix} + \Phi_{PRPPs} \begin{pmatrix} 0 \\ 0 \\ 0 \\ 0 \\ 0 \\ 0 \\ 0 \\ 0 \\ 2/3 \\ -2/3 \\ 1 \\ -1/3 \\ -1/3 \\ -1/3 \\ 5/6 \\ 5/6 \\ 5/6 \\ 1/6 \\ 1/6 \\ 1/6 \\ 0 \end{pmatrix} + \Phi_{G6PD} \begin{pmatrix} 0 \\ 0 \\ 0 \\ 0 \\ -2 \\ 1 \\ 1 \\ 1 \\ 1/3 \\ 2/3 \\ 0 \\ 1/3 \\ 1/3 \\ 1/3 \\ 1/6 \\ 1/6 \\ -5/6 \\ -1/6 \\ -1/6 \\ -1/6 \\ 0 \end{pmatrix} \tag{4.17}$$

To finally obtain elementary modes, these vectors are combined in order to create a new basis composed of biological vectors with integer values and the maximum number of zeros. For an irreversible flux, the corresponding value in these vectors has to be positive. Thus, we obtain 5 elementary modes $\vec{V_i}$ with $i = \{1, ..., 5\}$ corresponding to specific pathways of the metabolic network (Figure 4.2) :

- First, $\vec{V_1}$ is a mode which displays a H_2O_2 detoxification by using glutathiones and $NADPH$. Recycling of the cofactor would be made here by all the reactions that consume and produce $NADPH$ which is known to be negligible during oxidative stress [15].

- Second, $\vec{V_2}$ is a mode using only catalase to detoxify oxidative stress. This enzyme that removes H_2O_2 is known not to be the main pathway for extreme oxidative stress [11].

- Third, $\vec{V_3}$ is a mode that shows an incoming glucose flux Φ_{GLU} going through the glycolysis with a flux rate equal to $2\Phi_{GLU}$ toward the lower glycolysis. This is the mode that sends the most carbon atoms coming from the incoming glucose molecules through the lower glycolysis. This mode is the one that will produce the most ATP and cellular energy. It is known that without perturbation such as oxidative stress, the flux state is mainly using this mode allowing to have 90% of Φ_{GLU} through the glycolysis [18, 17].

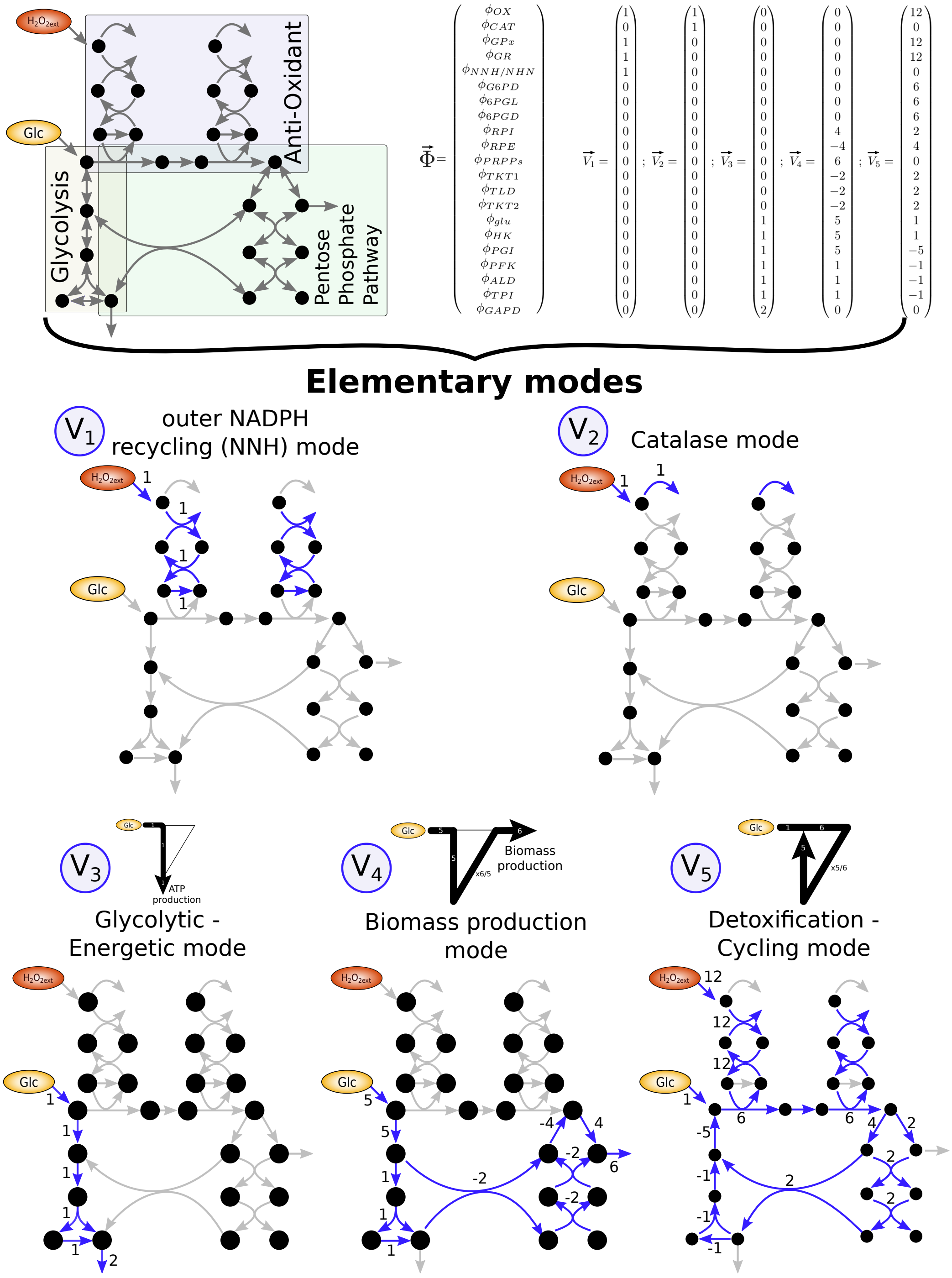

$$\vec{\Phi}=\begin{pmatrix}\phi_{OX}\\ \phi_{CAT}\\ \phi_{GPx}\\ \phi_{GR}\\ \phi_{NNH/NHN}\\ \phi_{G6PD}\\ \phi_{6PGL}\\ \phi_{6PGD}\\ \phi_{RPI}\\ \phi_{RPE}\\ \phi_{PRPPs}\\ \phi_{TKT1}\\ \phi_{TLD}\\ \phi_{TKT2}\\ \phi_{glu}\\ \phi_{HK}\\ \phi_{PGI}\\ \phi_{PFK}\\ \phi_{ALD}\\ \phi_{TPI}\\ \phi_{GAPD}\end{pmatrix}\quad \vec{V_1}=\begin{pmatrix}1\\0\\1\\1\\1\\0\\0\\0\\0\\0\\0\\0\\0\\0\\0\\0\\0\\0\\0\\0\\0\end{pmatrix};\ \vec{V_2}=\begin{pmatrix}1\\1\\0\\0\\0\\0\\0\\0\\0\\0\\0\\0\\0\\0\\0\\0\\0\\0\\0\\0\\0\end{pmatrix};\ \vec{V_3}=\begin{pmatrix}0\\0\\0\\0\\0\\0\\0\\0\\0\\0\\0\\0\\0\\0\\1\\1\\1\\1\\1\\1\\2\end{pmatrix};\ \vec{V_4}=\begin{pmatrix}0\\0\\0\\0\\0\\0\\0\\0\\4\\-4\\6\\-2\\-2\\-2\\5\\5\\5\\1\\1\\1\\0\end{pmatrix};\ \vec{V_5}=\begin{pmatrix}12\\0\\12\\12\\0\\6\\6\\6\\2\\4\\0\\2\\2\\2\\1\\1\\-5\\-1\\-1\\-1\\0\end{pmatrix}$$

Figure 4.2: Flux balance analysis of PPP. Flux balance analysis identifies 5 elementary modes $\vec{V_i}$. Theses modes are represented using metabolic network scheme. Blue arrows represent used fluxes. Values near to arrows correspond to flux rates normalised by incoming glucose flux used by the corresponding elementary modes. Black circles denote metabolites.

- Fourth, $\vec{V_4}$ is a mode that directs the incoming glucose flux through the glycolysis and then the reverse noxPPP inducing flux toward the purine metabolism via $PRPPs$ output flux in order to produce nucleotides. This is the mode of production of cellular biomass.
- Finally, $\vec{V_5}$ has the most impact on the oxidative stress response. Indeed, the incoming glucose flux is going through the oxidative and then non-oxidative pentose phosphate pathway. Instead of going out of the metabolism network through $GAPD$, the carbons take the reverse glycolysis allowing to come back to the oxPPP. Therefore, the carbons can cycle in the network allowing to increase the flux inside the PPP to 6 times Φ_{GLU}. Because $NADPH$ is reduced by the first and third oxPPP enzyme, i.e. $G6PD$ and $6PGD$, the $NADPH$ recycling increases to 12 times Φ_{GLU} which makes this mode highly powerful in terms of oxidative stress detoxification. It has been shown that the network is rerouting the incoming glucose flux from glycolytic modes toward the PPP [18, 17]. For extreme stress, the network continues to shift to this cycling mode. However, this mode could allow an $NADPH$ recycling 12 times Φ_{GLU} but rarely exceed 1.5 or 2 Φ_{GLU} experimentally depending of the cell type [17, 18, 131, 132].

Flux balance analysis allows to extract a new basis composed of 5 elementary flux modes in the metabolic network composed of PPP, glycolysis and anti-oxidant pathways. The actual of flux state associated to a particular cellular and environmental context will be a combination of these modes. 2 of them correspond to direct hydrogen peroxide degradation while the 3 other modes correspond to the use of glucose resources, either to produce energy (i.e. $\vec{V_3}$), biomass (i.e. $\vec{V_4}$) or $NADPH$ (i.e. $\vec{V_5}$). It is therefore convenient to represent the flux state of PPP and glycolysis as a combination of $\vec{V_3}$, $\vec{V_4}$ and $\vec{V_5}$ with coefficients associated to 3 specific flux rates (i.e. Φ_{GAPD}, Φ_{PRPPs} and Φ_{G6PD}) :

$$\vec{\Phi} = \Phi_{GAPD}\frac{\vec{V_3}}{2} + \Phi_{PRPPs}\frac{\vec{V_4}}{6} + \Phi_{G6PD}\frac{\vec{V_5}}{6} \tag{4.18}$$

which becomes with the normalized elementary modes $\vec{V_i^n}$:

$$\vec{\Phi} = \Phi_{GAPD}\vec{V_3^n} + \Phi_{PRPPs}\vec{V_4^n} + \Phi_{G6PD}\vec{V_5^n} \tag{4.19}$$

Because there is no passive degradation in the system, fluxes are directly proportional to the incoming glucose flux Φ_{GLU}. Thus, a flux state normalized by Φ_{GLU} can be expressed as :

$$\frac{\vec{\Phi}}{\Phi_{GLU}} = \lambda_3\vec{V_3^n} + \lambda_3\vec{V_4^n} + \lambda_3\vec{V_5^n} \tag{4.20}$$

where

$$\lambda_3 = \frac{\Phi_{GAPD}}{\Phi_{GLU}} \; ; \; \lambda_4 = \frac{\Phi_{PRPPs}}{\Phi_{GLU}} \; ; \; \lambda_5 = \frac{\Phi_{G6PD}}{\Phi_{GLU}} \tag{4.21}$$

Moreover, no passive degradation also induces the conservation relation :

$$\frac{\lambda_3}{2} + \frac{5\lambda_4}{6} + \frac{\lambda_5}{6} = 1 \tag{4.22}$$

In these conditions, the parameters are constrained as $0 < \lambda_3 < 2$; $0 < \lambda_4 < 6$; $0 < \lambda_5 < 6$. For instance, a full glycolytic mode is characterized by $\frac{\Phi_{GAPD}}{\Phi_{GLU}} = \lambda_3 = 2$ or a full cycling mode by $\frac{\Phi_{G6PD}}{\Phi_{GLU}} = \lambda_5 = 6$. Moreover, using this conservation relation, a flux state can be now expressed with only two modes. It has been shown that there is a drastic change of modes during oxidative stress from glycolytic to cycling mode for extreme perturbation allowing high $NADPH$ recycling and then high H_2O_2 detoxification [18, 17, 131, 132].

4.3 13C-MFA of flux rerouting in the PPP

Knowing a flux state of a metabolic network is an important feature allowing to characterise functional state of a cellular metabolism. ^{13}C-MFA is now a standard method to investigate a flux state of a metabolic network. In the context of oxidative stress response, glycolysis and PPP are studied by labeling glucose molecules. Used as input flux, labeled carbons are spread in the network allowing to estimate flux. In this section will be presented a class of method that allows to proceed to ^{13}C-MFA based on Stochastic Simulation Algorithm (SSA) used here in the context of oxidative stress response. This method is simple to implement and efficient even in complex MFA.

4.3.1 Labeling patterns of elementary modes

The flux state of a metabolic network is a combination of elementary modes identified with FBA. Efficiency of ^{13}C-MFA techniques to accurately estimate flux state depends on the efficiency is related to the efficiency of ^{13}C-MFA techniques to discriminate between different elementary flux modes. To illustrate this point, let consider the glycolytic mode and the PPP mode in different labeling conditions : 100% of $[1 -^{13} C]\ Glc$, $[2 -^{13} C]\ Glc$ and $[1, 2 -^{13} C]\ Glc$ (Figure 4.3). The glycolytic mode is V_3 while a PPP mode is where the carbon flux is only using the oxidative, noxPPP and $GAPD$ as output flux which corresponds to $5V_3 + V_5$. These two modes are both going out of the network only through $GAPD$ toward the lower glycolysis making them easy to compare by looking after this node.

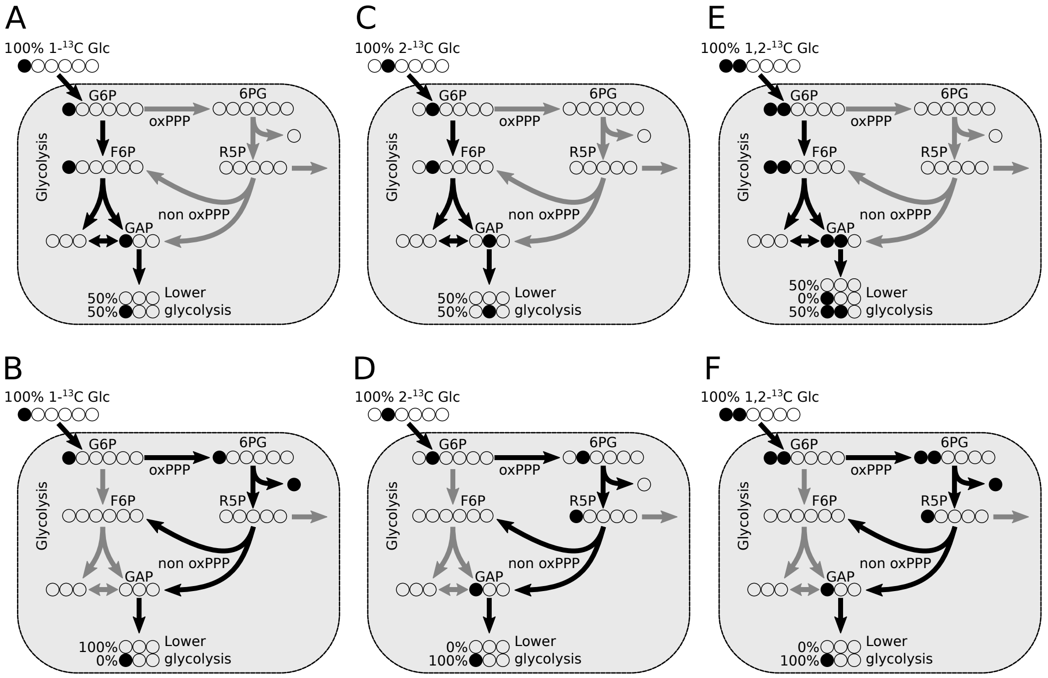

Figure 4.3: ^{13}C labeling experiments for two elementary modes. ^{13}C labeling patterns for the two elementary modes V_3 (A-C-E) and $5V_3 + V_5$ (B-D-F) (Figure 4.3) identified by black arrows. Non-labeled and labeled carbons are represented by empty and black circles. The labeling experiments are 100% $[1-^{13}C]$ Glucose (A-B), 100% $[2-^{13}C]$ Glucose (C-D) and 100% $[1,2-^{13}C]$ Glucose (E-F).

The first labeling experiments that can be made is by labeling the first carbon of glucose molecules giving 100% of m+1 at the beginning of the metabolic pathways. By only considering the glycolytic mode (Figure 4.3-A), all the incoming glucose flux is going through the glycolysis inducing a cut of FBP in two separated molecules, i.e. $DHAP$ and GAP. Thus, one of these two molecules is receiving the labeled carbons. All $DHAP$ molecules can be converted in GAP inducing half of labeled molecules, i.e. 50% of m+0 and the other half not labeled, i.e. 50% of m+1. However, by considering a PPP mode (Figure 4.3-B), the entire flux is going through the oxPPP where the first carbon is lost by using $6PGD$ enzyme and then going through the non-oxidative where the carbons are mixed. Because there is a loss of the first carbon, the labeling disappears at the same time inducing 100% of m+0 after $6PGD$ reaction. The efficiency of carbon labeling in order to estimate the flux state appears. Indeed, the flux going through the PPP can be known by measuring after the output flux at the end of the glycolysis and by comparing the ratio between m+0 and m+1 in this specific labeling condition. However, it is important to say that this analysis is valid only because we assume only 2 existing modes. As there are complex carbon rearrangement during the metabolic reactions happening mainly in the noxPPP, it induces more complex mass isotopomer distribution.

Experiments with $[2 -^{13} C]$ Glc labeling, i.e. the second carbon of a glucose molecule is a ^{13}C, induces the same distributions in glycolytic mode as $[1 -^{13} C]$ Glc labeling (Figure 4.3-C). However, it induces 100% m+1 instead of 0% in $[2 -^{13} C]$ Glc labeling due to loss of the first carbon, in the PPP mode (Figure 4.3-D). The same remark can be made for the $[1, 2 -^{13} C]$ Glc labeling experiment where the two first carbons are labeled, inducing 100% m+1 (Figure 4.3-F). Concerning the glycolytic mode, labeling the two first carbon of glucose molecules induces 50% m+0 and 50% m+2 due to the split of FBP in $DHAP$ and GAP (Figure 4.3-E). Thus, measuring the MID after the output flux $GAPD$ makes possible the differentiation of the 2 modes. As mention previously, there are a lot of recombinations that are not taken into account with the elementary modes which makes appear more complex distributions. It is then necessary to combine measurements in different labeling conditions at different nodes of the metabolic pathways. For instance, measuring the MIDs for $6PG$ will directly reflect the cycling flux. Indeed, when the first carbon of a molecule is labeled and going through the oxPPP, it induces loss of labeling. When this molecule is coming back to the PPP after going through the reverse glycolysis corresponding to cycling molecule, the m+1/m+0 labeling ratio for $6PG$ is reduced.

4.3.2 13C-MFA based on stochastic simulation algorithm

Stochastic simulation algorithms (SSA) are classes of method to investigate numerically the biochemical reactions [89] which have been here adapted to ^{13}C-MFA [123]. A new algorithm based on SSA has first been developed and will be explained here [1] in order to proceed to ^{13}C-MFA of the PPP and glycolysis during oxidative stress response. It is a method simple to implement and also efficient to proceed to complex MFA.

Isotopomer index and addressing operators

^{13}C-labeling consists in replacing a 12 carbon (^{12}C) by its isotope ^{13}C called labeled carbon inducing two different states for each carbon of a molecule. Thus, a labeling state L_i^j can be defined for each state of a labeled carbon j corresponding to $L_0^j = 0$ for a non-labeled meaning a ^{12}C and $L_1^j = 1$ for

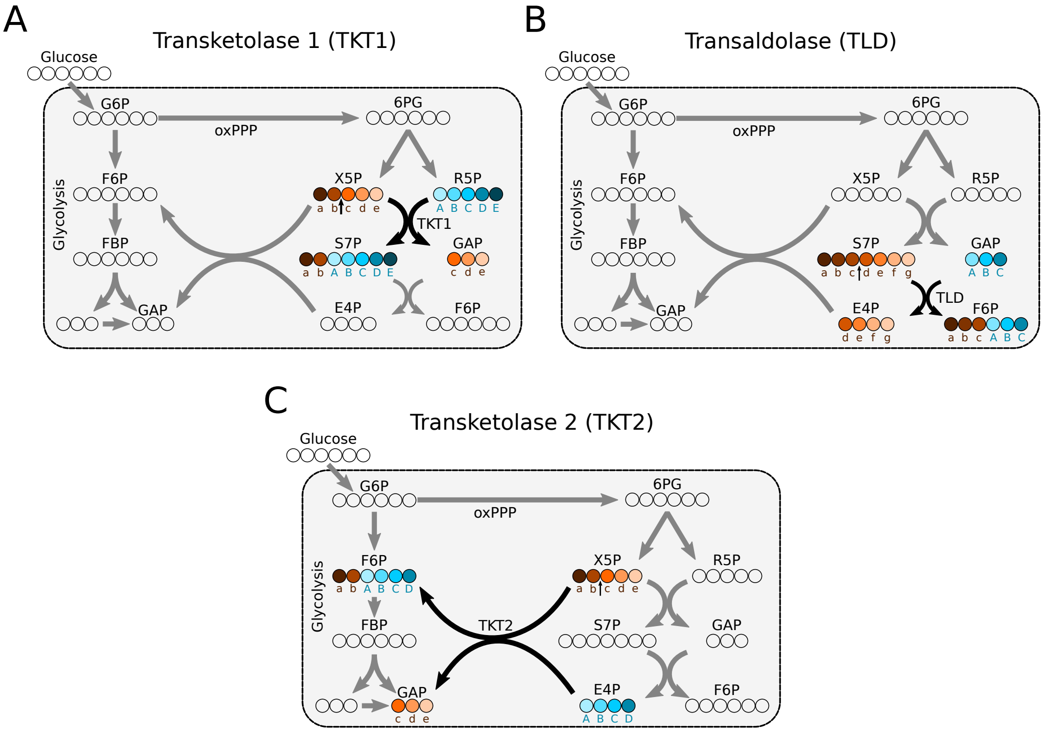

Figure 4.4: Carbons rearrangement during $TKT1/2$ and TLD reactions. The carbons rearrangement of the noxPPP reactions are represented here : (A) transketolase 1 ($TKT1$), (B) transaldolase (TLD) and (C) transketolase 2 ($TKT2$). The carbons of the reactants schematically shown by coloured circles are reorganized by the corresponding enzymes to form the products. Carbons of a molecule are also associated to letter sequences as it is conventionally written for a chemical reaction. Each arrow in a reaction points the place where enzyme cuts the reactant. All these enzymatic reactions are reversible allowing the reverse carbons rearrangement.

---

a labeled carbon. The maximum number of labeling state q becomes equal here to 2. A molecule m comprising n carbons with a specific labeling state is called an isotopomer and can be defined by the sequence of the carbons c_j by $\mathrm{I}_m = (c_{1,L^1}, c_{2,L^2}, ..., c_{n,L^n})$ called isotopomer index. In the context of the PPP and glycolysis, labeling experiments are often using glucose molecules composed of 6 carbons and often label for instance the first carbon where the sequence of this glucose isotopomer becomes $(1, 0, 0, 0, 0, 0)$. In the PPP and glycolysis, most of the molecules are composed of 6 carbons inducing 2^6 possible isotopomers. In general, the total number of isotopomer is equal to $q^n = 2^n$ per molecules inside a network in ^{13}C-labeling experiment. Different labeling atoms can be used in complement to extract more flux information but drastically increase the value of q and then the number of isotopomer.

A metabolic network is made of chemical reactions that proceed the transformation of chemical components. Each reaction follows a specific permutation rule that can be defined by addressing operators. They compute the isotopomer index of the products of a reaction from the isotopomer index of the reactants and reversely for the reversible reaction. PPP and glycolysis are well suited metabolic pathways to respond to oxidative stress and are composed of enzymatic reactions where most of the carbon rearrangements are made in the noxPPP, i.e. transketolase 1/2 ($TKT1/2$) and transaldolase (TLD) shown in Figure 4.4 :

$$X5P(abcde) + R5P(ABCDE) \xrightarrow{\text{TKT1}} S7P(abABCDE) + GAP(cde) \tag{4.23}$$

$$S7P(abcdefg) + GAP(ABC) \xrightarrow{\text{TLD}} F6P(abcABC) + E4P(defg) \tag{4.24}$$

$$X5P(abcde) + E4P(ABCD) \xrightarrow{\text{TKT2}} F6P(abABCD) + GAP(cde) \tag{4.25}$$

where the lowercase and uppercase script letters correspond to a more condensed and traditional convention to represent here the carbons c. All these reactions can be related to their corresponding addressing operators σ :

$$\sigma^{TKT1}_{S7P}(c^{X5P}, c^{R5P}) = (c^{X5P}_1, c^{X5P}_2, c^{R5P}_1, c^{R5P}_2, c^{R5P}_3, c^{R5P}_4, c^{R5P}_5) \tag{4.26}$$

$$\sigma^{TKT1}_{GAP}(c^{X5P}, c^{R5P}) = (c^{X5P}_3, c^{X5P}_4, c^{X5P}_5) \tag{4.27}$$

$$\sigma^{TLD}_{F6P}(c^{S7P}, c^{GAP}) = (c^{S7P}_1, c^{S7P}_2, c^{S7P}_3, c^{GAP}_1, c^{GAP}_2, c^{GAP}_3) \tag{4.28}$$

$$\sigma^{TLD}_{E4P}(c^{S7P}, c^{GAP}) = (c^{S7P}_4, c^{S7P}_5, c^{S7P}_6, c^{S7P}_7) \tag{4.29}$$

$$\sigma^{TKT2}_{F6P}(c^{X5P}, c^{E4P}) = (c^{X5P}_1, c^{X5P}_2, c^{E4P}_1, c^{E4P}_2, c^{E4P}_3, c^{E4P}_4) \tag{4.30}$$

$$\sigma^{TKT2}_{GAP}(c^{X5P}, c^{E4P}) = (c^{X5P}_3, c^{X5P}_4, c^{X5P}_5) \tag{4.31}$$

allowing to compute the product index from the reactant index $\mathrm{I}^j = (\sum_i^{n_j} c_i^j)$ where $j_{TKT1} = \{X5P, R5P\}$, $j_{TLD} = \{S7P, GAP\}$, $j_{TKT2} = \{X5P, E4P\}$ and $n_{j_{TKT1}} = \{5, 5\}$, $n_{j_{TLD}} = \{7, 3\}$, $n_{j_{TKT2}} = \{5, 4\}$. For the reverse reactions, the addressing operators could also be defined computing the reactant indexes from the product indexes. As an example, $TKT1$ reaction with $X5P$ $(1, 0, 0, 0, 0)$ and $R5P$ $(1, 0, 0, 0, 0)$ as reactants produces $S7P$ $(1, 0, 1, 0, 0, 0, 0)$ and GAP $(0, 0, 0)$.

Description via chemical master equation

A biochemical network composed of reactions is well described by chemical master equation (CME) [91]. In the context of stochastic dynamics, this formalism can also be used to describe labeling dynamics of chemical species.

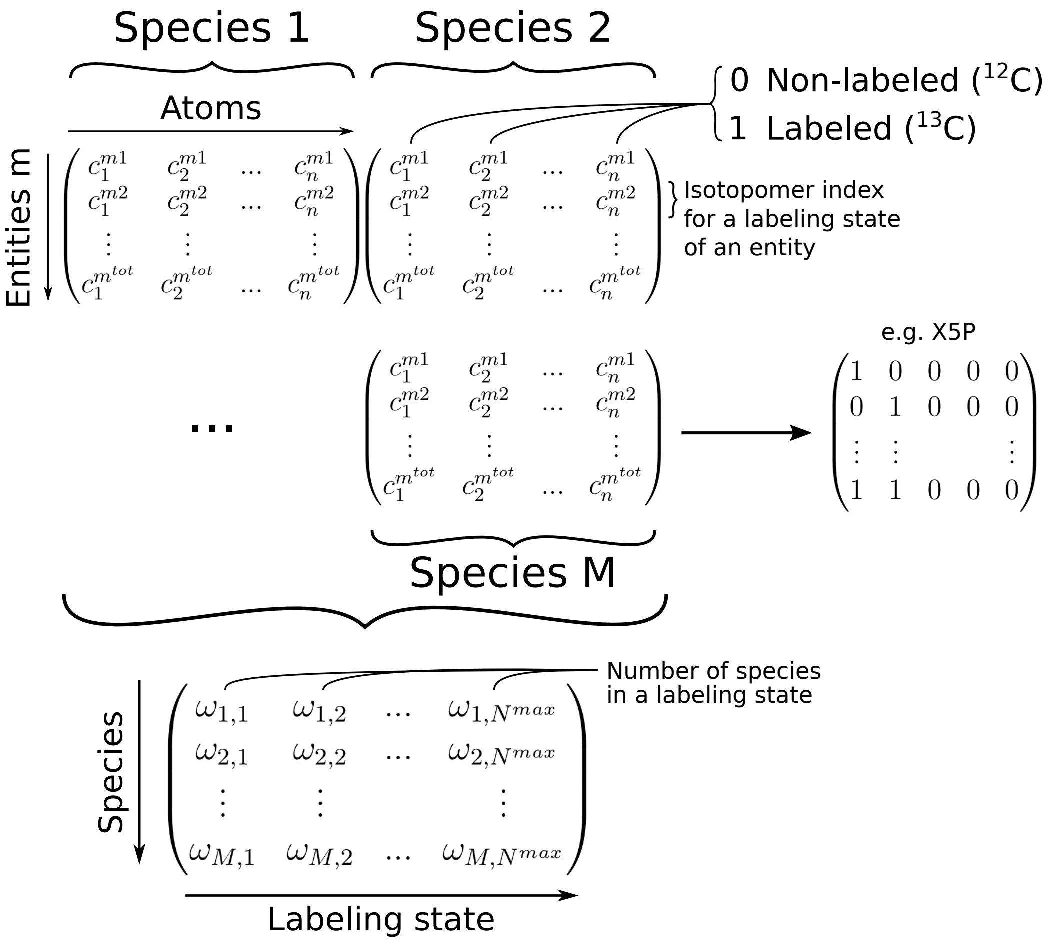

Figure 4.5: Mathematical formalism for the ^{13}C-MFA algorithm based on SSA. For a metabolic network composed of M species, each entities made of n carbons c of a species is characterized by a matrix composed of its isotopomer index. An example is given with a possible labeling state of a population of $X5P$ molecules made of 5 carbons. All these matrices are merged in a single matrix representing the number of entities in a specific labeling state ω for each species.

It has been presented previously the isotopomer index and addressing operator allowing to describe how a reaction induces carbon rearrangements of a specific set of isotopomer whether it is for reactants or products. These notations can be applied in the CME framework to compute the probabilistic dynamics in isotope labeling network. For a given species i composed of n atoms that can be labeled, more specifically carbons in the context of

^{13}C-labeling, the number of all the possible isotopomers is given by $N_i = 2^n_i$. A species i composed of m^{tot} entities can be directly related to its concentration x_i by defining a volume Ω inducing $m_i^{tot} = \Omega x_i$. Then, Ω serves as a scaling factor between all the different species in the network. For instance, $\Omega = 1000 copies/\mu M$ indicates that there are 1000 copies of a chemical species in a concentration of $1\mu M$. A set of m^{tot} entities of a species is characterized by a $m_i^{tot} \times n_i$ matrix where each element is an integer representing the labeling condition of the corresponding carbon of a molecule. Thus, the m-th row of a matrix is the isotopomer index of the m-th molecule of the corresponding species. Then, it exists the same matrix for each species present in the network allowing to have all the labeling states, i.e. isotopomer index of all the entities in the system.

In a metabolic network composed of M species ($M = \sum_i m_i^{tot}$), the matrices representing the isotopomer index of all the entities can be combined in one single mathematical element defined by a $M \times N^{max}$ matrix where the chosen N^{max} will be here the maximum value among all the numbers of isotopomers N_i values of all the species in the system. This general matrix is composed of integer ω_i representing the number of entities of a species i being in a specific labeling state corresponding to an isotopomer index I. In this thesis, the anti-oxidant is not taken into account during the flux estimation due to lake of data. Then, the metabolic pathways take into account 12 metabolites ($M = 12$) and the highest number of isotopomer N^{max} is given by $S7P$ with 7 carbons that can be labeled ($N^{max} = 2^7 = 128$). A species i is then characterized by its corresponding row where all entities m^{tot} are distributed in all the possible labeling conditions. Finally, the probability that a labeling condition of a species corresponds to a specific isotopomer is then $\rho_i = \omega_i / \Omega x_i$. The CME can be applied to such formalism allowing to describe the temporal evolution of the probability of the system to be in the state ω [1].

Method of the stochastic simulation algorithm

The idea of the algorithm is to mimic the chemical reactions by a discrete and stochastic process in order to propagate the labeled atoms. Populations of the chemical compounds are represented by samples with a finite size directly proportional to Ω. The labeling conditions of the atoms that can be labeled for all the entities of a species are sampled by a matrix at a certain time. The reactants of a reaction are randomly taken inside their corresponding matrix by selecting a row representing an isotopomer index. To make occur a reaction, the addressing operator following the permutation rules of the reaction is applied to the reactant indexes in order to compute the product indexes which will be added to the matrices of their corresponding species. The new produced entities will be part of the system and could be used for a future reaction.

Because the reactions are applied step by step, each iteration can be seen as a time unit. When the sample size is large, labeled atoms will need more iteration to propagate along the metabolic pathway meaning that the algorithm will need more iterations to reach an equilibrium. The step-by-step reactions are determined by an adapted method of the standard next reaction method, thus the SSA can be summarized by :

Initiation : Define a flux vector Φ_k and compute the corresponding reaction time :

$$\tau_k = \frac{1}{\Omega \Phi_k} \tag{4.32}$$

Step 1 : Select the minimum time $\tau_{k'} = min(\tau_k)$ and apply the corresponding reaction k' by randomly picking the substrates in their sample matrices and by applying on them the addressing operator which follows the permutation rules. The new synthesized molecules are added to the product sample matrix.

Step 2 : Increment the iteration time t by $\tau_{k'}$ and compute next time reaction k'.

Step 3 : Modify the reaction vector τ_k to take into account the variation of the sample size due to the reaction k'.

Iterate to Step 1

Following these steps, the mass isotopomer distributions can be computed as a function of a flux state and followed at any time of the labeled atom propagation. Different flux rates would induce different carbon propagation and then different MIDs. A simulation example is given in Figure 4.6. It shows the propagation of $G6P$ and $6PG$ metabolite MIDs $m_{i,j}$ for a labeling condition i of a metabolite j as a function of the iteration time which can also be written as $m_{i,j} = m + i$. Without labeling, the MIDs for both molecules are initially at 100% m+0. At time equal to 0, 50% of the entering glucose molecules are labeled by their first carbon in this simulation (i.e. $[1-^{13}C]$ *Glc* labeling condition). Fluxes taken as input for the algorithm are chosen in order to have the incoming glucose flux Φ_{GLU} going through the glycolysis with a small leak through the PPP which would correspond to a flux state of a non-perturbed cell [18, 17]. This chosen flux state has no cycling flux ensuring to have MIDs at 50% m+0 and 50% m+1 for both molecules as

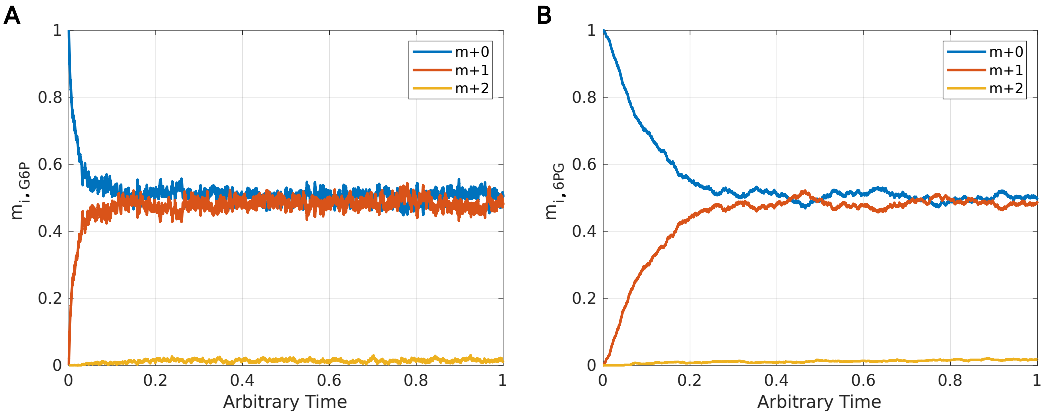

Figure 4.6: Example of the mass isotopomer distribution repartition during SSA. Mass isotopomer distribution $m_{i,j}$ of (A) $j = G6P$ or (B) $j = 6PG$ as a function of the iteration time made by stochastic simulation algorithm in 50% $[1 -^{13} C]$-glucose labeling. Input fluxes are set in order to have the incoming glucose flux Φ_{GLU} going through the glycolysis with a small leak through the PPP. Mass isotopomer distribution $m_{i,j}$ can be 3 different states i : m+0 (Blue), m+1 (Red) and m+2 (Yellow).

final steady state. Indeed, in Figure 4.6, the labeled carbons propagate into the network inducing around 50% m+0 and 50% m+1 at steady state. The difference of time to reach the steady state from $G6P$ to $6PG$ is coming from the difference of flux rate from glycolysis to PPP. As the PPP flux is lower, the carbons propagate slower which is clearly visible in this example.

In the example of Figure 4.6, the fluxes are given as input for the algorithm allowing to simulate the propagation of the labeled carbons and then to compute the MIDs as a function of time which corresponds to the forward problem. Another input flux state would have induced another MIDs dynamics. However, the algorithm can be used in order to infer a set of fluxes from a giving set of MIDs as input which corresponds to the inverse problem. Then, a first set of fluxes is given as initial condition. The corresponding MIDs are simulated and can be compared to a set of experimental data. In our interesting case, only experimental measured distributions at steady state will be used for the inverse problem which allows to take the mean of the steady state of the MIDs temporal dynamic. A Root Mean Square Error (RMSE) will be used to compare simulation to experimental data and to represent the gap between them :

$$RMSE(\vec{\Phi}) = \sqrt{\frac{1}{\mathcal{N}_m} \sum_{i,j,k} \left(m^k_{i,j,sim}(\vec{\Phi}, t) - m^k_{i,j,exp}(t) \right)^2} \tag{4.33}$$

where $m^k_{i,j,sim/exp}$ are the MIDs j of a species i for a labeling condition k of the incoming glucose in the simulation (sim) and experimental data (exp). The total number of the used $m^k_{i,j}$ is $\mathcal{N}_m$. The aim will be to reduce the gap between simulation results and experimental data by reducing this quantity by step-by-step modifying the set of fluxes inducing change of simulated MIDs. This can be made by the use of optimisation algorithm such as MCMC. Finally, the best score following the Cauchy's criterion for convergence will corresponds to the minimum of the RMSE and will lead to the resulting sets of fluxes.

4.3.3 Flux estimation

In this section will be presented the analysis of the ^{13}C labeling data in order to convert them into flux data. The method used is presented in the previous sections and comes from Thommen et al. 2022 [1]. It uses a stochastic simulation algorithm which computes the time evolution of the isotopomers by mimicking the reactions that can happen in a metabolic pathway inducing the conformation changes with sample size $\Omega = 200$. The experimental data are coming from Kuehne et al. 2015 [17] and are regrouped in 4 different ^{13}C-labeling conditions of the incoming glucose molecules, i.e. in first carbon position ($[1 -^{13} C]\ Glc$) at 50%, in second position ($[2 -^{13} C]\ Glc$) at 50% and the first two positions ($[1, 2 -^{13} C]\ Glc$) at both 50% and 100%. The experiments are produced without and with stress conditions induced by a $500\mu M$ of external H_2O_2, on neonatal human skin fibroblasts. In these experiments, the mass isotopomer distributions of the metabolite $G6P$, FBP, GAP, $F6P$, $S7P$, $R5P$ and $6PG$ are measured. Only the steady state data from m+0 to m+2 (i.e. from no labeled carbon to 2 in the metabolites) at 5 min are used which induces 3 values per metabolite per experiment, thus 84 experimental values of MIDs. Each individual experimental value will be compared by the simulation result by computing the RMSE. Minimisation of the RMSE is made by MCMC more specifically Metropolis Hastings algorithm. Two separated simulations are made to distinguish the basal condition (i.e. without stress) from the stress condition.

By finding the minimum area of the RMSE function, the resulting flux distributions can be obtained and represented by a violin plot (Figure 4.7-A). A flux rate Φ_{ENZ} for a corresponding enzyme is defined positive when the

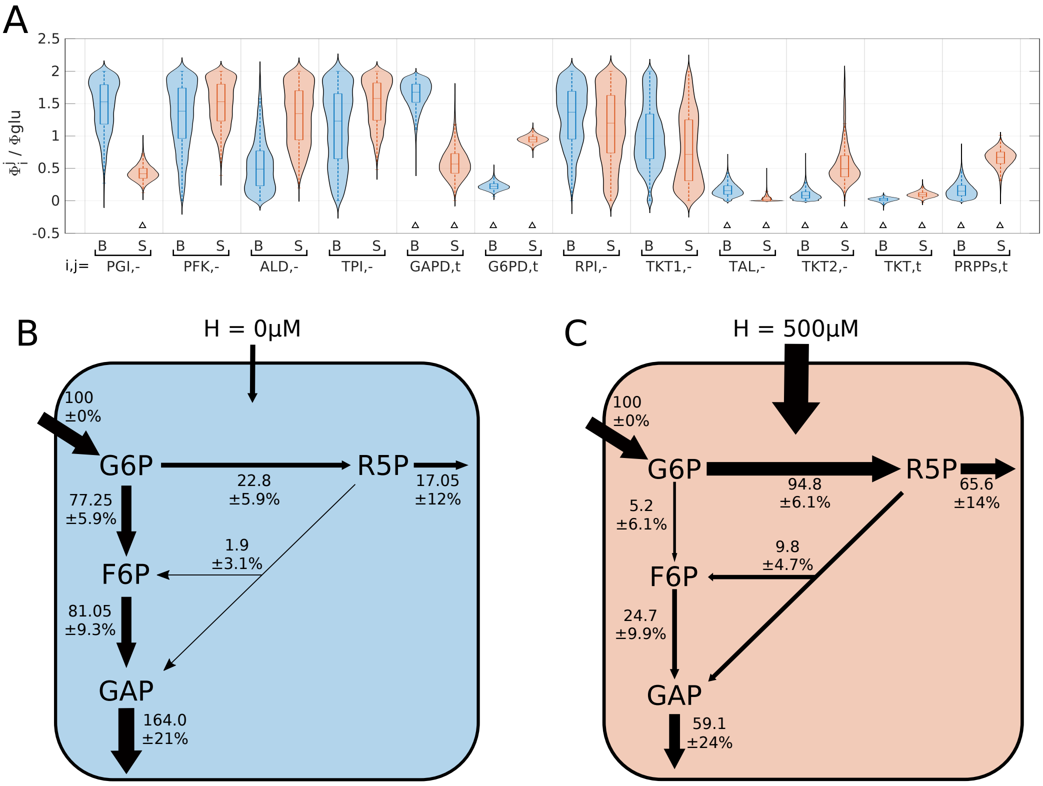

Figure 4.7: Estimated fluxes during ^{13}C-based metabolic flux analysis. From Hurbain et al. 2022 [3]. Representation of the fluxes obtained using stochastic simulation algorithm blue (B) and red (S) represent basal ($H = 0\mu M$) and stress ($H = 500\mu M$) conditions at steady state. (A) Violin plot of the estimated flux distributions. Φ_i^j are flux rate of an enzyme i for a specific direction j (± correspond to directional flux, t to net flux). Fluxes are normalised by incoming glucose flux Φ_{GLU}. Triangles represent confidence interval widths below 0.4 (Figure 4.9) meaning well estimated fluxes. (B-C) Schematic representations of the net flux rates in the metabolic pathway in (B) basal and (C) stress conditions.

---

enzymatic reaction is irreversible. For the reversible ones, they can be defined using directional flux rates (i.e. positive Φ^+_{ENZ} and negative Φ^-_{ENZ}) as $\Phi_{ENZ} = \Phi^+_{ENZ} - \Phi^-_{ENZ}$. Maximum boundaries for the flux rate values are set as twice the incoming glucose flux Φ_{GLU} in order to avoid extreme and non-realistic fluxes. A flux state of the PPP and glycolysis can be decomposed in 3 net fluxes (see Section 4.2). However, due to degenerations coming from directional fluxes, the number of flux rates needed to fully characterize the

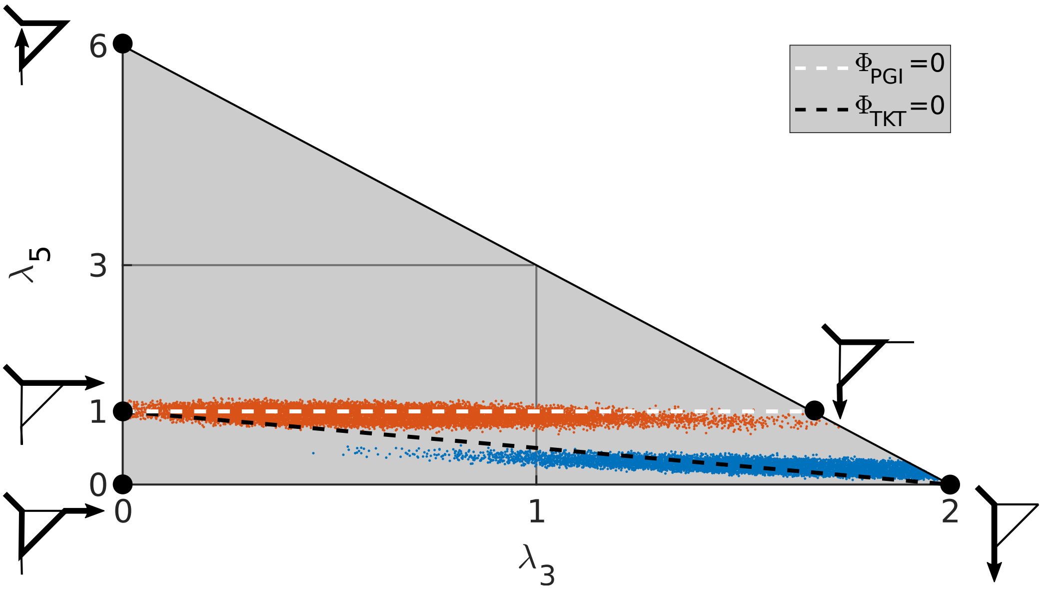

Figure 4.8: Flux state in the space of elementary modes. Fluxes shown in Figure 4.7 are expressed as function of the 3 last elementary modes (Figure 4.3). This decomposition is represented in the mode space shown by a triangle due to the conservation relation $\frac{\lambda_3}{2} + \frac{5\lambda_4}{6} + \frac{\lambda_5}{6} = 1$. Each axe of the space corresponds to components of elementary mode $\vec{V}_3^n$ and $\vec{V}_5^n$. Each flux state is a combination of the 2 elementary modes. In $\{\lambda_3, \lambda_5\} = \{0, 0\}$, the flux state is fully in $\vec{V}_4^n$. Representation of the estimated fluxes in basal condition ($H = 0\mu M$) in blue. Representation of the estimated fluxes in stress condition ($H = 500\mu M$) in red. $\Phi_{PGI} = 0$ and $\Phi_{TKT} = 0$ are represented by white and black dashed lines.

---

flux state is increasing to 12 flux rates which are all estimated here during minimisation of the RMSE function. The found flux distributions whether it is for the basal or stress conditions, are differently spread with very large distributions representing non-constrained fluxes while others are confined in a small flux area and are notified by a small Δ. To better understand the results, schematic representations of the flux states of the metabolic pathways in basal and stress conditions are given in Figure 4.7-B&C. Without stress, the fluxes are directed mainly through the glycolysis with a small proportion going through the PPP and going out respectively via $GAPD$ and $PRPPs$. However, the flux state is completely redefined during oxidative stress by having a flux rerouting toward the PPP inducing an increase of H_2O_2 detoxification.

The flux state can be decomposed into the normalised elementary modes $\vec{V}_i^n$ presented in Section 4.2. Because the estimated fluxes here are only in the PPP and glycolysis, the decomposition will be made as a function of the 3 last modes, i.e. $\vec{V}_3^n$, $\vec{V}_4^n$ and $\vec{V}_5^n$. Due to the lack of experimental data of MIDs in the anti-oxidant pathways, the first two modes cannot be used to extract information in the anti-oxidant pathways. Thus, a flux state $\vec{\Phi}$ can be expressed as a function of these modes. Using the normalized elementary modes $\vec{V}_i^n$ allows to decompose the flux states as a function of the λ_i (eq 4.20) which are directly proportional to the flux rates Φ_{GAPD}, Φ_{PRPPs} and Φ_{G6PD} (eq 4.19), and which can be represented in a 2D graph (Figure 4.8) using the conservation relation (eq 4.22) :

- Computing the elementary mode decomposition in basal condition induces $\lambda_3 = 1.64$, $\lambda_4 = 0.17$ and $\lambda_5 = 0.22$. The glycolytic mode prevails compared to the others at around 92.5%. λ_2 and λ_3 are closed to each other inducing a very small flux through the noxPPP.
- During oxidative stress induced by a $500 \mu M$ of external H_2O_2, there is a flux rerouting from glycolytic to mainly a PPP flux. A decomposition of this new flux state into normalised elementary modes reveals $\lambda_3 = 0.60$, $\lambda_4 = 0.66$ and $\lambda_5 = 0.95$ showing a high flux rerouting toward the PPP and to the cycling flux mode with a fold change of λ_4 and λ_5 at ≈ 4 (Figure 4.8). It is important to note that, in mean, λ_3 and λ_4 are not sufficiently low, or λ_5 sufficiently high to have a real cycling flux which would correspond to $\Phi_{oxPPP} = \lambda_5 > 1$ or equivalent $\Phi_{GLY} = (\frac{1}{2}\lambda_3 + \frac{5}{6}\lambda_4 - \frac{5}{6}\lambda_5) < 0$. A potential higher stress level would reveal higher cycling mode inducing fully cycling flux.

The flux estimation is made by minimising a RMSE function allowing to extract sets of fluxes which reveal low score function. The distribution of these estimated fluxes could then be extracted revealing that a non-negligible proportion of them have large distribution meaning that they are not well estimated or that their values do not impact enough the MIDs to be constrained in a specific flux space. Other fluxes have their distributions very narrow indicating that they impact significantly the MIDs in order to reproduce the experimental data. To distinguish the large to narrow fluxes distributions, a confidence interval (CI) is computed and separated in two groups (Figure 4.9). For each estimated flux in basal and stress conditions, a smaller CI width than 0.4 is targeted by a small Δ meaning that the distribution is narrow (Figure 4.7). By taking 3 well determined net fluxes such as $G6PD$, $GAPD$ and $PRPPs$, it is possible to fully characterise the

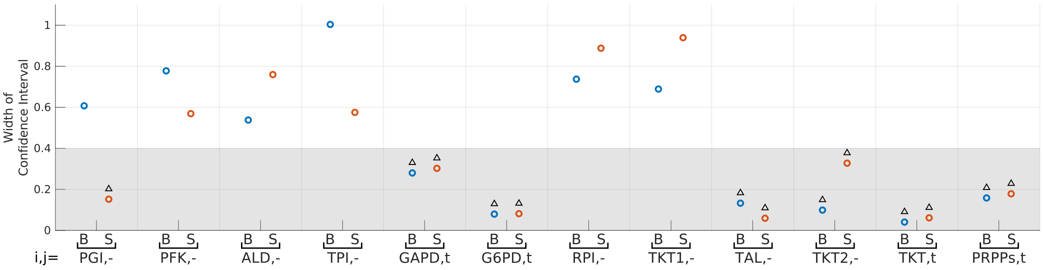

Figure 4.9: Confidence interval of the estimated flux distributions. From Hurbain et al. 2022 [3]. 50% Confidence intervals (CI) of flux distributions in Figure 4.7. The grey area correspond to CI below 0.4 which are indicated by a small Δ, meaning that flux estimation is accurate enough to be used in future model construction (Chapter 5).

---

flux state of the PPP and glycolysis in term of net fluxes. Then, directional fluxes of the noxPPP are well estimated which allows to remove a part of the degeneration. All these fluxes display a small CI width in both basal and stress conditions. Finally, only Φ^{-}_{PGI} have a narrow distribution in stress condition. It can be understood due to the inhibition on PGI by $6PG$ which would be activated by the flux rerouting during oxidative stress constraining the reverse PGI flux rate. Once the mathematical model described in this chapter will be expressed mathematically as a function of kinetic parameters and metabolite concentrations using reaction laws, the estimated fluxes that have a small CI width will fuel a data-driven parameter estimation in order to reproduce experimental behaviours. Then, the metabolic regulation mechanisms such as PGI inhibition activation, can be investigated during oxidative stress.

4.3.4 Stochastic algorithm for non-stationary 13C-MFA

The new ^{13}C-MFA algorithm is a different class of method that simulates isotope propagation based on SSA. As made in this thesis, most of the well known ^{13}C-MFA are limited to stable analyses with both metabolic and isotopic steady state. However, more complex ^{13}C-MFA can be computed without steady state condition as it has been made for transient isotopic labeling corresponding to non-stationary MFA (^{13}C-NMFA or ^{13}C-instMFA) [121] or for non-stationary metabolic fluxes corresponding to dynamic MFA (^{13}C-DMFA) [109]. When metabolic or isotopic labeling is not constant in time, the use of non-stationary MFA is well suited. While ^{13}C-instMFA can be implemented for instance in INCA software with an EMU decomposition, it

Metabolic network size	**Method used**	**Computational time**
12 metabolites / 21 reactions	SSA	$\approx 0.03s$
	EMU (by INCA)	$\approx 0.6s$

Table 4.1: Comparison of algorithm efficiencies in non-stationary labeling. For a metabolic network presented in this thesis comprising PPP and glycolysis, the computational time for the forward simulation of isotopomer distributions in non-stationary labeling condition are compared between the EMU method implemented by INCA and the new ^{13}C-MFA algorithm based on SSA presented in this thesis with $\Omega = 100$. Simulation are made using an Intel(R) Core(TM) i7-10610U CPU at 1.80GHz without parallelisation.

does not exist highly efficient software that implements ^{13}C-DMFA.

The new proposed method is able to compute both ^{13}C-instMFA and ^{13}C-DMFA with a high computational efficiency. During the fluxes estimation, the reaction inducing the labeled carbon propagation are chosen stochastically as a function of a given set of fluxes. Thus, the algorithm can easily take into account the time-varying fluxes during the iterations allowing to proceed to ^{13}C-DMFA and similarly for transient isotopic labeling in ^{13}C-instMFA. Moreover, during an inverse problem, a simulation for estimating the MIDs according to a flux state is calculated a very large number of times, making the calculation time a very important information. Then, the computational time of the SSA and the EMU decomposition computed by INCA software is compared for the metabolic network presented in this thesis in the table 4.1. It appears that the new proposed ^{13}C-MFA algorithm is around 20 times faster than the EMU decomposition via INCA software for a metabolic network composed of the PPP and glycolysis. This metabolic network is particularly interesting despite its size due to its capacity to mix the carbons in metabolites via the noxPPP reactions making the new ^{13}C-MFA algorithm already efficient. Indeed, while EMU decomposition size can drastically increase as a function of the number of isotopomer impacting the computational time, one of the main advantage of the SSA is that this new method has a very weak dependence of the computational time on the number of isotopomer. Another important advantage is that SSA's computational time is not impacted by the number of labeled atoms making the method well suited to study parallel labeling, for instance with hydrogen or oxygen labeling [1].

The use of non-stationary MFA methods often depend of their implementations in a software. While ^{13}C-MFA can be computed by many software such as COBRA [116] and ^{13}C-instMFA by other software such as INCA [118] using EMU decomposition as the core algorithm, most of the DMFA are not implemented in highly efficient software. However, the proposed method does not require implementation in any particular software and can be easily achieved in any programming language as it would be made for chemical kinetics modeling.

Chapter 5

Kinetic model of PPP

Mathematical models are often used to simulate and investigate metabolic pathways behaviour which is also used in the context of oxidative stress [34, 124, 133, 126, 134]. Moreover, data-driven estimation in mathematical model is a common procedure to reproduce experimental measurements [135]. A metabolic network of the PPP (PPP) and glycolysis will be modeled in this thesis to investigate the enzyme regulatory mechanisms allowing resources reallocation during fast oxidative stress response. Using model optimisation algorithms such as Monte Carlo Markov chain and genetic algorithm, parameter distributions will be estimated allowing to build a model ensemble reproducing experimental measurements. A biphasic response and an adaptation phenotype will be observed during temporal dynamics and flux rerouting via dose response analysis which confirms the network regulation work during oxidative stress to reorganise the incoming glucose flux resource. All these data are published in Hurbain et al. 2022 [3].

5.1 Model construction : complexity vs efficiency

Glycolysis and pentose phosphate pathway combined to a detoxification pathway made of glutathione and cofactor $NADPH$ is modeled mathematically using ordinary differential equation as a function of fluxes (Section 4.1). It allowed to analyse the flux state of the model during rapid oxidative stress response. A next step can be made by expressing mathematically the flux rates as a function of kinetic parameters and metabolite concentrations. This step is necessary to implement interactions between metabolites and enzymes. Indeed, allosteric regulation or competitive inhibition are not taken into account with the ordinary differential equation expressed as a function of fluxes

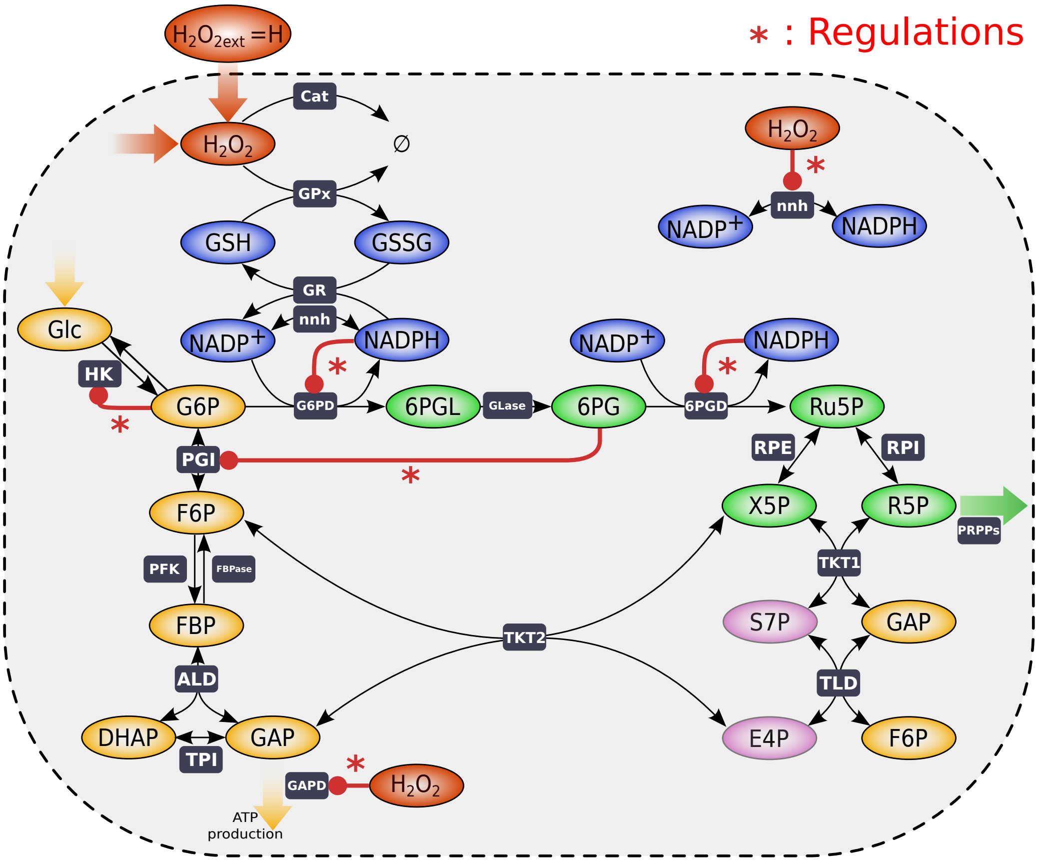

Figure 5.1: Metabolic pathways with their regulations used in the mathematical modeling. From Hurbain et al. 2022 [3]. Schematic representation of the network comprising the metabolites shown by coloured ellipses, chemical reactions shown by black arrows with their corresponding enzymes in black squares. OxPPP is in green, non-oxidative in pink, glycolysis in yellow, anti-oxidant system in blue and oxidant molecules in red. Input and output fluxes are represented by big arrows. Metabolic regulations are shown by red arrows and notified by an ∗.

and can have an important impact on the oxidative stress response. Moreover, these expressions are made to characterize rapid dynamics and do not take into account longer responses.

The metabolic network described here has 21 reversible or irreversible fluxes which can be described by using different kinetic laws as mass action law, Michaelis-Menten dynamics. As they are mainly enzymatic reactions, they could be design with Michaelis-Menten law. It would induce at least

2 parameters per irreversible reactions, i.e. maximum speed and saturation parameter. When the reaction is reversible, it adds potentially 2 other parameters, i.e. equilibrium constant and another saturation parameter. Therefore, by adding regulation inside the model, the total number of parameters for the entire system of equations would be more than 90. Most of these parameters are difficult to determine precisely experimentally in-vivo but can be data-driven estimated. The higher the number of parameter, the longer and more difficult the estimation. It clearly shows the necessity to decrease the number of parameter. Therefore, the reaction rates will be first described with linear expression by using mass action law. Then, non-linearities that are non-negligible, such as saturation, or regulation are added afterwards to the network following the generalized expressions given in Section 2.1. Indeed, we consider saturation terms only in the reactions for which substrates significantly increase during oxidative stress (i.e. $6PG$, $R5P$, $X5P$ etc...). The flux rates expression are listed in table 5.1.

Reaction	Law	Equation
OX		$k_{OX} + k_{diff}([H_2O_2]_{ext} - [H_2O_2])$
CAT	Eq 2.6	$k_{CAT}[H_2O_2]$
GPx	Eq 2.9	$k_{GPx}[H_2O_2][GSH]/(\frac{[GSH]}{KmG_{GPx}} + \frac{[H2O2]}{KmH_{GPx}})$
GR	Eq 2.9	$k_{GR}[NADPH][GSSG]/(1 + \frac{[GSSG]}{KmG_{GR}} + \frac{[NADPH]}{KmN_{GR}})$
NHN	Eq 2.6	$k_{NADP}[NADP^+]$
NNH	Eq 2.11	$k_{NADPH}[NADPH]/(1 + \frac{[H_2O_2]}{Ki_{NNH}})$
G6PD	Eq 2.11	$k_{G6PD}[G6P][NADP^+]/(1 + \frac{[NADPH]}{Ki_{G6PD}})$
6PGL	Eq 2.6	$k_{GLase}[6PGL]$
6PGD	Eq 2.12	$k_{6PGD}[6PG][NADP^+]/(1 + \frac{[NADPH]}{Ki_{6PGD}} + \frac{[6PG]}{Km_{6PGD}})$
RPI	Eq 2.6	$k_{RPE}([Ru5P] - \frac{[X5P]}{Keq_{RPE}})$
RPE	Eq 2.6	$k_{RPI}([Ru5P] - \frac{[R5P]}{Keq_{RPI}})$

PRPPs	Eq 2.9	$k_{PRPPs}[R5P]/(1+\frac{[R5P]}{Km_{PRPPs}})$
TKT1	Eq 2.10	$k_{TKT1}([R5P][X5P]-\frac{[GAP][S7P]}{Keq_{TKT1}})/(1+\frac{([R5P][X5P]}{Km_{TKT1}}+\frac{[GAP][S7P])}{Km_{TKT1}})$
TLD	Eq 2.10	$k_{TLD}([GAP][S7P]-\frac{[F6P][E4P]}{Keq_{TLD}})/(1+\frac{([GAP][S7P]}{Km_{TLD}}+\frac{[F6P][E4P])}{Km_{TLD}})$
TKT2	Eq 2.10	$k_{TKT2}([E4P][X5P]-\frac{[F6P][GAP]}{Keq_{TKT2}})/(1+\frac{([E4P][X5P]}{Km_{TKT2}}+\frac{[F6P][GAP])}{Km_{TKT2}})$
HK	Eq 2.11	$k_{HK}[Glc]/(1+\frac{[G6P]}{Ki_{HK}})$
PGI	Eq 2.11	$k_{PGI}([G6P]-\frac{[F6P]}{Keq_{PGI}})/(1+\frac{[6PG]}{Ki_{PGI}})$
PFK	Eq 2.6	$k_{PFK}[F6P]-k_{FBPase}[FBP]$
ALD	Eq 2.6	$k_{ALD}([FBP]-\frac{[DHAP][GAP]}{Keq_{ALD}})$
TPI	Eq 2.6	$k_{TPI}([DHAP]-\frac{[GAP]}{Keq_{TPI}})$
GAPD	Eq 2.11	$k_{GAPD}[GAP]/(1+\frac{[H_2O_2]}{([GSH]/[GSH]_{tot})Ki_{GAPD}})$

Table 5.1: Mathematical model reactions rates expressions. Generalized expression are introduced in Section 2.1 Mathematical expression of GPx and GR are taken from Benfeitas et al. 2014 [124]. $GAPD$ flux rate is a simplified version of the complex oxidative inhibition from H_2O_2 and reduction from GSH.

In these conditions, all reactions of the metabolic pathways are expressed in order to keep the important metabolic mechanisms without having very high number of parameters. For the entire model, the fluxes can be expressed mathematically via their reaction rates as a function of 48 parameters. Mathematical terms and saturations for ϕ_{GPx} and ϕ_{GR} follow expression based on an existing model [124]. Finally, saturation in the noxPPP reactions are considered equal in both direction which assumes to take the same saturation constant for substrates and products. A specific treatment is made for $GAPD$. Because its regulation is made by an oxidation from H_2O_2 and reduced by GSH [35], two type of molecules are considered : non-oxidized and oxidized $GAPD$. The transition between these two states depend of the concentration of H_2O_2 and GSH. The change of state is very fast, thus quasi steady state concentration can be considered inducing the expression shown in the 5.1.

This model is built in order to study the respective roles of a group of metabolic regulations that is known to impact the fast oxidative stress response : $G6PD$ is inhibited by $NADPH$, PGI by $6PG$, $GAPD$ by H_2O_2, HK by $G6P$ [17, 18, 34, 36]. All reactions that consume $NADPH$ into $NADP^+$ are characterized by a rapid decrease of biosynthetic pathways during oxidative stress [15, 16] which is symbolized by an inhibition of the effective reaction NNH by H_2O_2. However, other regulations listed in Figure 1.4 have not been taken into account such as the inhibitions of PK, TPI, or PFK enzymes [19, 37, 52, 53].

5.2 Estimation of model parameters

Mathematical model used to describe variations of metabolite concentrations as a function of time is dependent of parameters. This system of equations is made of 48 parameters. Because of the difficulty to measure them precisely experimentally, a specific parameter estimation method based on experimental data is used. The aim of this method is not to estimate one specific set of parameter but a distribution of sets of parameters that create an ensemble of plausible models able to reproduce experimental data.

5.2.1 Reduction of the parameter space

Before applying a specific procedure to estimate model parameters and even if the flux rates are expressed in order to minimise the number of parameter, dimensionality of the parameter space is still very high as the model comprises 48 parameters. Thus, this space still needs to be reduced by fixing parameters at a certain value or by confining other between boundaries. The boundaries are generally one decade below and above from an unique data. These values or boundaries are defined from experimental measurement or existing models. All of them are given in the following table :

Parameter	Value	Range	References
k_{GPx}	1s^{-1}	$[10^{-1}; 10^1]$	[124]
KmH_{GPx}	0.04μM	$[10^{-1}; 10^1]$	[124]
KmG_{GPx}	9.72μM	$[10^{-1}; 10^1]$	[124]
k_{GR}	49s^{-1}	$[10^{-1}; 10^1]$	[124]
KmN_{GR}	8.5μM	$[10^{-1}; 10^1]$	[124]

KmG_{GR}	65μM $[10^{-1}; 10^{1}]$	[124]
Ki_{G6PD}	10μM $[10^{-1}; 10^{1}]$	[17, 45]
Ki_{6PGD}	10μM $[10^{-1}; 10^{1}]$	[45, 136]
Ki_{PGI}	100μM $[10^{-2}; 10^{1}]$	[17]
Ki_{GAPD}	100μM $[10^{-2}; 10^{1}]$	[36]
Ki_{NNH}	100μM $[10^{-1}; 10^{1}]$	
Km_{G6PD}	50μM	[25, 137]
Km_{PRPP}	65μM	[138]
Keq_{RPE}	1.68	[70]
Keq_{RPI}	1.23	[70]
Keq_{TKT1}	1.62	[70]
Keq_{TLD}	0.36	[70]
Keq_{TKT2}	30	[70]
Keq_{PGI}	0.34	[70]
Keq_{ALD}	66μM	[70]
Keq_{TPI}	19.2	[70]
k_{diff}	1s^{-1} $[10^{-1}; 10^{1}]$	[124]
Φ_{GLU}	40μM.s^{-1}	
$[NADP(H)]_{tot}$	30μM	[124]
$[GSH]_{tot}$	3mM	[124, 139]
k_i	1s^{-1} $[10^{-4}; 10^{1}]$	

Table 5.2: Parameter space and values. Range defines the range of variation around the indicated value. Blank range indicates fixed value.

5.2.2 Parameter estimation procedure

After reducing the parameter space, it still remains 36 to estimate, i.e. 36 non-fixed parameters. A specific procedure is made to deduce a distribution of these parameters in order to be able to reproduce experimental data by numerical simulation. This experimental data are taken from Kuehne et al. paper [17] which shows rapid changes in metabolite concentrations and metabolomic distribution as a function of time and different external H_2O_2 concentrations during oxidative stress response in fibroblast cell line. Data consist in fast oxidative stress response with a steady state at 5 min and do not take into account longer dynamic using transcription response. Mass isotopomer distributions data are not usable directly for the mathematical model but can be translated into flux values in basal and stress state (chapter 4). Thus, a function representing the gap between experimental and theoretical (i.e. from numerical simulation) data can be defined by taking only steady state values i.e. at 5min after a step from $[H_2O_2]_{ext} = H = 0\mu M$ to $500\mu M$ stress. The remaining experimental data, i.e. the temporal dynamic and the steady state concentration for different dose of stress, will be used as confirmation of the model ensemble after the parameter distribution estimation. The function representing the gap between experimental and theoretical results is defined as the following normalized Root Mean Square Error (nRMSE) function :

$$nRMSE(\vec{p} \in \mathcal{P}) = \sqrt{\frac{1}{\mathcal{N}_R + \mathcal{N}_\Phi} \left(\sum_{i=1,\mathcal{N}_R} \left(\frac{R_{i,sim}(\vec{p}) - R_{i,exp}}{\Delta R_{i,exp}} \right)^2 + \sum_{i=1,\mathcal{N}_\Phi} \left(\frac{\Phi_{i,sim}(\vec{p}) - \Phi_{i,exp}}{\Delta \Phi_{i,exp}} \right)^2 \right)} \tag{5.1}$$

where $R_i = log_2(\frac{X_i(H=500)}{X_i(H=0)})$ are concentration ratio in log scale and Φ_i are the estimated fluxes of reaction i in basal and stress conditions at steady state. $X_{i,sim/exp}$ corresponds to a quantity coming from a simulation result of a model with a set of parameter $\vec{p}$ taken from the parameter space $\mathcal{P}$, or from experimental data. Once the nRMSE becomes optimal, the parameter sets have been estimated creating a statistical ensemble of kinetic models $\mathcal{P}^*$. The experimental data consist in $\mathcal{N}_R = 12$ values of metabolite concentration ratios R_i and $\mathcal{N}_\Phi = 13$ values of estimated fluxes Φ_i (Section 4.3). $\Delta R_i = 1$ corresponds to experimental errors of the concentration ratios and $\Delta\Phi_i$ are standard deviations estimated from fluxes estimation which are also related to experimental errors. Therefore, this nRMSE represents the gap between experimental and simulated values, and as it is normalized by experimental errors, a value lower than 1 for the nRMSE induces a difference lower than experimental error and validates the Cauchy's criterion.

Simulations of the model ensemble $\mathcal{P}^*$ that reproduce experimental data are characterized by a nRMSE function value lower than 1 and a specific distribution of parameter sets. Looking at this function for random parameters clearly shows that the correct parameter distributions cannot be found because it only gives very high nRMSE values (Figure 5.2). Indeed, the randomly sampled sets of one million of parameters sets lies with a 50% confidence interval between 55.4 and 2.6. Thus, a genetic algorithm, described in Section 2.4, is used to travel into the parameter space by changing a small percentage of the total number of parameters step by step and to keep the

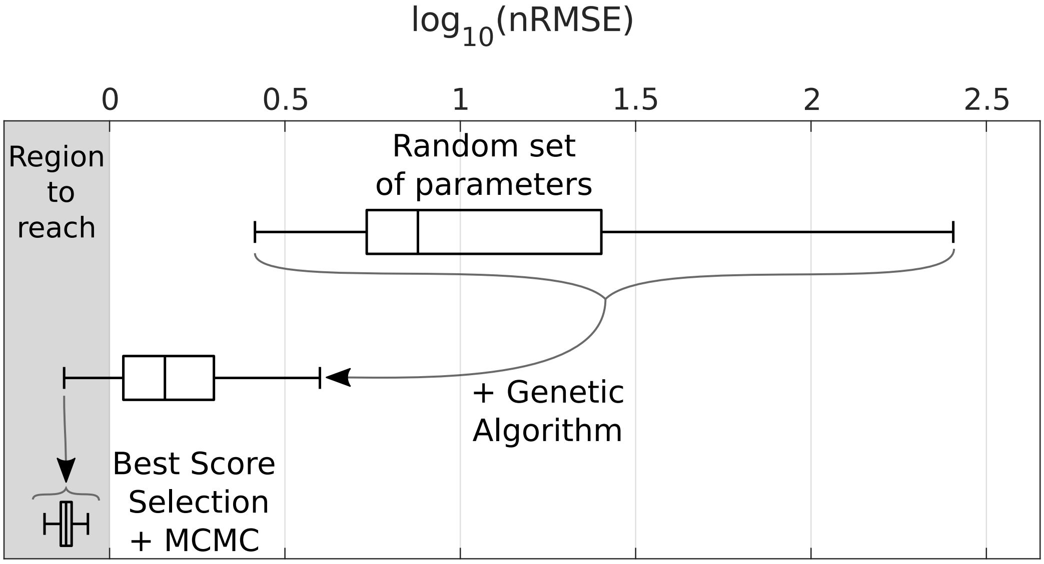

Figure 5.2: Minimisation procedure of the nRMSE function. From Hurbain et al. 2022 [3]. Whisker plots associated to 10^6 random parameter sets, 10^4 optimized parameter sets using evolutionary genetic algorithm and 10^6 parameter sets sampled using Monte Carlo Markov chain algorithm. Normalised Root Mean Square Error (nRMSE) function below 1 describes fitted value below experimental errors. Distribution of the parameter sets sampled using MCMC algorithm with a $nRMSE < 1$ will represent the model ensemble $\mathcal{P}^*$ for future analysis.

---

best parameter set which corresponds to the lower nRMSE. This algorithm decreases drastically the value of the nRMSE which induces 50% confidence interval nRMSE values lying between 3 and 0.8. The lower boundary reveals that a part of the parameter sets already has nRMSE value lower than the experimental error. Thus, as a final step, MCMC is used to scan the parameter space locally from the previous lower nRMSE sets of parameters as initial condition. Indeed, this algorithm allows to obtain a large enough sample (10^6 accepted points) of the parameter space with a nRMSE lower than 1, so a sufficiently large parameter sets that can be used to reproduce experimental data via numerical simulation creating the model ensemble $\mathcal{P}^*$. This distribution has a 50% confidence interval nRMSE values between 0.63 and 0.86. A low total nRMSE means that the errors between experimental and simulation data are in mean under experimental errors. However, it doesn't mean that each sub-element which corresponds to the fit of each concentration ratio or flux, has a good fit. Looking at the distribution of

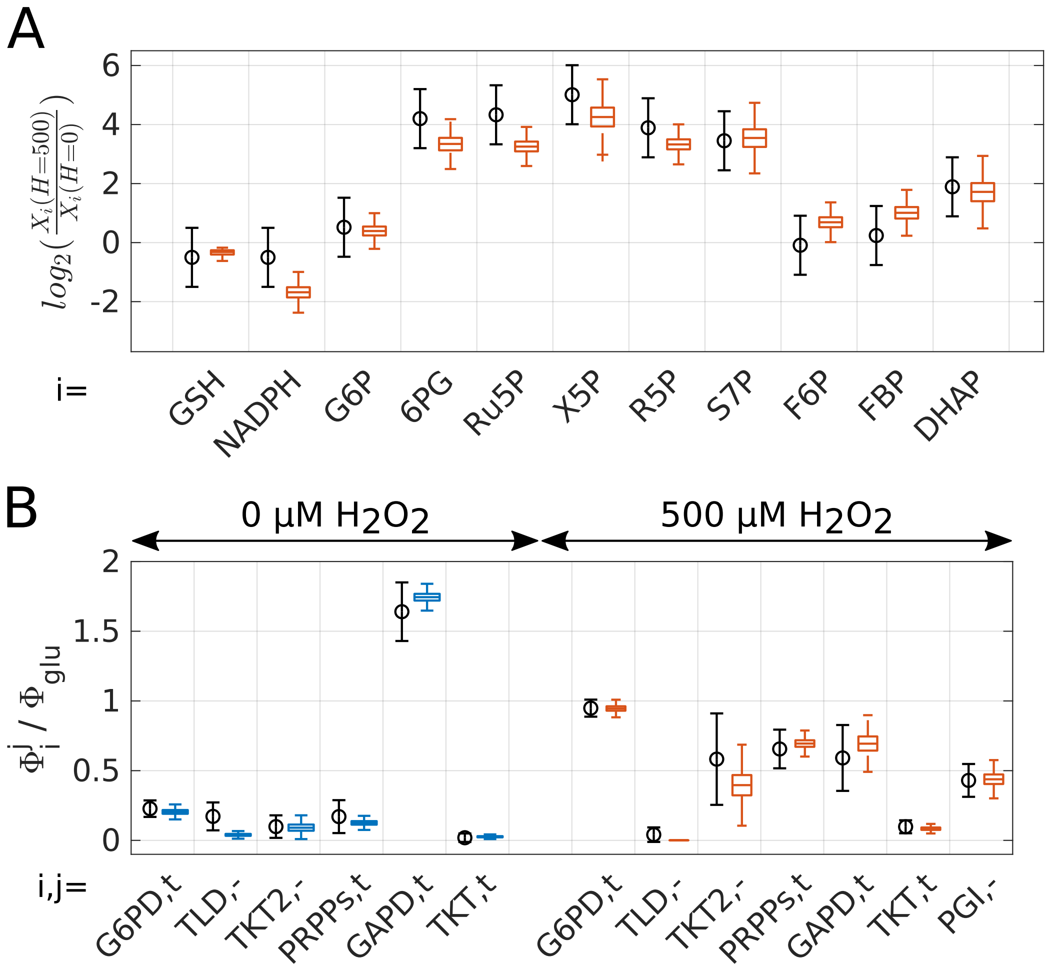

Figure 5.3: Agreement between model and experimental data. From Hurbain et al. 2022 [3]. Experimental (black) and simulated (blue and red) sub-elements of the normalised Root Mean Square Error (nRMSE) function after the minimisation process shown in Figure 5.2. (A-B) Experimental sub-elements in black are represented by the means (circle) and standard deviations (error bars). (A) Whisker plot of the metabolite fold changes $X_i(H = 500)/X_i(H = 0)$ between stress $H = 500\mu M$ and basal $H = 0\mu M$ conditions for the model ensemble $\mathcal{P}^*$ (red). (B) Whisker plots of the normalised fluxes rate Φ_i/Φ_{GLU} for the model ensemble $\mathcal{P}^*$ in basal condition $H = 0\mu M$ (blue) and stress condition $H = 500\mu M$ (red).

each sub-element compared to the corresponding experimental interval (Figure 5.3) clearly shows that they all fall within the range of experimental uncertainties.The determination coefficients R^2 for the concentration ratios and fluxes for each parameter set are respectively $R^2_{R_i} = 0.86 \pm 0.03$ and $R^2_{\Phi_i} = 0.96 \pm 0.02$ which shows the goodness of the fit.

Once the nRMSE clearly shows a good agreement between experimental and simulated data, the parameter distribution values can be evaluated (Figure 5.4). It shows that a part of the parameters has a wide distribution corresponding to a 50% confidence interval spanning several orders of magnitude of parameter variations. It means that whatever the value taken in this interval, the models are able to reproduce the experimental data. Because these data show rapid oxidative stress response, these parameters would not have high impact on the oxidative stress response. Other parameters have narrow distributions corresponding to a 50% confidence interval spanning on a few percent of the parameter variation. It means that the value taken in order to defend against oxidative stress are very constrained. It is particularly the case for some specific parameter such as inhibition parameter Ki_{G6PD}, Ki_{6PGD}, Ki_{GPI} or Ki_{GAPD}. These phenotypes clearly show that adding regulations are necessary to account for the fast metabolic response to oxidative stress.

To conclude, a mathematical model has been constructed in order to reproduce rapid oxidative stress response. The parameters of this model are estimated by a specific procedure comprising genetic and MCMC algorithm, in order to fit experimental data. It generates a distribution of parameter sets which corresponds to sets of plausible kinetic model. It shows that some

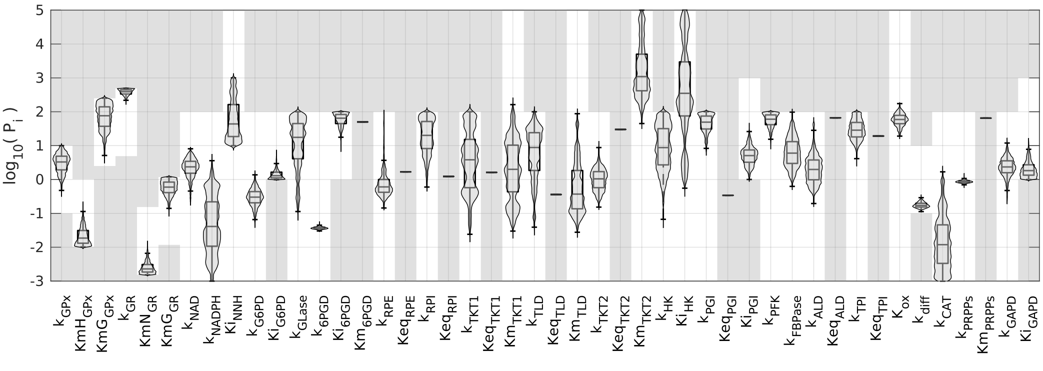

Figure 5.4: Parameter Distributions of the model ensemble. From Hurbain et al. 2022 [3]. Violin plots of parameters p_i for the model ensemble $\mathcal{P}^*$ where the explored parameter space is represented in white area (non-grey).

parameter has no important effect on the data adjustment but others which have a narrow distribution, are important in order to be able to reproduce experimental data. It is particularly the case for most of the regulation parameters confirming the need of these regulation mechanisms inside the mathematical model.

5.2.3 Correlation analysis of the model parameters

A mathematical model ensemble has been created via an estimation of distributions of parameters sets in order to reproduce oxidative stress experimental data taken from the Kuehne et al. 2015 [17]. These parameters distributions reveal that some of them are highly constrained while others do not show specific value and can vary more or less freely to keep a small nRMSE value. To be able to estimate the model parameters, most of them have been constrained by applying boundaries for some and by fixing others. However, the question of dependency between each parameters is not known and can be investigated by looking at the correlation coefficients. Indeed, two parameters could be linked which would induce related distributions allowing a possible parameter space reduction.

The correlation matrix shows the correlation coefficients between two parameters (Figure 5.5-A). The color code explains how these parameters are correlated. High correlation between two parameters means that when one is changing, the other will change in the same manner while high anti-correlation between two parameters means will be in the reserve direction. Correlation or anti-correlation blocks appear which mainly correspond to parameters within the same flux rates or at least to neighbouring reactions. Indeed, it exists high correlation/anti-correlation between parameters inside the oxPPP, the noxPPP or glycolysis. However, no huge correlation or anti-correlation block appears meaning that the model cannot be drastically reduced and there are not high number of parameter that has been over-fitted. Moreover, a spectral analysis of the correlation matrix allows to compute the eigenvalues (Figure 5.5-B) showing that it exists few parameters that are not precisely estimated.

5.3 Analysis of temporal dynamics

To analyse how the metabolic pathways are regulated during oxidative stress, the statistical ensemble of the mathematical model $\mathcal{P}^*$ is used to reproduce experimental measurement from Kuehne et al. 2015 [17] which has been calibrated via a specific methodology allowing to estimate distributions of

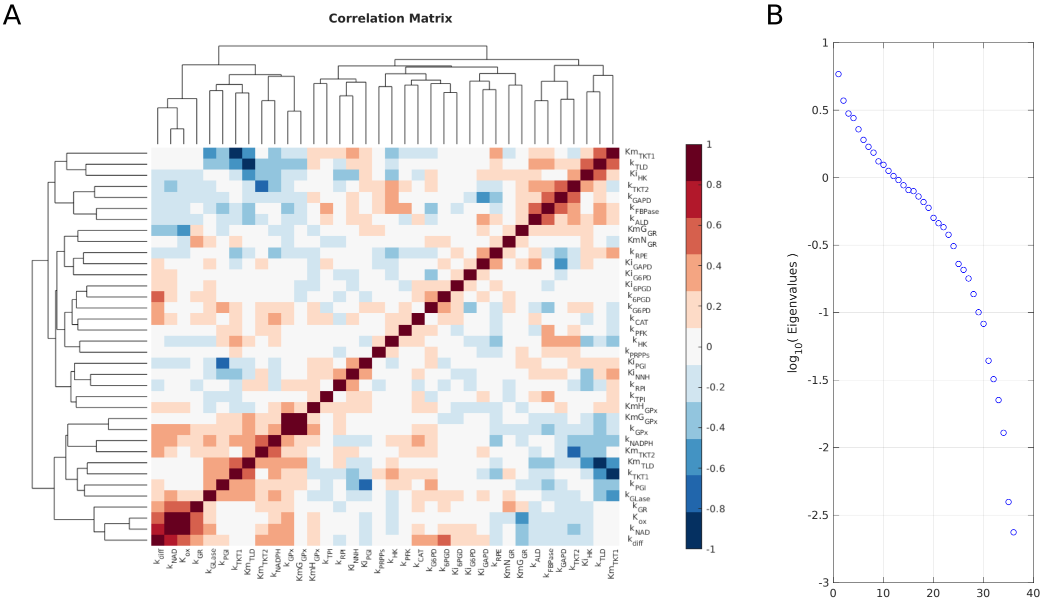

Figure 5.5: Parameters correlations. From Hurbain et al. 2022 [3]. (A) Correlation matrix heatmap with the accompanying dendrogram for the estimated kinetic parameters p_i of the model ensemble $\mathcal{P}^*$. Parameters are reordered by bundles of their corresponding flux rates. 1 (Red) and -1 (blue) mean respectively correlation and anti-correlation while 0 (white) means no correlation. (B) Ordered eigenvalues of the correlation matrix. 50% of the variance can be captured by the 5 highest eigenvalues, i.e. by four linear combinations of parameters.

---

parameter sets. Data used during this parameter estimation is fold change concentration between basal (i.e. without stress) and stress conditions, and ^{13}C labeling distributions converted into fluxes in basal and stress conditions (Section 4.3) for a step of hydrogen peroxide $[H_2O_2]_{ext} = 500\mu M$ and at steady state at 5 min after application of this stress. Then, the temporal dynamic of the entire model ensemble $\mathcal{P}^*$ can provide more information. The experimental data of temporal dynamic are not taken into account for the parameter estimation but they can be compared with the simulated results.

Simulated temporal dynamics can provide preliminary information about how the metabolic pathways are regulated under oxidative stress before reaching steady state. Indeed, experimental data are measured with a resolution in minute time scale but more precise dynamics can be identified with a second time scale [34] which can be done by numerical simulations. It appears different steps of the metabolites concentration variations during the tran-

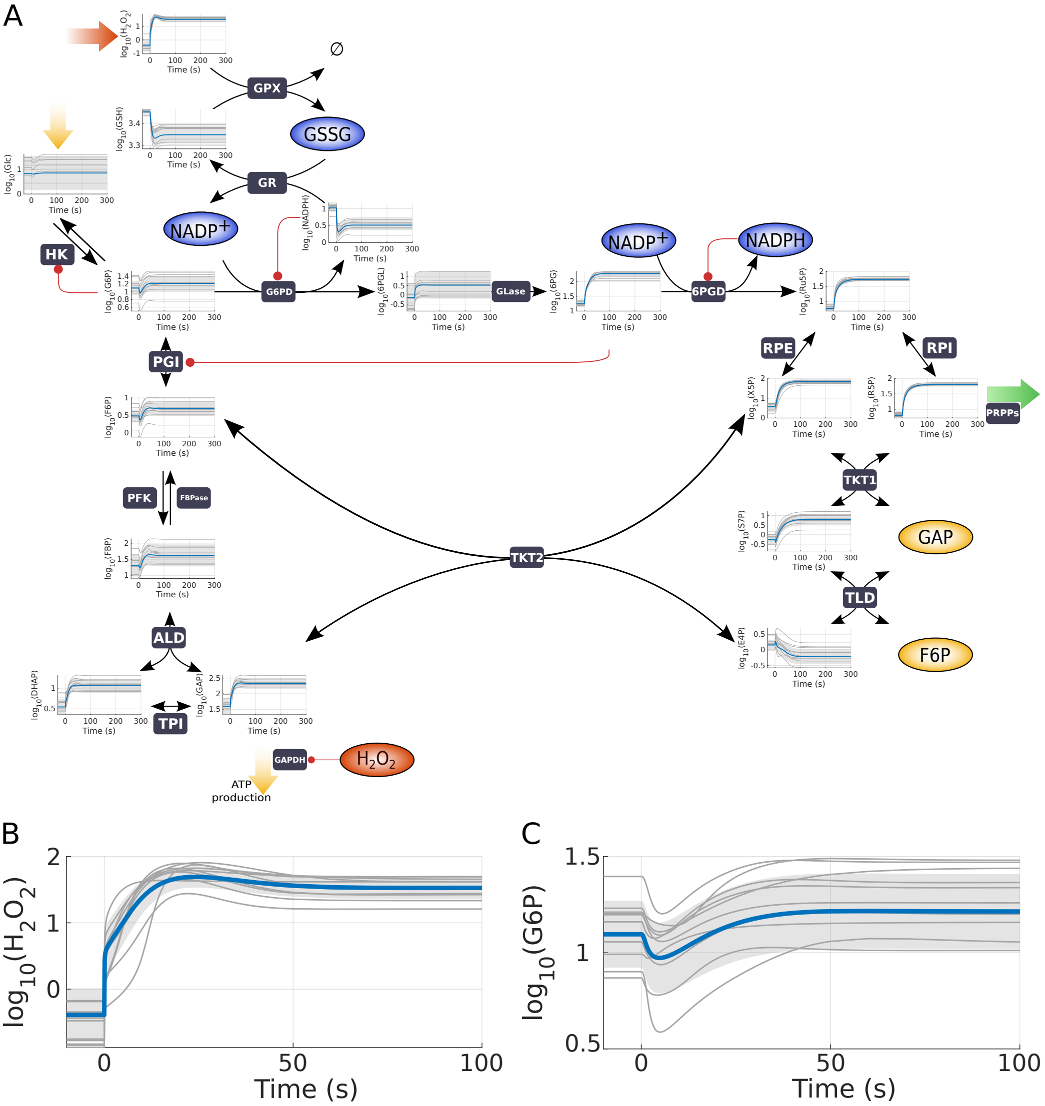

Figure 5.6: Metabolite temporal dynamic during oxidative stress response. From Hurbain et al. 2022 [3]. Temporal dynamics of metabolite concentration during oxidative stress response made by $H = 500\mu M$ step started at $t = 0s$. At $t < 0s$, the system is at steady state in basal condition made by a simulation with $H = 0\mu M$. Simulations are made with the parameters sets from the model ensemble $\mathcal{P}^*$. Results are shown by the mean in blue line and the standard deviation shown by the grey shadow. Examples of few parameter sets are shown by grey lines. (A) Temporal dynamic of metabolite concentrations in their corresponding metabolic pathway position. Simulations are shown until 5min. (B)-(C) Zoomed temporal dynamic of metabolite concentration until 100s.

sient response of oxidative stress (Figure 5.6-A). The stress is induced by a step from $0\mu M$ to $500\mu M$ for the external H_2O_2 concentration which induces a sharp increase of the internal H_2O_2 and then a slow relaxation to a steady state known as non-perfect adaptation phenotype. This has for consequence to highly consume GSH and $NADPH$ shown by a sharp decrease of their respective concentration and then to a slow increase to a steady state. The PPP metabolites see their concentration increasing in two step with a rapid and then a slow rise. Finally, metabolites in the glycolysis show also a two steps concentration variation. They first decrease rapidly within a second time scale and then increase slowly to relax to a steady state. All these concentration variations display a biphasic change during oxidative stress.

This biphasic variation can be seen in Figure 5.6-B&C where the internal H_2O_2 and $G6P$ concentrations are displayed during the 100 first seconds of the oxidative stress response. First, H_2O_2 concentration shows a sharp increase within the second time scale of several order of magnitude which is related to the time scale of basal degradation $k_{GR} \times KmG_{GPx} \sim 10$s. Then, it displays a slow relaxation to a steady state concentration much lower than the external one. Indeed, the ratio between internal and external H_2O_2 concentration at steady state is about 1 order of magnitude. The biphasic transient dynamics concerning detoxification molecules GSH and $NADPH$ are symmetric to that of internal H_2O_2 which corresponds to the upregulation of glycolytic concentrations as $G6P$. Indeed, $G6P$ shows a rapid decrease until ~ 10s and then an increase to a steady state. The first decrease step can be explained by the consumption of $NADPH$ which increases $NADP^+$ concentration decreasing the inhibition on $G6PD$ and $6PGD$ which induces an increase of $G6P$ consumption. Because the PPP fluxes increase, it higher consumes $G6P$ but it also increases PPP metabolite concentrations which is probably due to the saturation of $6PGD$. Time scale of $6PG$ global increase corresponds to $G6P$ increases which is due to lower PGI flux rate, probably linked to an inhibition increase of PGI and $GAPD$ enzymes.

One of the major phenotype during the early oxidative stress response is the fast flux rerouting from the glycolysis to the PPP. Only regulations that could act in early response are implemented in our model and some of them can be used to increase the flux in the PPP. For instance, a decrease of the inhibition of $G6PD$ or $6PGD$ could release the PPP or an increase of the inhibition on PGI and $GAPD$ could avoid the materials to go through the glycolysis in favour of the PPP. These metabolic responses via the regulations can be responsible of the presence of the biphasic dynamic and therefore of the adaptation phenotype. Looking at the temporal dynamic of for instance H_2O_2 with or without inhibitions allows to investigate their impact on the ox-

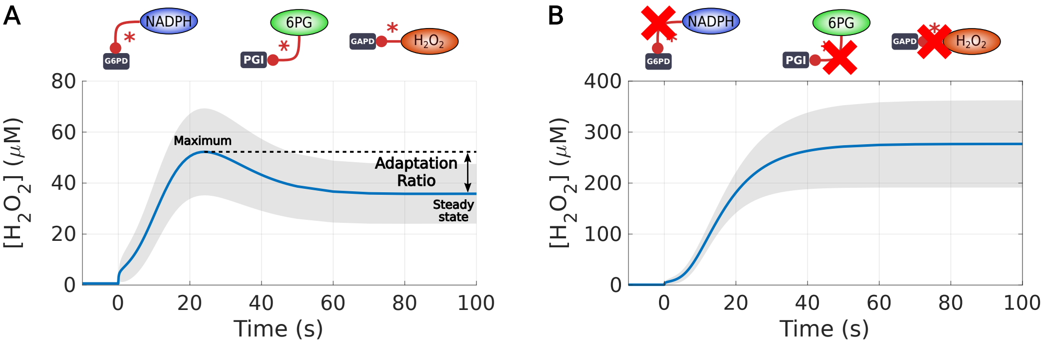

Figure 5.7: Impact of the regulation on the temporal dynamic. Temporal dynamics during oxidative stress response made by $H = 500\mu M$ step started at $t = 0s$. At $t < 0s$, the system is at steady state in basal condition made by a simulation with $H = 0\mu M$. Simulations are made with the parameters sets from the model ensemble $\mathcal{P}^*$. Results are shown by the mean in blue line and the standard deviation shown by the grey shadow. Temporal dynamic of H_2O_2 concentration with (A) or without (B) regulations on $G6PD$, PGI and $GAPD$. Regulations are deleted by increasing their corresponding parameters to infinity (i.e. $Ki_i \rightarrow \infty$). (A) From Hurbain et al. 2022 [3] and shown in Figure 5.6-B.

idative stress temporal response (Figure 5.7). Indeed, the temporal dynamic with regulations shows an adaptation ratio (eq. 3.18) higher than 1 characterizing the presence of the adaptation phenotype (Figure 5.7-A). However, removing the main inhibitions of our model make the adaptation phenotype disappear confirming that this typical dynamic is here due to the effect of the regulations (Figure 5.7-B). It is important to note that in addition of the disappearance of the adaptation phenotype, the overall detoxification is also highly reduced without regulation resulting in a 7.73-fold increase in steady-state concentration.

The transient biphasic response of the metabolite concentration during oxidative stress are produced by numerical resolution of the model ensemble $\mathcal{P}^*$ built by fitting experimental data at steady state. However, the experimental data of temporal dynamic are not taken into account for the parameter estimation but can be compared with the simulated results. Looking at the Figure 5.8, metabolite concentration variations as a function of time roughly well follow the experimental measurements with a determination coefficient $R^2 = 0.82 \pm 0.05$. It exists differences, specifically for $F6P$ concentration which is increasing in simulations while it is decreasing in experimental measurements in order to reach a steady state. It could be explained by

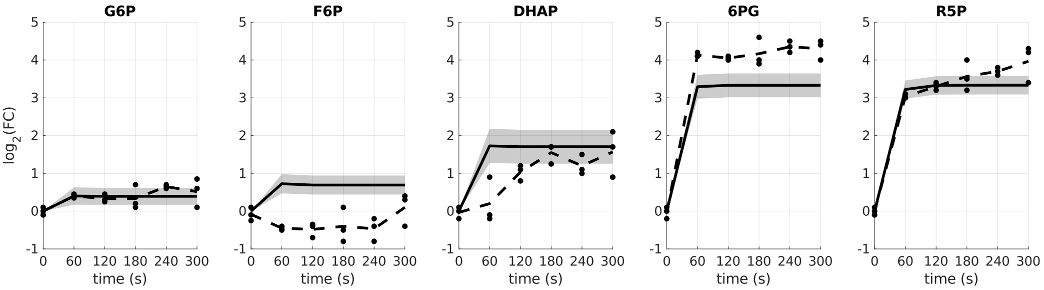

Figure 5.8: Comparison of temporal dynamic prediction to experimental data. From Hurbain et al. 2022 [3]. Each plot corresponds to temporal dynamics of each metabolite concentration. Predicted results of the model ensemble $\mathcal{P}^*$ (from figure 5.6) are shown by the mean in black solid line, and standard deviation with grey shadow. Experimental data are represented by the 3 replicates measures and their means in dashed line (Kuehne et al. 2015 [17]). Goodness-of-fit is evaluated by computing the R-squared distribution of the model ensemble $\mathcal{P}^*$ giving $R^2 = 0.82 \pm 0.05$.

---

the fact that the models do not take into account fructose-2,6-bisphosphate $F26BP$ which could be used as regulator of PFK and $FBPase$, and therefore modify the $F6P$ transient dynamic.

In summary, the model ensemble $\mathcal{P}^*$ built to reproduce oxidative stress response to a step of $500 \mu M$ of external H_2O_2 concentration, shows a biphasic response during transient dynamic. It is related to first the detoxification response during a second time scale thanks to the reserve of GSH and $NADPH$ molecules. Then, fluxes inside glycolysis are rerouted toward the PPP in tenth of seconds thanks to a change of the metabolic concentration configuration increasing $NADPH$ recycling. This is a common procedure to highly respond to an oxidative stress [18, 17]. The decrease of $NADPH$ concentration would release the inhibition on PPP enzyme and would be responsible of this rerouting flux. Moreover, it would also involve inhibition of glycolysis in order to restore $G6P$ concentration. Finally, these temporal dynamic behaviour are not visible in experimental data but the model ensemble predictions are in well accordance to these data.

5.4 Analysis of dose responses

A model ensemble $\mathcal{P}^*$ has been created to reproduce experimental data of oxidative stress response. The used data are fold change concentrations and metabolomic distributions converted into flux data in basal and stress con-

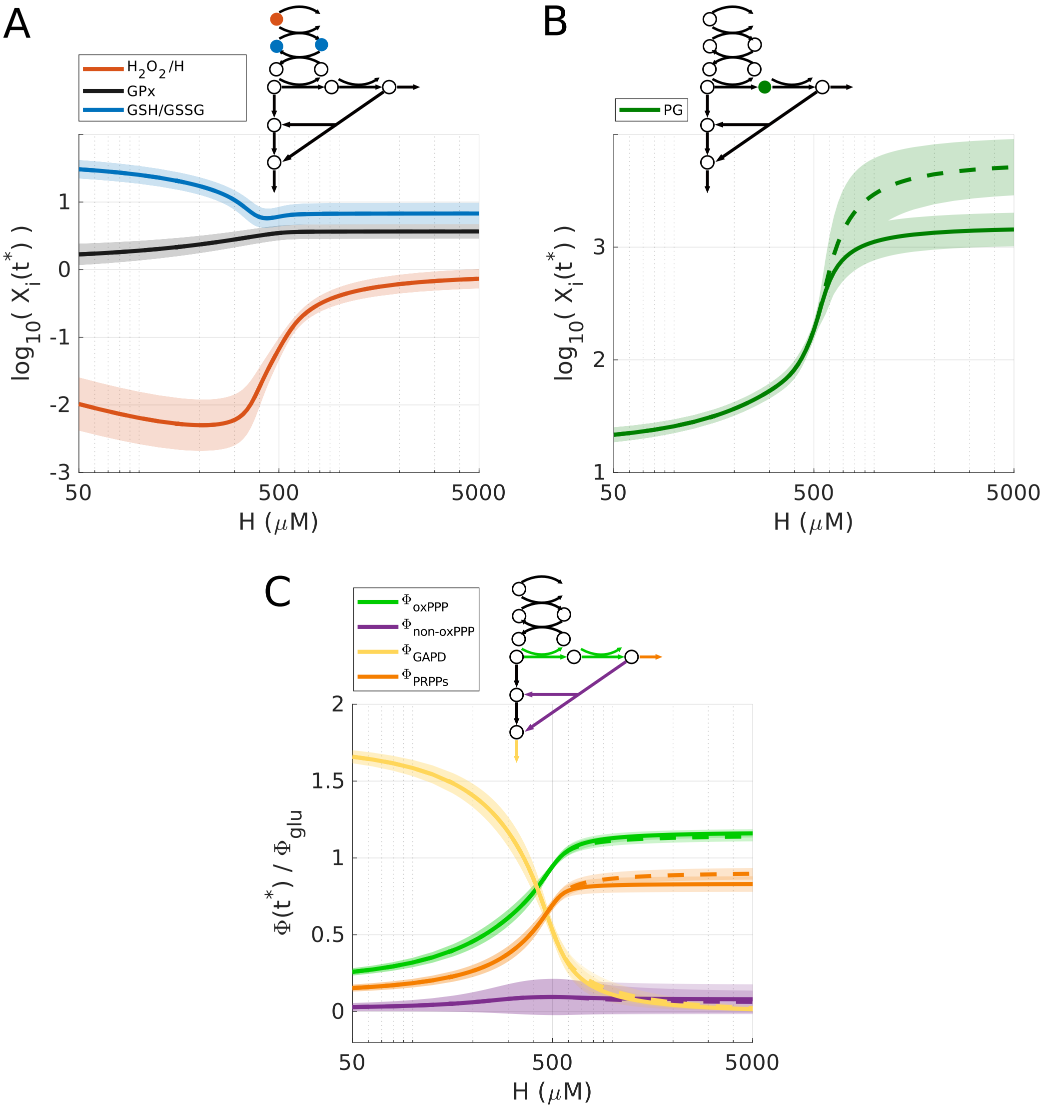

Figure 5.9: Dose-dependent profiles of the oxidative stress responses. From Hurbain et al. 2022 [3]. Steady state dynamics of several metabolites and fluxes as a function of the external hydrogen peroxide H level. Simulations are made with the parameter sets of the model ensemble $\mathcal{P}^*$. Means of the steady states measured at 5min are represented with solid lines and at 30min in dashed lines. Standard deviations of the steady states correspond to coloured shadows. Smaller metabolic pathway schemes show the position of the corresponding plotted variables. (A) Dose response in glutathione pathway : H_2O_2/H, GPx and glutathiones ratio $GSH/GSSG$. (B) Dose response of $6PG$ metabolite. Other metabolite dose responses are shown in Hurbain et al. 2022 [3]. (C) Dose response of the main fluxes normalized by the incoming glucose flux Φ_{GLU} through enzymatic reaction $G6PD$ representing the oxPPP fluxes Φ_{oxPPP}, TKT representing the noxPPP fluxes Φ_{noxPPP}, and the output fluxes $GAPD$ and $PRPPs$.

ditions at steady state for an external perturbation of H_2O_2. This stress is made by a step of concentration from $0\mu M$ to $500\mu M$. However, in the Kuehne et al. 2015 [17], there is also metabolite concentration at steady state as a function of different external perturbations made of different concentrations of external H_2O_2 written as H. The parameter distribution estimation is made to reproduce a specific type of oxidative stress. Thus, the model ensemble $\mathcal{P}^*$ can be simulated for different type of stress profile, or different concentration of external H_2O_2. Before comparing simulation results to experimental data, dose-response of metabolite concentrations or fluxes can provide information of the oxidative stress response of the model ensemble and could potentially provide information on the regulatory mechanisms of this response (Figure 5.9).

It has been shown previously that the system is able to detoxify H_2O_2 during $500\mu M$ oxidative stress from the temporal dynamic (Figure 5.6). However, it is interesting to know the detoxification capacity and its limit (Figure 5.9-A). The metabolic responses at 5min as a function of the external H_2O_2 (H) display a ratio between internal and external H_2O_2 very low level for smaller stress doses than $500\mu M$, a transition around $500\mu M$ and then a ratio close to 1. It means that the mechanism is well detoxifying stress for small doses, then starts to work but arrives at a certain maximum capacity which induces approximately the same H_2O_2 concentration inside than outside the cell. It coincides with the dose-response of flux rateGPx which displays an increasing phase meaning that the system adapts to the stress and then to a plateau around $500\mu M$ dose. This saturation clearly means that the system is not able to remove more stress after a certain quantity. Indeed, the GPx flux rate (eq 5.1) which is the first link in the internal H_2O_2 detoxification, becomes independent of the H_2O_2 concentration which means that whatever the dose, past this threshold, the system will not change conformation and will no longer detoxify. The $GSH/GSSG$ ratio confirms this result by showing a plateau at the same threshold. After this dose, the metabolic network is saturated but the catalase Cat is still able to eliminate H_2O_2 molecules which confirms that both glutathiones and catalase are both actively involved the oxidative stress detoxification in a dose-dependent manner [140, 141].

The concentration of $6PG$ displays an increasing curve (Figure 5.9-B). It could induce an increase of PGI inhibition which would prevent the flux to go through the glycolysis favouring the flux rerouting. However, for extreme doses, $6PG$ metabolite concentration displays a slower relaxation than the other metabolites where the observed saturation is before the 5min of stress. Indeed, $6PG$ takes much longer to reach its steady state and has its concentration still increasing between 5 and 30 min after the start of the ox-

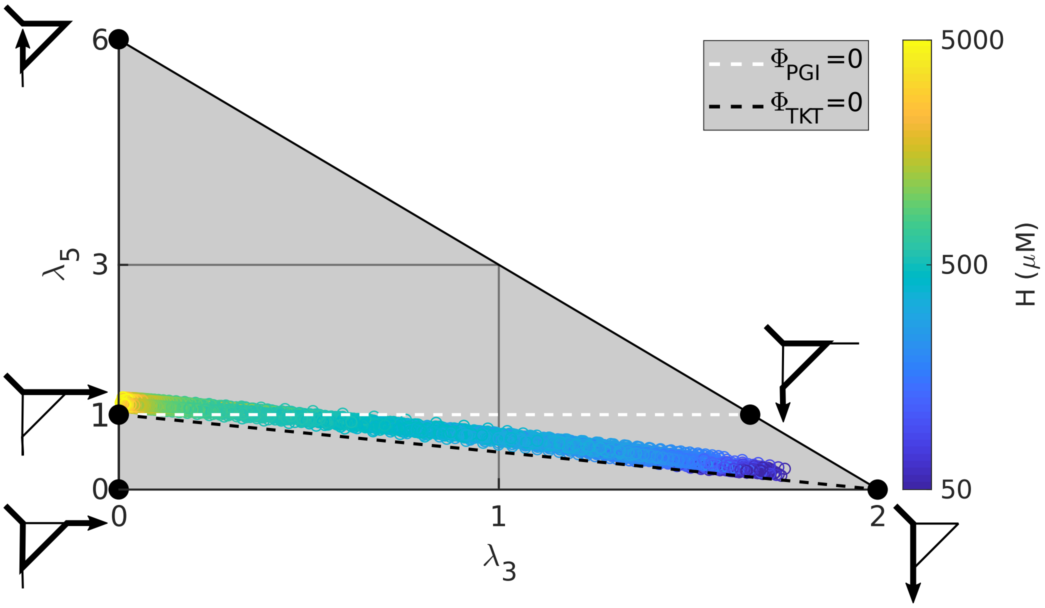

Figure 5.10: Dose-dependent flux response in the solution subspace. Fluxes shown in Figure 5.9-C are expressed as function of only the 3 last elementary modes (Figure 4.3). This decomposition is represented in the mode space shown by a triangle due to the conservation relation $\frac{\lambda_3}{2}+\frac{5\lambda_4}{6}+\frac{\lambda_5}{6}=1$. Each axe of the space corresponds to components of elementary mode V_3^n and V_5^n. Each flux state is a combination of the 2 elementary modes. In $\{\lambda_3,\lambda_5\}=\{0,0\}$, the flux state is fully in V_4^n. Representation of the estimated fluxes in basal condition ($H=0\mu M$) in blue. Representation of the estimated fluxes in stress condition ($H=500\mu M$) in red. $\Phi_{PGI}=0$ and $\Phi_{TKT}=0$ are represented by white and black dashed lines.

idative stress. This behaviour is linked to the saturation of $6PGD$ reaction rate. During high perturbation, $6PG$ steady state concentration is highly increasing and becomes higher than the saturation parameter Km_{6PGD} which induces saturation of the corresponding flux rate. Therefore, the ODE describing the variation of $6PG$ becomes independent of its concentration and because all other metabolites have already reached their steady state, the $6PG$ variation equation becomes constant. It induces a very slow temporal dynamic and then a very high time to reach the steady state.

It has been shown previously that the system is able to reroute its flux capacity from the glycolysis toward the PPP during fast oxidative stress response. Indeed, these metabolic pathways are built to highly reroute its flux capacity from a sequential mode useful to produce energy, i.e. through the glycolysis, to the cycling mode passing through PPP and the reverse glycolysis. The flux rerouting during $500\mu M$ H_2O_2 step allows to reach a PPP flux from ≈ 0.1 to a maximum of 0.95 time the incoming glucose flux Φ_{GLU} inducing increasing oxidative stress detoxification even if it is far from the maximum value of $6\Phi_{GLU}$ given by the cycling flux. Therefore, it is easy to assume that when the system is able to reroute the flux capacity in order to highly detoxify the stress, the total capacity could be used for extreme doses. Looking at the flux rates normalized by the incoming glucose flux (i.e. Φ_i/Φ_{GLU}) as a function of H doses (Figure 5.9-C), the flux capacity shows a rerouting in favour of the cycling mode but does not reach its maximum value. Indeed, for low doses, Φ_{GAPD} is much higher than Φ_{PPP} showing a glycolytic mode. When the external stress is increasing, Φ_{GAPD} is decreasing potentially due to its inhibition by H_2O_2 and the flux inside the PPP is increasing which clearly shows a rerouting to reach the value of 1.3 the incoming glucose flux. The fluxes is represented in 2D graph in the basis of elementary modes as it has been made in Figure 4.8 for the data-driven estimated fluxes which confirms the flux capacity rerouting as a function of the oxidative stress doses. The maximum value of the PPP flux is higher than 1 meaning that the system is cycling but is much smaller than 6 which is the maximum capacity. This difference can be explained by the $6PGD$ saturation. Because oxPPP is an irreversible chain of reactions, $6PGD$ saturation restricts maximum flux inside the PPP and therefore limits the cycling mode. This limit of the cycling flux can be calculated by neglecting smaller terms of Φ_{6PGD} :

$$\Phi_{6PGD}^{max} = k_{6PGD} Km_{6PGD} [NADP^+] \tag{5.2}$$

The important information of this expression is that the limitation of the cycling mode is linearly dependent of the activity of $6PGD$ enzyme. Therefore, a change of this enzyme activity would change the cell capacity of oxidative stress detoxification. Increasing the cycling flux capacity could be a good solution to highly remove hydrogen peroxide but this limitation can be useful to keep production of energy and DNA repair, necessary for cells to live, by keeping non zero reaction rate of $GAPD$ and $PRPPs$. Indeed, even if $GAPD$ flux rate is decreasing, these output fluxes are higher than zero showing a need a energy and biomass production. The increasing $PRPPs$ flux rate could be related to repair of the damages caused by the oxidative stress.

Finally, the dose response results can be compared to the experimental data that have not been used during the parameter distribution estimation. Simulations of the dose-responses correspond roughly well to the data with a determination coefficient $R^2 = 0.48 \pm 0.04$. This value is smaller than the

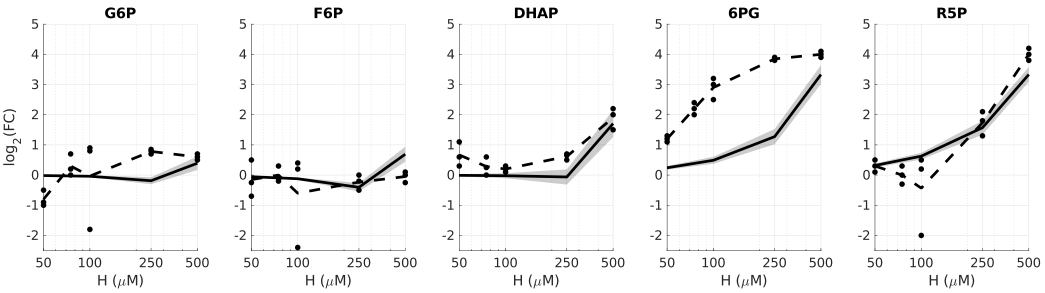

Figure 5.11: Comparison of the dose response prediction to experimental data. From Hurbain et al. 2022 [3]. Each plot corresponds to dose responses of each metabolites concentration. Predicted results of the model ensemble $\mathcal{P}^*$ (from figure 5.9) are shown by the mean in black solid line, and standard deviation with grey shadow. Experimental data are represented by the 3 replicates measures and their means in dashed line (Kuehne et al. 2015 [17]). Goodness-of-fit is evaluated by computing the R-squared distribution of the model ensemble $\mathcal{P}^*$ giving $R^2 = 0.48 \pm 0.04$.

---

one for the temporal dynamic which is probably due to the dose-response of $6PG$. Indeed, the experimental data shows higher increase of its concentration compared to simulation results. Because the saturation of $6PGD$ reaction rate is already present at the observed concentrations during the simulation, higher value of $6PG$ concentration won't change the phenotype inducing the same oxidative stress response. Moreover, this difference can be corrected by adding a term inside the nRMSE function specifically focused on this change of concentration.

In conclusion, dose-response analysis displays detoxification limitation given by the GPx saturation. The corresponding flux rate becomes independent of internal H_2O_2 which removes link to the network. The detoxification capacity is also limited by the maximum cycling flux given by the saturation of $6PGD$ reaction rate. This limitation is linearly dependent of the $6PGD$ enzyme activity allowing the possibility to lift this barrier. All these results are overall consistent with the experimental data. Finally, there is a high flux rerouting capacity which can be induced by a decrease of $NADPH$ concentration releasing the inhibition of PPP, by the increasing $6PG$ concentration preventing the flux to go through the glycolysis. Then, the high PPP flux showing cycling flux could be induced by the decrease of $GAPD$ potentially induced by its inhibition by H_2O_2. A crucial question is now to understand how the different regulations contribute to such flux rerouting.

Chapter 6

Analysis of the regulatory scheme

Metabolic regulation is an important feature in cells used to reorganised the network resources in order to respond to a change or a perturbation. In the context of oxidative stress, rapid regulations have been observed in the PPP and glycolysis [17, 34, 36, 35]. A mathematical model has been constructed in previous chapters in order to reproduce experimental data which allows to investigate the regulations in this metabolite network. In this chapter, specific parameters of the model ensemble will be modified and a sensitivity quantity will allow to clarify the impact of regulation on the rapid oxidative stress response. It appears that regulations on $G6PD$, GPI and $GAPD$ have important effect on allocation of the metabolic resources. They act in a dose-dependent manner and in synergistic cooperation to favour the detoxification of stress.

6.1 Sensitivity measures

To analyse the regulation effect during oxidative stress response induced by a step of external hydrogen peroxide H, parameters of the model ensemble $\mathcal{P}^*$ will be modified in order to change the regulation or enzyme activity. It will induce change in metabolic concentration or flux rate. Sensitivity quantity $\Delta_{p_i}^{Y}$ will estimate the change of a quantity Y which can be variable concentration or flux rate, after a modification of a parameter p_i during oxidative stress response. Indeed, the model ensemble $\mathcal{P}^*$ is the group of all the set of model corresponding to the parameters sets $\vec{p}^{j=1,n_M}$ where n_M is the number of model. For a kinetic model corresponding to a parameter set $\vec{p}^j$, a parameter p_i^j will under a modification of the multiplication factor Δp_i.

Then, the sensitivity quantity $\Delta_{p_i}^{Y}$ can be defined as :

$$\Delta_{p_i}^{Y}(H, \Delta p_i) = \frac{Y(H, \vec{q^j})}{Y(H, \vec{p^j})}, \tag{6.1}$$

where $q_i^j = \Delta p_i p_i^j$.

To analyse the regulation effect during oxidative stress, the inhibition parameter Ki will be modified : $\Delta Ki = \infty$. The strength of inhibition is given by the ratio $\frac{[I]}{Ki}$ where I is the inhibitor. If $[I] = Ki$, then the reaction rate is divided by 2 (Section 2.1). So, increasing the parameter Ki to infinity induces infinitely small inhibition. To analyse enzyme activities, the corresponding parameter k_{ENZ} will be modified : $\Delta k_{ENZ} = \pm 1$. As this parameter is linked to enzyme activity, inducing this type of modification is similar to change the enzyme activity by an order of magnitude below and above the value determined during the data-driven parameter estimation which allows to mimic overexpression or knockdown experiments of enzyme activity. When $\Delta_{p_i}^{Y}$ is smaller or higher to 1, it indicates that removing the regulation respectively decrease or increase the Y steady-state level.

Instead of removing inhibition by increasing the inhibition parameter or inducing overexpression or knockdown of enzyme activity, steady state sensitivity of the models can be analysed as a function of the regulation by using the response coefficient $R_{p_i}^{Y}$ and as a function of enzyme activity with control coefficient $C_{e_i}^{X}$ (Section 2.1). This two coefficients differ from the previous one by the type of modification leading to different type of effect. The sensitivity quantity $\Delta_{p_i}^{Y}$ analyses the steady state under high modifications, i.e. by complete removing inhibition or enzyme activity overexpression/knockdown, while the response and control coefficients analyse the sensitivity to a small change of inhibition or enzyme activity. However, they can be linked by :

$$R_{p_i}^{Y}(H) = \lim_{\Delta p_i \to 1} [(\Delta_{p_i}^{Y}(H, \Delta p_i) - 1)/(\Delta p_i - 1)] \tag{6.2}$$

where

$$\lim_{\Delta p_i \to 1} \Delta_{p_i}^{Y}(H, \Delta p_i) = \frac{Y(H) + \partial Y(H)}{Y(H)} \tag{6.3}$$

$$\lim_{\Delta p_i \to 1} \Delta p_i = \frac{p_i + \partial p_i}{p_i} \tag{6.4}$$

6.2 Gain-Loss of function analysis

Regulation of the metabolic pathways are important to reallocate the resources in order to highly respond to oxidative stress. The investigation of their effects will be made in this section by the use of gain-of-function or loss-of-function associated to modification of regulatory mechanisms or enzyme activity. These analyses will applied on the model ensemble $\mathcal{P}^*$ using the parameters distributions estimated to reproduce experimental data. They will be characterized using sensitivity coefficients showing the relative change of the simulation results during fast oxidative stress response induced by a step of external hydrogen peroxide H.

6.2.1 Effect of perturbing regulation pattern

The model is constructed with the main regulatory mechanisms in order to reproduce experimental data during oxidative stress which shows fast flux rerouting. However, the link between this change of flux mode and the regulation is not clearly established. As explained in Section 1.5, there are regulations that inhibit the glycolysis using the parameters Ki_{GAPD}, Ki_{PGI} and Ki_{HK} acting on respectively $GAPD$, PGI and HK while others regulate the $NADPH$ production using the parameters Ki_{G6PD}, Ki_{6PGD} and Ki_{NNH} acting on respectively $G6PD$, $6PGD$ and NNH. Using the estimated value for each of these parameter, it is possible to modify them and compute the sensitivity quantity of the model to regulations.

Inhibition strength

Firstly, the strength of each regulation has to be known before starting to modify their activity in order to better understand their effects without and with stress of $500\mu M$ of external hydrogen peroxide H (Figure 6.1). The inhibition level calculated by the ratio $\frac{X_i}{p_i}$ where X_i is the concentration of inhibitor I_i at steady state and p_i is the corresponding inhibition parameter. When the ratio is equal to 1, the reaction rate si divided by 2. Regulation on hexokinase HK displays a range of inhibition strength spanned on 6 orders of magnitude both in basal and stress conditions revealing that the fact that this regulation has not impact on the metabolic pathways during fast oxidative stress which is confirmed by the distribution of the inhibition parameter Ki_{HK} (Figure 5.4). Inhibition on reactions consuming $NADPH$ (.i.e NNH) is increasing during oxidative stress showing the need of producing more $NADPH$. Regulations on $G6PD$ and $6PGD$ are high in basal and decrease during oxidative stress which induces high pentose phosphate pathway flux which also favours the production of $NADPH$. Inhibition on $6PGD$ is lower than the one on $G6PD$ probably because it is the first flux of the PPP. Because the oxPPP is a metabolic pathway made of reactions in chain, increasing the first flux will induce increase of the entire oxPPP. Thus,

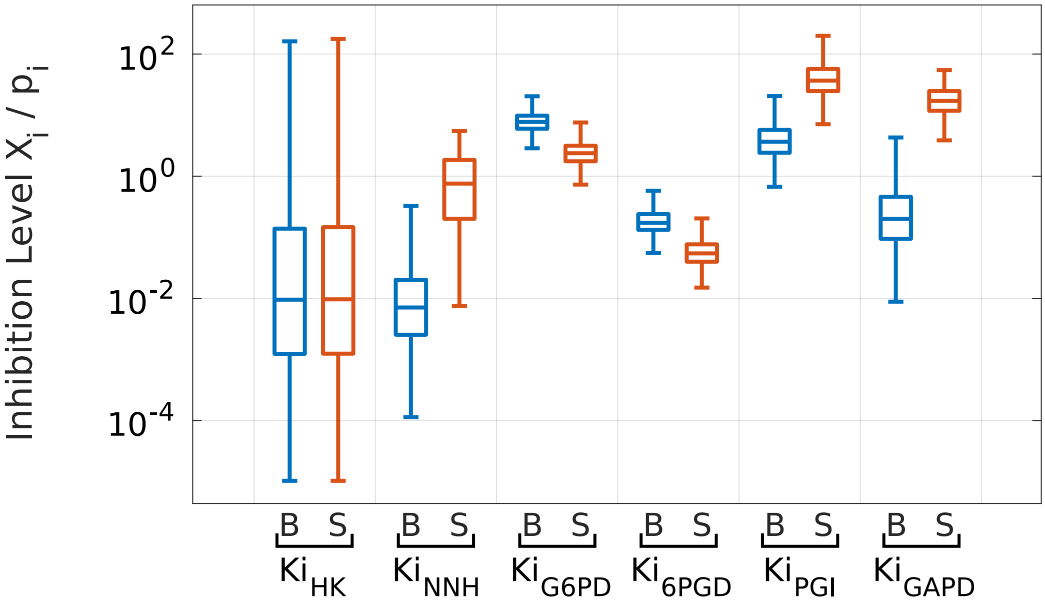

Figure 6.1: Inhibition strength in basal or stress conditions From Hurbain et al. 2022 [3]. Inhibitory strength X_i/p_i linked to an inhibition j associated to the corresponding metabolite X_i and parameter p_i equal to an inhibition parameter Ki_i. Each distribution corresponds to values of all the parameter sets of the model ensemble $\mathcal{P}^*$. Blue distribution corresponds to basal condition, i.e. $H = 0\mu M$ and red to stress condition, i.e. $H = 500\mu M$. $X_j/p_j = 1$ indicates that inhibition reduces enzymatic activity by two-fold.

---

higher control on $G6PD$ induces better control of the resources allocation. Concerning the glycolysis, inhibition on PGI and $GAPD$ are already high in basal condition but increase during oxidative stress. This implies that the first flux of the glycolysis PGI is much smaller allowing higher rerouting from glycolytic flux toward the PPP. It is similar with the output flux of the glycolysis $GAPD$ allowing to keep molecules inside the network, probably to shift to a cycling mode to favour the hydrogen peroxide removal (Section 4.2).

To sum up, regulations linked to the PPP allow to increase the $NADPH$ production by either decreasing its consumption or by increasing the flux inside the PPP which consumes more $G6P$. Regulations of the glycolysis allow to increase flux inside the PPP and to keep flux in the system in order to compensate the higher $G6P$ consumption. Without regulation, carbon flux resource would be much less rerouted and the flux won't be able to cycle inside these metabolic pathways. Indeed, the ratio of flux going through the

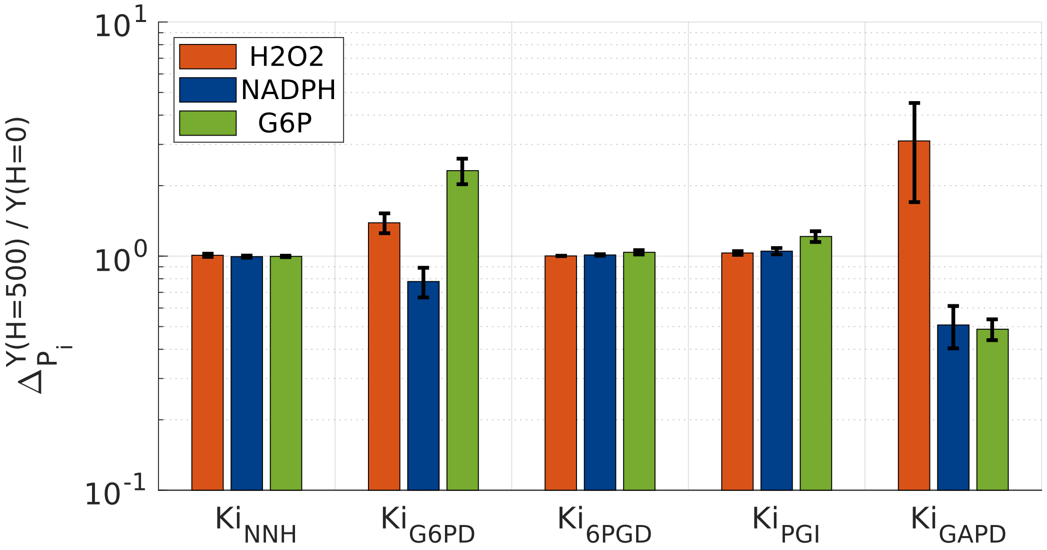

Figure 6.2: Regulation deletion sensitivity. From Hurbain et al. 2022 [3]. Sensitivity factor $\Delta_{p_i}^{Y}$ under regulation deletion ($\Delta Ki_i = \infty$) (eq 6.1). Y corresponds to the metabolite response H_2O_2, $NADPH$ and $G6P$ under oxidative stress ($H = 500\mu M$) relative to basal condition ($H = 0\mu M$). Simulations are made using the model ensemble $\mathcal{P}^*$. Bars correspond to mean values and error bars to standard deviations at steady state of the model ensemble simulations.

PPP compared to the glycolysis would be the ratio of the kinetic parameter of the corresponding enzymes without possibility to modify this ratio, the $NADPH$ recycling and then the detoxification capacity.

Effect of deleting regulations

The regulation strength allows to understand what are the state of each regulation in basal and stress conditions. To understand the impact of these regulations on the variables of the system, variations inside the metabolic pathways are analysed during regulation removal (Figure 6.2). Each regulation is analysed here with a change of their corresponding inhibition parameter to infinity ($\Delta Ki_i = \infty$) inducing a complete loss of the inhibition without modifying any other characteristic of the model ensemble. Thus, the variation of the ratio between basal ($H = 0\mu M$) and stress ($H = 500\mu M$) steady state of a variable concentration $Y(H)$ induced by a regulation suppression, i.e. inhibition parameter modification $\Delta Ki_i = \infty$ is measured by the sensitivity coefficient $\Delta_{p_i}^{Y(500)/Y(0)}$. This gain-of-function or loss-of-function analysis is made for each parameter set of the model $\mathcal{P}^*$. Because there are regulations that are active in basal condition, removing their inhibition can already have an impact on the basal steady state. Thus, a particular protocol is applied for $G6PD$ because its basal steady state is completely divergent without $G6PD$ inhibition making impossible the analysis. Thus, to compensate the inhibition suppression in basal condition, the corresponding steady state will be maintained without the regulation by modifying the $G6PD$ reaction parameter as : $k'_{G6PD} = \frac{k_{G6PD}}{1+\frac{[NADPH]}{Ki_{G6PD}}}$ and $\Phi'_{G6PD} = k'_{G6PD}[G6P]$. In this condition, the basal steady state won't be divergent anymore without regulation suppression but also keep the effect of regulation suppression during oxidative stress.

Removing regulations on $G6PD$ or $GAPD$ drastically increase H_2O_2 and decrease $G6P$ concentrations but have a reverse effect on $NADPH$. It can be justified by the fact that removing regulation dynamic on $G6PD$ keeps low the flux inside PPP which does not increase the $G6P$ consumption, the $NADPH$ production and therefore do not favour the H_2O_2 detoxification. Removing $GAPD$ inhibition induces a loss of molecule inside the metabolic pathway which does not allow the $GAPD$ inhibition to favour cycling flux inducing a decrease of the $G6P$ and $NADPH$ concentrations and thus the H_2O_2 detoxification too.

Removing regulations on the reactions consuming $NADPH$ do not alter H_2O_2, $NADPH$ or $G6P$ ratio. This surprising result could means that, even if its strength is not negligible, this regulation does not have impact on the detoxification due to the small values of the reaction rate. While the one on $G6PD$ allows to increase the entering PPP flux, the $6PGD$ regulation does not seem to change significantly the variables. Indeed, removing the $6PGD$ inhibition could has no effect in basal condition due to the high $G6PD$ regulation and in stress condition because the $6PGD$ inhibition strength is already low which does not induce change in the network during the regulation suppression. Non significant effect of the PGI regulation deletion can be understood by the fact that, during oxidative stress, PGI flux is reversed where $\Phi^+_{PGI} \sim \Phi^-_{PGI}$ for this level of stress (Figure 4.7) which does not favour production or consumption of $G6P$. Deeper investigations of the effect of regulation deletions have to be made for different dose of stress in order to have a clear idea of the scope of the regulation works on the resources allocation during fast oxidative stress.

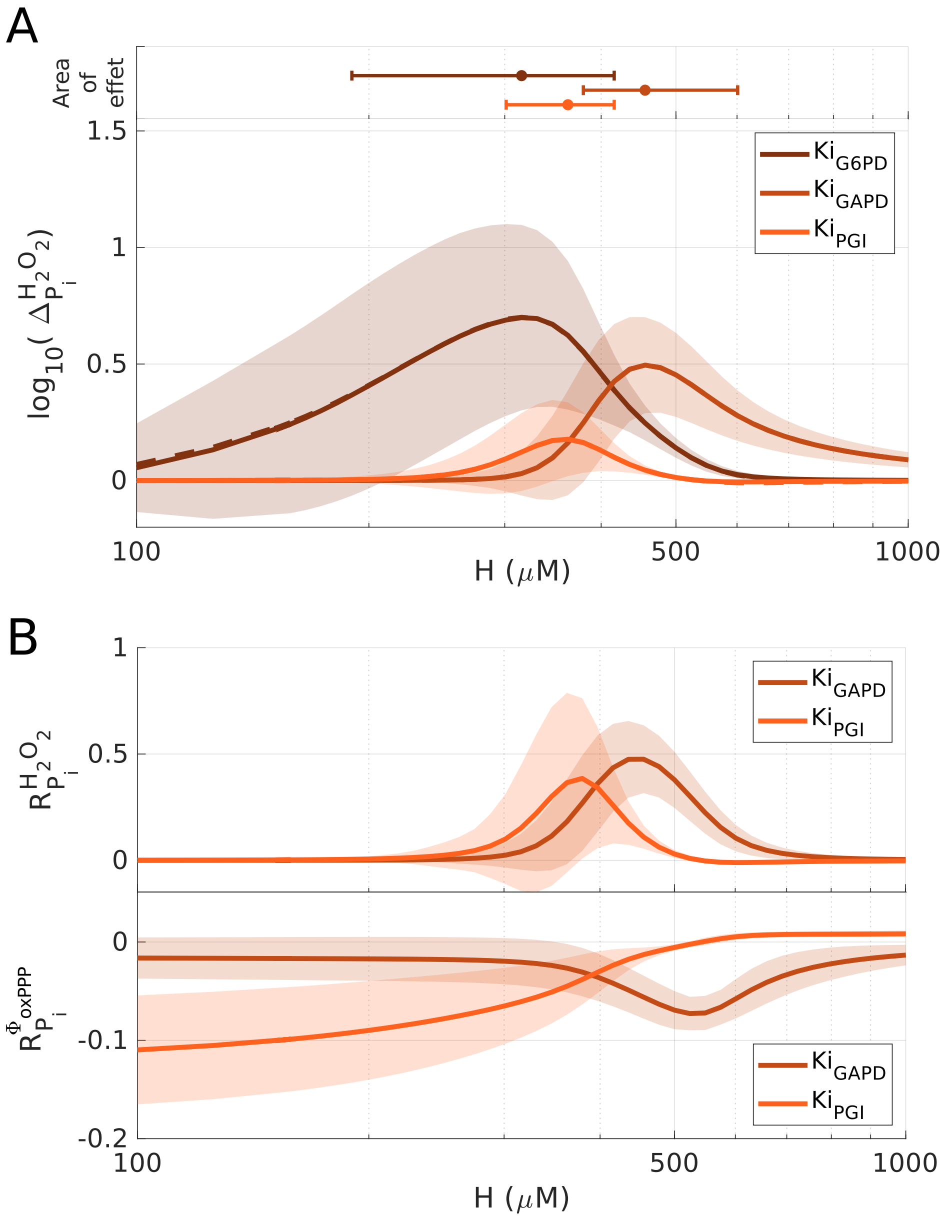

Figure 6.3: Regulation analysis during oxidative stress dose responses. From Hurbain et al. 2022 [3]. (A) Sensitivity factor $\Delta_{p_i}^{H_2O_2}$ which reflects the variation of internal H_2O_2 under regulation deletion $p_i = Ki_i$ ($\Delta_{Ki_i} = \infty$) of a specific regulated enzyme i (eq 6.1) as a function of the external hydrogen peroxide H dose. The studied regulation are made by modifying the corresponding parameters, i.e. Ki_{G6PD}, Ki_{PGI} and Ki_{GAPD}. The corresponding dose-specific areas of each regulation effect ($\Delta^{H_2O_2}/\Delta max > 0.5$) is shown upper to the panel. (B) Response coefficient $R_{p_i}^{H_2O_2}$ and $R_{p_i}^{\Phi_{oxPPP}}$ respectively for the H_2O_2 concentration and Φ_{oxPPP} rate (eqs 2.22) for each regulation deletion $p_i = Ki_i$ ($\Delta_{Ki_i} = \infty$) of a specific regulated enzyme i as a function of the external hydrogen peroxide H dose. The studied regulation are made by modifying the corresponding parameters, i.e. Ki_{G6PD} and Ki_{PGI}.

Dose-dependent effect

Model parameter distributions have been estimated at a specific stress level induced by a step of external hydrogen peroxide H from $0\mu M$ to $500\mu M$. Deletion of regulation at this specific type of stress shows that regulations on NNH or $6PGD$ do not have impact on variables of the system while removing the one on $G6PD$ and $GAPD$, drastically deteriorate the capacity to detoxify the stress. A surprising result was found for deletion of the regulation on PGI where no significant change appears even if the inhibition is non negligible. Inhibition of $G6PD$ allows to direct the flux through the glycolysis without stress by closing the possibility to go through the PPP. Thus, decrease of the regulation helps to increase the flux inside the PPP in order to improve the H_2O_2 removing via $NADPH$ recycling. Inhibition on $GAPD$ allows to avoid loss of materials inside the metabolic pathways, potentially to favour the shift of the flux state to the flux cycling mode. Inhibition on PGI tends to close the glycolysis in both direction (i.e. glycolysis or reversely), allowing to favour flux rerouting toward the PPP.

The loss-of-function induced by regulation deletion can be analysed in dose response to clarify the role of the three last regulations, .i.e. on $G6PD$, PGI and $GAPD$, as function of H (Figure 6.3). Thus, the induced modification of the oxidative stress detoxification can be characterized by the sensitivity coefficient $\Delta_{Ki_i}^{H_2O_2}(H)$ of the internal H_2O_2 concentration as a function of the stress dose (Figure 6.3-A). When $\Delta_{Ki_i}^{H_2O_2}(H)$ is higher than 1 during regulation deletion, H_2O_2 concentration increase, so the detoxification is worse meaning that the regulation favour detoxification in its presence. The figure makes appear that removing the regulations does not affect the oxidative stress detoxification for the same level of stress :

- First, $G6PD$ regulation has the highest impact for smaller doses than $500\mu M$. This regulation is high in basal condition and decrease during oxidative stress inducing the possibility for the PPP flux to increase. Removing the $G6PD$ regulation dynamic induces a still low $G6PD$ flux rate. Thus, this enzyme regulation can be the first step to favour the flux rerouting by freeing the PPP.

- Second, when the $G6PD$ regulation impact starts to decline, PGI regulation takes over for doses still smaller than $500\mu M$ confirming that this regulation has no drastic effect at $H = 500\mu M$. Because the inhibition is induced by $6PG$, its concentration needs to increase to have an impact which happens for sufficiently high stress (Figure 5.9-B). The higher $6PG$ production occurs when the PPP flux is also increasing. Moreover, the PGI regulation also needs not-too-high stresses because inhibiting PGI flux in the condition of higher downstream than upstream PGI flux corresponding to a PPP flux lower than 1 (Figure 5.9-C), decreases the $G6P$ consumption and then favours flux toward the PPP.

- Finally, $GAPD$ regulation acts for higher level of stress. During high stress perturbations, the PPP flux is high compared to the basal condition (Figure 5.9-C). Then, a part of this flux goes through the noxPPP. In this condition, the inhibition of $GAPD$ closes the way to the lower glycolysis avoiding loss of metabolic contents. These resources can therefore restore $G6P$ level by using the reverse glycolysis favouring high flux cycling mode, i.e. $\Phi_{G6PD}/\Phi_{GLU} > 1$.

These analyses of steady state sensitivities during regulation deletions reveal that regulations on $G6PD$, PGI and $GAPD$ have a dose-dependant effect on the fast oxidative stress response.

The steady state sensitivity can also be analysed by a small perturbation of the regulation strength via the response coefficient. The mathematical terms are similar to the control coefficient but instead of changing a kinetic parameter of an enzyme. Contrary to the previous study induced by regulation deletion with $\Delta Ki_i = \infty$, the analysis of the steady state sensitivity of a variable Y using the response coefficient $R^Y_{p_i}$ is induced by an infinitesimal modification of a inhibition parameter $p_i = Ki$. This infinitesimal modification of the regulation strength could reveal how a steady state is sensitive to a very small perturbation of the regulatory mechanisms and then how the regulation are important to maintain this steady state. $G6PD$ regulation won't be analysed here due to the particular treatment that has been made in the previous study. The response coefficient of H_2O_2 and Φ_{oxPPP} as a function of H shows that the $GAPD$ and PGI regulations do not act for the same region of stress level (Figure 6.3-B). Moreover, a tiny modification of these regulations change the PPP flux confirming that they are already active for low level of stress even if they only impact H_2O_2 for high stress level.

- Inhibition of $GAPD$ promotes the increase of oxPPP flux by increasing of the upstream glycolytic flux. However, this effect needs a sufficiently high noxPPP flux which is not the case for small stress, justifying the low impact on Φ_{oxPPP} in low stress level.

- Inhibition of PGI is effective when $6PG$ drastically increases which is also not the case for small stress. However, an infinitesimal increase of the PGI inhibition parameter induces a small decrease of the glycolytic inhibition favouring a lower PPP flux. This Φ_{oxPPP} decrease in low level of stress has no impact on H_2O_2 because the $NADPH$ recycling is probably already sufficient to detoxify this incoming H_2O_2 at these doses.

To summarise, the dose responses of the regulation deletions show that they are dose-dependent and have different amplitudes of effects on the internal H_2O_2 concentration. Each regulation is effective at different stress level probably due to their respective work which would have different impact depending of the stress. $G6PD$ inhibition appears to be a first step to favour the resource allocation by rerouting the flux and by releasing the oxPPP. Then, PGI inhibition act to compensate the $G6P$ consumption in order to increase more the flux through the PPP when the system needs more $NADPH$ recycling. For extreme doses, $GAPD$ inhibition closes the output flux allowing to reduce the loss of content and then, to increase even more the oxPPP. Reusing resources coming from the PPP favours the cycling flux mode inducing extreme oxidative stress response. Finally, these regulations act on complementary regions of stress level.

Regulatory synergy

Regulations of the metabolic pathways are directly or indirectly acting to favour the $NADPH$ recycling by reallocating the resources. Regulations on $G6PD$, PGI and $GAPD$ have dose-dependant effect on the H_2O_2 detoxification. Moreover, when one regulation effect is becoming low, another takes other. As a next step, dual regulation deletions will be investigated in order to clarify the cooperative works of these regulations. The regulation cooperativity will be characterized by the sensitivity quantity $\Delta_{p_{i,j}}^{H_2O_2}(H)$ representing the modifications of internal H_2O_2 during dual deletion of regulation i and j induced by the modification $\Delta p_{i,j} = \infty$ of the corresponding inhibition parameters $p_{i,j} = Ki_{i,j}$. All the analyses of dual regulation deletions will be combined into Synergy Factor $SF_{i,j}$ which can compare their coupled efficiency by :

$$SF_{i,j} = \Delta_{p_{i,j}}^{H_2O_2} - (\Delta_{p_i}^{H_2O_2} + \Delta_{p_j}^{H_2O_2}) \tag{6.5}$$

where $SF_{i,j} > 0$ means that the dual regulation deletion is more impacting the oxidative stress detoxification than addition of the two regulation deletions separately and vice-versa, inducing a synergistic work of the regulations on i and j. When $SF_{i,j} = 0$, the dual regulation deletion does not show more impact leading to no synergy.

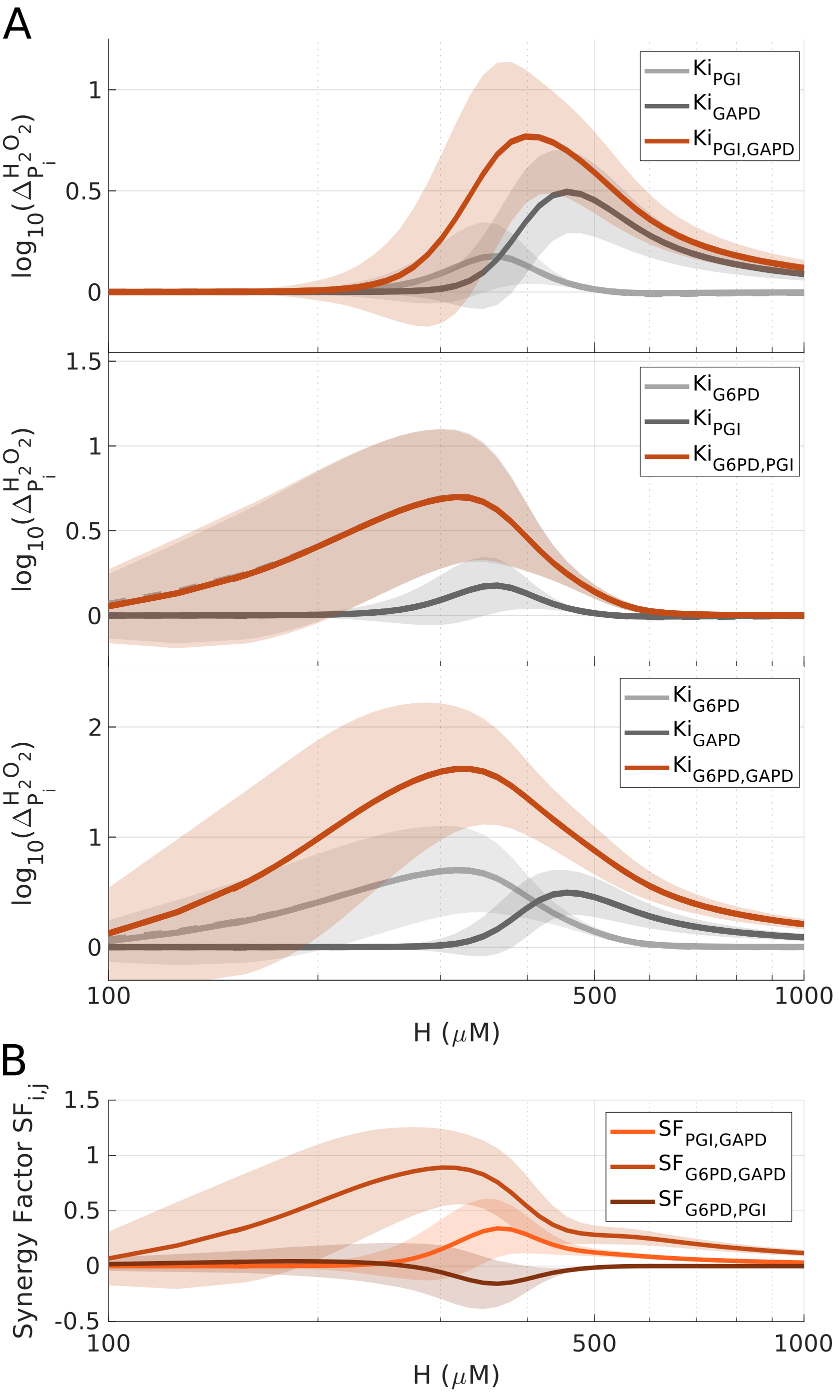

Figure 6.4: Combined deletion of regulations. From Hurbain et al. 2022 [3]. (A) Second-order sensitivity factor $\Delta_{p_i}^{H_2O_2}$ (eq 6.1) with respect to the combined deletion of two regulations in comparison to the single deletions as a function of the external hydrogen peroxide H. The parameters deletion is made by following $\Delta_{Ki_i} = \infty$ of a specific regulated enzyme i. (B) Synergy Factor $SF_{i,j}$ corresponding difference between the 2 single regulation deletions i and j to the combined deletion $\{i, j\}$ (eq 6.5) as a function of the external hydrogen peroxide H.

The effect of the dual inhibition deletion on internal H_2O_2 concentration as a function of the stress level H shows that $G6PD$, PGI and $GAPD$ regulations work in synergy (Figure 6.4-A), which is specifically visible with non-negative synergy factor (Figure 6.4-B).

- First, dual deletion of PGI and $GAPD$ regulations is higher than the separated regulation deletion meaning that this inhibition have higher impact together on the oxidative stress detoxification. The synergy factor is positive for the same range of stress level than the effect of the dual regulation deletion confirming the synergistic work of these two regulations. This can be understood by the fact that at medium and large range of stress level, PGI inhibition allows to reroute incoming glucose flux toward the oxidative and then to the noxPPP which can be sent back through the reverse glycolysis favouring the cycling mode.

- Second, the same analysis can be made with the regulation on $GAPD$ and $G6PD$ which also displays higher effect together than alone. Surprisingly, deleting regulations on $GAPD$ and $G6PD$ together drastically shows high impact on the oxidative stress detoxification even in dose regions where one regulation has no impact. This is particularly the case in low level of stress where $GAPD$ regulation seems to have no impact but with $G6PD$ inhibition in complement, the effect on H_2O_2 concentration is highly increased. This non-linear phenotype could be understood by the fact that $GAPD$ inhibition favours decrease of content loss to compensate the $G6P$ consumption in order to further shift of the flux state toward the cycling flux mode but needs the release of the PPP induced by the $G6PD$ inhibition decrease.

- Third, removing both regulation dynamics of $G6PD$ and PGI displays the same impact on the H_2O_2 concentration than the $G6PD$ regulation deletion alone which induces a negative synergy. Indeed, the regulation on $G6PD$ releases the PPP allowing a flux rerouting which increases the concentration of $6PG$ and then the PGI inhibition. Removing the regulation on PGI has no impact without $6PG$ concentration increase which does not happen without the $G6PD$ regulation decrease. This phenotype displays a specific type of synergistic work of the regulation on $G6PD$ and PGI.

To summarize, the comparison of effect of the dual regulation deletions with the addition of impact of their separated regulation deletion shows that $GAPD$ regulation works in synergy with $G6PD$ and PGI by non-linearly increasing the flux cycling in order to highly respond during oxidative stress.

However, this study shows that PGI inhibition has no effect without the decrease of the $G6PD$ regulation that happen during oxidative stress.

Conclusion

Analysis of our metabolic pathway regulations allows to better understand how they work during oxidative stress response. First, it exists some regulations that have no major impact in our model ensemble tending to reproduce fast experimental oxidative stress detoxification in fibroblast cells. Indeed, inhibition of HK, NNH and $6PGD$ do not significantly favour the oxidative stress detoxification (Figure 6.2) even if some of their inhibition level are important (Figure 6.1). However, regulation on $G6PD$, PGI and $GAPD$ favour H_2O_2 detoxification for different ranges of stress level. $G6PD$ inhibition has the highest impact of these three regulation and acts for small stress favouring flux rerouting from glycolytic to PPP by decreasing its inhibition level. If its strength fall to 0, the flux distribution will be given be the reaction speed constant between $G6PD$ and PGI. When oxidative stress increases, higher flux rerouting is needed. Because PPP flux rate is increasing, $6PG$ concentration is also increasing leading to high PGI inhibition. This regulation allows to close the glycolytic pathway favouring higher flux rerouting. In this condition, the maximum speed inside the oxPPP is approximately equal to the incoming glucose flux. when oxidative stress level is still higher, this flux could be insufficient. However, inhibition of $GAPD$ shows its effect for stress level because it allows to keep materials inside the metabolic pathways inducing the reverse glycolysis in order to shift toward a cycling mode. This increases even more the flux inside oxPPP allowing to highly improve stress response.

6.2.2 Effect of perturbing enzyme activities

To study metabolic pathways, modification of enzyme activity is often used during experimental measurement. Concerning glycolysis and pentose phosphate pathway, the three enzymes $G6PD$, $6PGD$ and TKT are used to be targeted during oxidative stress response [142, 17, 143, 144, 145, 146, 48]. Using the mathematical model ensemble, enzyme activity perturbation can be investigated by modifying their corresponding parameter p_i and can be characterized by sensitivity quantity $\Delta_{p_i}^{Y}$ of a variable Y. Experimental enzyme knockdown or overexpression will be reproduced by a modification of the parameter respectively from 10-fold reduction to 10-fold increase ($-1 < \Delta_{p_i} < 1$). This gain/loss-of-function study could provide deeper information on the regulatory mechanisms present in the fast oxidative stress response

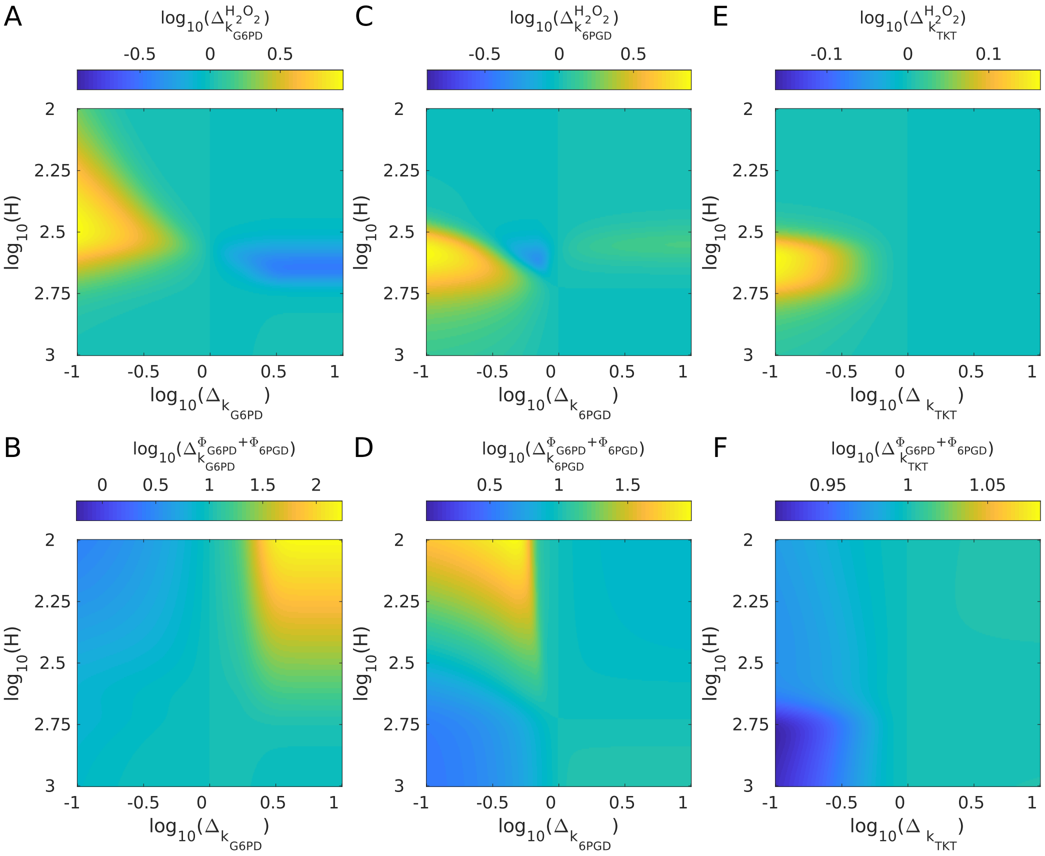

Figure 6.5: Gain/loss-of-function associated with modulated activity of PPP enzymes. From Hurbain et al. 2022 [3]. Sensitivity Δ_X^Y of output Y with respect to modulation of X (eq 6.1) as a function of H and the extent of parameter modulation. The output variable Y is either H_2O_2 (A,C,E) or NADPH-producing fluxes (B,D,F). The modulated parameter is either k_{G6PD} (A,B), k_{6PGD} (C,D) and k_{TKT} (E,F) corresponding to the enzyme activities of respectively $G6PD$, $6PGD$ and TKT.

---

which have been focused previously.

The mean of sensitivity quantity of H_2O_2 and the $NADPH$-producing oxPPP flux are displayed with a color-code as a function of the external hydrogen peroxide H and as a function of the parameter modification of the corresponding enzyme activity (Figure 6.5).

- First, the perturbation of the $G6PD$ enzyme activity shows expected behaviour concerning the change of internal H_2O_2 and $NADPH$ production (Figure 6.5-A,B). Indeed, during gradual overexpression ($\Delta_{p_i} >$

0), the system sees its PPP flux increased allowing a higher $NADPH$ production inducing higher H_2O_2 detoxification corresponding to a blue color. During gradual enzyme knockdown ($\Delta_{p_i} < 0$), the system displays the reverse phenotype, i.e. a reduced H_2O_2 detoxification corresponding to a yellow color, due to lower $NADPH$ production and PPP flux.

- Second, modulation of the $6PGD$ enzyme activity shows a non-linear metabolic response (Figure 6.5-C,D). Indeed, contrary to $G6PD$, $6PGD$ activity modulation increases H_2O_2 concentration during enzyme overexpression and has an ambivalent response during enzyme activity reduction. This ambivalent phenotype could be induced to the presence of the $6PGD$ saturation as a function of its substrate $6PG$ and the presence of the regulation on PGI by $6PG$.

- Third, modulation of TKT enzyme activity shows moderate modification of the oxidative stress detoxification and on the flux rerouting via $NADPH$ production (Figure 6.5-E,F) which does not allow to extract any specific mechanism. This result is consistent with the increase of the noxPPP flux during the dose response analysis (Figure 5.9).

Results of the modulation of $G6PD$ and TKT enzyme activities are consistent qualitatively with the experimental measurement in Kuehne et al. 2015. [17].

The ambivalent result of the $6PGD$ enzyme activity modulation needs to be clarified to better understand the role of the regulations (Figure 6.6). Without modification, $6PGD$ enzyme is working when the incoming glucose flux has been rerouted toward the PPP which increases $6PG$ concentration and activates the inhibition one PGI by $6PG$. This regulation favours flux rerouting by closing the glycolytic pathway which has for consequence to increase the oxidative stress detoxification. However, during $6PGD$ enzyme activity modulation, this behaviour is perturbed and can be separated in three regions :

- First, during high reduction of enzymatic activity, $6PGD$ does not consume enough $6PG$ which induces very high inhibition on PGI and then very high flux rerouting even for small stress level. Thus, PPP flux is higher but is blocked at $6PGD$ which limits the total PPP flux and the $NADPH$ production. This limit is also consistent with the dose response study which already shows this limit where $6PGD$ is saturated by the high $6PG$ concentration inducing a limit of the detoxification (Section 5.4).

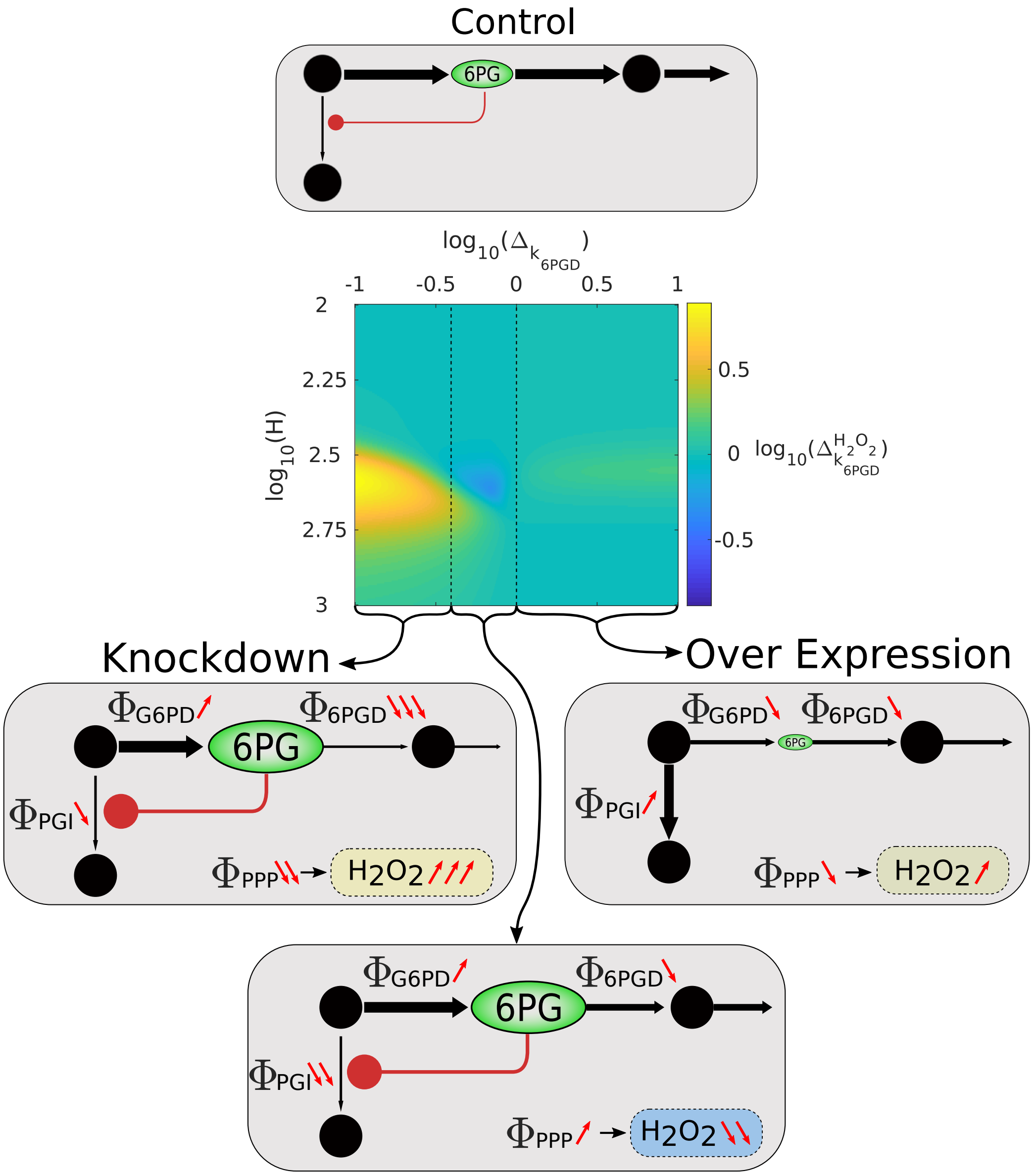

Figure 6.6: Gain/loss of function associated with modulated activity of the 6PGD enzyme. Metabolic pathway scheme in different region of the $6PGD$ enzyme activity analysis made in Figure 6.5-C representing internal H_2O_2 modification during dose responses of oxidative stress and during enzyme activity modification. The metabolic scheme circles and ellipse represent metabolites and arrows to fluxes. Size of arrows and ellipses reflect the corresponding flux rates and metabolite concentrations. The bigger the arrow, the higher the rate. The result is splitted in 3 separated areas which corresponds to higher or lower H_2O_2 detoxification respectively shown in yellow and blue.

- Second, trying to lift the barrier of $6PGD$ flux by overexpressing its activity shows that $6PGD$ consumes more $6PG$ which removes the PGI inhibition, decreases the PPP flux and then reduces the oxidative stress detoxification.

- Finally, it exists a region between these two extreme modifications where a small decrease of the enzymatic activity provides a compromises. Indeed, this small reduction of $6PGD$ enzyme activity induces smaller $6PG$ concentration, higher PGI inhibition and higher flux rerouting which corresponds so far to high enzymatic activity decrease. However, in this third region, because the $6PGD$ enzyme activity reduction is low, it allows to keep the $6PGD$ flux sufficiently high to have a higher total PPP flux inducing higher oxidative stress detoxification. So, decreasing a little the $6PGD$ enzyme activity allows to preset the network to favour PPP flux by increasing the PGI inhibition a little. This reconfiguration of the resource allocation promotes the oxidative stress detoxification with a maximum decrease in H_2O_2 concentration by a factor of $\approx 1/4$. This small change of activity has only effect on a certain region of stress level because for small doses, the system succeeds to detoxify and for high doses, this amplitude of change is still not enough to favour the detoxification.

In summary, the modulation of enzyme activities allows to show trivial phenotype for $G6PD$ and no effect for TKT. However, to increase the detoxification by modifying $6PGD$ enzyme activity, it is not necessary to increase this enzyme activity as the relation of the maximum flux rate would suggest but the right method is to reduce the $6PGD$ enzyme activity a little in order to slowly increase the inhibition on PGI inducing better resource allocations. This resource reallocation can drastically favour the oxidative stress response.

6.3 Metabolic control coefficients in the PPP

The regulatory pattern of the PPP and glycolysis has been investigated during oxidative stress response which reveals a complementary ranges of efficiency and a synergistic cooperative effects. To complement this study done with simulations of a model ensemble, a theoretical approach using Metabolic Control Analysis (MCA) framework will compute the control coefficient associated to the PPP, glycolysis and detoxification pathway as a function of the regulation and steady state variable.

The control coefficients are quantities that reflect the sensitivity of a variable, i.e. a metabolite concentration or a flux at steady state, to a small variation of a parameter. The parameter could reflect an enzyme concentration, enzyme activity or a reaction rate constant in general. To link the metabolite control coefficients to fluxes control coefficients, the equation 2.20 can be applied to the mathematical model :

$$\begin{pmatrix} C_{\Phi_l}^{J,OX} \\ C_{\Phi_l}^{J,CAT} \\ C_{\Phi_l}^{J,GPx} \\ C_{\Phi_l}^{J,GR} \\ C_{\Phi_l}^{J,NNH/NHN} \\ C_{\Phi_l}^{J,G6PD} \\ C_{\Phi_l}^{J,6PGL} \\ C_{\Phi_l}^{J,6PGD} \\ C_{\Phi_l}^{J,RPI} \\ C_{\Phi_l}^{J,RPE} \\ C_{\Phi_l}^{J,PRPPs} \\ C_{\Phi_l}^{J,TKT1} \\ C_{\Phi_l}^{J,TLD} \\ C_{\Phi_l}^{J,TKT2} \\ C_{\Phi_l}^{J,HK} \\ C_{\Phi_l}^{J,PGI} \\ C_{\Phi_l}^{J,PFK} \\ C_{\Phi_l}^{J,ALD} \\ C_{\Phi_l}^{J,TPI} \\ C_{\Phi_l}^{J,GAPD} \end{pmatrix} = \vec{\Pi}_{\Phi_l} + \boldsymbol{\epsilon}_{\vec{X}}^{\vec{J}} \begin{pmatrix} C_{\Phi_l}^{X,H_2O_2} \\ C_{\Phi_l}^{X,GSH} \\ C_{\Phi_l}^{X,NADPH} \\ C_{\Phi_l}^{X,G6P} \\ C_{\Phi_l}^{X,6PGL} \\ C_{\Phi_l}^{X,6PG} \\ C_{\Phi_l}^{X,Ru5P} \\ C_{\Phi_l}^{X,X5P} \\ C_{\Phi_l}^{X,R5P} \\ C_{\Phi_l}^{X,S7P} \\ C_{\Phi_l}^{X,E4P} \\ C_{\Phi_l}^{X,GLU} \\ C_{\Phi_l}^{X,F6P} \\ C_{\Phi_l}^{X,FBP} \\ C_{\Phi_l}^{X,DHAP} \\ C_{\Phi_l}^{X,GAP} \end{pmatrix} \tag{6.6}$$

where $C_{\Phi_l}^{J_j}$ and $C_{\Phi_l}^{X_i}$ are control coefficients of respectively the metabolite concentration X_i and fluxes J_j at steady state associated to the perturbation of the reaction rate Φ_l. $\vec{\Pi}$ is a unitary vector as a function of the perturbation l. $\boldsymbol{\epsilon}_{\vec{X}}^{\vec{J}}$ is the matrix of elasticities $\epsilon_{X_i}^{J_j}$. Each element of the elasticities matrix can be computed in the metabolic pathways and are given in equation 6.20 where $\tilde{J}_j^{+/-} = J_j^{+/-}/J_j$. The elasticities ϵ_k are the elasticities associated to the regulation or saturation k and are given by :

$$\epsilon_{NADPH}^{G6PD}(Ki_{G6PD}) = -\frac{[NADPH](1+1/Ki_{G6PD})}{(1-[NADPH])(1+\frac{[NADPH]}{Ki_{G6PD}})} \equiv \epsilon_1 \tag{6.7}$$

$$\epsilon_{NADPH}^{6PGD}(Ki_{6PGD}) = -\frac{[NADPH](1+1/Ki_{6PGD})}{(1-[NADPH])(1+\frac{[NADPH]}{Ki_{6PGD}})} \equiv \epsilon_2 \tag{6.8}$$

$$\epsilon_{G6P}^{HK}(Ki_{HK}) = -\frac{[G6P]/Ki_{HK}}{1+[G6P]/Ki_{HK}} \equiv \epsilon_3 \tag{6.9}$$

$$\epsilon_{6PG}^{PGI}(Ki_{PGI}) = -\frac{[6PG]/Ki_{PGI}}{1+[6PG]/Ki_{PGI}} \equiv \epsilon_4 \tag{6.10}$$

$$\epsilon^{GAPD}_{H_2O_2}(Ki_{GAPD}) = -\frac{1}{1+\frac{[GSH]Ki_{GAPD}}{[H_2O_2][GSH]_{tot}}} \equiv \epsilon_5 \tag{6.11}$$

$$\epsilon^{6PGD}_{6PG}(Km_{6PGD}) = \frac{1}{1+[6PG]/Km_{6PGD}} \equiv \epsilon_6 \tag{6.12}$$

The mathematical model is designed to reproduce experimental data during oxidative stress which can be mimicked by computing the control coefficients during a perturbation of the H_2O_2 production flux, i.e. $\Phi_l = \Phi_{OX}$ made by a perturbation of the endogenous production of H_2O_2, inducing $\vec{\Pi}_{\Phi_{OX}} = [1, 0, ..., 0]^T$. The system is considered at steady state which induces $J_{oxPPP} = J_{G6PD} = J_{6PGD} = J_{GR}/2 = J_{GLU} - J_{PGI}$. During oxidative stress, the main anti-oxidant system is made by glutathiones allowing to neglect the catalase and the flux NNH/NHN inducing $J_{oxPPP} = k_{OX}$ and $C^{J,oxPPP}_{\Phi_{OX}} = 1$. Then, a relation between the corresponding control coefficients can be found as :

$$C^{J,oxPPP}_{\Phi_{OX}} = C^{J,G6PD}_{\Phi_{OX}} = C^{J,6PGD}_{\Phi_{OX}} = C^{J,GR}_{\Phi_{OX}} = -\frac{J_{PGI}}{J_{oxPPP}} C^{J,PGI}_{\Phi_{OX}} = 1 \tag{6.13}$$

Then, a relevant set of relations from the equation 6.6 becomes :

$$C^{J,oxPPP}_{\Phi_{OX}} = 1 \tag{6.14}$$

$$C^{J,oxPPP}_{\Phi_{OX}} = \epsilon_1 C^{X,NADPH}_{\Phi_{OX}} + C^{X,G6P}_{\Phi_{OX}} \tag{6.15}$$

$$C^{J,oxPPP}_{\Phi_{OX}} = \epsilon_2 C^{X,NADPH}_{\Phi_{OX}} + \epsilon_6 C^{X,6PG}_{\Phi_{OX}} \tag{6.16}$$

$$C^{J,oxPPP}_{\Phi_{OX}} = (-J^+_{PGI} C^{X,G6P}_{\Phi_{OX}} + J^-_{PGI} C^{X,F6P}_{\Phi_{OX}} - \epsilon_4 C^{X,6PG}_{\Phi_{OX}} J_{PGI})/J_{oxPPP} \tag{6.17}$$

By combining these equations, the following equation can be found :

$$C^{X,NADPH}_{\Phi_{OX}} = \frac{-1 - \epsilon_3 \bar{J}_{PGI} + (C^{X,F6P}_{\Phi_{OX}})\bar{J}^-_{PGI}}{\epsilon_2 \epsilon_3 \bar{J}_{PGI} - \epsilon_1 \bar{J}^+_{PGI}} \tag{6.18}$$

where $\bar{J}_j = J_j/J_{GLU}$. This equation defines a regulatory manifold $\mathcal{F}(C^{X,NADPH}_{\Phi_{OX}}, C^{X,F6P}_{\Phi_{OX}}, \bar{J}_{PGI}, \bar{J}^+_{PGI})$. In order to study specific regulatory mechanism, this control manifold can be reduced for instance without regulation on PGI, i.e. $r3 = 0$:

$$C^{X,NADPH}_{\Phi_{OX}}(r3 = 0) = \frac{(C^{X,F6P}_{\Phi_{OX}} - 1)\bar{J}^-_{PGI} - 1}{-\epsilon_1 \bar{J}^+_{PGI}} \tag{6.19}$$

$$
\epsilon^{\vec{J}}_{\vec{X}} = \left(\begin{array}{cccccccccccccccc}
\epsilon^{H_2O_2}_{\Phi OX} & 0 & 0 & 0 & 0 & 0 & 0 & 0 & 0 & 0 & 0 & 0 & 0 & 0 & 0 & 0 \\
1 & 0 & 0 & 0 & 0 & 0 & 0 & 0 & 0 & 0 & 0 & 0 & 0 & 0 & 0 & 0 \\
\epsilon^{H_2O_2}_{GPx} & \epsilon^{GSH}_{GPx} & 0 & 0 & 0 & 0 & 0 & 0 & 0 & 0 & 0 & 0 & 0 & 0 & 0 & 0 \\
0 & \epsilon^{GSH}_{GR} & \epsilon^{NADPH}_{GR} & 0 & 0 & 0 & 0 & 0 & 0 & 0 & 0 & 0 & 0 & 0 & 0 & 0 \\
0 & 0 & \epsilon^{NADPH}_{NNH/NHN} & 0 & 0 & 0 & 0 & 0 & 0 & 0 & 0 & 0 & 0 & 0 & 0 & 0 \\
0 & 0 & \epsilon_1 & 1 & 0 & 0 & 0 & 0 & 0 & 0 & 0 & 0 & 0 & 0 & 0 & 0 \\
0 & 0 & 0 & 0 & 1 & 0 & 0 & 0 & 0 & 0 & 0 & 0 & 0 & 0 & 0 & 0 \\
0 & 0 & \epsilon_2 & 0 & 0 & \epsilon_6 & 0 & 0 & 0 & 0 & 0 & 0 & 0 & 0 & 0 & 0 \\
0 & 0 & 0 & 0 & 0 & 0 & \tilde{J}^{+}_{RPI} & -\tilde{J}^{-}_{RPI} & 0 & 0 & 0 & 0 & 0 & 0 & 0 & 0 \\
0 & 0 & 0 & 0 & 0 & 0 & \tilde{J}^{+}_{RPE} & 0 & -\tilde{J}^{-}_{RPE} & 0 & 0 & 0 & 0 & 0 & 0 & 0 \\
0 & 0 & 0 & 0 & 0 & 0 & 0 & 0 & \epsilon^{R5P}_{PRPPs} & 0 & 0 & 0 & 0 & 0 & 0 & 0 \\
0 & 0 & 0 & 0 & 0 & 0 & 0 & \epsilon^{X5P/R5P}_{TKT1} & \epsilon^{X5P/R5P}_{TKT1} & \epsilon^{S7P}_{TKT1} & 0 & 0 & \epsilon^{S7P/F6P}_{TKT1} & 0 & 0 & 0 \\
0 & 0 & 0 & 0 & 0 & 0 & 0 & 0 & 0 & \epsilon^{S7P/F6P}_{TLD} & \epsilon^{E4P/GAP}_{TLD} & 0 & \epsilon^{S7P/F6P}_{TLD} & 0 & 0 & \epsilon^{E4P/GAP}_{TLD} \\
0 & 0 & 0 & 0 & 0 & 0 & 0 & \epsilon^{X5P/E4P}_{TKT2} & 0 & 0 & \epsilon^{X5P/E4P}_{TKT2} & 0 & \epsilon^{GAP/F6P}_{TKT2} & 0 & 0 & \epsilon^{GAP/F6P}_{TKT2} \\
0 & 0 & 0 & \epsilon_3 & 0 & 0 & 0 & 0 & 0 & 0 & 0 & 1 & 0 & 0 & 0 & 0 \\
0 & 0 & 0 & \tilde{J}^{+}_{PGI} & 0 & \epsilon_4 & 0 & 0 & 0 & 0 & 0 & 0 & -\tilde{J}^{-}_{PGI} & 0 & 0 & 0 \\
0 & 0 & 0 & 0 & 0 & 0 & 0 & 0 & 0 & 0 & 0 & 0 & \tilde{J}^{+}_{PFK} & -\tilde{J}^{-}_{PFK} & 0 & 0 \\
0 & 0 & 0 & 0 & 0 & 0 & 0 & 0 & 0 & 0 & 0 & 0 & 0 & 0 & 0 & 0 \\
0 & 0 & 0 & 0 & 0 & 0 & 0 & 0 & 0 & 0 & 0 & 0 & 0 & \tilde{J}^{+}_{PFK} & -\tilde{J}^{-}_{ALD} & -\tilde{J}^{-}_{ALD} \\
0 & 0 & 0 & 0 & 0 & 0 & 0 & 0 & 0 & 0 & 0 & 0 & 0 & 0 & \tilde{J}^{+}_{TPI} & -\tilde{J}^{-}_{TPI} \\
\epsilon_5 & -\epsilon_5 & 0 & 0 & 0 & 0 & 0 & 0 & 0 & 0 & 0 & 0 & 0 & 0 & 0 & 1
\end{array}\right) \tag{6.20}
$$

Table 6.1: Elasticities matrix associated to the mathematical model. $\epsilon^{J_j}_{X_i}$ are the elasticities of the metabolite concentration X_i as a function of the flux rate J_j a steady state. ϵ_k is the elasticity associated to the regulation or saturation k. $\tilde{J}^{+/-}_j = J^{+/-}_j / J_j$

This relation indicates that the efficiency of the feedback inhibition for $NADPH$ homeostasis decreases as a function of the increase of J_{PGI} because it induces $C^{X,F6P}_{\Phi_{OX}} < 0$ and then a more negative term $(C^{X,F6P}_{\Phi_{OX}} - 1)\bar{J}^{-}_{PGI} - 1$. The elasticity characterized by the regulation on $G6PD$ by $NADPH$, is negative ($\epsilon_1 < 0$) which means that the $NADPH$ homeostasis is promoted by high and positive $C^{X,F6P}_{\Phi_{OX}}$ and $\bar{J}^{-}_{PGI}$. However, a limit case can be calculated in the condition of high directional fluxes ($J^{+/-}_{PGI}$) and low net PGI flux inducing almost instantaneous exchange between $G6P$ and $F6P$ which can be called high futile cycling flux in the PGI reactions :

$$\lim_{J^{+/-}_{PGI} \to \infty} C^{X,NADPH}_{\Phi_{OX}}(r3 = 0) \approx \frac{C^{X,F6P}_{\Phi_{OX}} - 1}{-\epsilon_1} \tag{6.21}$$

This relation defines an upper boundary which grows like $(C^{X,F6P}_{\Phi_{OX}} - 1)(1 - (1 - [NADPH])/Ki_{G6PD})$, limits the regulation efficiency to maintain the $NADPH$ homeostasis and therefore the H_2O_2 detoxification. This limit is found without regulation on PGI. While $G6PD$ inhibition reroutes the flux toward the PPP, the PGI regulation would serve to reduce the $G6P$ consumption which favours the flux rerouting, revealing a cooperative work of the regulation on $G6PD$ and PGI. Moreover, the limit is directly proportional to the control coefficient of $F6P$ which would reveal that control the $F6P$ concentration would allow to reverse PGI. Adding inhibition on PFK would induce change in $F6P$ concentration variation contributing to the $NADPH$ homeostasis.

The previous relations do not link directly the regulation on $GAPD$ by H_2O_2. The only equation that takes into account the elasticity ϵ_5 is :

$$C^{J,GAPD}_{\Phi_{OX}} = \epsilon_5(C^{X,H_2O_2}_{\Phi_{OX}} - C^{X,GSH}_{\Phi_{OX}}) + C^{X,GAP}_{\Phi_{OX}} \tag{6.22}$$

However, no simple relation can be found due to non-evident direct relations with the oxPPP flux as it has been made previously with PGI. Assuming that the output flux $PRPPs$ is negligible would simplify the flux relations but it is not the case for most of the flux states during oxidative stress (Figure 5.9-C).

In conclusion, MCA framework is used to investigate the regulatory mechanisms of the PPP and glycolysis in a context of oxidative stress. A limit of the regulation efficiency is found in the case of extremely high forward and backward fluxes PGI and without regulation on PGI. This boundary which depends directly on the $G6PD$ regulation, reveals that regulations on $G6PD$ and PGI work cooperatively to maintain the $NADPH$ homeostasis. Indeed, inhibition on PGI favours to reduce net flux in order to operate near equilibrium. Computing the control coefficients via numerical simulation of the model ensemble would allow to confirm these results.

Chapter 7

Adaptation dynamics contributes to fate-response heterogeneity

Living cells are often exposed to various types of perturbations such as oxidative stress. When perturbations occur in cells, the metabolism is used in order to defend to it. During the defence, different cellular fates can happen depending of the quantity of the produced damage such as stop of cellular growth or cell death. It has been shown that the presence of adaptation phenotype could impact the cellular fate during external perturbation such as during oxidative stress [61]. The main objective of this thesis was to study the effect of fast regulations on the resources reallocation in order to defend to a hydrogen peroxide burst. This theoretical study revealed the presence of adaptation phenotype in temporal dynamic of most of the metabolites during fast oxidative stress response. This project does not aim to link this observed phenotypes to the possible cellular fates. This chapter will introduce a parallel theoretical study published in Hurbain et al. 2020 [2]. In this study, we investigate the impact of the presence of adaptation phenotype on the cellular fates during a general source of perturbation which shows that the adaptation dynamics improves the cell-fate heterogeneity.

7.1 Cell fate responses during oxidative stress

7.1.1 From cell survivability to death

Oxidative stress is a perturbation of the redox state of a cell. It is induced by molecules called reactive oxygen species which transfer their oxidation and oxidise molecules inside cell creating damages. The cells reorganise the allocation of the resources available in order to defend against such oxidant

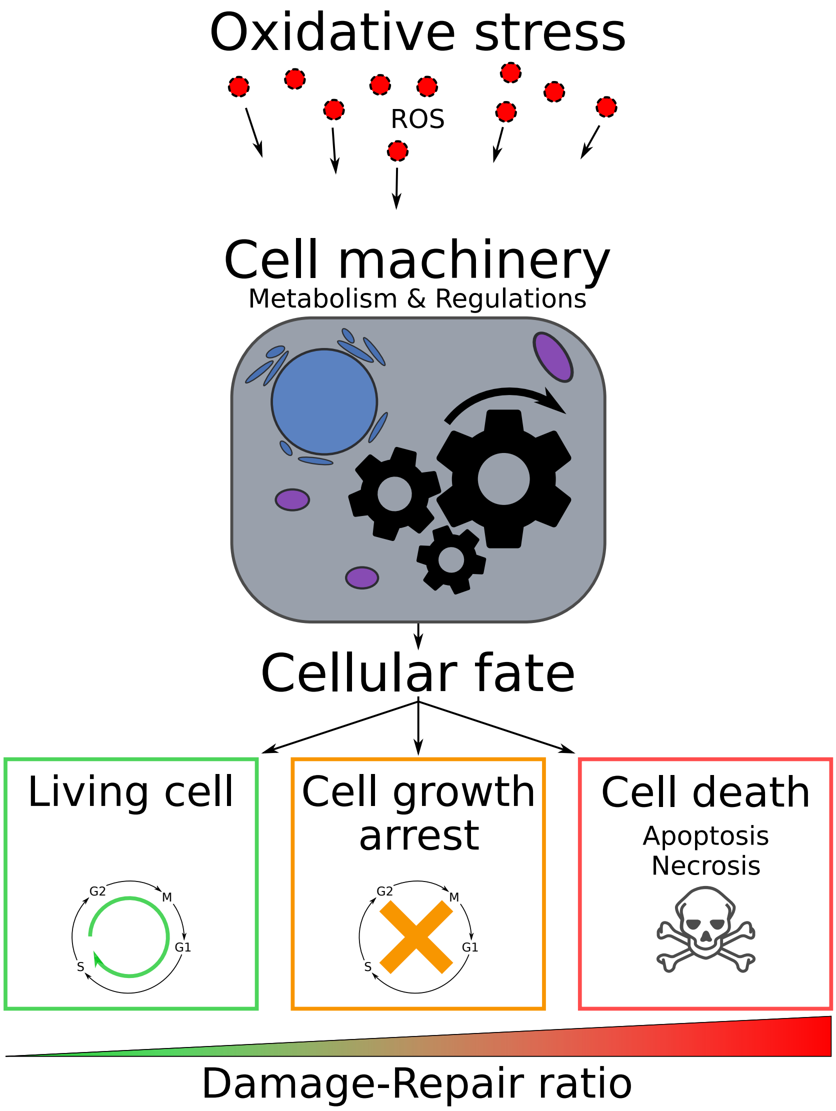

Figure 7.1: Different cell fates following oxidative stress.

molecules. Regulations are major mechanisms to modify a flux state in order to shift its function from energy or biomass production to defence mechanisms and reversely. In the context of oxidative stress, this thesis shows that regulations of $G6PD$, PGI and $GAPD$ are important source of resource reallocation via flux rerouting toward the PPP allowing high $NADPH$ recycling and then to high H_2O_2 detoxification, but at the cost of depletion of ATP production. Moreover, they act in dose-dependant manner with important synergistic cooperation so that cells can defend against large range of oxidative stress dose. Finally, this study also shows that regulatory mechanisms could induce adaptation phenotype in temporal dynamics. The difference of cellular growth induced by the presence of adaptation during oxidative stress has been investigated for instance in yeast in Goulev et al. 2017 [61]. However, the question of the impact of the adaptation induced by the regulatory mechanisms, on the cellular fate remains unclear.

The damages induced by oxidative stress can lead to different cell fate going from the survivability to the death (Figure 7.1). When the damages are low or the capacity to repair, the cells can adapt to the perturbation and survive. When the quantity of damages increases, the cells can reallocate their resources toward stress management generally associated to cell-cycle and growth arrest. Then, when the damages are to high to be repaired even during a short time scale, mechanisms of cell death will be initiated. These mechanisms can be programmed by the cell, i.e. the apoptosis, or not programmed corresponding for instance to necrosis (Figure 7.2).

Necrosis is a cell death mechanisms due to extreme damages [147] which is not programmed by cells which induces lost of bio-components by release all components in extra-cellular space which are not usable by other cells, contrary to apoptosis. It can be considered as the harmful cell death pathway. Necrosis can be induced by cellular stresses as apoptosis but, in general, for more extreme regimes. Apoptosis is the programmed cell death mechanism allowing no harmful death by releasing reusable component. This pathway has been investigated via a mathematical model showing cell-fate heterogeneity [148] and will be focused in this chapter.

7.1.2 Cell death mechanisms : apoptosis

Apoptosis is a cellular mechanism that triggers cell death in response to a signal. This mechanism is a programmed cell death inducing morphologic change in order to split cell components in small compartments called apoptotic bodies [149]. They are engulf via phagocytosis mechanisms by phagocyte cells which are cells that can swallow foreign bodies and dying or dead cells. These processes are highly regulated because a high frequency of apoptosis in a population would induce entire cell population degeneration and a very low frequency would induce extreme growth and then diseases such as cancer [150]. Thus, apoptosis can be started from two different pathways : intrinsic and extrinsic pathway.

- Intrinsic apoptosis pathway leads to self-induced cell death due to cellular stress. This pathway aims to trigger apoptosis by releasing molecules in cell cytosol from mitochondria. We will focus on the

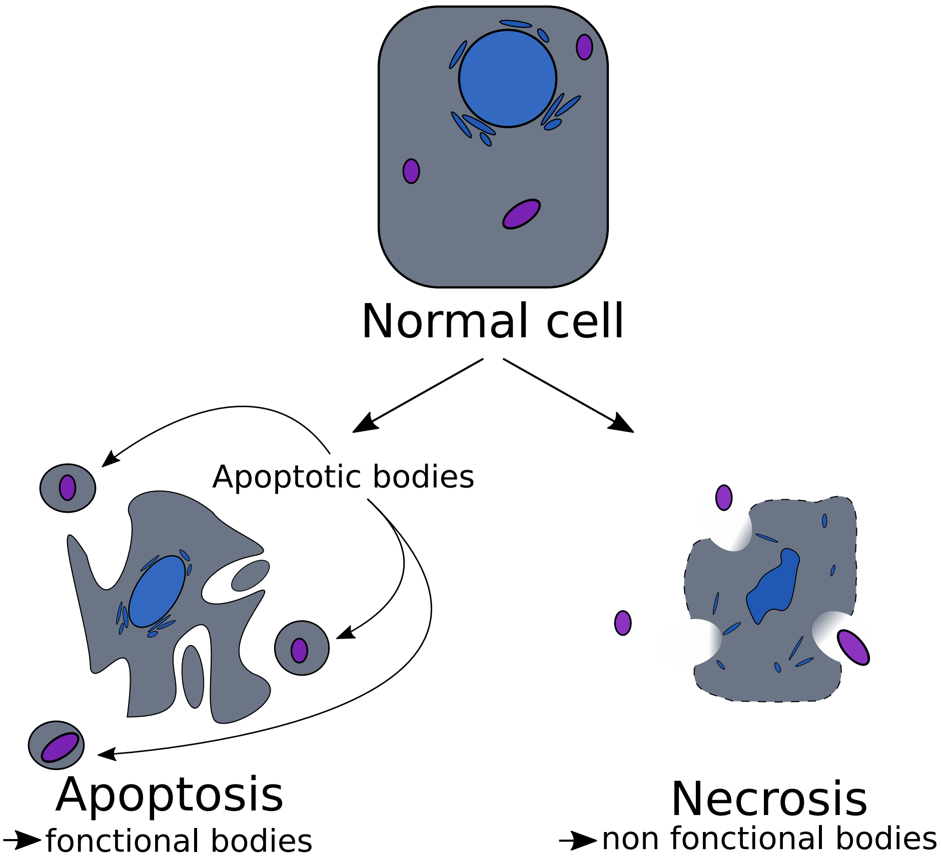

Figure 7.2: Cell death mechanisms : Apoptosis and Necrosis. A normal cell can undergo two possible death mechanisms. Apoptosis releases apoptotic bodies that are usable by other cells. Necrosis release the cellular content without envelope inducing loss of the materials.

---

model from Ballweg et al. 2017 [148] representing intrinsic apoptosis network (Figure 7.3). It is initiated by several modules linked to transcription factor $p53$ and $caspase8$ which are molecules allowing to control cell life or death and inducing the production of $Bh3$ proteins in order to mediates apoptosis. $Bh3$ induces the transport from cytosol to mitochondria of the Bcl-2–associated X (BAX) proteins producing activated BAX molecules written $BAXm$. While the family of anti-apoptotic Bcl proteins can form a complex with $Bh3$, Bcl can also be captured by $BAXm$ releasing the complexed-$Bh3$. The activation of the apoptosis program needs a sufficiently high production of $Bh3$ to transfer into mitochondria a sufficiently high quantity of BAX

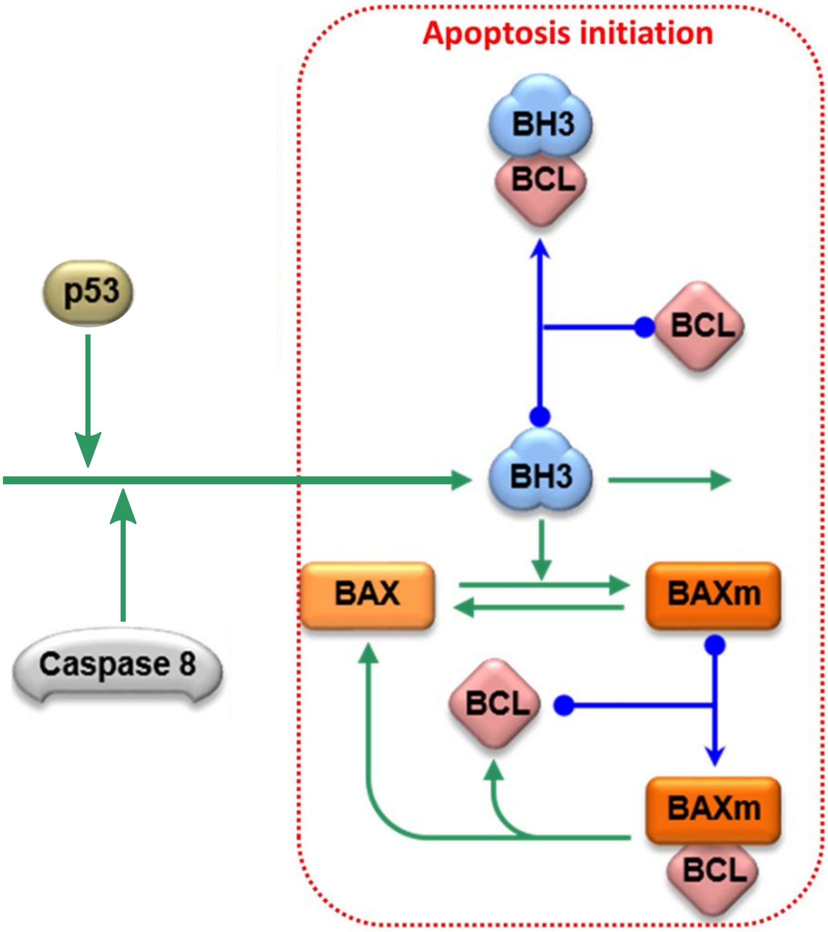

Figure 7.3: Intrinsic apoptosis model. Adapted from Ballweg et al. 2017 [148]. Production of $Bh3$ made by caspase 8 ($C8$) induces mitochondrial transport of the BAX producing $BAXm$. The cytoplasmic BAX is inactive and the mitochondrial $BAXm$ is active. Both $Bh3$ and $BAXm$ can form a complex with Bcl inducing inactivation of the corresponding molecules.

---

to capture the Bcl and to release the complexed-mBh3. These steps avoid activation of apoptosis with a small signal induced for instance by a noisy perturbation. $BAXm$ can be seen as an inducer of apoptosis by activating pro-apoptosis molecules and inhibiting anti-apoptosis molecules. Finally, this small network aims to increase the concentration of BAX inside mitochondria to activate further pathway and to induce apoptosis.

- Extrinsic apoptosis pathway leads to self-induced cell death due to other signals [151] which is transmitted by death receptor such as Fas receptors, tumor necrosis factor (TNF) receptors and TNF-related apoptosis-inducing ligand ($TRAIL$) receptors. They will sense and capture the corresponding molecules, for instance TNF-receptor will sense TNF in order to induce recruitment of adaptor protein, then to downstream factors as caspase 8 and activate cell apoptosis. These death receptors can be present during oxidative stress because TNF can induce production of ROS [4].

7.2 Model of cell fate decision

In the context of cell death decisions, cell-fate heterogeneity is known as fractional killing [152, 153]. The fate choice between life and death induced by an oxidative stress perturbation is likely to depend on the presence and characteristics of the adaptation phenotype as shown for the cellular growth phenotypes in yeast [61]. This section will introduced a study of the impact of adaptation to a general perturbation on the cellular decision. A stochastic mathematical model will be built by combining a coarse-grained model displaying an adaptation phenotype with the published model of the mitochondrial apoptosis initiation from Ballweg et al. 2017 [148]. This study shows that the presence of adaptation favours the fractional killing. These results are published in Hurbain et al. 2020 [2].

7.2.1 Modeling of the probabilistic fate decision

In this study is built a mathematical model comprising the published model of mitochondrial apoptosis initiation [148] with a coarse-grained model showing an adaptation profile (Figure 7.4). The structure of this coarse-grained model is a negative feedback loop between x_1 and x_2. Indeed, the stress S produces damages x_1 which induces the activation of the repair system x_2 which decreases the damage quantity. This feedback loop is characterized by the parameter β which also represents the strength of the adaptation phenotype. Thus, x_1 is a variable that can display an adaptative curve. In another side, the damages $x1$ upregulates the synthesis of the pro-apoptotic $Bh3$-only proteins. The mitochondrial apoptosis can then be initiated as a function of the damages. As explained in the previous section, the cursor of the apoptosis initiation can be the quantity of mitochondrial BAX, i.e. $BAXm$, which frees the complexed $Bh3$.

The positive feedback loop made by the formation and dissociation of the

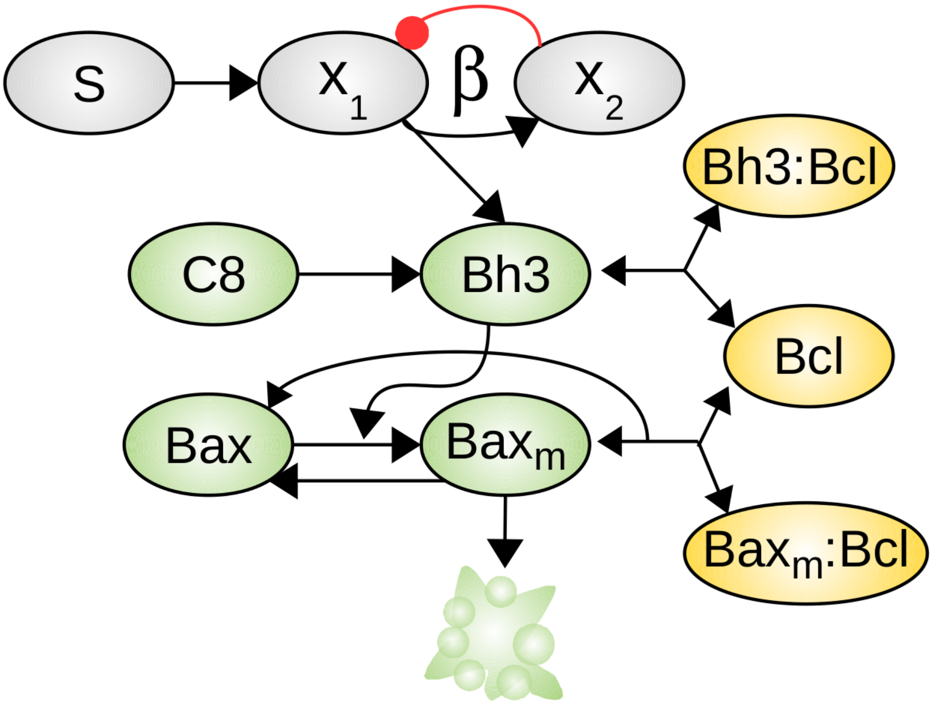

Figure 7.4: Schematic representation of the apoptosis model. From Hurbain et al. 2020 [2]. Ellipses are variables of the network and the arrows represent the chemical reactions. The stress S from a general source induces the damages x_1 which activates the repair system x_2. x_1 is linked to the published model of mitochondrial apoptosis initiation of Ballweg et al. 2017 [148].

---

complexed-$Bh3$ produces a bistable switch from low to high quantity of free mitochondrial BAX [148] which could induce the execution of apoptosis. This study links this bistable switch with the adaptation behaviour to a general stress. This bistable switch corresponds to surviving or dying cells. At the scale of a population, a fraction of cells will converge toward one or another state defining the fractional killing characterized by a probability of death. This probabilistic decision has been investigated via theoretical framework of Langevin differential equation description (from eq 2.24) which computes the stochastic dynamics of the biochemical reactions of the network presented here.

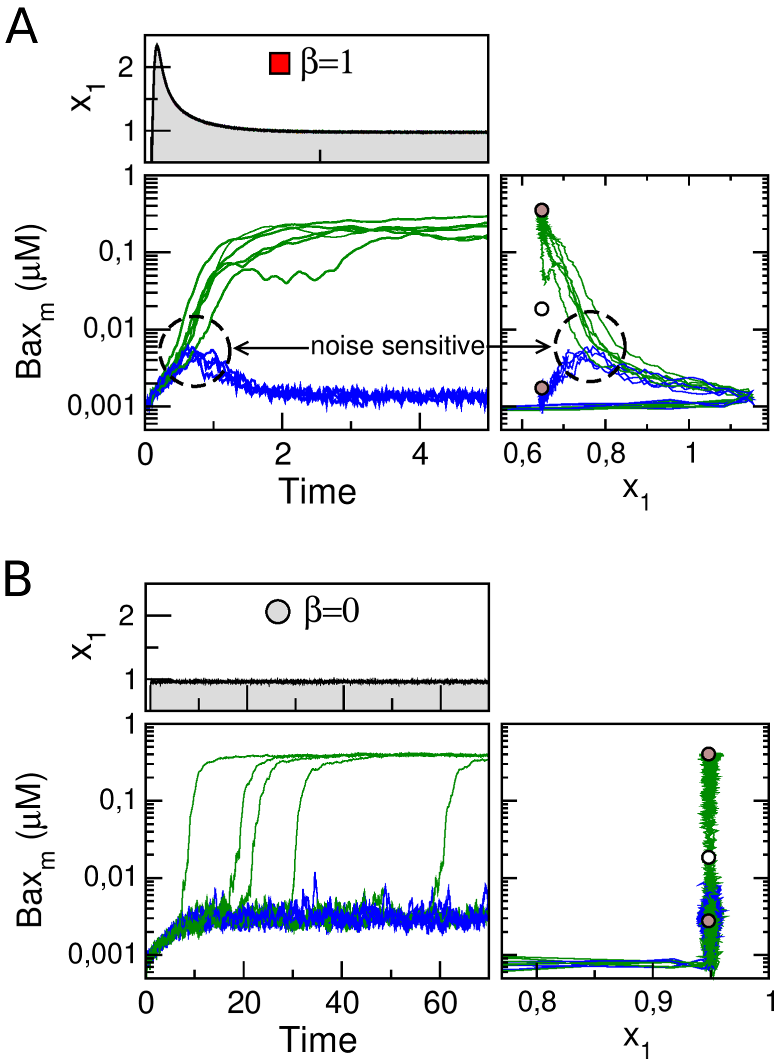

Figure 7.5: Adaptation impact on temporal trajectories. From Hurbain et al. 2020 [2]. Temporal trajectories of x_1 and $BAXm$ in the presence or the absence of adaptation (A: $\beta = 1$; B: $\beta = 0$). Adaptation timescale is set to $\tau = 1.25hr$ to match with the timescale of the apoptotic switch (time unit is hour). Right panels show a 2D state-space projection of the high-dimensional dynamics with respect to the stable and saddle fixed points (brown and white circles) of the deterministic system.

7.2.2 Adaptation and cell-fate heterogeneity

The apoptosis model is simulated at the scale of a population of cells which undergoes a stress quantity $S(t)$ built by a heaviside function of amplitude

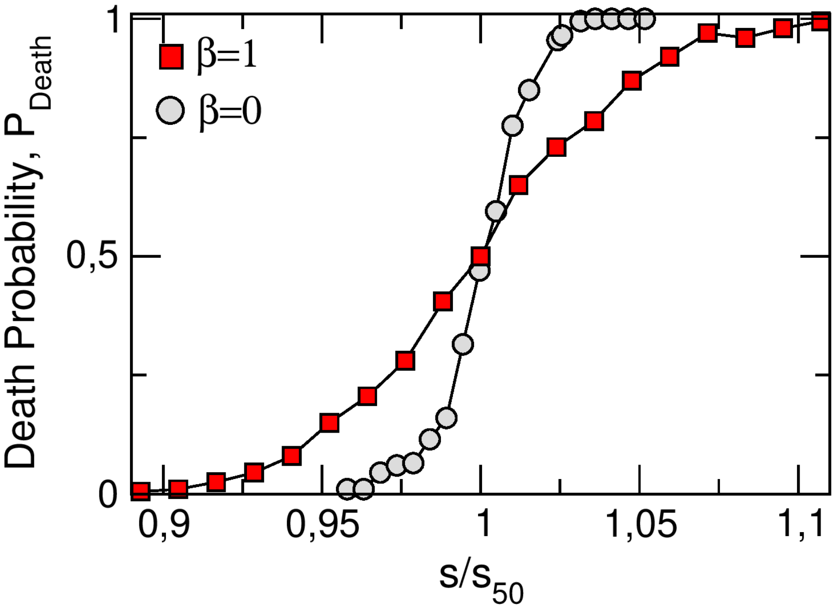

Figure 7.6: Adaptation impact on cell death probability. From Hurbain et al. 2020 [2]. The probability of death P_{Death} is computed with the apoptotic model with ($\beta = 1$) or without ($\beta = 0$) adaptation as a function of the stress heaviside amplitude s. s_{50} corresponds to the stress amplitude at $P_{death} = 50\%$. Time unit is hour.

---

s. For a given stress level, the stochastic trajectory of several cells are computed with two different adaptation amplitudes, i.e. $\beta = 1$ for high amplitude or $\beta = 0$ for low amplitude (Figure 7.5). When x_1 displays an adaptation profile, the system has a proportion of cell that converges to a stable point corresponding to the survival state with low $BAXm$ concentration while another proportion converges to a death state with high $BAXm$ concentration (Figure 7.5-A). The groups of survival and death cells have the same temporal dynamic within the first minute but diverge after a bifurcation point : the group of cells that survive have globally all the same temporal dynamic with an overshot of $BAXm$ while those who die have an increasing and then saturation curve. However, when the system has not adaptation profile, the entire population of cell converge to the same state with high $BAXm$ concentration, i.e. the death state (Figure 7.5-B). The temporal dynamic reveals that all cells do not bifurcate and converge at a certain time to the death state due to the stochasticity of the system.

The adaptative response to a stress appears to impact the fate of a group of cells. To clarify this result, the death probability is computed as a function of the stress doses (Figure 7.6). The doses are normalized by the stress s_{50} corresponding to the stress at 50% of death probability. The adaptation phenotype, i.e. $\beta = 1$, modifies the profile of the death probability by smoothing the curve compared to the curve without adaptation, i.e. $\beta = 0$. Instead of having a sharp curve inducing a total survivability or a total death of the population of cell, the adaptation induces a fractional killing of the population which higher depends of the dose. This fractional killing can improve the global survivability of the cell population. Indeed, during a perturbation, when the entire population dies, there is no possibility to recover, while if there are few cells that survive, they can potentially recreate the population afterwards.

Even if the oxidative stress model does not aim to link the response to the cellular fate, this study reveals that the presence adaptation favours fractional killing, and thus the survivability of the population to high stress. Given that the kinetic model of PPP response to oxidative stress shows an adaptative phenotype due to the resource reallocation made by the regulations, it is tempting to conjecture that such phenotype could impact the heterogeneity of cell fate response. It is however not clear what is the long term phenotypes of cells for the oxidative stress experiments used to develop our kinetic model.

Chapter 8

Discussion & perspective

The objective of this thesis was to study the resource allocation during early oxidative stress response of the PPP and glycolysis : how are the metabolic pathways regulated to reorganise the carbon flux in order to increase $NADPH$ production to recycle the anti-oxidant system ? A mathematical model ensemble of these metabolic pathways has been built in order to reproduce experimental data coming from Kuehne et al. 2015 [17] via a data-driven estimation of parameter distribution. These data comprise fold change concentration data and ^{13}C labeling data which has been converted into flux states data via a novel metabolic flux analysis algorithm based on a stochastic simulation algorithm. Data-driven kinetic modeling is a method often used to investigate interactions of metabolites on enzymes in order to control the metabolic phenotypes [34, 133, 154, 155, 156]. Our study reveals efficient oxidative stress response via metabolic regulation of the PPP and glycolysis enzymes to highly produce $NADPH$ molecules in order to support the anti-oxidant system (Figure 8.1).

8.1 Regulation scheme during oxidative stress

The main objective of this thesis was to study the regulation effects on the carbon resource allocations in early oxidative stress response. The use of data-driven kinetic models is common to investigate the role of allosteric regulation [34, 133, 154, 155, 156, 157]. The regulations on $G6PD$, PGI and $GAPD$ appear to have important impacts in several cell types in many studies [17, 35, 36]. The decrease in $NADPH$-dependant inhibition on $G6PD$ is made by the oxidation of $NADPH$ into $NADP^+$ allowing to release PPP flux. Consumption of $G6P$ is then increased and can be compensated by

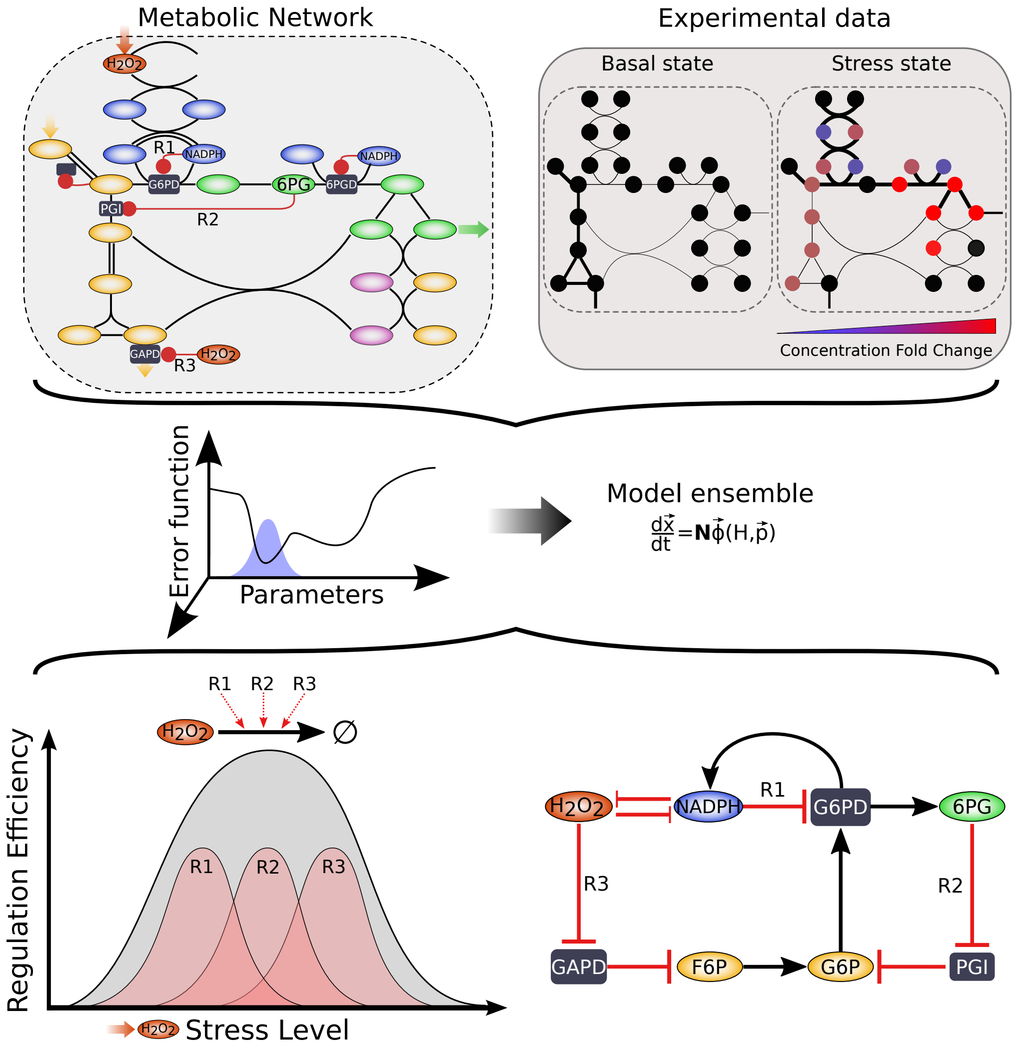

Figure 8.1: Graphical abstract of the procedure for the study of the regulation scheme. From Hurbain et al. 2022 [3]. The metabolic network composed of the PPP, glycolysis and the detoxification system is combined to experimental data of fast oxidative stress response which allows to estimate a distribution of the parameter set. The model ensemble can then be analysed to investigate the role of the regulations during the fast oxidative stress response. *R*1, *R*2 and *R*3 correspond respectively to the regulations on *G*6*PD*, *PGI* and *GAPD*.

---

either the inhibition on *PGI* or by increasing the *G*6*P* production. As the incoming glucose flux is kept constant, increase the *G*6*P* production is induced by the increase of the upward glycolytic flux which can be produced via the regulation on $GAPD$ in our model. Interestingly, these regulations appear to be dose dependent. When regulation on $G6PD$ is needed as a first step in low doses to release the PPP and regulation on PGI as a second step in medium doses to compensate the first flux rerouting, regulation of $GAPD$ is efficient later in higher doses when the carbons are coming from the noxPPP favouring the possible cycling flux. Moreover, these three regulations appear to work in synergistic cooperation meaning that their effects are coupled allowing to contribute efficiently to diverse oxidative stress in large range of doses. These results provide a new understanding of the regulatory mechanism in large scope of oxidative stress contributing altogether to a flexible adaptation of the metabolic response. However, to fully understand the effect of regulations on the flux rerouting to favour the $NADPH$ production, systematic studies have to be made [154, 156].

The effect of metabolic regulation of the PPP and glycolysis during oxidative stress has also been investigated via the computation of the control coefficient during H_2O_2 production perturbation with MCA which is a common method to investigate metabolic pathways sensitivities [82]. A limit of the $NADPH$ control coefficient has been revealed preventing the high efficiency to maintain the $NADPH$ homeostasis and then to highly detoxify the stress. This limit depends on the $G6PD$ regulation and occurs for a specific set of net and directional PGI fluxes and without the regulation on PGI, which reveals a cooperation between the regulations on $G6PD$ and PGI. However, the interaction with $GAPD$ inhibition needs deeper investigations. Moreover, these theoretical results clearly need a validation with numerical simulation with the model ensemble. More control coefficients can also be computed during other flux rate perturbation to complete the analysis of how regulations operate and cooperate.

8.2 Flux rerouting during oxidative stress

The flux balance analysis allows to compute elementary modes of the PPP combined to the glycolysis and to identify three elementary modes. Two of them represent respectively production of cellular energy and biomass. The third corresponds to a carbon cycling allowing a very important $NADPH$ production going to 12 $NADPH$ molecules for 1 of glucose by reusing several times the same molecule [18]. The two other modes corresponding to the detoxification system of the catalase and the glutathiones are not considered

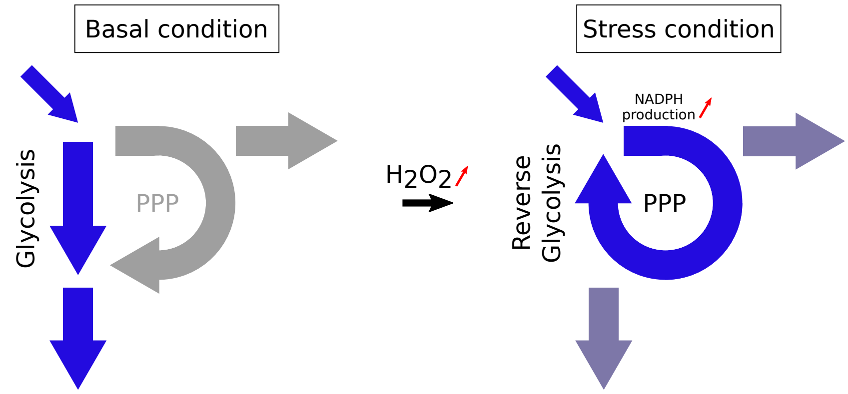

Figure 8.2: Flux rerouting during oxidative stress. Schematic representation of the flux state before stress (left side) and after stress (right side). Arrows represent the fluxes in blue color scale.

---

due to the lack of MID data in the detoxification system. A flux state is a combination of these modes. Even if the cycling mode is made for high oxidative stress detoxification, the estimated fluxes show a rerouting flux from a glycolytic mode for high energy production in basal state (i.e. without stress) to a PPP mode favouring high $NADPH$ production but still with a consequent production of cellular energy and biomass (Figure 8.2). This specific carbon resource reallocation can be understood by the need of energy to make happen the chemical reactions even during oxidative stress, and by the need to repair potential damages. This flux rerouting phenotype has also been observed in the dose response analysis where the flux state is rerouted from a glycolytic mode to a PPP mode with still a production of cellular energy and damage repairs. The maximum PPP flux observed is 1.5 times the incoming glucose flux corresponding to the production of 3 $NADPH$ per incoming glucose molecule which is far from the possible 12 with an 100% cycling mode. The maximum value of PPP flux during oxidative stress can vary but have never been observed approaching the maximum capacity of the metabolic network. An important amount of studies display a low increase of the oxPPP flux during oxidative stress with less than 1 times the entering flux such as in Christodoulou et al. 2018 [34] or Nikel et al. 2021 [158] which does not characterize a cycling flux. This low cycling flux phenotype could be understood because the output fluxes $GAPD$ and $PRPPs$ are not completely inhibited. However, a cycling flux mode can be observed more rarely such as in neonatal human skin fibroblasts with Kuehne et al. 2015 [17] or in neutrophils with Britt et al. 2022 [131] where the oxPPP flux reaches 2 times the entering glucose flux which is one of the highest value that has been observed.

One key characteristic of the coupling between PPP and glycolysis is the capability to make cycle the carbon resources inducing high $NADPH$ recycling. The regulations are necessary to reroute the flux in order to shift to the cycling mode. However, in most of the experimental data, the measure of the PPP flux rarely exceeds 2 times the incoming flux which is far from the possible 6 [17, 61, 131]. In the model ensemble built in this thesis, the PPP flux limit has been expressed mathematically showing a linear dependence of the $6PGD$ enzyme activity. Contrary to the modulation of the $G6PD$ enzyme activity, an ambivalent response of the $6PGD$ during enzyme activity modulation complements the problem of PPP flux saturation shown in dose responses curves. Increasing the $6PGD$ enzyme activity does not contribute to raise the barrier of the maximum value of 1.3 the incoming glucose flux. Moreover, strong down-regulation of $6PGD$ can also penalize this limit. It is only for a smaller level of $6PGD$ down-regulation that it contributes to raise the barrier of the maximum PPP flux allowing to increase the oxidative stress detoxification. $6PGD$ saturation combined to inhibition on PGI are responsible of these phenotypes. The effect of the $6PGD$ activity on the oxidative stress detoxification is highly experimentally studied in the recent past years due to contradicting results. Indeed, genetic or pharmacologic inhibition of $6PGD$ show either a reduced or an increased level of ROS during oxidative stress response in mammalian cells [25, 48, 145]. These contrasting phenotypes are agreement with the ambivalent effect of the results presented here. Even if the modification of the $G6PD$ enzyme activity has been major of interest [159, 160] showing more linear behaviours, these ambivalent results could favour the use of the $6PGD$ enzyme modulation in the defence against oxidative stress.

8.3 Adaptation dynamic during stress response

A coarse-grained model has been built as an preliminary study of the rapid oxidative stress response. Even if this model construction is not as rigorous as the detailed model, it already shows that the metabolic pathways composed of PPP and glycolysis are able to detoxify the stress by rerouting the flux made by the metabolic regulations. A phenotype of adaptation has been observed and corresponds to a transient overshoot of a variable followed by a relaxation to a steady state (Figure 8.3). Moreover, delaying the response

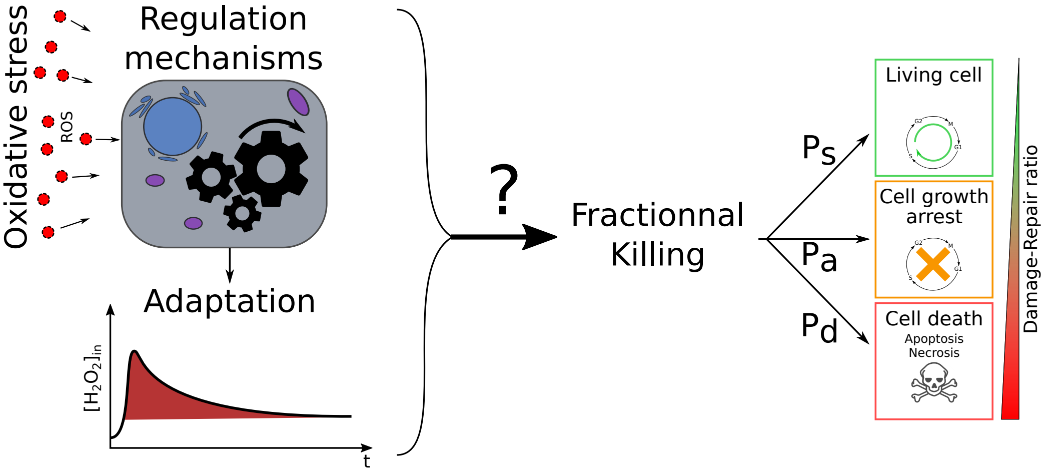

Figure 8.3: Oxidative stress could induce fractional killing. Oxidative stress response is made by the regulation of the metabolism. This regulatory mechanism displays adaptation in temporal dynamic of several molecules of the network (e.g. of intracellular H_2O_2). Adaptation phenotype impacts the probability to survive (P_s), to arrest the cellular growth (P_a) or to die (P_d) improving the fractional killing and the global survivability.

---

by increasing artificially the number of metabolites in the noxPPP increases the adaptation for a specific region of stress level. It confirms the well established compromise between fast reactions inducing excessive metabolic cost and slow reactions inducing potential damages. An adaptation phenotype as also been observed in the detailed model during the temporal dynamic response. Even if the adaptation ratio is not high, it already shows that the regulations play a role in the fast oxidative stress response. The adaptation phenotype has already been observed experimentally in the minute time scale in yeast cell during oxidative stress for instance in the study of Goulev et al. 2017 [61]. They performed different profiles of stress which impact the adaptation phenotype and therefore the cellular growth, or in general the cellular fate. They also build a highly reduced model representing an oxidative stress detoxification which also displays an adaptation phenotype with a ratio depending of the external dose. In our lab, Simiuc et al. 2020 [65] investigates the adaptative response of mammalian cell to a step of oxidative stress showing an adaptation ratio depending of dose but for longer response within a hour time scale. These experimental results confirm the presence of an adaptation profile and thus the role of the regulations during the oxidative stress response.

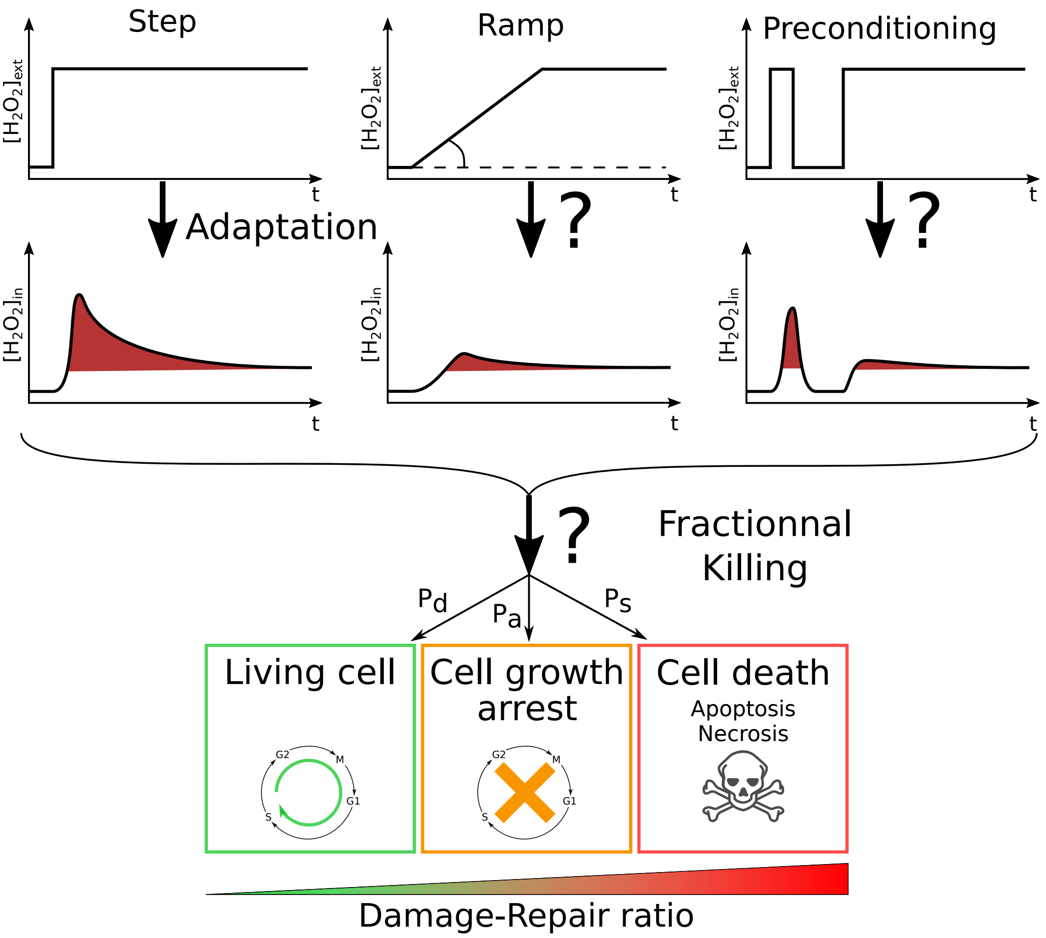

Figure 8.4: Impact of stress profile on adaptation phenotype. Several stress profile (e.g. external H_2O_2) could induce different adaptation phenotype (e.g. in intracellular H_2O_2) : an infinite step, a ramp and a preconditioning of an oxidative stress. Adaptation phenotype impacts the probability to survive (P_s), to arrest the cellular growth (P_a) or to die (P_d) improving the fractional killing and the global survivability.

The mathematical models presented here represent the early oxidative stress response in order to understand the effect of the regulations. A complementary study has been made to investigate the impact of an adaptative response to the cellular fate during a general perturbation. In this study, adaptation contributes to the fractional killing by flattening the death probability curve. Having a smoother curve of the death probability drastically reduces the probability for a population to have all their cells dead allowing the possibility of the population to recover. The adaptation profile inducing a fractional killing is produced during a general perturbation. The adaptation profile is also present during oxidative stress which allow to assume that the fractional killing could also be present. The cellular fate, more specifically the cellular growth during oxidative stress has been investigated in yeast with the study of Goulev et al. 2017 [61]. Even if the different dose or profile of oxidative stress modify the fractional killing and the adaptation profile, the link is not clearly established (Figure 8.4). However, there is no reason that the PPP and glycolysis do not display a fractional killing in order to favour the survivability during oxidative stress in mammalian cell. A combination of the model reproducing the fast oxidative stress response to a model of apoptosis initiation could be a solution to verify this statement. The different stress profiles, including a pre-treatment of the cells have been investigated in Goulev et al. [61] showing an impact on the adaptation profile and cellular growth, and could also be simulated with the detailed model allowing to investigate the direct impact on the adaptation and thus the fractional killing. Other metabolic stress in complement also seem to modify the adaptation profile such as, for instance during a perturbation of glucose income with an oxidative in Simiuc et al. 2020 [65] which can be simply simulated in the presented detailed model by modifying Φ_{GLU}. Deeper investigation need to be done to fully establish the effect of the dual perturbation and therefore the importance of the glucose import in the defence against oxidative stress and then in the fractional killing.

8.4 Data-driven modeling and 13C-MFA

The construction of the mathematical model follows a specific procedure in order to reproduce experimental data (Figure 8.1). First, decisions have been made in term of model structures to favour identifiability of the parameters creating possible biases when leaving aside large-scale metabolic pathway of for instance ATP, NAD, $NADP$ or glutathiones. Because PPP and glycolysis are the metabolic pathways which seem to be highly regulated in order to favour the most the oxidative stress response, only these pathways have been used. However, other linked metabolic pathways seem to also contribute to the oxidative stress response such as with PK and TPI enzymes regulations [37, 53]. Glutathiones have been taken as anti-oxidant network because experimental data was available but others such as Peroxiredoxins/Thioredoxins also contribute [61, 161, 162]. Moreover, the chosen regulations appear to be the most contributors [17, 18, 34, 36]. However, it exists regulations that can also participate to flux rerouting such as the inhibition of TPI [52] or PFK [125]. Moreover, $AMPK$ is a regulator of many metabolic processes and would also be regulated by PPP metabolites [163]. The balance between realism and complexity of a model is often a difficult problem. Although many studies favour a highly realistic and complex models [126, 164], others favour less complex models in order to focus on the analysis of the network regulations [34]. More mechanisms could be implemented in the model step-by-step but it would need much more iterations during the optimisation or more efficient techniques.

Before going through the parameter estimation, experimental data of MIDs have been converted into flux data in order to have usable targets. A different class of method that simulates isotope propagation in metabolic systems by a Stochastic Simulation Algorithm (SSA) has been presented [1] in order to convert ^{13}C labeling data into flux data without any assumptions about restrictions. Current methods such as EMU decompositions, allow to proceed to complex metabolic flux analysis (MFA) such as non-stationary MFA but it does not exist highly efficient software to proceed to dynamic MFA [123]. However, the new proposed method allows to compute complex metabolic flux analysis (MFA) such as non-stationary MFA or dynamic MFA. It is simple to implement and has low computational cost compared to classic methods. In the context of this thesis, this new method has been used in ^{13}C-MFA to estimate fluxes from labeling data in steady state conditions. Then, it has the advantage to have a small computational time which poorly depends on the length of the marking procedure and thus of the number of isotopomers contrary to cumomers or EMU decompositions [115]. Moreover, it is also efficient even when parallel labeling are used such as hydrogen or oxygen labeling in complement of carbon labeling. Finally, contrary to most of the used methods, this one has no tinkering or approximations necessary to be implemented. The only point that can be tricky would be the choice of the sample size Ω which would increase the computational cost which scales directly with Ω. A large value reduces the noise fluctuations but increases the simulation time and reversely. Our chosen sample size is typically around 100-1000 which allows to have a good compromise between uncertainties and computational efficiency. In these conditions, error scores have narrow distributions with induced residual fluctuations of isotopomers which allows the use of Monte Carlo Markov chain [96, 165, 166, 167]. However, the estimated fluxes display rather diverse widths of distributions where 11 fluxes have large confidence interval preventing their further use in the parameter estimation. Next, data correspond to 3 mass isotopomer distribution (MID) per metabolite per experiment with 7 metabolites and 4 total different experiments which makes 84 individual MIDs in both basal and stress states which is a relatively high number of data in different conditions [17]. However, each experiment has been made in triplicate and displays large experimental errors which prevents the possibility to have accurate flux estimation. More MIDs in more accurate measurements would refine the flux estimation. Taking more data from diverse cell types or with different protocols could generalize the results but could also drastically increase the simulation time and difficulty of the estimation.

The parameter set of the detailed model has been estimated in order to reproduce experimental data of fast oxidative stress response coming from neonatal human skin fibroblasts [17]. The data-driven estimation is proceeded by optimisation algorithm such as MCMC or genetic algorithm. As the model is complex comprising a large number of parameters, the parameter space is large which drastically complicates the model optimisation [96]. Thus, instead of keeping one parameter set, a distribution of parameter sets is estimated in a restricted area of the parameter space which is often assumed in other studies [34] and which takes into account the experimental errors. Although many studies with a large amount of data do not have sub-minute resolution [17, 34], more experimental data or more precise measurement would refine the distributions and the model ensemble phenotypes. Further comparisons of temporal dynamics or dose responses reveal that the model ensemble well reproduce the experimental dynamics. However, these data could also be used in the model optimisation to take into account the dynamics directly in the parameter distribution but it would remove possible confirmations. Finally, experimental data coming from various type of cells or with different stress profile and source would again generalise the model, for instance, by integrating the data in keratinocyte from Kuehne et al. 2015 [17], or in bacteria from Christodoulou et al. 2018 [34] or others from Christodoulou et al. 2019 [168].

8.5 Experimental validation

The last six months of my thesis were devoted to the development of an experimental device aiming to check the surprising theoretical prediction about the ambivalent response during perturbation of 6PGD enzyme activity (Figure 8.5). A specific protocol has been built to allow the detection of the

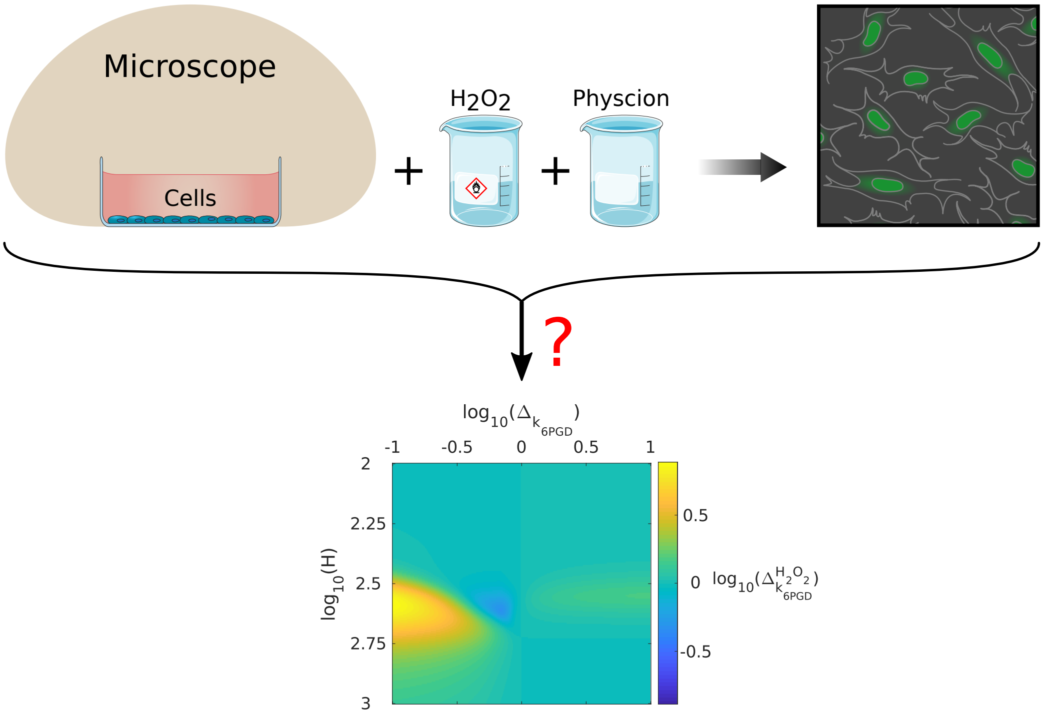

Figure 8.5: Experimental procedure for testing model predictions. Cultured cells can be put under microscope. The internal level of the redox state could be captured by using fluorescence. Oxidative stress can be applied by adding H_2O_2. Down-regulation of the $6PGD$ enzyme activity can be done by the specific inhibitor physcion.

---

redox state in mammalian cell via fluorescence-microscopy imagery [65]. In this study, MCF7 cancer cell line has been used but other similar cell lines could also work. They are cultured via a classic protocol, i.e. in supplemented DMEM medium at $37°C$ in a humidified atmosphere with 5% CO_2 without extreme confluence to avoid possible additional stress. In these culture conditions, cells are in good environment to actively grow. Then, to be able to localize the cells under fluorescence imagery and to avoid possible mycoplasma contamination, they are marked by nuclear dye Hoechst which ensure to not collect data from other sources. Green fluorescence protein sensitive to redox state ($roGFP2$) can be linked to anti-oxidant enzyme allowing to measure the redox state under microscope [169]. This fluorescent protein is often linked to glutaredoxin (GRx) enzyme due to its ability to sense the redox state [170]. It has been shown that $GRx - roGFP2$ fusion protein is a good probe to capture the dynamic of the glutathione redox potential in cells with high sensitivity [171]. As $roGFP2$ can be excited with two different wavelengths characterizing either the reduced or the oxidized state of the molecule, the redox state will be the ratio of the two channels [169].

The aim will be to capture the fluorescence in cells under different oxidative stress levels and $6PGD$ enzyme activities. To apply an oxidative stress, H_2O_2 is directly added to the medium at different concentrations. The modification of the $6PGD$ enzyme activity can be made by the specific inhibitor physcion [163, 172, 173]. In these conditions, the space of stress level and enzyme activity which has been investigated in numerical simulation, could be scan and reproduced. The internal redox state can then be measured after 5 min of the perturbation application in order to be consistent with the result of the simulations. Moreover, the simulations are made with a large number of parameter sets which could mimic the cell-to-cell variability. As the results of the model ensemble are averaged, the single-cell measurement of the redox state is not necessary but can refine the measures and decrease the experimental uncertainties. In the same idea, the more cells there are, the more precise the information will be, provided that they grow in good conditions, i.e. without extreme confluence. This work is still in progress and would reveal a possibility to favour or penalise the oxidative stress response by modulating $6PGD$ enzyme activity. In the proposed protocol, hydrogen peroxide and physcion are added directly in the medium which could influence local concentration. As the diffusion is not instantaneous, the local concentration could be different and increase the response noise along the plate during measurements. In addition of this protocol, a microfluidic device could be used which would serve to control the environment in a specific condition by continuously sending fresh medium in the entire cell plate [61, 174, 175].

Abbreviations

1-9

6PG : 6-phosphogluconate
6PGD : 6-phosphogluconate dehydrogenase
6PGL : 6-phosphoglucono-δ-lactone
^{13}**C-DMFA :** Dynamic ^{13}C-MFA
^{13}**C-inst/NMFA :** Non-stationary ^{13}C-MFA
^{13}**C-MFA :** ^{13}C-based MFA

A

ALD : Fructose-bisphosphate aldolase
AMPK : 5' AMP-activated protein kinase
AR : Adaptation ratio
ATP : Adenosine triphosphate

B

BAX : Bcl-2–associated X
BAXm : mitochondrial BAX
Bcl-2 : B-cell lymphoma 2
BH3 : Bcl-2 homology (BH) 3

C

Cat : Catalase
CI : Confidence interval
CME : Chemical master equation

D

DHAP : Dihydroxyacetone phosphate

E
E4P : Erythrose 4-phosphate
EMU : Elementary Metabolic Units

F
F26BP : Fructose 2,6-bisphosphate
F6P : Fructose 6-phosphate
FBA : Flux balance analysis
FBP : Fructose 1,6-bisphosphate
FBPase : Fructose 1,6-bisphosphatase
FBPase2 : Fructose bisphosphatase-2
FOA : Fatty Acid Oxidation

G
G6P : Glucose 6-phosphate
G6PD : Glucose 6-phosphate dehydrogenase
GA : Genetic algorithm
GAP : Glyceraldehyde 3-phosphate
GAPD : Glyceraldehyde-3-phosphate dehydrogenase
GLase : 6-phosphogluconolactonase
Glc : Glucose
GPx : Glutathion peroxydase
GR : Glutaredoxins
GSH/GSSG : Reduced/Oxidized glutathiones

H
$\mathbf{H_2O_2}$: Hydrogen peroxide
HK : Hexokinase

I
Isotopomers : Isotope isomers

M
MCA : Metabolic control analysis
MCMC : Monte Carlo Markov Chain
MID : Mass isotopomer distribution
MFA : Metabolic flux analysis

N

NADP(+/H) : Reduced/Oxidized nicotinamide adenine dinucleotide phosphate
NNH/NHN : effective NADPH consumption/production
Nrf2 : Nuclear factor erythroid-derived 2-related factor 2
nRMSE : normalized RMSE

O

ODE : Ordinary differential equations
ox/noxPPP : Oxidative/non-oxidative PPP

P

PFK : Phosphofructokinase-1
PFK2 : Phosphofructokinase-2
PGI : Glucose-6-phosphate isomerase
PGK : phosphoglycerate kinase
PK : pyruvate kinase
PPP : Pentoses Phosphates Pathway
PRPP : Phosphoribosylpyrophosphate
PRPPs : Phosphoribosyl Pyrophosphate synthetase
PRX : Thioredoxins

R

R5P : Ribose 5-phosphate
RMSE : Root mean square error
roGFP2 : Green fluorescence protein sensitive to redox state
ROS : Reactive oxygen species
RPE : Ribulose 5-Phosphate 3-Epimerase
RPI : Ribose-5-phosphate isomerase
Ru5P : Ribulose 5-phosphate

S

S7P : Sedoheptulose 7-phosphate
SSA : Stochastic stimulation algorithm

T

TKT1/2 : Transketolase 1/2
TLD : Transaldolase
TNF : Tumor Necrosis Factor
TPI : Triosephosphate isomerase
TRX : Peroxiredoxins

X

X5P : Xylulose 5-phosphate

Mathematical symbols

All mathematical elements used in the thesis are grouped in these tables with their corresponding first definition in an equation or a chapter.

Modeling tools

	Notation	Signification	Equation	Chapter
Oxidative Stress	H	External hydrogen peroxide		3/5.2.2
	$[H_2O_2]^{max}$	Maximal value of hydrogen peroxide concentration	3.18	
	$[H_2O_2]^*$	Hydrogen peroxide concentration at steady state	3.18	
	AR	Adaptation Ratio	3.18	
Reversible Reaction	S	Substrate / Reactant	2.2	
	P	Product	2.2	
	I	Inhibitor	2.11	
	a / b	Stoichiometric number, order in mass action law	2.2	
ODE	x	Variable concentration	2.1	
	X	Variable concentration at steady state	2.14	
	R	Variable concentration ratio between basal and stress condition in log scale	5.1	

	Notation	Signification	Equation	Chapter
ODE	ΔR	Experimental error of R	5.1	
	$\mathbf{N}$	Stoichiometric matrix	2.1	
	ϕ_{ENZ}	Flux rate of a specific enzyme	2.1	
	Φ_{ENZ} / J	Flux rate at steady state	2.14 / 2.2.2	
	$\phi_{ENZ}^{+/-}$	Directional flux rate	2.3	
	$\Delta\Phi$	Experimental error of a flux rate at steady state	5.1	
	Y	Variable concentration or flux rate at steady state	6.1	
	p	Parameter of the mathematical model	2.1	
	$\mathcal{P}$	Parameter space		5.2.2
	$\mathcal{P}^*$	Optimal parameter sets / Model ensemble		5.2.2
	k_{ENZ}	Kinetic parameter	2.2	
	Keq_{ENZ}	Equilibrium constant	2.4/2.5	
	Km_{ENZ}	Michaelis-Menten / Saturation parameter	2.8	
	Ki_{ENZ}	Inhibition parameter	2.11	
GA / MCMC	$\mathcal{N}$	Number of fitted data	2.26/5.1	
	ξ	Score function value		2.4.1
	N_f	Family size		2.4.1
	α	Acceptation probability		2.4.2
	$\mathcal{V}$	Variance of α		2.4.2
	R^2	Determination coefficient		5.2.2
Gain/loss function	Δ_{pi}^{Y}	Sensitivity coefficient		6.1

	Notation	Signification	Equation	Chapter
	$SF_{i,j}$	Synergy factor	6.5	

Steady state analysis tools

	Notation	Signification	Equation	Chapter
FBA	$\vec{V}_i$	Elementary mode vector	2.17	
	$\vec{V}_i^n$	Normalised elementary mode vector	4.19	
	λ_i	Decomposition parameter	2.17	
MCA	$C_\Phi^{X/J}$	Control coefficient	2.18	
	ϵ_J^X	Elasticities	2.20	
	R_p^X	Response coefficient	2.22	
	$\vec{\Pi}_\Phi$	Unitary vector in the direction of Φ	2.20	

Stochastic simulation algorithms tools

	Notation	Signification	Equation	Chapter
CME	P	Probability	2.23	
	η	Propensities	2.23	
	ζ	Gaussian white noises	2.24	
	$\delta_{j,j'}$	Dirac delta function	2.24	
SSA	q	Number of labeled atom		4.3.2
	N	Total number of isotopomer		4.3.2
	M	Number of species		4.3.2

	Notation	Signification	Equation	Chapter
SSA	m^{tot}	Number of entities for a specific species		4.3.2
	ω	Metabolomic state		4.3.2
	Ω	Volume / Scaling factor		4.3.2
	ρ	Probability to be in a state ω		4.3.2
	I	Isotopomer index		4.3.2
	L_i^j	Labeling state		4.3.2
	c	Carbon atom		4.3.2
	σ	Addressing operator	4.26-4.31	
	$m_{i,j}^k = m + i$	Mass isotopomer distribution		2.5/4.3.2
	τ	Time interval		4.3.2

Fractional killing tools

	Notation	Signification	Equation	Chapter
Fractional Killing	S	General stress profile		7.2
	s	Amplitude of the stress		7.2
	s_{50}	Stress value for $P_{Death} = 50\%$		7.2
	P_{Death}	death probability		7.2
	β	Adaptation amplitude		7.2

Bibliography

[1] Q. Thommen, J. Hurbain, and B. Pfeuty, "Stochastic simulation algorithm for isotope-based dynamic flux analysis," *Metab. Eng.*, vol. 75, pp. 100–109, 2022.

[2] J. Hurbain, D. Labavić, Q. Thommen, and B. Pfeuty, "Theoretical study of the impact of adaptation on cell-fate heterogeneity and fractional killing," *Sci. Rep.*, vol. 10, no. 1, pp. 1–13, 2020.

[3] J. Hurbain, Q. Thommen, F. Anquez, and B. Pfeuty, "Quantitative modeling of pentose phosphate pathway response to oxidative stress reveals a cooperative regulatory strategy," *iScience*, vol. 25, no. 8, p. 2022.02.04.478659, 2022.

[4] C. Migdal and M. Serres, "Espèces réactives de l'oxygène et stress oxydant," *Médecine/Sciences*, vol. 27, no. 4, pp. 405–412, 2011.

[5] J. Navarro-Yepes, L. Zavala-Flores, A. Anandhan, F. Wang, M. Skotak, N. Chandra, M. Li, A. Pappa, D. Martinez-Fong, L. M. Del Razo, B. Quintanilla-Vega, and R. Franco, "Antioxidant gene therapy against neuronal cell death," *Pharmacol. Ther.*, vol. 142, no. 2, pp. 206–230, 2014.

[6] M. Valko, D. Leibfritz, J. Moncol, M. T. Cronin, M. Mazur, and J. Telser, "Free radicals and antioxidants in normal physiological functions and human disease," *Int. J. Biochem. Cell Biol.*, vol. 39, no. 1, pp. 44–84, 2007.

[7] B. Halliwell, "Oxidative stress and cancer: Have we moved forward?," *Biochem. J.*, vol. 401, no. 1, pp. 1–11, 2007.

[8] G. Pizzino, N. Irrera, M. Cucinotta, G. Pallio, F. Mannino, V. Arcoraci, F. Squadrito, D. Altavilla, and A. Bitto, "Oxidative Stress: Harms and Benefits for Human Health," *Oxid. Med. Cell. Longev.*, vol. 2017, 2017.

[9] K. Bedard and K. H. Krause, “The NOX family of ROS-generating NADPH oxidases: Physiology and pathophysiology,” *Physiol. Rev.*, vol. 87, no. 1, pp. 245–313, 2007.

[10] W. Droge, “Free radicals in the physiological control of cell function,” *Physiol. Rev.*, vol. 82, no. 1, pp. 47–95, 2002.

[11] E. B. Kurutas, “The importance of antioxidants which play the role in cellular response against oxidative/nitrosative stress: Current state,” *Nutr. J.*, vol. 15, no. 1, pp. 1–22, 2016.

[12] L. S. Capella, M. R. Gefé, E. F. Silva, O. Affonso-Mitidieri, A. G. Lopes, V. M. Rumjanek, and M. A. Capella, “Mechanisms of vanadate-induced cellular toxicity: Role of cellular glutathione and NADPH,” *Arch. Biochem. Biophys.*, vol. 406, no. 1, pp. 65–72, 2002.

[13] X. Ren, L. Zou, X. Zhang, V. Branco, J. Wang, C. Carvalho, A. Holmgren, and J. Lu, “Redox Signaling Mediated by Thioredoxin and Glutathione Systems in the Central Nervous System,” *Antioxidants Redox Signal.*, vol. 27, no. 13, pp. 989–1010, 2017.

[14] H. Q. Ju, J. F. Lin, T. Tian, D. Xie, and R. H. Xu, “NADPH homeostasis in cancer: functions, mechanisms and therapeutic implications,” *Signal Transduct. Target. Ther.*, vol. 5, no. 1, pp. 1–12, 2020.

[15] J. Fan, J. Ye, J. J. Kamphorst, T. Shlomi, C. B. Thompson, and J. D. Rabinowitz, “Quantitative flux analysis reveals folate-dependent NADPH production,” *Nature*, vol. 510, no. 7504, pp. 298–302, 2014.

[16] L. Chen, Z. Zhang, A. Hoshino, H. D. Zheng, M. Morley, Z. Arany, and J. D. Rabinowitz, “NADPH production by the oxidative pentose-phosphate pathway supports folate metabolism,” *Nat. Metab.*, vol. 1, no. March, 2019.

[17] A. Kuehne, H. Emmert, J. Soehle, M. Winnefeld, F. Fischer, H. Wenck, S. Gallinat, L. Terstegen, R. Lucius, J. Hildebrand, and N. Zamboni, “Acute Activation of Oxidative Pentose Phosphate Pathway as First-Line Response to Oxidative Stress in Human Skin Cells,” *Mol. Cell*, vol. 59, no. 3, pp. 359–371, 2015.

[18] T. P. Dick and M. Ralser, “Metabolic Remodeling in Times of Stress: Who Shoots Faster than His Shadow?,” *Mol. Cell*, vol. 59, no. 4, pp. 519–521, 2015.

[19] E. Mullarky and L. C. Cantley, “Diverting Glycolysis to Combat Oxidative Stress,” in *Innov. Med.*, pp. 3–23, Springer Japan, 2015.

[20] T. McKee and J. R. McKee, “Biochemistry: The molecular basis of life.,” in *Oxford Oxford Univ. Press.*, vol. 234, pp. 205–206, 2012.

[21] S. M. Jeon, N. S. Chandel, and N. Hay, “AMPK regulates NADPH homeostasis to promote tumour cell survival during energy stress,” *Nature*, vol. 485, no. 7400, pp. 661–665, 2012.

[22] H. Q. Ju, Y. X. Lu, Q. N. Wu, J. Liu, Z. L. Zeng, H. Y. Mo, Y. Chen, T. Tian, Y. Wang, T. B. Kang, D. Xie, M. S. Zeng, P. Huang, and R. H. Xu, “Disrupting G6PD-mediated Redox homeostasis enhances chemosensitivity in colorectal cancer,” *Oncogene*, vol. 36, no. 45, pp. 6282–6292, 2017.

[23] L. Ma and Q. Cheng, “Inhibiting 6-phosphogluconate dehydrogenase reverses doxorubicin resistance in anaplastic thyroid cancer via inhibiting NADPH-dependent metabolic reprogramming,” *Biochem. Biophys. Res. Commun.*, vol. 498, no. 4, pp. 912–917, 2018.

[24] K. C. Patra and N. Hay, “The pentose phosphate pathway and cancer,” *Trends Biochem. Sci.*, vol. 39, no. 8, pp. 347–354, 2014.

[25] R. Liu, W. Li, B. Tao, X. Wang, Z. Yang, Y. Zhang, C. Wang, R. Liu, H. Gao, J. Liang, and W. Yang, “Tyrosine phosphorylation activates 6-phosphogluconate dehydrogenase and promotes tumor growth and radiation resistance,” *Nat. Commun.*, vol. 10, no. 1, pp. 1–14, 2019.

[26] L. G. Boros and G. K. Haines, “Oxythiamine and dehydroepiandrosterone inhibit the nonoxidative synthesis of ribose and tumor cell proliferation,” *Cancer Res.*, vol. 58, no. 14, p. 3188, 1997.

[27] P. Vizán, G. Alcarraz-Vizán, S. Díaz-Moralli, O. N. Solovjeva, W. M. Frederiks, and M. Cascante, “Modulation of pentose phosphate pathway during cell cycle progression in human colon adenocarcinoma cell line HT29,” *Int. J. Cancer*, vol. 124, no. 12, pp. 2789–2796, 2009.

[28] I. M. J. Xu, R. K. H. Lai, S. H. Lin, A. P. W. Tse, D. K. C. Chiu, H. Y. Koh, C. T. Law, C. M. Wong, Z. Cai, C. C. L. Wong, and I. O. L. Ng, “Transketolase counteracts oxidative stress to drive cancer development,” *Proc. Natl. Acad. Sci. U. S. A.*, vol. 113, pp. E725–E734, feb 2016.

[29] S. A. Mookerjee, A. A. Gerencser, D. G. Nicholls, and M. D. Brand, "Quantifying intracellular rates of glycolytic and oxidative ATP production and consumption using extracellular flux measurements," *J. Biol. Chem.*, vol. 292, no. 17, pp. 7189–7207, 2017.

[30] C. B. Scott, "Quantifying the Immediate Recovery Energy Expenditure of Resistance Training," vol. 25, no. 4, pp. 1159–1163, 2011.

[31] B. C. Mulukutla, A. Yongky, S. Grimm, P. Daoutidis, and W. S. Hu, "Multiplicity of steady states in glycolysis and shift of metabolic state in cultured mammalian cells," *PLoS One*, vol. 10, mar 2015.

[32] A. A. Shestov, X. Liu, Z. Ser, A. A. Cluntun, Y. P. Hung, L. Huang, D. Kim, A. Le, G. Yellen, J. G. Albeck, and J. W. Locasale, "Quantitative determinants of aerobic glycolysis identify flux through the enzyme GAPDH as a limiting step," pp. 1–18, 2014.

[33] J. M. Lemons, H. A. Coller, X. J. Feng, B. D. Bennett, A. Legesse-Miller, E. L. Johnson, I. Raitman, E. A. Pollina, H. A. Rabitz, and J. D. Rabinowitz, "Quiescent fibroblasts exhibit high metabolic activity," *PLoS Biol.*, vol. 8, no. 10, 2010.

[34] D. Christodoulou, H. Link, T. Fuhrer, K. Kochanowski, L. Gerosa, and U. Sauer, "Reserve Flux Capacity in the Pentose Phosphate Pathway Enables Escherichia coli's Rapid Response to Oxidative Stress," *Cell Syst.*, vol. 6, no. 5, pp. 569–578.e7, 2018.

[35] M. Ralser, M. M. Wamelink, A. Kowald, B. Gerisch, G. Heeren, E. A. Struys, E. Klipp, C. Jakobs, M. Breitenbach, H. Lehrach, and S. Krobitsch, "Dynamic rerouting of the carbohydrate flux is key to counteracting oxidative stress," *J. Biol.*, vol. 6, no. 4, 2007.

[36] D. Peralta, A. K. Bronowska, B. Morgan, É. Dóka, K. Van Laer, P. Nagy, F. Gräter, and T. P. Dick, "A proton relay enhances H2O2 sensitivity of GAPDH to facilitate metabolic adaptation," *Nat. Chem. Biol.*, vol. 11, pp. 156–163, feb 2015.

[37] D. Anastasiou, G. Poulogiannis, J. M. Asara, M. B. Boxer, J.-k. Jiang, M. Shen, G. Bellinger, A. T. Sasaki, J. W. Locasale, D. S. Auld, C. J. Thomas, M. G. V. Heiden, and C. Lewis, "Contributes To Cellular Antioxidant Responses," *Science (80-.).*, vol. 334, no. 6060, pp. 1278–1283, 2012.

[38] O. Warburg, “The metabolism of carcinoma cells 1,” *J. Cancer Res.*, vol. 9, no. 1, pp. 148–163, 1925.

[39] H. G. Crabtree, “Observations on the carbohydrate metabolism of tumours,” *Biochem. J.*, vol. 23, no. 3, pp. 536–545, 1929.

[40] M. V. Liberti and J. W. Locasale, “The Warburg Effect: How Does it Benefit Cancer Cells?,” *Trends Biochem. Sci.*, vol. 41, no. 3, p. 211, 2016.

[41] M. Basan, S. Hui, H. Okano, Z. Zhang, Y. Shen, J. R. Williamson, and T. Hwa, “Overflow metabolism in Escherichia coli results from efficient proteome allocation,” *Nature*, vol. 528, no. 7580, pp. 99–104, 2015.

[42] R. Tian, C. Yang, S. M. Chai, H. Guo, I. Seim, and G. Yang, “Evolutionary impacts of purine metabolism genes on mammalian oxidative stress adaptation,” *Zool. Res.*, vol. 43, no. 2, pp. 241–254, 2022.

[43] A. M. Pedley and S. J. Benkoic, “A New View into the Regulation of Purine Metabolism – The Purinosome,” *Physiol. Behav.*, vol. 176, no. 1, pp. 139–148, 2016.

[44] O. Warburg and W. Christian, “Pyridin, der wasserstoffubertragende Bestandteil von Garungsfermenten,” *1936*.

[45] A. Yoshida and M. Lin, “Dehydrogenase Hemolytic Subjects,” vol. 41, no. 6, pp. 877–891, 1973.

[46] J. Van Der Reest, S. Lilla, L. Zheng, S. Zanivan, and E. Gottlieb, “Proteome-wide analysis of cysteine oxidation reveals metabolic sensitivity to redox stress,” *Nat. Commun.*, vol. 9, no. 1, 2018.

[47] M. K. Gaitonde, E. Murray, and V. J. Cunningham, “Effect of 6-Phosphogluconate on Phosphoglucose Isomerase in Rat Brain In Vitro and In Vivo,” *J. Neurochem.*, vol. 52, no. 5, pp. 1348–1352, 1989.

[48] M. M. Dubreuil, D. W. Morgens, K. Okumoto, M. Honsho, K. Contrepois, B. Lee-McMullen, G. M. A. Traber, R. S. Sood, S. J. Dixon, M. P. Snyder, Y. Fujiki, and M. C. Bassik, “Systematic Identification of Regulators of Oxidative Stress Reveals Non-canonical Roles for Peroxisomal Import and the Pentose Phosphate Pathway,” *Cell Rep.*, vol. 30, no. 5, pp. 1417–1433.e7, 2020.

[49] J. Boada, T. Roig, X. Perez, A. Gamez, R. Bartrons, M. Cascante, and J. Bermúdez, "Cells overexpressing fructose-2,6-bisphosphatase showed enhanced pentose phosphate pathway flux and resistance to oxidative stress," *FEBS Lett.*, vol. 480, no. 2-3, pp. 261–264, 2000.

[50] D. A. Okar, A. J. Lange, À. Manzano, A. Navarro-Sabatè, L. Riera, and R. Bartrons, "PFK-2/FBPase-2: Maker and breaker of the essential biofactor fructose-2,6-bisphosphate," *Trends Biochem. Sci.*, vol. 26, no. 1, pp. 30–35, 2001.

[51] C. M. Jenkins, J. Yang, H. F. Sims, and R. W. Gross, "Reversible high affinity inhibition of phosphofructokinase-1 by Acyl-CoA: A mechanism integrating glycolytic flux with lipid metabolism," *J. Biol. Chem.*, vol. 286, no. 14, pp. 11937–11950, 2011.

[52] N. M. Grüning, M. Rinnerthaler, K. Bluemlein, M. Mülleder, M. M. Wamelink, H. Lehrach, C. Jakobs, M. Breitenbach, and M. Ralser, "Pyruvate kinase triggers a metabolic feedback loop that controls redox metabolism in respiring cells," *Cell Metab.*, vol. 14, no. 3, pp. 415–427, 2011.

[53] N. M. Grüning, D. Du, M. A. Keller, B. F. Luisi, and M. Ralser, "Inhibition of triosephosphate isomerase by phosphoenolpyruvate in the feedback-regulation of glycolysis," *Open Biol.*, vol. 4, no. MARCH, 2014.

[54] X. Liu, C. S. Kim, F. T. Kurbanov, R. B. Honzatko, and H. J. Fromm, "Dual mechanisms for glucose 6-phosphate inhibition of human brain hexokinase," *J. Biol. Chem.*, vol. 274, no. 44, pp. 31155–31159, 1999.

[55] P. A. Hyslop and M. O. Chaney, "Mechanism of GAPDH Redox Signaling by H2O2 Activation of a TwoCysteine Switch," *Int. J. Mol. Sci.*, vol. 23, no. 9, 2022.

[56] C. Tonelli, I. I. C. Chio, and D. A. Tuveson, "Transcriptional Regulation by Nrf2," *Antioxidants Redox Signal.*, vol. 29, no. 17, pp. 1727–1745, 2018.

[57] J. D. Hayes and A. T. Dinkova-Kostova, "The Nrf2 regulatory network provides an interface between redox and intermediary metabolism," 2014.

[58] A. J. Levine and A. M. Puzio-Kuter, “The control of the metabolic switch in cancers by oncogenes and tumor suppressor genes,” *Science (80-.).*, vol. 330, no. 6009, pp. 1340–1344, 2010.

[59] D. A. Franklin, Y. He, P. L. Leslie, A. P. Tikunov, N. Fenger, J. M. MacDonald, and Y. Zhang, “P53 coordinates DNA repair with nucleotide synthesis by suppressing PFKFB3 expression and promoting the pentose phosphate pathway,” *Sci. Rep.*, vol. 6, no. March, pp. 1–13, 2016.

[60] C. R. Berkers, O. D. Maddocks, E. C. Cheung, I. Mor, and K. H. Vousden, “Metabolic regulation by p53 family members,” *Cell Metab.*, vol. 18, no. 5, pp. 617–633, 2013.

[61] Y. Goulev, S. Morlot, A. Matifas, B. Huang, M. Molin, M. B. Toledano, and G. Charvin, “Nonlinear feedback drives homeostatic plasticity in H2O2 stress response,” *Elife*, vol. 6, pp. 1–33, 2017.

[62] C. Briat, A. Gupta, and M. Khammash, “Antithetic Integral Feedback Ensures Robust Perfect Adaptation in Noisy Bimolecular Networks,” *Cell Syst.*, vol. 2, no. 1, pp. 15–26, 2016.

[63] S. K. Aoki, G. Lillacci, A. Gupta, A. Baumschlager, D. Schweingruber, and M. Khammash, “A universal biomolecular integral feedback controller for robust perfect adaptation,” *Nature*, vol. 570, no. 7762, pp. 533–537, 2019.

[64] J. E. Ferrell, “Perfect and near-perfect adaptation in cell signaling,” *Cell Syst.*, vol. 2, no. 2, pp. 62–67, 2016.

[65] D. Simiuc, F. Dahmani, A. Pruvost, M. Guilbert, M. Brulé, C. Lagadec, Q. Thommen, B. Pfeuty, E. Courtade, and F. Anquez, “Measuring adaptation dynamics to hydrogen peroxide in single human cells using fluorescent reporters,” *bioRxiv*, p. 2020.11.14.382911, 2020.

[66] C. J. Foster, L. Wang, H. V. Dinh, P. F. Suthers, and C. D. Maranas, “Building kinetic models for metabolic engineering,” *Curr. Opin. Biotechnol.*, vol. 67, pp. 35–41, 2021.

[67] E. O. Voit, “The Best Models of Metabolism,” *Wiley Interdiscip Rev Syst Biol Med*, vol. 9, no. 6, pp. 1–38, 2017.

[68] B. Ingalls, *Mathematical Modelling in Systems Biology: An Introduction.* 2012.

[69] W. Liebermeister, J. Uhlendorf, and E. Klipp, "Modular rate laws for enzymatic reactions: Thermodynamics, elasticities and implementation," *Bioinformatics*, vol. 26, no. 12, pp. 1528–1534, 2010.

[70] X. Li, F. Wu, F. Qi, and D. A. Beard, "A database of thermodynamic properties of the reactions of glycolysis, the tricarboxylic acid cycle, and the pentose phosphate pathway," *Database*, vol. 2011, pp. 1–15, 2011.

[71] J. M. Rohwer, A. J. Hanekom, C. Crous, J. L. Snoep, and J. H. Hofmeyr, "Evaluation of a simplified generic bi-substrate rate equation for computational systems biology," *IEE Proc. Syst. Biol.*, vol. 153, no. 5, pp. 338–341, 2006.

[72] E. Klipp, W. Liebermeister, C. Wierling, and A. Kowald, *Systems Biology.*

[73] A. Varma and B. O. Palsson, "Metabolic Flux Balancing," *Biotechnol. J.*, pp. 1248–1248, 1994.

[74] M. W. Covert, C. H. Schilling, I. Famili, J. S. Edwards, I. I. Goryanin, E. Selkov, and B. O. Palsson, "Metabolic modeling of microbial strains in silico," *Trends Biochem. Sci.*, vol. 26, no. 3, pp. 179–186, 2001.

[75] K. J. Kauffman, P. Prakash, and J. S. Edwards, "Advances in flux balance analysis," *Curr. Opin. Biotechnol.*, vol. 14, no. 5, pp. 491–496, 2003.

[76] E. Murabito, E. Simeonidis, K. Smallbone, and J. Swinton, "Capturing the essence of a metabolic network: A flux balance analysis approach," *J. Theor. Biol.*, vol. 260, no. 3, pp. 445–452, 2009.

[77] R. Schuetz, N. Zamboni, M. Zampieri, M. Heinemann, and U. Sauer, "Multidimensional optimality of microbial metabolism," *Science (80-.).*, vol. 336, no. 6081, pp. 601–604, 2012.

[78] M. Yasemi and M. Jolicoeur, "Modelling cell metabolism: A review on constraint-based steady-state and kinetic approaches," *Processes*, vol. 9, no. 2, pp. 1–38, 2021.

[79] S. Schuster, C. Hilgetag, J. H. Woods, and P. A. Fell, "Reaction routes in biochemical reaction systems: Algebraic properties, validated calculation procedure and example from nucleotide metabolism," *J. Math. Biol.*, vol. 45, no. 2, pp. 153–181, 2002.

[80] D. Fell, “Understanding the control of metabolism,” *Biochem. Educ.*, vol. 25, no. 4, pp. 250–251, 2004.

[81] M. P. Joy, T. C. Elston, A. N. Lane, J. M. MacDonald, and M. Cascante, “Introduction to metabolic control analysis (MCA),” *Methods Pharmacol. Toxicol.*, vol. 17, no. December 2019, pp. 279–297, 2012.

[82] R. Moreno-Sánchez, E. Saavedra, S. Rodríguez-Enríquez, and V. Olín-Sandoval, “Metabolic Control Analysis: A tool for designing strategies to manipulate metabolic pathways,” *J. Biomed. Biotechnol.*, no. 1, 2008.

[83] D. T. Gillespie, “Stochastic simulation of chemical kinetics,” *Annu. Rev. Phys. Chem.*, vol. 58, pp. 35–55, 2007.

[84] R. A. Meyers, *Encyclopedia of Complexity and Systems Science*, vol. 7. 2009.

[85] V. H. Thanh, L. Marchetti, F. Reali, and C. Priami, “Incorporating extrinsic noise into the stochastic simulation of biochemical reactions: A comparison of approaches,” *J. Chem. Phys.*, vol. 148, no. 6, 2018.

[86] P. S. Swain, M. B. Elowitz, and E. D. Siggia, “Intrinsic and extrinsic contributions to stochasticity in gene expression,” *Proc. Natl. Acad. Sci. U. S. A.*, vol. 99, no. 20, pp. 12795–12800, 2002.

[87] D. J. Wilkinson, “Stochastic modelling for quantitative description of heterogeneous biological systems,” *Nat. Rev. Genet.*, vol. 10, no. 2, pp. 122–133, 2009.

[88] J. Fisher and T. A. Henzinger, “Executable cell biology,” *Nat. Biotechnol.*, vol. 25, no. 11, pp. 1239–1249, 2007.

[89] D. T. Gillespie, “Approximate accelerated stochastic simulation of chemically reacting systems,” *J. Chem. Phys.*, vol. 115, no. 4, pp. 1716–1733, 2001.

[90] H. Luo, T. Shen, and X. Xie, “Stochastic simulation of enzymatic kinetics for 13C isotope labeling at the single-cell scale,” *React. Kinet. Mech. Catal.*, no. 0123456789, 2022.

[91] D. T. Gillespie, “Chemical Langevin equation,” *J. Chem. Phys.*, vol. 113, no. 1, pp. 297–306, 2000.

[92] M. A. Gibson and J. Bruck, "Efficient exact stochastic simulation of chemical systems with many species and many channels," *J. Phys. Chem. A*, vol. 104, no. 9, pp. 1876–1889, 2000.

[93] D. T. Gillespie, "Exact stochastic simulation of coupled chemical reactions," *J. Phys. Chem.*, vol. 81, no. 25, pp. 2340–2361, 1977.

[94] D. F. Anderson, "A modified next reaction method for simulating chemical systems with time dependent propensities and delays," *J. Chem. Phys.*, vol. 127, no. 21, pp. 1–10, 2007.

[95] P. A. Saa and L. K. Nielsen, "Construction of feasible and accurate kinetic models of metabolism: A Bayesian approach," *Sci. Rep.*, vol. 6, no. June, pp. 1–13, 2016.

[96] G. I. Valderrama-Bahamóndez and H. Fröhlich, "MCMC Techniques for Parameter Estimation of ODE Based Models in Systems Biology," *Front. Appl. Math. Stat.*, vol. 5, no. November, pp. 1–10, 2019.

[97] A. Theorell and K. Nöh, "Reversible jump MCMC for multi-model inference in Metabolic Flux Analysis," *Bioinformatics*, vol. 36, no. 1, pp. 232–240, 2019.

[98] M. Melanie, "Introduction to genetic algorithms," *Sadhana - Acad. Proc. Eng. Sci.*, vol. 24, no. 4, pp. 293–315, 1999.

[99] S. Mirjalili, *Evolutionary Algorithms and Neural Networks.* 2019.

[100] A. H. Wright, *Genetic Algorithms for Real Parameter Optimization*, vol. 1. Morgan Kaufmann Publishers, Inc., 1991.

[101] B. T. Polyak, *Introduction to Optimization.* No. July, 2010.

[102] H. B. Curry, "The method of steepest descent for non-linear minimization problems," *Q. Appl. Math.*, vol. 2, no. 3, pp. 258–261, 1944.

[103] Y. Tohsato, K. Ikuta, A. Shionoya, Y. Mazaki, and M. Ito, "Parameter optimization and sensitivity analysis for large kinetic models using a real-coded genetic algorithm," *Gene*, vol. 518, no. 1, pp. 84–90, 2013.

[104] S. Katare, A. Bhan, J. M. Caruthers, W. N. Delgass, and V. Venkatasubramanian, "A hybrid genetic algorithm for efficient parameter estimation of large kinetic models," *Comput. Chem. Eng.*, vol. 28, no. 12, pp. 2569–2581, 2004.

[105] W. K. Hastings, “Monte Carlo sampling methods using Markov chains and their applications,” *Biometrika*, vol. 57, no. 1, pp. 97–109, 1970.

[106] J. L. Beck and S.-K. Au, “Bayesian Updating of Structural Models and Reliability using Markov Chain Monte Carlo Simulation,” *J. Eng. Mech.*, vol. 128, no. 4, pp. 380–391, 2002.

[107] M. R. Antoniewicz, “Parallel labeling experiments for pathway elucidation and 13C metabolic flux analysis,” *Curr. Opin. Biotechnol.*, vol. 36, pp. 91–97, 2015.

[108] W. Wiechert, “13C Metabolic Flux Analysis,” *Metab. Eng.*, vol. 206, 2001.

[109] M. R. Antoniewicz, “Methods and advances in metabolic flux analysis: a mini-review,” *J. Ind. Microbiol. Biotechnol.*, vol. 42, no. 3, pp. 317–325, 2015.

[110] S. B. Crown, C. P. Long, and M. R. Antoniewicz, “experiments in Escherichia coli,” *Metab Eng*, pp. 151–158, 2015.

[111] C. P. Long and M. R. Antoniewicz, “High-resolution 13C metabolic flux analysis,” *Nat. Protoc.*, vol. 14, no. 10, pp. 2856–2877, 2019.

[112] M. R. Antoniewicz, “Tandem mass spectrometry for measuring stable-isotope labeling,” *Curr. Opin. Biotechnol.*, vol. 24, no. 1, pp. 48–53, 2013.

[113] M. Koubaa, S. Mghaieth, B. Thomasset, and A. Roscher, “Gas chromatography-mass spectrometry analysis of 13C labeling in sugars for metabolic flux analysis,” *Anal. Biochem.*, vol. 425, no. 2, pp. 183–188, 2012.

[114] E. Fischer, N. Zamboni, and U. Sauer, “High-throughput metabolic flux analysis based on gas chromatography-mass spectrometry derived 13C constraints,” *Anal. Biochem.*, vol. 325, no. 2, pp. 308–316, 2004.

[115] J. D. Young, J. L. Walther, M. R. Antoniewicz, H. Yoo, and G. Stephanopoulos, “An Elementary Metabolite Unit (EMU) Based Method of Isotopically Nonstationary Flux Analysis,” *J. Anat.*, vol. 189 (Pt 3, no. Ii, pp. 503–505, 1996.

[116] H. García Martín, V. S. Kumar, D. Weaver, A. Ghosh, V. Chubukov, A. Mukhopadhyay, A. Arkin, and J. D. Keasling, "A Method to Constrain Genome-Scale Models with 13C Labeling Data," *PLoS Comput. Biol.*, vol. 11, no. 9, pp. 1–34, 2015.

[117] J. Schellenberger, R. Que, R. M. Fleming, I. Thiele, J. D. Orth, A. M. Feist, D. C. Zielinski, A. Bordbar, N. E. Lewis, S. Rahmanian, J. Kang, D. R. Hyduke, and B. Palsson, "Quantitative prediction of cellular metabolism with constraint-based models: The COBRA Toolbox v2.0," *Nat. Protoc.*, vol. 6, no. 9, pp. 1290–1307, 2011.

[118] J. D. Young, "INCA: A computational platform for isotopically non-stationary metabolic flux analysis," *Bioinformatics*, vol. 30, no. 9, pp. 1333–1335, 2014.

[119] W. Wiechert, M. Mollney, N. Isermann, M. Wurzel, and A. A. de Graaf, "Bidirectional reaction steps in metabolic networks: IV. Optimal design of isotopomer labeling experiments," *Biotechnol. Bioeng.*, vol. 66, no. 2, pp. 86–103, 1999.

[120] M. R. Antoniewicz, "Elementary Metabolite Units (EMU): a novel framework for modeling," *Metab. Eng.*, vol. 9, no. 1, pp. 68–86, 2007.

[121] J. D. Young, A. A. Shastri, G. Stephanopoulos, and J. A. Morgan, "Mapping photoautotrophic metabolism with isotopically nonstationary 13C flux analysis," *Metab. Eng.*, vol. 13, no. 6, pp. 656–665, 2011.

[122] R. W. Leighty and M. R. Antoniewicz, "Dynamic metabolic flux analysis (DMFA): A framework for determining fluxes at metabolic non-steady state," *Metab. Eng.*, vol. 13, no. 6, pp. 745–755, 2011.

[123] M. R. Antoniewicz, "A guide to metabolic flux analysis in metabolic engineering : Methods , tools and applications," *Metab. Eng.*, vol. 63, pp. 2–12, 2021.

[124] R. Benfeitas, G. Selvaggio, F. Antunes, P. M. Coelho, and A. Salvador, "Hydrogen peroxide metabolism and sensing in human erythrocytes: A validated kinetic model and reappraisal of the role of peroxiredoxin II," *Free Radic. Biol. Med.*, vol. 74, pp. 35–49, 2014.

[125] M. Seo and Y.-H. Lee, "PFKB3 regulates oxidative stress homeostasis via its S-glutathionylation in cancer," *Mol. Cell. Biochem.*, vol. 23, no. 1, pp. 1–7, 2014.

[126] A. Marín-Hernández, J. C. Gallardo-Pérez, S. Rodríguez-Enríquez, R. Encalada, R. Moreno-Sánchez, and E. Saavedra, "Modeling cancer glycolysis," *Biochim. Biophys. Acta - Bioenerg.*, vol. 1807, no. 6, pp. 755–767, 2011.

[127] Z. P. Gerdtzen, P. Daoutidis, and W. S. Hu, "Non-linear reduction for kinetic models of metabolic reaction networks," *Metab. Eng.*, vol. 6, no. 2, pp. 140–154, 2004.

[128] K. Hiller, C. Metallo, and G. Stephanopoulos, "Elucidation of Cellular Metabolism Via Metabolomics and Stable-Isotope Assisted Metabolomics," *Curr. Pharm. Biotechnol.*, vol. 12, no. 7, pp. 1075–1086, 2011.

[129] Y. Toya, K. Nakahigashi, M. Tomita, and K. Shimizu, "Metabolic regulation analysis of wild-type and arcA mutant Escherichia coli under nitrate conditions using different levels of omics data," *Mol. Biosyst.*, vol. 8, no. 10, pp. 2593–2604, 2012.

[130] J. F. Moxley, M. C. Jewett, M. R. Antoniewicz, S. G. Villas-Boas, H. Alpera, R. T. Wheeler, L. Tong, A. G. Hinnebusch, T. Ideker, J. Nielsen, and G. Stephanopoulos, "Linking high-resolution metabolic flux phenotypes and transcriptional regulation in yeast modulated by the global regulator Gcn4p," *Proc. Natl. Acad. Sci. U. S. A.*, vol. 106, no. 16, pp. 6477–6482, 2009.

[131] E. C. Britt, J. Lika, M. A. Giese, T. J. Schoen, G. L. Seim, Z. Huang, P. Y. Lee, A. Huttenlocher, and J. Fan, "Switching to the cyclic pentose phosphate pathway powers the oxidative burst in activated neutrophils," *Nat. Metab.*, vol. 4, no. 3, pp. 389–403, 2022.

[132] N. J. Kruger and A. Von Schaewen, "The oxidative pentose phosphate pathway: Structure and organisation," *Curr. Opin. Plant Biol.*, vol. 6, no. 3, pp. 236–246, 2003.

[133] S. Grimbs, J. Selbig, S. Bulik, H. G. Holzhütter, and R. Steuer, "The stability and robustness of metabolic states: Identifying stabilizing sites in metabolic networks," *Mol. Syst. Biol.*, vol. 3, 2007.

[134] A. Salvador and M. A. Savageau, "Quantitative evolutionary design of glucose 6-phosphate dehydrogenase expression in human erythrocytes," *Proc. Natl. Acad. Sci. U. S. A.*, vol. 100, no. SUPPL. 2, pp. 14463–14468, 2003.

[135] J. Hasenauer, N. Jagiella, S. Hross, and F. J. Theis, "Data-Driven Modelling of Biological Multi-Scale Processes," *J. Coupled Syst. Multiscale Dyn.*, vol. 3, no. 2, pp. 101–121, 2015.

[136] D. Holten, D. Procsal, and H. L. Chang, "Regulation of pentose phosphate pathway dehydrogenases by NADP+ NADPH ratios," *Biochem. Biophys. Res. Commun.*, vol. 68, no. 2, pp. 436–441, 1976.

[137] D. Ceyhan, A. Danişan, I. H. Öğüş, and N. Özer, "Purification and kinetic properties of 6-phosphogluconate dehydrogenase from rat small intestine," *Protein J.*, vol. 24, no. 5, pp. 293–301, 2005.

[138] B. Hove-Jensen, K. R. Andersen, M. Kilstrup, J. Martinussen, R. L. Switzer, and M. Willemoës, "Phosphoribosyl Diphosphate (PRPP): Biosynthesis, Enzymology, Utilization, and Metabolic Significance," *Microbiol. Mol. Biol. Rev.*, vol. 81, no. 1, pp. 1–83, 2017.

[139] K. Shankar and H. M. Mehendale, *Oxidative Stress*, vol. 3. Elsevier, third edit ed., 2014.

[140] N. Makino, K. Sasaki, K. Hashida, and Y. Sakakura, "A metabolic model describing the H2O2 elimination by mammalian cells including H2O2 permeation through cytoplasmic and peroxisomal membranes: Comparison with experimental data," *Biochim. Biophys. Acta - Gen. Subj.*, vol. 1673, no. 3, pp. 149–159, 2004.

[141] C. F. Ng, F. Q. Schafer, G. R. Buettner, and V. G. Rodgers, "The rate of cellular hydrogen peroxide removal shows dependency on GSH: Mathematical insight into in vivo H2O2 and GPx concentrations," *Free Radic. Res.*, vol. 41, no. 11, pp. 1201–1211, 2007.

[142] B. Chan, P. A. VanderLaan, and V. P. Sukhatme, "6-Phosphogluconate dehydrogenase regulates tumor cell migration in vitro by regulating receptor tyrosine kinase c-Met," *Biochem. Biophys. Res. Commun.*, vol. 439, no. 2, pp. 247–251, 2013.

[143] S. Nóbrega-Pereira, P. J. Fernandez-Marcos, T. Brioche, M. C. Gomez-Cabrera, A. Salvador-Pascual, J. M. Flores, J. Viña, and M. Serrano, "G6PD protects from oxidative damage and improves healthspan in mice," *Nat. Commun.*, vol. 7, pp. 1–9, 2016.

[144] N. Wan, D. M. DeLorenzo, L. He, L. You, C. M. Immethun, G. Wang, E. E. Baidoo, W. Hollinshead, J. D. Keasling, T. S. Moon, and Y. J. Tang, "Cyanobacterial carbon metabolism: Fluxome plasticity and oxygen dependence," *Biotechnol. Bioeng.*, vol. 114, no. 7, pp. 1593–1602, 2017.

[145] Y. Sun, M. Bandi, T. Lofton, M. Smith, C. A. Bristow, A. Carugo, N. Rogers, P. Leonard, Q. Chang, R. Mullinax, J. Han, X. Shi, S. Seth, B. A. Meyers, M. Miller, L. Miao, X. Ma, N. Feng, V. Giuliani, M. Geck Do, B. Czako, W. S. Palmer, F. Mseeh, J. M. Asara, Y. Jiang, P. Morlacchi, S. Zhao, M. Peoples, T. N. Tieu, M. O. Warmoes, P. L. Lorenzi, F. L. Muller, R. A. DePinho, G. F. Draetta, C. Toniatti, P. Jones, T. P. Heffernan, and J. R. Marszalek, "Functional Genomics Reveals Synthetic Lethality between Phosphogluconate Dehydrogenase and Oxidative Phosphorylation," *Cell Rep.*, vol. 26, no. 2, pp. 469–482.e5, 2019.

[146] Y. Li, C. F. Yao, F. J. Xu, Y. Y. Qu, J. T. Li, Y. Lin, Z. L. Cao, P. C. Lin, W. Xu, S. M. Zhao, and J. Y. Zhao, "APC/CCDH1 synchronizes ribose-5-phosphate levels and DNA synthesis to cell cycle progression," *Nat. Commun.*, vol. 10, no. 1, pp. 1–16, 2019.

[147] P. Golstein and G. Kroemer, "Cell death by necrosis: towards a molecular definition," *Trends Biochem. Sci.*, vol. 32, no. 1, pp. 37–43, 2007.

[148] R. Ballweg, A. L. Paek, and T. Zhang, "A dynamical framework for complex fractional killing," *Sci. Rep.*, vol. 7, no. 1, pp. 1–12, 2017.

[149] M. Battistelli and E. Falcieri, "Apoptotic bodies: Particular extracellular vesicles involved in intercellular communication," *Biology (Basel).*, vol. 9, no. 1, 2020.

[150] S. W. Lowe and A. W. Lin, "Apoptosis in cancer," *Acta Soc. Med. Ups.*, vol. 64, no. 3, pp. 313–321, 2000.

[151] P. Nair, M. Lu, S. Petersen, and A. Ashkenazi, *Apoptosis initiation through the cell-extrinsic pathway*, vol. 544. Elsevier Inc., 1 ed., 2014.

[152] A. L. Paek, J. C. Liu, A. Loewer, W. C. Forrester, and G. Lahav, "Cell-to-Cell Variation in p53 Dynamics Leads to Fractional Killing," *Cell*, vol. 165, no. 3, pp. 631–642, 2016.

[153] J. Roux, M. Hafner, S. Bandara, J. J. Sims, H. Hudson, D. Chai, and P. K. Sorger, “Fractional killing arises from cell-to-cell variability in overcoming a caspase activity threshold,” *Mol. Syst. Biol.*, vol. 11, no. 5, p. 803, 2015.

[154] D. Machado, M. J. Herrgård, and I. Rocha, “Modeling the contribution of allosteric regulation for flux control in the central carbon metabolism of E. coli,” *Front. Bioeng. Biotechnol.*, vol. 3, no. OCT, pp. 1–11, 2015.

[155] P. Millard, K. Smallbone, and P. Mendes, “Metabolic regulation is sufficient for global and robust coordination of glucose uptake, catabolism, energy production and growth in Escherichia coli,” *PLoS Comput. Biol.*, vol. 13, no. 2, pp. 1–24, 2017.

[156] S. Britton, M. Alber, and W. R. Cannon, “Enzyme activities predicted by metabolite concentrations and solvent capacity in the cell: Enzyme activities predicted by metabolite concentrations and solvent capacity in the cell,” *J. R. Soc. Interface*, vol. 17, no. 171, 2020.

[157] H. Link, K. Kochanowski, and U. Sauer, “Systematic identification of allosteric protein-metabolite interactions that control enzyme activity in vivo,” *Nat. Biotechnol.*, vol. 31, no. 4, pp. 357–361, 2013.

[158] P. I. Nikel, T. Fuhrer, M. Chavarría, A. Sánchez-Pascuala, U. Sauer, and V. de Lorenzo, “Reconfiguration of metabolic fluxes in Pseudomonas putida as a response to sub-lethal oxidative stress,” *ISME J.*, vol. 15, no. 6, pp. 1751–1766, 2021.

[159] J. M. Bermúdez-Muñoz, A. M. Celaya, S. Hijazo-Pechero, J. Wang, M. Serrano, and I. Varela-Nieto, “G6PD overexpression protects from oxidative stress and age-related hearing loss,” *Aging Cell*, vol. 19, no. 12, pp. 1–18, 2020.

[160] A. B. Aurora, V. Khivansara, A. Leach, J. G. Gill, M. Martin-Sandoval, C. Yang, S. Y. Kasitinon, D. Bezwada, A. Tasdogan, W. Gu, T. P. Mathews, Z. Zhao, R. J. DeBerardinis, and S. J. Morrison, “Loss of glucose 6-phosphate dehydrogenase function increases oxidative stress and glutaminolysis in metastasizing melanoma cells,” *Proc. Natl. Acad. Sci. U. S. A.*, vol. 119, no. 6, 2022.

[161] L. E. Netto and F. Antunes, “The Roles of peroxiredoxin and thioredoxin in hydrogen peroxide sensing and in signal transduction,” *Mol. Cells*, vol. 39, no. 1, pp. 65–71, 2016.

[162] F. Antunes and P. M. Brito, “Quantitative biology of hydrogen peroxide signaling,” oct 2017.

[163] R. Lin, S. Elf, C. Shan, H. B. Kang, Q. Ji, L. Zhou, T. Hitosugi, L. Zhang, S. Zhang, J. H. Seo, J. Xie, M. Tucker, T. L. Gu, J. Sudderth, L. Jiang, M. Mitsche, R. J. DeBerardinis, S. Wu, Y. Li, H. Mao, P. R. Chen, D. Wang, G. Z. Chen, S. J. Hurwitz, S. Lonial, M. L. Arellano, H. J. Khoury, F. R. Khuri, B. H. Lee, Q. Lei, D. J. Brat, K. Ye, T. J. Boggon, C. He, S. Kang, J. Fan, and J. Chen, “6-Phosphogluconate dehydrogenase links oxidative PPP, lipogenesis and tumour growth by inhibiting LKB1-AMPK signalling,” *Nat. Cell Biol.*, vol. 17, pp. 1484–1496, nov 2015.

[164] E. Mosca, R. Alfieri, C. Maj, A. Bevilacqua, G. Canti, and L. Milanesi, “Computational modeling of the metabolic states regulated by the kinase Akt,” *Front. Physiol.*, vol. 3 NOV, no. November, pp. 1–26, 2012.

[165] A. Theorell, S. Leweke, W. Wiechert, and K. Nöh, “To be certain about the uncertainty: Bayesian statistics for 13C metabolic flux analysis,” *Biotechnol. Bioeng.*, vol. 114, no. 11, pp. 2668–2684, 2017.

[166] M. Heinonen, M. Osmala, H. Mannerström, J. Wallenius, S. Kaski, J. Rousu, and H. Lähdesmäki, “Bayesian metabolic flux analysis reveals intracellular flux couplings,” *Bioinformatics*, vol. 35, no. 14, pp. i548–i557, 2019.

[167] A. Theorell and K. Nöh, “Reversible jump MCMC for multi-model inference in Metabolic Flux Analysis,” *Bioinformatics*, vol. 36, no. 1, pp. 232–240, 2020.

[168] D. Christodoulou, A. Kuehne, A. Estermann, T. Fuhrer, P. Lang, and U. Sauer, “Reserve Flux Capacity in the Pentose Phosphate Pathway by NADPH Binding Is Conserved across Kingdoms,” *iScience*, vol. 19, pp. 1133–1144, 2019.

[169] B. C. Campbell, G. A. Petsko, and C. F. Liu, “Crystal Structure of Green Fluorescent Protein Clover and Design of Clover-Based Redox Sensors,” *Structure*, vol. 26, no. 2, pp. 225–237.e3, 2018.

[170] J. J. Song, J. G. Rhee, M. Suntharalingam, S. A. Walsh, D. R. Spitz, and Y. J. Lee, “Role of glutaredoxin in metabolic oxidative stress: Glutaredoxin as a sensor of oxidative stress mediated by H2O2,” *J. Biol. Chem.*, vol. 277, no. 48, pp. 46566–46575, 2002.

[171] M. Gutscher, A. L. Pauleau, L. Marty, T. Brach, G. H. Wabnitz, Y. Samstag, A. J. Meyer, and T. P. Dick, “Real-time imaging of the intracellular glutathione redox potential,” *Nat. Methods*, vol. 5, no. 6, pp. 553–559, 2008.

[172] J. L. Gillis, J. A. Hinneh, N. Ryan, S. Irani, M. Moldovan, L. E. Quek, R. Shrestha, A. R. Hanson, J. Xie, A. J. Hoy, J. Holst, M. M. Centenera, I. G. Mills, D. J. Lynn, L. A. Selth, and L. M. Butler, “A feedback loop between the 1 androgen receptor and 6-phosphogluoconate dehydrogenase (6PGD) drives prostate cancer growth: Cooperativity between 6PGD and AR drives prostate cancer growth,” *Elife*, vol. 10, pp. 1–27, 2021.

[173] C. Shan, S. Elf, Q. Ji, H. B. Kang, L. Zhou, T. Hitosugi, L. Jin, R. Lin, L. Zhang, J. H. Seo, J. Xie, M. Tucker, T. L. Gu, J. Sudderth, L. Jiang, R. J. DeBerardinis, S. Wu, Y. Li, H. Mao, P. R. Chen, D. Wang, G. Z. Chen, S. Lonial, M. L. Arellano, H. J. Khoury, F. R. Khuri, B. H. Lee, D. J. Brat, K. Ye, T. J. Boggon, C. He, S. Kang, J. Fan, and J. Chen, “Lysine acetylation activates 6-phosphogluconate dehydrogenase to promote tumor growth,” *Mol. Cell*, vol. 55, no. 4, pp. 552–565, 2014.

[174] M. M. Crane, I. B. Clark, E. Bakker, S. Smith, and P. S. Swain, “A microfluidic system for studying ageing and dynamic single-cell responses in budding yeast,” *PLoS One*, vol. 9, no. 6, pp. 1–10, 2014.

[175] M. Yew, Y. Ren, K. S. Koh, C. Sun, and C. Snape, “A Review of State-of-the-Art Microfluidic Technologies for Environmental Applications: Detection and Remediation,” *Glob. Challenges*, vol. 3, no. 1, p. 1800060, 2019.

Publications

- **Theoretical study of the impact of adaptation on cell-fate heterogeneity and fractional killing**
  Julien Hurbain, Darka Labavić, Quentin Thommen and Benjamin Pfeuty
  Scientific Reports (2020) - https://doi.org/10.1038/s41598-020-74238-y
- **Quantitative modeling of pentose phosphate pathway response to oxidative stress reveals dose-dependent regulatory strategy**
  Julien Hurbain, Quentin Thommen, François Anquez and Benjamin Pfeuty
  iScience (2022) - https://doi.org/10.1016/j.isci.2022.104681
- **Stochastic simulation algorithm for isotope labeling metabolic networks**
  Quentin Thommen, Julien Hurbain and Benjamin Pfeuty
  arXiv (2022) (attached version) -
  https://doi.org/10.48550/arXiv.2201.00663
  Metabolic Engineering (2022) -
  https://doi.org/10.1016/j.ymben.2022.11.001

www.nature.com/scientificreports

scientific reports

OPEN

Theoretical study of the impact of adaptation on cell-fate heterogeneity and fractional killing

Julien Hurbain[1,2], Darka Labavić[1,2], Quentin Thommen[1] & Benjamin Pfeuty[1]✉

Fractional killing illustrates the cell propensity to display a heterogeneous fate response over a wide range of stimuli. The interplay between the nonlinear and stochastic dynamics of biochemical networks plays a fundamental role in shaping this probabilistic response and in reconciling requirements for heterogeneity and controllability of cell-fate decisions. The stress-induced fate choice between life and death depends on an early adaptation response which may contribute to fractional killing by amplifying small differences between cells. To test this hypothesis, we consider a stochastic modeling framework suited for comprehensive sensitivity analysis of dose response curve through the computation of a fractionality index. Combining bifurcation analysis and Langevin simulation, we show that adaptation dynamics enhances noise-induced cell-fate heterogeneity by shifting from a saddle-node to a saddle-collision transition scenario. The generality of this result is further assessed by a computational analysis of a detailed regulatory network model of apoptosis initiation and by a theoretical analysis of stochastic bifurcation mechanisms. Overall, the present study identifies a cooperative interplay between stochastic, adaptation and decision intracellular processes that could promote cell-fate heterogeneity in many contexts.

In many adaptation and developmental contexts, isogenic cells make stochastic fate decisions to generate diversified cell types and subpopulations[1]. Cell-fate heterogeneity is indeed a key feature of microbial adaptation to adverse environments[2], of the development and homeostasis of tissues and organs[3] or of tumor resistance to drug therapy[4]. The differential fate outcome of isogenic cells exposed to the same environmental stimuli involves the interplay of stochastic and deterministic mechanisms[5–7], where regulatory mechanisms can determine both the statistics and dynamics of stochastic events and the effect of those stochastic events on molecular trajectories dictating cell fate choices. Several experimental studies have shown that cell-fate decisions are often preceded by a highly fluctuating intracellular dynamics. Pulsatile or oscillatory activities have been observed in signaling pathways operating during the stochastic choice of various differentiation or proliferation fates[8–13]. The profile characteristics of those dynamic signaling activities have been proposed to either direct decision outcomes or promote cell-fate heterogeneity[14,15]. Transient dynamics occurring at epigenetics, transcriptome-wide or multicellular levels[16–18] have also been proposed to regulate cell-fate heterogeneity and plasticity. All these examples support a key role of transient dynamics in orchestrating fate decisions from diverse signaling and stochastic cues.

An attractive case study is the stochastic fate decision between life and death, commonly termed fractional killing, for which the systematic measure of probabilistic dose-response curves coupled with single-cell analysis of stochastic and dynamical signatures are possible[19]. On this issue, several modelling studies have been devoted to identify which sources of fluctuations and which parts of the apoptotic network could contribute the most to the variability of decision time and outcomes[20–23], while the impact of the transient dynamics has been seldomly addressed[24]. Yet, singe-cell analysis of the temporal trajectories of caspase 8 activity in response to TRAIL has revealed a signature of adaptation dynamics whose transient kinetics determines whether a cell survives or dies[25]. Caspase 8 is likely to be part of negative feedback regulation involving for instance the formation of inactive heterodimers of procaspase-8[26]. The importance of transient dynamics of apoptotic inducers has been also emphasized in the case of cisplatin drug exposure[24,27]. The proposed mechanism involves a competition between positive and negative regulation of caspase 8-dependent apoptosis, thereby defining an incoherent feedforward loop. More generally, environmental stressors are prone to upregulate both pro-survival and pro-death pathways[28–31] through negative feedback or incoherent feedforward loop motifs which ultimately lead to a dynamical adaptation response[32–34]. These stochastic and deterministic features associated with fractional

---

[1]Univ. Lille, CNRS, UMR 8523 – PhLAM – Physique des Lasers Atomes et Molécules, 59000 Lille, France. [2]These authors contributed equally: Julien Hurbain and Darka Labavić. ✉email: benjamin.pfeuty@univ-lille.fr

Symbol	Description	Equations/Figures
$x_i^l, \vec{x}^l$	Concentration of biochemical species i of cell l	Eq. (1)
$k_i^l, \vec{k}^l$	Biochemical network parameter i of cell l	Eq. (1)
a_j, ν_{ji}	Rate and stoichiometries of the biochemical reaction j	Eq. (1)
ξ_j^l	Langevin noise associated to reaction j in cell l	Eq. (1)
σ	Standard deviation of random variable	Eq. (1)
s^l	Stimulus (e.g., stress) level of cell l	Eq. (1)
s_{sn}	Stimulus level associated with saddle-node bifurcation	Fig. 2
$P(\vec{x}, t)$	Time-dependent probability distribution function in state space	Eq. (2)
$P_{D/Death}$	Decision (e.g., death) probability	Eq. (2)
s_{50}	Stimulus level inducing 50% of fate probability	Eq. (3)
t^*	Measurement time for P_D	Eq. (2)
η	Fractionality index	Eq. (3)
$x_{1,2,3}$	Adaptive (e.g., damage/repair) and fate-decision (e.g., death) species	Eq. (4)
β, τ	Adaptation strength and timescale	Eq. (4)
$\vec{x}_{st1,2/sn/sad}$	Stable/saddle-node/saddle fixed point associated with bistability	Figs. 2, 3 and 4
$\mathcal{W}^{s/u}(\vec{x})$	Stable/unstable manifold of the fixed point $\vec{x}$	Eqs. (2) and (9)
s_c	Critical stimulus level without noise $s_c = s_{50}(\sigma = 0)$	Fig. 2
$\vec{x}_c(t, s_c)$	Critical trajectory	Fig. 2 and Eqs. (7–8)
$\vec{y}(t), y_N$	Small deviations of $\vec{x}(t)$ from $\vec{x}_c(t)$	Fig. 5 and Eqs. (7–9)
$\Pi(t, t')$	Principal fundamental matrix	Eq. (7)
$U(x), \Delta, r_K$	Effective potential, barrier height and Kramers rate	Fig. 5 and Eq. (10)

Table 1. List of mathematical symbols and notations.

killing raise the more general question of the role of adaptation dynamics in shaping the timing and probabilities of stochastic fate decisions.

Diverse modelling approaches have proved useful to study stochastic switching in regulatory networks, ranging from the discrete chemical master equations and stochastic simulation algorithms to the continuous Fokker-Planck and Langevin equations. Those diverse tools and their refinements have been broadly used to study the interplay between noise properties and network topologies in shaping the steady-state bimodal distribution and transition rates associated with two phenotypic states[35–39]. In the present study, we use the joint framework of chemical Langevin equations[40] and bifurcation theory to address the interplay of stochasticity, transient adaptation and bistable switching. The deterministic and stochastic analysis of a simple model combining adaptation and bistability deciphers how the adaptation overshoot dynamics modulate, concomitantly, the nonlinear decision-making properties and the probabilistic fate-response properties. The biological relevance of this behavior is assessed by simulating a more detailed model of programmed death pathways. Finally, the generality of the proposed noise-amplification mechanism is addressed within the theoretical framework of stochastic nonlinear dynamics.

Results

Stochastic modeling framework for probabilistic fate decisions.

Fractional killing can be defined as the population-level property by which isogenic cells exposed to increasing doses of death-inducing stimuli will tend to display a fraction of surviving cells and dying cells, although with increasing probability of death. This stochastic decision process can be studied in a general theoretical framework that applies to cases of fate decisions other than survival and death. Probabilistic cell-fate response commonly involves the interplay between intracellular mechanisms of fate decision and intracellular sources of cell-to-cell variability. Without loss of generality, a possible framework to study such probabilistic fate response to a step stimulus consists in a Langevin differential equation description of the stochastic dynamics of a biochemical reaction network (see Table 1 for notations):

$$\frac{dx_i^l}{dt} = \sum_j \nu_{ji}\, a_j^l(t) + \sum_j \nu_{ji} \sqrt{a_j^l(t)}\, \xi_j^l(t) \tag{1a}$$

$$a_j^l(t) = a_j(\vec{x}^l, s^l(t), \vec{k}^l) \tag{1b}$$

$$s(t) = s\, H(t) \tag{1c}$$

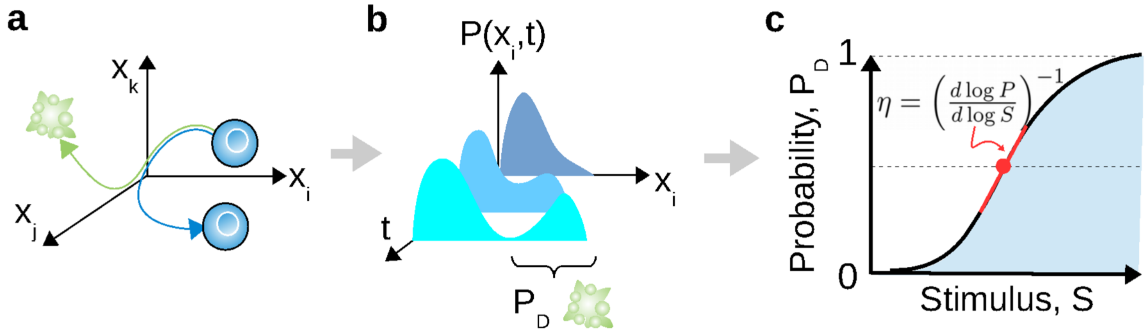

Figure 1. Dynamical and probabilistic schemes of cell-fate decisions. (**a**) State-space trajectories diverging toward distinct cellular phenotypic states. (**b**) Establishment of a bimodal probability density function. (**c**) Fate probability curves whose slope is quantified by a fractionality index (η).

$$\langle \xi_j^l(t)\, \xi_{j'}^{l'}(t') \rangle = \sigma^2\, \delta(t-t')\delta_{j,j'}\delta_{l,l'}\,. \tag{1d}$$

where $H(t)$ and $\delta(t)$ are respectively the Heaviside and the Dirac delta functions. In this model, the cell-to-cell variability of stimulus-induced response trajectories $\vec{x}^l$ can originate either from noisy biochemical reactions involving stochastic processes $\xi_j^l(t)$ or from heterogeneities in stimulus exposure/sensitivity s^l or network parameters $\vec{k}^l$ from cell to cell. Although limited or inaccurate to describe some stochastic behaviors of biochemical networks[41], chemical Langevin equation approach is nevertheless convenient to study asymptotic cases of small noise, large size or separated timescales and, thus, to relate with noise-free dynamical properties[42].

For the deterministic part of the equation, the fate-decision behavior (e.g., death) can be minimally implemented in the nonlinear dynamics of the biochemical network by the presence of a saddle-node bifurcation mechanism at a critical stimulus level s_{sn} through which the (survival) steady state $\vec{x}_{st1}$ is destabilized toward the other (death) steady state $\vec{x}_{st2}$, generally in an irreversible manner. Accordingly, near-identical cells exposed to the same stimulus may display divergent trajectories toward survival or death (Fig. 1a). The population dynamics of noisy or heterogeneous cells described by Eq. (1) can be statistically represented by a probability distribution $P(\vec{x},t)$, which typically follows a Fokker-Planck equation. Stimulus-induced fate decision relates with the establishment of a bimodal distribution such that one can define the decision probability P_D (Fig. 1b):

$$P_D = \int_{\vec{x}\in\mathcal{W}^s(\vec{x}_{st2})} P(\vec{x},t^*)d\vec{x}\,. \tag{2}$$

where t^* is the typical measurement time and $\mathcal{W}^s(\vec{x}_{st})$ is the fate attractor basin. It is to emphasize that we consider the typical case of an irreversible fate decision associated with a low or null probability to revert from the state $\vec{x}_{st2}$ to $\vec{x}_{st1}$, which is typically the case for death, proliferation or terminal differentiation fate outcomes. From the dose-response curve $P_D(s)$, one can define a *fractionality index* (Fig. 1c) which quantifies the derivative of this curve around the 50% fate probability ($P_D(s_{50}) = 0.5$):

$$\eta = \left(\frac{d\ln P}{d\ln s}(s_{50})\right)^{-1} \tag{3}$$

Based on this simple sensitivity measure of the stochastic fate response, systematic analysis of how η varies with noise strength σ and network parameters $\vec{k}$ should provide key insights into the interplay of stochastic and nonlinear properties of networks in shaping probabilistic features of fate response.

Adaptation dynamics enforces a saddle-collision mechanism for decision making.

To evaluate the impact of adaptation dynamics on the probabilistic properties of stochastic fate decisions, the biochemical reaction model used in Eq. (1) must implement adaptation and switching behaviors. For the ease of mathematical and graphical analysis, we consider a low-dimensional biochemical reaction network[43], whose interactions between three coarse-grained variables implement a basic setting of a negative feedback-driven adaptation and a positive feedback-driven decision switch (Fig. 2a,b). Starting from a set of biochemical reactions associated with this architecture, a suitable factorization and normalization procedure (see "Methods" section) allows one to derive the following set of differential equation,

$$\tau_1 \frac{dx_1}{dt} = 1 - k_1 + k_1\, s(t) - x_2\, x_1\,, \tag{4a}$$

$$\tau \frac{dx_2}{dt} = 1 - \beta + \beta x_1 - x_2\,, \tag{4b}$$

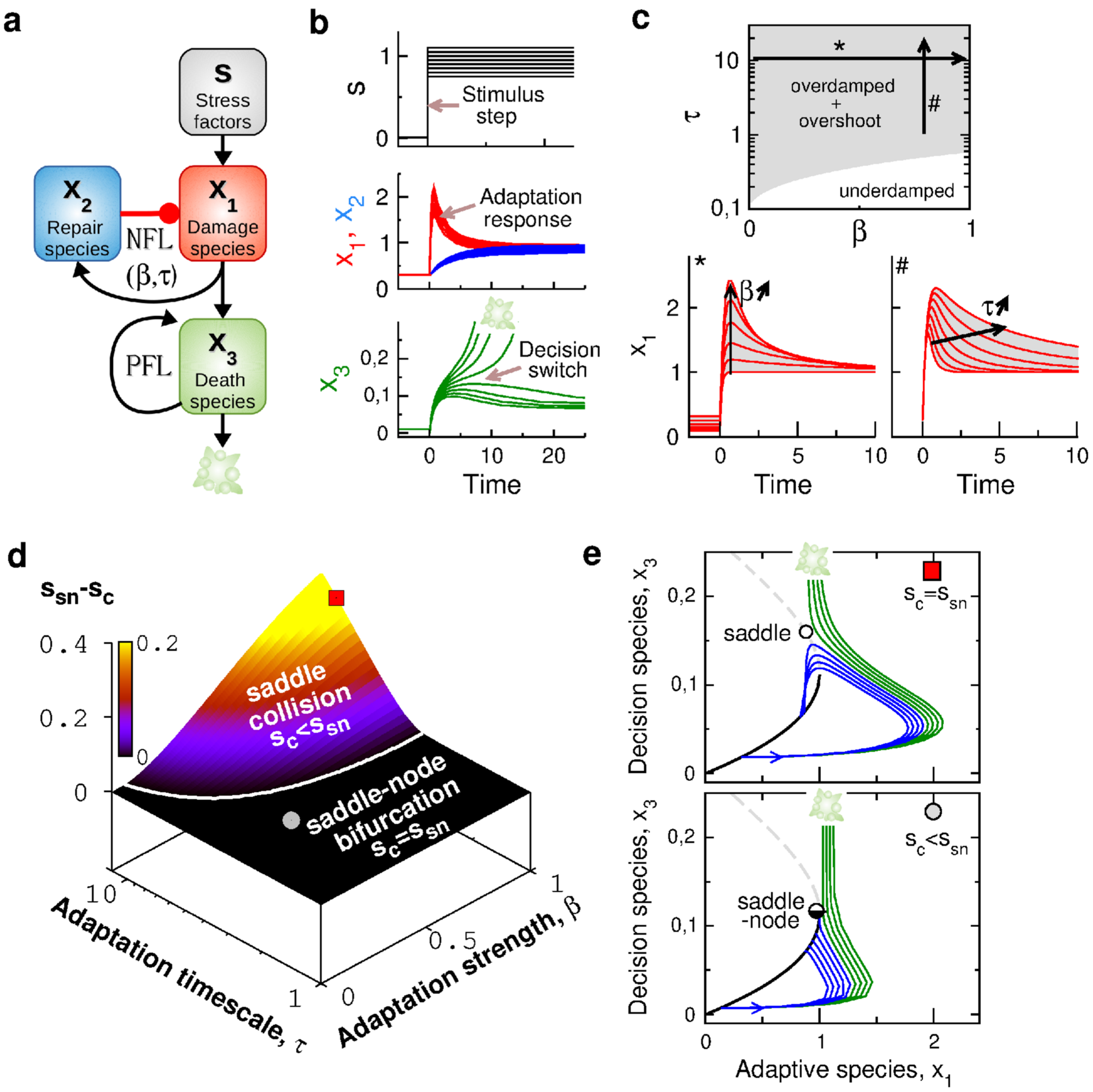

Figure 2. Adaptation alters the nonlinear mechanism of decision making. (**a**) Coarse grained model combining a negative feedback loop (NFL) between x_1 and x_2 species and self-activation positive feedback loop (PFL) of x_3 species. (**b**) Typical adaptation and switching dynamics in response to a stimulus step. Color code relates to that of panel (**a**) and model parameters are $\beta = 1$ and $\tau = 10$. (**c**) Effect of adaptation parameters β and τ on the linear response regime (upper panel) and the overshoot profile of the adaptation response of $x_1(t)$ (left and right bottom panel). (**d**) Plot of $s_{sn} - s_c$ as a function of β and τ where two distinct transition regimes ($s_c = s_{sn}$ and $s_c < s_{sn}$) are separated by the white boundary. (**e**) Single-cell trajectories plotted in the $\{x_1, x_3\}$ space for increasing level of stimulus s (blue for $s < s_c$ and green for $s > s_c$): Upper panel (red square: $\beta = 1$ and $\tau = 10$) shows a saddle collision for $s = s_c$ and bottom panel (grey circle: $\beta = 0.3$; $\tau = 3$) shows a saddle-node bifurcation. Black full and gray dashed lines represent the steady state branches $\vec{x}_{st1}(s)$ and $\vec{x}_{sad}(s)$.

$$\frac{dx_3}{dt} = k_2\, x_1 + k_3\, \frac{x_3^2}{k_4 + x_3^2} - x_3\,. \tag{4c}$$

The reaction rates a_i of the corresponding Langevin equations are detailed in "Methods" section. Most parameter values are fixed within a range consistent with some biological assumptions. First, self-activation parameters $k_3 = 1$ and $k_4 = 0.2$ implement a positive feedback that is strong enough to produce an irreversible transition to death fate. Second, the parameters $k_1 = 0.9$ and $\tau_1 = 0.1 < 1 < \tau$ implement a significant and fast stimulus-induced response of x_1, which gives rise to a marked overshoot dynamics through negative feedback with x_2. Third, the synthesis rate parameters $1 - \beta, 1 - k_1$ and $k_2 = 0.056$ satisfy the normalization condition that saddle-node bifurcation occurs for $x_1 = x_2 = s = 1$ whatever the values of the other model parameters (k_i, β, τ).

In this way, the parameters β ($\in [0:1]$) and τ can be systematically varied to modulate the overshoot characteristics of adaptation with limited impact on steady-state properties. Indeed, the steady state of x_1 depends on the stimulus according to:

$$x_1(s) = \frac{\beta - 1 + \sqrt{(1-\beta)^2 + 4(1 - k_1 + k_1 s)\,\beta}}{2\beta}\,, \tag{5}$$

which satisfies $x_1(s=1) = 1$ for any β and k_1 values. Furthermore, stability analysis of this steady state establishes the following criteria for the existence of an overdamped overshoot response to the step stimulus $s = 1$:

$$\tau/\tau_1 > (1 + 2\beta) + \sqrt{4\beta(\beta+1)}\,. \tag{6}$$

Accordingly, the adaptation parameters $\beta \in [0:1]$ and $\tau > 1$ control the amplitude and timescale of the overshoot response without changing the steady-state value for $s = 1$ (Fig. 2c). More details regarding the relation between the negative-feedback parameters and the adaptation behavior can be found in a previous modeling study[43].

Before considering a source of variability, we first need to investigate the main effect of transient adaptation dynamics on the fate decision properties. In this case, probabilistic response and fractional killing do not occur, and the system response to a step stimulus is essentially determined by a threshold s_c: a stress amplitude s greater (resp. lower) than s_c leads to a fate decision toward death (resp., survival). For an adiabatically-slow increase of the stimulus, the system follows the steady-state branch $\vec{x}_{st1}(s)$ of low x_3 values before escaping from it for $s > s_{sn}$ through a saddle-node bifurcation. This is not necessarily the case for a step increase of the stimulus, for which transition to death can occur for a stimulus level $s < s_{sn}$ so that $s_{sn} - s_c > 0$. The plot of $s_{sn} - s_c$ as function of adaptation parameters in Fig. 2d shows that $s_c = s_{sn}$ for weak enough or fast enough adaptation, while s_c is below s_{sn} for large enough values of both β and τ. These two qualitative regimes manifest, in fact, the existence of distinct instability mechanisms (Fig. 2e). For low values of β or τ and thus a small or no overshoot, the threshold property $s = s_c = s_{sn}$ relates with a dynamical trajectory that is destabilized in the vicinity of a saddle-node instability (lower panel of Fig. 2e). In this scenario, x_3 species trigger the fate decision depending on the steady-state value of the adaptive species x_1, which carries out the role of a bifurcation parameter. In sharp contrast, for high enough value of both β and τ and thus for a significant overshoot response of x_1, the threshold property $s = s_c < s_{sn}$ relates with a dynamical trajectory that collides with a saddle instability (upper panel of Fig. 2e).

In summary, while varying β and τ leads to gradual changes of the amplitude and the timescale of the overshoot adaptation profile, we could identify a threshold boundary in the $\{\beta, \tau\}$ space which separates between a saddle-node and a saddle-collision instability scenario. In the saddle-collision scenario, the threshold value s_c becomes very sensitive to the transient characteristics of the overshoot profile, which suggests that fate decision may also become more sensitive to the sources of cell-to-cell variability that impact transient dynamics.

Adaptation dynamics promotes heterogeneous cell-fate decisions.

Based on our comprehensive analysis of the deterministic decision dynamics in the coarse-grained model combining adaptation and bistability, we aim to investigate how adaptation influences cell-fate heterogeneity in a population of noisy cells. We therefore apply the general stochastic modeling framework to this biochemical network model (see "Methods" section) and perform a systematic analysis of the probabilistic properties in the $\{\beta, \tau\}$ parameter space and for several noise sources and levels (Fig. 3).

To begin with, we consider the case of cell-to-cell variability arising from molecular noise solely ($s^l = s$ and $\vec{k}^l = \vec{k}$) and focus on the two archetypical parameter sets depicted in Fig. 2 that are associated with weak/fast adaptation ($\beta = 0.3$ and $\tau = 3$) and strong/slow adaptation ($\beta = 1$ and $\tau = 10$), respectively. Simulation of Langevin equations for 2000 trials shows that, for the same level of noise, strong/slow adaptation leads to probabilistic response associated with a much larger stimulus range and a much smaller derivative at $P = 0.5$ (Fig. 3a). These differences are quantified by the fractionality index η that is about four-fold larger for strong adaptation ($\eta \approx 0.05$) as compared to weak adaptation ($\eta \approx 0.012$). To illustrate how adaptation may amplify noise to generate more heterogeneous fate response, we plot the noisy single-cell trajectories in the two scenarios associated with the noise level and the same relative change of stimulus level. When adaptation is strong and slow enough, noisy trajectories remain within some neighborhood of the noise-free trajectory until diverging from it toward different fates when approaching the saddle fixed point, with a slight change of respective fate probability when the stimulus increases (Fig. 3b). This is in sharp contrast with the case of weak (or no) adaptation for which noisy trajectories reach first the neighborhood of a stable fixed point, before eventually escaping over the saddle fixed point toward the other fate when the stimulus slightly increases (Fig. 3c). The qualitative difference between these two stochastic decision scenario is confirmed by the distinct scaling laws $\eta \propto \sigma^b$, where $b = 1$ for strong/slow adaptation and $b \approx 1.2$ for weak/fast adaptation (Fig. 3d). This body of evidences strongly suggest that adaptation dynamics promotes cell-fate heterogeneity, mostly by changing the underlying nonlinear mechanism of decision-making. This is confirmed by the plot $\eta = f(\beta, \tau)$ (Fig. 3e), which unambiguously shows a qualitative increase of fractionality index η specifically in the parameter domain where the saddle-collision scenario occurs (above the white boundary).

Besides molecular noise, other sources of cell-to-cell variability have been tested, such as stimulus exposure or sensitivity s^l (Fig. 3f) or initial conditions $\vec{x}^l(t_0)$ (Fig. 3g). Again, a qualitative increase of η is observed in the parameter region associated with a saddle-collision scenario (above the white boundary), though the extent of such increase is much more important for the case of variable initial conditions. This is because variability of initial conditions impacts only transient dynamics, not steady state, while variability of s^l impacts steady-state

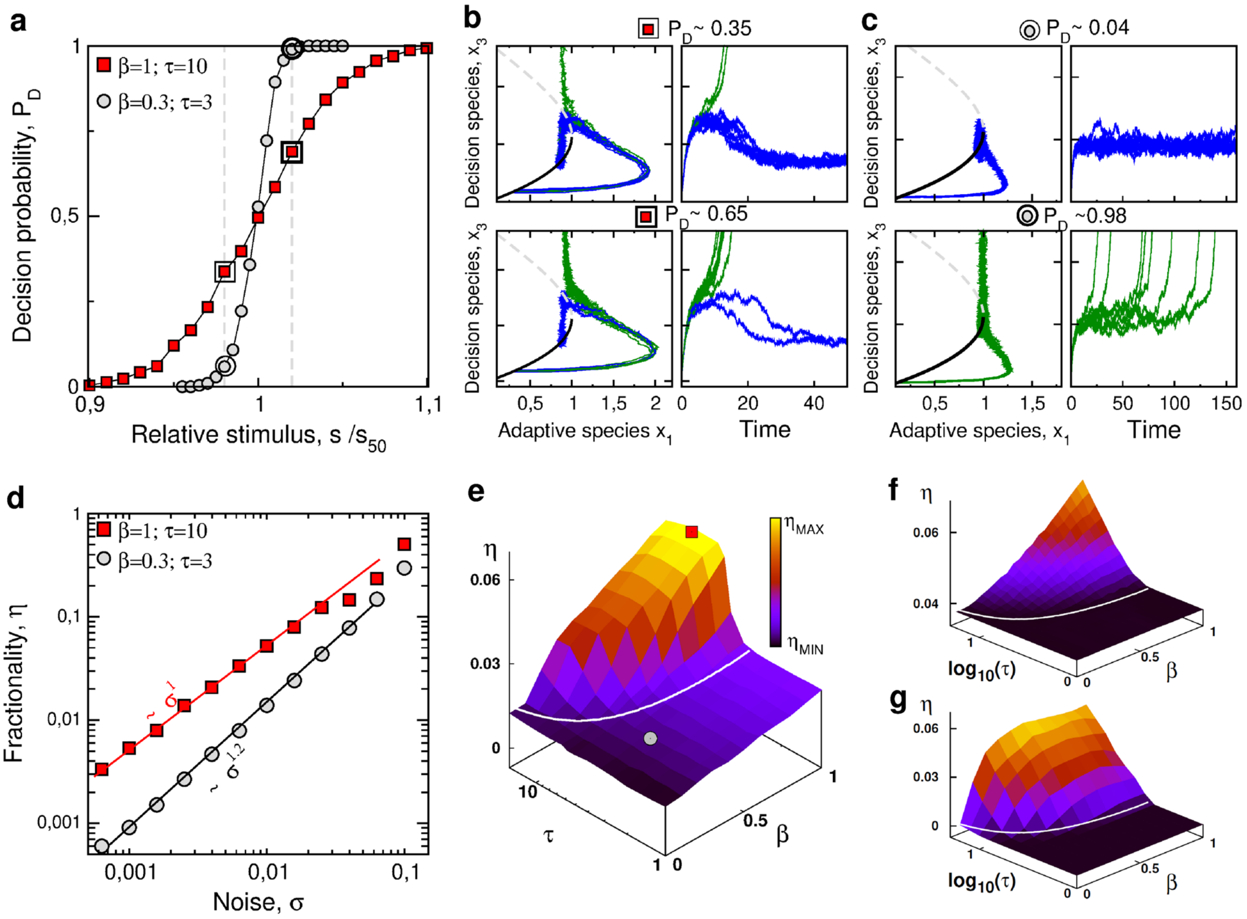

Figure 3. The critical impact of adaptation on cell-fate heterogeneity. Fate decision probability is studied in presence of molecular noise level (**a**–**e**) or other sources of cell-cell variability (**f**–**g**). (**a**) Fate probability curves as function of relative stimulus for the cases of strong/slow adaptation (red squares) and weak/fast adaptation (gray circles). (**b**–**c**) Sample of noisy single-cell trajectories associated with a ±2% change of stimulus level around $s = s_{50}$ (dashed line of panel **a**), which are plotted in the $\{x_1, x_3\}$ state space where steady-state branches $\vec{x}(s)$ are also represented. (**d**) Fractionality index η as function of noise with their asymptotic scaling exponents. (**e**) Fractionality index η as a function of adaptation parameters τ and β for molecular noise level $\sigma = 0.01$. White line delimits the parameter domains of saddle-collision and saddle-node transition scenario (redrawn from Fig. 2c). Red squares ($\beta = 1$ and $\tau = 10$) and grey circles ($\beta = 0.3$ and $\tau = 3$) correspond to the two archetypical parameter sets associated to each scenario, which are compared in panels **a**–**d**. (**f**–**g**) Fractionality index η as function of β and τ for two sources of cell-cell variability: (**f**) a uniform distribution of stimulus exposure s^l with $\langle \delta s^l \delta s^{l'} \rangle = 0.01\delta_{l,l'}$; (**g**) a uniform distribution of initial conditions $\vec{x}_{st1}(s = 0) + \vec{\delta x}$ with $\langle \delta x_i^l \delta x_j^{l'} \rangle = 0.1\delta_{i,j}\delta_{l,l'}$.

properties. Adaptation dynamics can promote cell-fate heterogeneity in a qualitative manner, but to varying extent depending on the source of variability and the time profile of the overshoot.

Adaptation dynamics contributes to fractional killing in an apoptosis model. The nonlinear nature of the adaptation-related amplification of noise effect suggests that this mechanism could be effective regardless the complexity of the network model. In other words, we expect to observe a similar noise amplification behavior in more detailed regulatory network model of stress-induced death fate decision as far as the adaptation dynamics leads to a collision to a saddle instability in the state-space of any dimensions. To check this conjecture, we need to replace the effective one-dimensional model of fate decision by a more realistic high-dimensional model of death fate decision. Fractional killing is commonly observed following many types of stress or death ligands, which may trigger death through different pathways[44,45] depending on the involved multi-protein signaling complexes, transcriptional factors and other signaling and metabolic cues (left of Fig. 4a). Among these many possibilities, we consider the canonical case where the stress signal and damage species mainly impact the intrinsic mitochondrial pathway of apoptosis through the control of the Bh3 member of Bcl-2 family[46]. An alternative possibility could have been to consider the case of TRAIL-induced apoptosis involving caspase 8-dependent activation of both extrinsic and mitochondrial pathways[20].

The choice of Bh3-dependent mitochondrial apoptosis is motivated by a previous biochemical model of apoptosis initiation[24], which exhibited several interesting features for our study. First, the model focuses on the

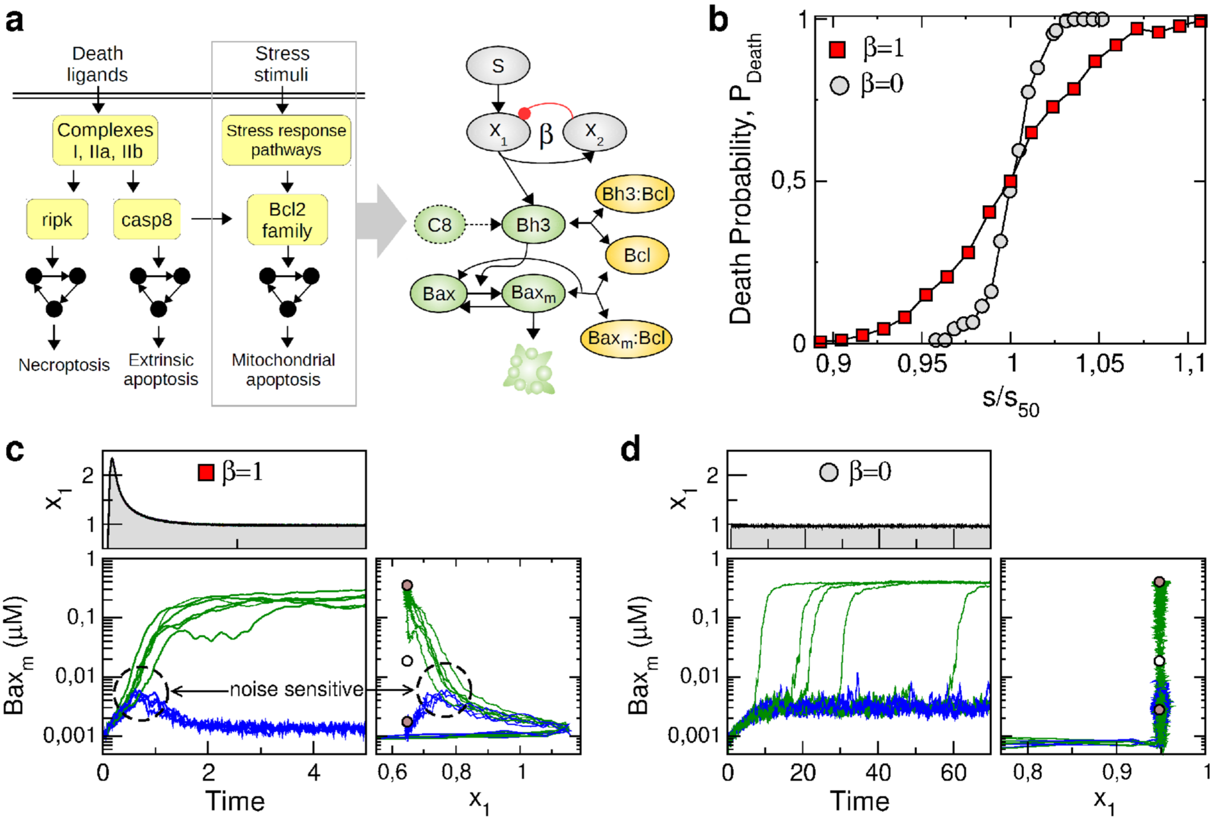

Figure 4. Adaptation-dependent fractional killing in an apoptosis model. (**a**) Some mammalian cell-death pathways associated with fractional killing including the stress-induced mitochondrial pathway of apoptosis (left panel). The detailed model of this study couples the coarse-grained model of stress-induced adaptation module (Eqs. 4a, b) and a published model of the mitochondrial apoptosis initiation module[24] (right panel). (**b**) Death probability as function of the relative stimulus level s/s_{50} obtained through numerical simulation of Eq. (1) with $\sigma = 0.002$, where η is about four-fold higher with adaptation ($\beta = 1$) compared to without ($\beta = 0$). (**c**–**d**) Temporal trajectories of x_1 and Bax$_m$ in the presence or the absence of adaptation (**c**: $\beta = 1$; **d**: $\beta = 0$). Adaptation timescale is set to $\tau = 1.25$hr to match with the timescale of the apoptotic switch (time unit is hour). Right panels show a 2D state-space projection of the high-dimensional dynamics with respect to the stable and saddle fixed points (brown and white circles) of the deterministic system.

initial stage of intrinsic mitochondrial apoptosis, providing a simple picture of the decision-making process by leaving aside the further stages of effector caspase activation and related apoptosis events as well as the complex crosstalk with other programmed death pathways. Second, the topology and parameters of the model are determined in close relation with biological hypothesis and experimental data in a context of chemical stress response. Last, the topological and dynamical properties of the model are featured with a single positive feedback and a bistable behavior which are fully consistent with the minimal set of ingredients that is needed to implement our adaptation-dependent noise-amplification mechanism. In particular, prior knowledge about the bifurcation properties is very helpful to compare s_c and s_{sn} thresholds and make the connection between the low-dimensional and high-dimensional models.

Therefore, the structure of the detailed model merely consists on the coupling between our above adaptation model (Eq. 4a, b) and the published model of mitochondrial apoptosis initiation[24] (right of Fig. 4a). Specifically, the adaptive species x_1 upregulates the synthesis of a pro-apoptotic BH3-only proteins (e.g., Bad, Bim, Bid), keeping in mind that intracellular stress-signaling pathways impacts the mitochondrial apoptosis pathway at various places[45,46]. Regarding the published apoptosis initiation model, the postranslational interactions between the pro-apoptotic Bh3 and Bax proteins and the anti-apoptotic Bcl-2 proteins implement a positive feedback mechanism. Pro-apoptotic signals are prone to increase the level of free Bh3 proteins with respect to the level of Bh3 proteins bound to Bcl-2. Free Bh3 proteins directly interact with inactive cytosolic Bax proteins, thereby inducing conformational change that leads to their activation and mitochondrial translocation. In turn, the activated mitochondria-localized form of Bax can also bind to Bcl-2, resulting in the release of additional free Bh3 proteins from Bh3-Bcl complexes. For a critical synthesis rate of Bh3 proteins, this positive feedback loop produces a bistable switching behavior via a saddle-node bifurcation from low to high levels of free mitochondrial Bax (Bax$_m$)[24]. Then, high enough levels of Bax$_m$ would typically induce the release of cytochrome C and mitochondrial outer membrane permeabilization (MOMP) followed by the formation and activation of the apoptosome and the execution of apoptosis.

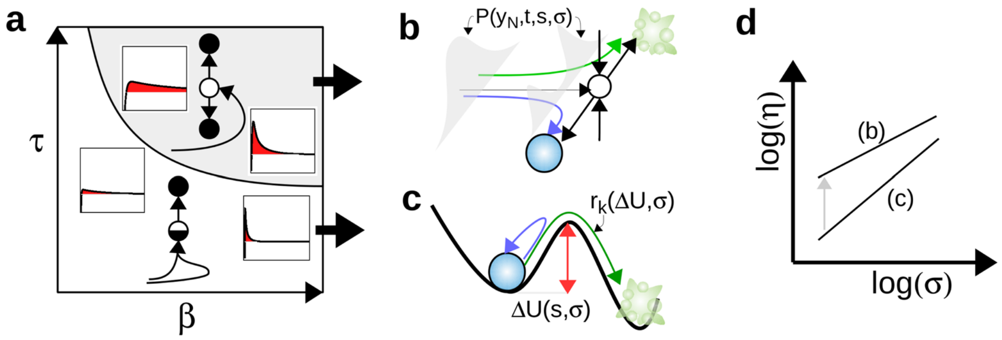

Figure 5. From deterministic to stochastic properties of two distinct cell-fate decision scenarios. (**a**) Deterministic decision mechanims in the space of adaptation parameters. (**b**–**c**) Corresponding stochastic decision mechanisms. (**d**) Qualitative change of fractionality index.

The stochastic dynamics of this regulatory network coupling an adaptation module and an apoptosis module is simulated using again the Langevin formalism of Eq. (1) (see "Methods" section) with fixed σ. Death initiation event is assumed to occur when Bax$_m$ reaches the neighborhood of the high-level steady-state branch. For large number of simulation trials, death probability can be measured as a function of the stress stimulus level, s, for distinct adaptation profiles, here with $\beta = 0$ or 1 (Fig. 4b). Simulation results reveal that the presence of adaptation leads to a probabilistic response for a broader range of stimulus, which manifests itself by a lower value of the derivative of P_{death} with respect to s/s_{50} associated to a four-fold higher value of η. Such significant difference in noise-sensitivity η correlates to well distinct types of dynamical trajectories associated with survival-death fate decisions (Fig. 4c–d). For $\beta = 1$, the overshoot response of x_1 species leads to a transient increase of Bax$_m$ during which trajectories finally diverge from each other toward the survival or death attractor (Fig. 4c). This decision is made when approaching the unstable saddle equilibria along its stable manifold (right panel of Fig. 4c). For $\beta = 0$, the level of Bax$_m$ reaches and fluctuates around a steady state of low values, before an eventual noise-induced switch toward the death state by escaping over the saddle instability along its unstable manifold (Fig. 4d).

The results obtained with a detailed model of apoptosis are thus consistent with those obtained with the model Eq. (4) involving a minimal decision module (Fig. 4b similar to Figs. 3a and 4c–d similar to Fig. 3b–c). To obtain a similar behavior, it should be noted that (i) adaptation and decision timescales had to be adjusted to each other in the detailed model such that the decrease of x_1 during the overshoot profile occurs before Bax$_m$ reaches its upper-branch steady state, and that (ii) the molecular noise impacts more the death species than the adaptive species (compare molecular noise of Bax_m and x_1 in Fig. 4c, d). A further step would thus be to check whether these two conditions are fullfiled in the detailed modeling of both the specific signaling pathways producing adaptation at the level of damage-repair pathways[47], stress-response patwhays[24] or death-ligand pathways[25,26], and of the specific death-regulatory pathways that are triggered by these diverse death-inducing stimuli. In these various cases, adaptation and fate decision processes are prone to be implemented by slightly different regulatory network topologies which may modulate the timescale and stochastic characteristics of the dynamical response and influence the extent of the adaptation-dependent fractional killing.

Theoretical description of stochastic decision properties. We have shown that the sensitivity of cell-fate decision to molecular noise depends on the state-space paths taken to reach a saddle instability, along, either, its stable manifold or its unstable manifold (Fig. 5a). In order to get further insights into the stochastic nonlinear dynamics involved in this process, we develop a perturbation approach in the limit of small noise and small stimulus changes for which specific scaling laws $\eta = a\sigma^b$ have been obtained (Fig. 3d). Scaling analysis near instabilities is a common approach to characterize qualitative dynamical behaviors as function of noise, timescales and bifurcation parameters (see textbook[42] or some case study[48,49]).

In the case of a saddle-collision scenario, perturbed trajectories evolve in the neighborhood of the deterministic trajectory $\vec{x}_c(t, s_c)$ that connects the initial condition $\vec{x}_c(t=0) = \vec{x}_{st1}(s=0)$ and the saddle fixed point $\vec{x}_c(t \to \infty) = \vec{x}_{sad}(s_c)$ (Figs. 2d and 3d) and, thus, live on the stable manifold of this saddle $\mathcal{W}^s(\vec{x}_{sad})$ that separates the different fate attractors. Along this singular deterministic trajectory, some local Lyapunov stability exponents (i.e., time-dependent eigenvalues of the Jacobian matrix $J(\vec{x}_c(t))$) become positive such as to amplify transverse perturbations due to molecular noise or heterogeneous initial conditions. Mathematically speaking, linearization of Eq. (1a) about $\vec{x}_c(t)$ defines a class of Langevin equations for the perturbed trajectories $\vec{y}(t) = \vec{x}(t, s_c + \delta s, \sigma) - \vec{x}_c(t)$ whose solution can be decomposed as $\vec{y}(t) = \delta s\, \vec{y}_{\delta s}(t) + \sigma\, \vec{y}_\sigma(t)$ where

$$\vec{y}_{\delta s/\sigma}(t) = \int_0^t \Pi(t, t')\, \vec{b}_{\delta s/\sigma}(t')dt' . \quad (7)$$

$\Pi(t, t')$ is the principal fundamental matrix and $\vec{b}_{\delta s/\sigma}$ are the normalized stimuli and noise perturbation vectors given by:

$$b_{\delta s,i}(t) = \sum_j \nu_{ji} \frac{\partial a_j}{\partial s}(\vec{x}_c(t)) \tag{8a}$$

$$b_{\sigma,i}(t) = \sum_j \nu_{ji} \sqrt{a_j(\vec{x}_c(t))}\tilde{\xi}_j(t)\,. \tag{8b}$$

To compute the fractionality index η, the key statement is that fate decisions (resp., probability) are determined by the deviation (resp., distribution) of trajectories onto the normal direction y_N of the $(N-1)$-dimensional stable manifold of the saddle. The mean and variance of the normal distribution $P(y_N, t)$ evolves in time until the decision time t^* at which the distribution splits and many trajectories leave the neighborhood of $\vec{x}_c(t)$ (Fig. 5b). Rewriting Eq. (2) as $P_D = \int_{\mathbb{R}+} P(y_N, t^*)dy_N$ and decomposing $\frac{dP_D}{ds} = (\frac{dP_D}{d\langle y_N\rangle})(\frac{d\langle y_N\rangle}{ds}) = (2\pi\sigma^2\langle y_{N,\sigma}^2\rangle)^{-1/2}(\langle y_{N,\delta s}\rangle)$, we can derive the following expression for η:

$$\eta = \sqrt{\frac{\pi}{2}} \frac{\sqrt{\langle y_{N,\sigma}(t^*)^2\rangle}}{s_{50}\langle y_{N,\delta s}(t^*)\rangle}\sigma\,. \tag{9}$$

This formula shows an asymptotic scaling law $\eta \propto \sigma$ (Figs. 3d and 5d) while the prefactor depends in a sophisticated manner on the local stability properties (via Π) and sensitivity properties (via $\vec{b}$) of the transient trajectory. A similar derivation in the 1D case has been previously performed to show that this scaling law also depends on the speed of the trajectory toward the saddle instability[48].

The sensitivity to noise is very different in the other scenario of noise-induced escape from a stable state ($\vec{x}_{st1}$) over a saddle barrier ($\vec{x}_{sad}$), which is a very common behavior associated with the escape from metastability[49,50]. For this decision-making regime, an effective potential U, a potential barrier $\Delta(s) = U(\vec{x}_{sad}(s)) - U(\vec{x}_{st1}(s))$ and a Kramers escape rate $r_K(s) \propto \exp(2\Delta(s)/\sigma^2)$ can be usually defined, even for multi-dimensional systems and multiplicative noise[51] (Fig. 5c). Given a fate-decision probability $P_D(t) \approx 1 - \exp(-r_K t)$, the fractionality index can be derived and approximated as :

$$\eta = \left(\frac{s_{50}\ln 2}{r_K}\frac{dr_K}{ds}\right)^{-1} \approx \frac{\sigma^2}{(2\ln 2)\, s_{50}\, \partial_s \Delta}\,. \tag{10}$$

For the one-dimensional model of bistability used in Eq. (4c), the particular scaling relation $s_{50}\,\partial_s\Delta \sim \sigma^{0.8}$ (as the threshold s_{50} depends on σ) leads to the scaling law $\eta \propto \sigma^{1.2}$ obtained in Fig. 3d.

To conclude, these very distinct formulas for η highlight that the conversion of intracellular fluctuations into heterogeneous cellular fate response sharply differ depending on the transition scenario. The saddle-collision scenario is characterized with the amplification of small perturbations due to the local instability of trajectories when approaching the saddle state during the overshoot of decision variables (e.g., x_3 or Bax$_m$). In contrast, the more common scenario of a noise-induced escape from a metastable state does not display this amplification mechanism, while the transition rate r_K is very sensitive to stimulus level due to the exponential-like dependency on the saddle barrier height.

Discussion

The present modeling study deciphers the role of adaptation dynamics in promoting cell-fate heterogeneity associated for instance with the fractional killing behavior. A common property of adaptation is the transient overshoot of some cellular variables above its steady state value, which can be implemented by diverse circuit topologies[32] and which is subjected to tradeoffs associated with homeostatic or sensory process[33,34,52,53]. In addition, we propose that this transient overshoot dynamics can also significantly impact fate-switching behaviors, so as to extend the stimulus range of fate heterogeneity and to allow for tunable fate probability. This adaptation-dependent fate stochasticity relies on the manner how the overshoot of some intracellular species drive cell state in the neighboorhohd of a saddle instability, rather than a saddle-node instability, along a path where molecular noise are more prone to promote divergent decisions. This noise-amplification behavior illustrates how molecular noise and instability mechanisms can cooperate to shape cellular dynamics, like genetic timers[54], boundary formation[55] or versatile sensory processing[56].

The biological relevance of the proposed mechanism is most likely in a context of fractional killing for which the choice between life and death depends on adaptation processes. The timescales of those adaptation responses range from half an hour to few hours depending on stress type and regulatory mechanisms[47,57,58] which is of the range of magnitude of the initiator caspase rise time and death onset timing. Moreover, noise-induced fate heterogeneity is the most effective when fluctuating variables are those involved in the positive feedback that triggers death initiation. This requirement is consistent with modeling evidences that variability in diverse regulatory molecules can contribute in very different ways to variability in cell death outcomes[20] and that the main contributions seem to occur in the initial decision commitement phase, whether it is at the level of the fluctuations of short-lived antiapoptotic proteins[22] or the stochastic assembly of DISC/RIPoptosome platform[23]. The manner how cell fate is determined by the impact of these fluctuations at the level of concentration trajectories has been also investigated[24,25,27]. In relation to these studies, our study presents a broad and comprehensive view of this cooperative process and, thus, provides strategies, by monitoring transient characteristics, to either increase or reduce fractional killing.

The profile characteristics of adaptation dynamics, such as the ratio between its maximal and steady-state values, are highly sensitive to the temporal profile of the stimulus. Ramp increase of a stimulus or a preconditioning stimuli are known to reduce the transient overshoot behavior. This feature has been exploited to test the role of adaptation in oxidative stress response of yeast[59], the osmotic stress response of yeast[60] or ethanol stress in Bacillus[61]. In case of stress-induced fate response, monitoring the stress stimulus profile would therefore be expected to modulate not only threshold stimulus level (s_{50}), but also the degree of heterogeneity of the response (η). This provides a practical mean to test the role of adaptation for cell-fate heterogeneity, and to design dose delivery protocols of treatment to cope with fractional killing of cancer cells or microbial organisms.

It is tempting to extrapolate the biological relevance of such adaptation-dependent mechanism beyond the scope of fractional killing and transient adaptation dynamics. The mechanism itself only requires a regulatory network featured with an upsteam overshoot response and a downstream switching response, which could be implemented by diverse network topologies and in diverse cell-fate contexts. For instance, overshoot dynamics can also occur in regulatory systems comprising incoherent feedforward loops[32], but also in excitable or pulsatile systems combining negative and positive feedback loops. For the latter case, numerous signaling pathways, such as P53, Erk or NF-κB, display a versatile pulsatile dynamics, which has been proposed to expand signal-processing capabilities and determine cell fate accordingly[14,15]. In relation to our result, the transient and stochastic characteristics of these signaling dynamics may also suggest a role for promoting cell-fate heterogeneity. This is supported by some experimental evidences that have mapped the cell-cell variability of the pulsing dynamics of Erk[10,11], p53[62,63], β-catenin[13] and NF-κB[12] with the heterogeneity of cell-fate outcomes. Data-driven and fine-grained modeling of specific dynamic signaling and fate-regulatory pathways[11,20,62,64] are definitively the step further to evaluate on a case-by-case basis to which extent transient adaptation or pulsing dynamics may contribute, fortuitously or functionally, to cell-fate heterogeneity.

Methods

Coarse-grained model. The set of regulatory reactions depicted in Fig. 3a consists in the following basal/regulated synthesis terms and basal/regulated degradation terms:

$$\overset{b_1}{\rightarrow} X_1 \ ; \ \overset{b_{S1}S}{\rightarrow} X_1 \ ; \ \overset{b_2}{\rightarrow} X_2 \ ; \ X_1 \overset{b_{12}}{\rightarrow} X_2 + X_1 \ ; \ X_1 \overset{b_{13}}{\rightarrow} X_3 + X_1 \ ; \ \xrightarrow{b_{33} f_h(X_3, K_3)} X_3 \tag{11a}$$

$$X_1 + X_2 \overset{d_1}{\rightarrow} X_2 \ ; \ X_2 \overset{d_2}{\rightarrow} \emptyset \ ; \ X_3 \overset{d_3}{\rightarrow} \emptyset \, , \tag{11b}$$

which can be translated into a system of differential equations using the law of mass action :

$$\dot{X_1} = b_1 + b_{S1} S - d_1 X_2 X_1 \, , \tag{12a}$$

$$\dot{X_2} = b_2 + b_{12} X_1 - d_2 R \, , \tag{12b}$$

$$\dot{X_3} = b_{13} X_1 + b_{33} \frac{X_3^2}{K_3 + X_3^2} - d_3 X_3 \, . \tag{12c}$$

To obtain the set of Eq. (4), we perform a nondimenzionalization procedure to reduce the number of parameters and to define effective parameters that control separately different features of the dynamics such as response timescales, transient nonlinear response and steady states. Accordingly, we have introduced dimensionless time $\tilde{t}$, concentration x_i and stimulus s and defined rescaling variables ($X_{i,0}$, S_0) and aggregate parameters (τ_i, β and k_i), as the following:

$$\tilde{t} = t \, d_3 \ ; \ x_i = X_i / X_{i,0} \ ; \ s = S / S_0 \tag{13a}$$

$$X_{1,0} = \frac{k_2 d_3 X_{3,0}}{b_{13}} \ ; \ X_{2,0} = \frac{b_{12} X_{1,0} + b_2}{d_2} \ ; \ X_{3,0} = \frac{b_{33}}{d_3} \ ; \ S_0 = \frac{d_1 X_{1,0} X_{2,0} - b_1}{b_{S1}} \tag{13b}$$

$$\tau = \frac{d_3}{d_2} \ ; \ \tau_1 = \frac{d_3}{d_1 X_{2,0}} \ ; \ k_1 = 1 - \frac{b_1}{d_1 X_{1,0} X_{2,0}} \ ; \ \beta = \frac{b_{12} X_{1,0}}{d_2 X_{2,0}} \ ; \ k_3 = \frac{K_3}{X_{3,0}^2} \, . \tag{13c}$$

These changes of variables and parameters simplify Eq. (12) into Eq. (4) where dimensionless time $\tilde{t}$ is noted t again for simplicity. The chemical Langevin equation associated to Eq. (4) is also characterised with a rescaled noise $\sigma = (\Omega d_3 X_0)^{-1/2}$ where Ω is the system size and $X_{i,0} \equiv X_0 \, \forall i$. Finally, reaction rates and stoichiometry matrices are given by:

$$\vec{a} = \left[\frac{1 - k_1}{\tau_1}, \frac{k_1 s}{\tau_1}, \frac{x_1 x_2}{\tau_1}, \frac{1 - \beta}{\tau}, \frac{\beta x_1}{\tau}, \frac{x_2}{\tau}, k_2 x_1, \frac{k_3 x_3^2}{k_4 + x_3^2}, x_3 \right]^T \ ; \quad \nu = \begin{bmatrix} 1 & 1 & -1 & 0 & 0 & 0 & 0 & 0 & 0 \\ 0 & 0 & 0 & 1 & 1 & -1 & 0 & 0 & 0 \\ 0 & 0 & 0 & 0 & 0 & 0 & 1 & 1 & -1 \end{bmatrix} \tag{14}$$

where $k_1 = 0.9$, $k_2 = 0.056$, $k_3 = 1$, $k_4 = 0.2$, $\tau_1 = 0.1$, while β and τ are varied.

Detailed model. Equations and parameters of the biochemical reaction model of apoptosis initiation have been taken from[24]. From the original model, the equations for CIAP, p53 and Mdm2 have been removed and the equation for Bh3T has been changed to incorporate activation by x_1 and to display a slower response:

$$\frac{d[Bh3T]}{dt} = k_{sBH3} + k_{s2}\, x_1 + k_{s3}[C8] - k_{dBH3}[Bh3T] \tag{15}$$

The corresponding Langevin equation (Eq. 1) considers the following state vectors, reaction rate vectors and stoichiometry matrix:

$$\vec{x} = [x_1, x_2, [Bh3T], [C8], [BaxmT], [Baxm:Bcl], [Bh3:Bcl])^T \,;\, \vec{y} = [[BaxT] - x_5, x_5 - x_6, x_3 - x_7, [BclT] - x_5 - x_6]^T \tag{16}$$

$$a_{1,.,12} = \left[\frac{1-k_1}{\tau_1}, \frac{k_1 s}{\tau_1}, \frac{x_1 x_2}{\tau_1}, \frac{1-\beta}{\tau}, \frac{\beta\, x_1}{\tau}, \frac{x_2}{\tau}, k_{sBh3}, k_{s2}\, x_1, k_{s3}\, x_4, k_{dBh3}\, x_3, k_{aC8}, k_{iC8}\, x_4\right]^T \tag{17a}$$

$$a_{13,.,20} = \left[k_{f1}\, y_1, k_{f2}\, y_3\, y_1, k_b\, x_5, k_{asXC}\, y_4\, y_2, k_{dsXC}\, x_6, k_b\, x_6, k_{asHC}\, y_4\, y_3, k_{dsHC}\, x_7\right]^T \tag{17b}$$

where $k_{sBH3} = 0.025,\ k_{s2} = 0.02\ k_{s3} = k_{dBH3} = 0.25,\ k_{aC8} = 0.03,\ k_{iC8} = 0.1,\ k_{f1} = 1,\ k_{f2} = 300,\ k_b = 2$, $k_{asXC} = 9000, k_{dsXC} = 0.05, k_{asHC} = 1000, k_{dsXC} = 0.01, [BaxT] = 1$ and $[BclT] = 0.85$.

$$\nu = \begin{bmatrix} 1 & 1 & -1 & 0 & 0 & 0 & 0 & 0 & 0 & 0 & 0 & 0 & 0 & 0 & 0 & 0 & 0 & 0 & 0 & 0 \\ 0 & 0 & 0 & 1 & 1 & -1 & 0 & 0 & 0 & 0 & 0 & 0 & 0 & 0 & 0 & 0 & 0 & 0 & 0 & 0 \\ 0 & 0 & 0 & 0 & 0 & 0 & 1 & 1 & 1 & -1 & 0 & 0 & 0 & 0 & 0 & 0 & 0 & 0 & 0 & 0 \\ 0 & 0 & 0 & 0 & 0 & 0 & 0 & 0 & 0 & 0 & 1 & -1 & 0 & 0 & 0 & 0 & 0 & 0 & 0 & 0 \\ 0 & 0 & 0 & 0 & 0 & 0 & 0 & 0 & 0 & 0 & 0 & 0 & 1 & 1 & -1 & 0 & 0 & 0 & 0 & 0 \\ 0 & 0 & 0 & 0 & 0 & 0 & 0 & 0 & 0 & 0 & 0 & 0 & 0 & 0 & 0 & 1 & -1 & -1 & 0 & 0 \\ 0 & 0 & 0 & 0 & 0 & 0 & 0 & 0 & 0 & 0 & 0 & 0 & 0 & 0 & 0 & 0 & 0 & 0 & 1 & -1 \end{bmatrix} \tag{18}$$

Numerical simulation and dynamical analysis. For both models, numerical integration of Langevin equations are performed with 4th-order Runge-Kutta method and probability distribution $P_D(s)$ are plotted with a statistics of 2000 trials with a measurement time of $t^* = 500$. η is computed by interpolating $P_D(s)$ and approximating $\partial_s P_D(s_{50}) \approx \frac{0.4}{s_{70} - s_{30}}$ where $P_D(s_x) = x/100$. State-space trajectories are represented in some relevant subspace of the state space where the steady states $\vec{x}_{st/sad/sn}$ satisfying $f(\vec{x}) = 0$ are represented by the conventional filled/empty/half-empty circles. The steady-state branches $\vec{x}_{st/sad}(s)$ are also represented for the sake of comparison for different parameter values. The set of mathematical notations used are given in the Table 1.

Received: 29 April 2020; Accepted: 22 September 2020

References

1. Johnston, R. J. Jr. & Desplan, C. Stochastic mechanisms of cell fate specification that yield random or robust outcomes. *Annu. Rev. Cell Dev. Biol.* **26**, 689–719 (2010).
2. Veening, J.-W., Smits, W. K. & Kuipers, O. P. Bistability, epigenetics, and bet-hedging in bacteria. *Annu. Rev. Microbiol.* **62**, 193–210 (2008).
3. Simons, B. D. & Clevers, H. Strategies for homeostatic stem cell self-renewal in adult tissues. *Cell* **145**, 851–862 (2011).
4. Pisco, A. O. *et al.* Non-darwinian dynamics in therapy-induced cancer drug resistance. *Nat. Commun.* **4**, 2467 (2013).
5. Losick, R. & Desplan, C. Stochasticity and cell fate. *Science* **320**, 65–68 (2008).
6. Balázsi, G., van Oudenaarden, A. & Collins, J. J. Cellular decision making and biological noise: From microbes to mammals. *Cell* **144**, 910–925 (2011).
7. Urban, E. A. & Johnston, R. J. Jr. Buffering and amplifying transcriptional noise during cell fate specification. *Front. Genet.* **9**, 591 (2018).
8. Schultz, D. *et al.* Turning oscillations into opportunities: Lessons from a bacterial decision gate. *Sci. Rep.* **3**, 1668 (2013).
9. Imayoshi, I. *et al.* Oscillatory control of factors determining multipotency and fate in mouse neural progenitors. *Science* **342**, 1203–8. https://doi.org/10.1126/science.1242366 (2013).
10. Albeck, J. G., Mills, G. B. & Brugge, J. S. Frequency-modulated pulses of ERK activity transmit quantitative proliferation signals. *Mol. Cell* **49**, 249–261 (2013).
11. Ryu, H. *et al.* Frequency modulation of ERK activation dynamics rewires cell fate. *Mol. Syst. Biol.* **11**, 838 (2015).
12. Zhang, Q. *et al.* NF-κB dynamics discriminate between TNF doses in single cells. *Cell Syst.* **5**, 638–645 (2017).
13. Kroll, J. R., Tsiaxiras, J. & van Zon, J. S. Variability in β-catenin pulse dynamics in a stochastic cell fate decision in *C. elegans*. *Dev. Biol.* **461**, 110–123 (2020).
14. Levine, J. H., Lin, Y. & Elowitz, M. B. Functional roles of pulsing in genetic circuits. *Science* **342**, 1193–1200 (2013).
15. Isomura, A. & Kageyama, R. Ultradian oscillations and pulses: Coordinating cellular responses and cell fate decisions. *Development* **141**, 3627–3636 (2014).
16. Pujadas, E. & Feinberg, A. P. Regulated noise in the epigenetic landscape of development and disease. *Cell* **148**, 1123–1131 (2012).
17. Antolović, V., Lenn, T., Miermont, A. & Chubb, J. R. Transition state dynamics during a stochastic fate choice. *Development* **146**, https://doi.org/10.1242/dev.173740 (2019).
18. Pfeuty, B. & Kaneko, K. Requirements for efficient cell-type proportioning: Regulatory timescales, stochasticity and lateral inhibition. *Phys. Biol.* **13**, 026007. https://doi.org/10.1088/1478-3975/13/2/026007 (2016).
19. Spencer, S. L., Gaudet, S., Albeck, J. G., Burke, J. M. & Sorger, P. K. Non-genetic origins of cell-to-cell variability in TRAIL-induced apoptosis. *Nature* **459**, 428–432. https://doi.org/10.1038/nature08012 (2009).
20. Gaudet, S., Spencer, S. L., Chen, W. W. & Sorger, P. K. Exploring the contextual sensitivity of factors that determine cell-to-cell variability in receptor-mediated apoptosis. *PLoS Comput. Biol.* **8**, e1002482 (2012).
21. Ooi, H. K. & Ma, L. Modeling heterogeneous responsiveness of intrinsic apoptosis pathway. *BMC Syst. Biol.* **7**, 65 (2013).
22. Bertaux, F., Stoma, S., Drasdo, D. & Batt, G. Modeling dynamics of cell-to-cell variability in TRAIL-induced apoptosis explains fractional killing and predicts reversible resistance. *PLoS Comput. Biol.* **10**, e1003893 (2014).
23. Matveeva, A. *et al.* Heterogeneous responses to low level death receptor activation are explained by random molecular assembly of the caspase-8 activation platform. *PLoS Comput. Biol.* **15**, e1007374 (2019).

24. Ballweg, R., Paek, A. L. & Zhang, T. A dynamical framework for complex fractional killing. *Sci. Rep.* **7**, 8002. https://doi.org/10.1038/s41598-017-07422-2 (2017).
25. Roux, J. *et al.* Fractional killing arises from cell-to-cell variability in overcoming a caspase activity threshold. *Mol. Syst. Biol.* **11**, 803. https://doi.org/10.15252/msb.20145584 (2015).
26. Schleich, K. *et al.* Molecular architecture of the DED chains at the DISC: Regulation of procaspase-8 activation by short DED proteins c-FLIP and procaspase-8 prodomain. *Cell Death Differ.* **23**, 681–694 (2016).
27. Paek, A. L., Liu, J. C., Loewer, A., Forrester, W. C. & Lahav, G. Cell-to-cell variation in p53 dynamics leads to fractional killing. *Cell* **165**, 631–642 (2016).
28. Ak, P. & Levine, A. J. p53 and NF-κB: different strategies for responding to stress lead to a functional antagonism. *FASEB J.* **24**, 3643–3652 (2010).
29. Fulda, S., Gorman, A. M., Hori, O. & Samali, A. Cellular stress responses: cell survival and cell death. *Int. J. Cell Biol.* **2010**, 214074 (2010).
30. Hotamisligil, G. S. & Davis, R. J. Cell signaling and stress responses. *Cold Spring Harb. Perspect. Biol.* **8**, a006072 (2016).
31. Buchbinder, J. H., Pischel, D., Sundmacher, K., Flassig, R. J. & Lavrik, I. N. Quantitative single cell analysis uncovers the life/death decision in cd95 network. *PLoS Comput. Biol.* **14**, e1006368 (2018).
32. Ma, W., Trusina, A., El-Samad, H., Lim, W. A. & Tang, C. Defining network topologies that can achieve biochemical adaptation. *Cell* **138**, 760–773 (2009).
33. Szekely, P., Sheftel, H., Mayo, A. & Alon, U. Evolutionary tradeoffs between economy and effectiveness in biological homeostasis systems. *PLoS Comput. Biol.* **9**, e1003163. https://doi.org/10.1371/journal.pcbi.1003163 (2013).
34. Jia, C. & Qian, M. Nonequilibrium enhances adaptation efficiency of stochastic biochemical systems. *PloS ONE* **11**, e0155838 (2016).
35. Tian, T. & Burrage, K. . Stochastic models for regulatory networks of the genetic toggle switch. *Proc. Natl. Acad. Sci. USA* **103**, 8372–8377 (2006).
36. Shu, C.-C., Chatterjee, A., Dunny, G., Hu, W.-S. & Ramkrishna, D. Bistability versus bimodal distributions in gene regulatory processes from population balance. *PLoS Comput. Biol.* **7**, e1002140 (2011).
37. Thomas, P. ., Popović, N. & Grima, R. Phenotypic switching in gene regulatory networks. *Proc. Natl. Acad. Sci. USA* **111**, 6994–6999 (2014).
38. Ge, H., Qian, H. & Xie, X. S. Stochastic phenotype transition of a single cell in an intermediate region of gene state switching. *Phys. Rev. Lett.* **114**, 078101 (2015).
39. Hortsch, S. K. & Kremling, A. Characterization of noise in multistable genetic circuits reveals ways to modulate heterogeneity. *PLoS ONE* **13**, e0194779 (2018).
40. Gillespie, D. T. The chemical langevin equation. *J. Chem. Phys.* **113**, 297–306 (2000).
41. Grima, R., Thomas, P. & Straube, A. V. How accurate are the nonlinear chemical Fokker–Planck and chemical langevin equations?. *J. Chem. Phys.* **135**, 084103 (2011).
42. Berglund, N. & Gentz, B. *Noise-induced phenomena in slow-fast dynamical systems: A sample-paths approach* (Springer, Berlin 2006).
43. Labavić, D., Ladjimi, M. T., Thommen, Q. & Pfeuty, B. Scaling laws of cell-fate responses to transient stress. *J. Theoret. Biol.* **478**, 14–25 (2019).
44. Fuchs, Y. & Steller, H. Live to die another way: Modes of programmed cell death and the signals emanating from dying cells. *Nat. Rev. Mol. Cell Biol.* **16**, 329–344 (2015).
45. Green, D. R. & Llambi, F. Cell death signaling. *Cold Spring Harb. Perspect. Biol.* **7**, a006080 (2015).
46. Jeng, P. S., Inoue-Yamauchi, A., Hsieh, J. J. & Cheng, E. H. Bh3-dependent and independent activation of BAX and BAK in mitochondrial apoptosis. *Curr. Opin. Physiol.* **3**, 71–81 (2018).
47. Guilbert, M., Anquez, F., Pruvost, A., Thommen, Q. & Courtade, E. Protein level variability determines phenotypic heterogeneity in proteotoxic stress response. *FEBS J.*, https://doi.org/10.1111/febs.15297 (2020).
48. Pfeuty, B. & Kaneko, K. Reliable binary cell-fate decisions based on oscillations. *Phys. Rev. E* **89**, 022707. https://doi.org/10.1103/PhysRevE.89.022707 (2014).
49. Herbert, C. & Bouchet, F. Predictability of escape for a stochastic saddle-node bifurcation: When rare events are typical. *Phys. Rev. E* **96**, 030201 (2017).
50. Hanggi, P. Escape from a metastable state. *J. Stat. Phys.* **42**, 105–148 (1986).
51. Rosas, A., Lindenberg, K. & Pinto, I. L. D. Kramers' rate for systems with multiplicative noise. *Phys. Rev. E* **94**, 012101 (2016).
52. Lan, G., Sartori, P., Neumann, S., Sourjik, V. & Tu, Y. The energy-speed-accuracy trade-off in sensory adaptation. *Nat. Phys.* **8**, 422–428 (2012).
53. Olsman, N. *et al.* Hard limits and performance tradeoffs in a class of antithetic integral feedback networks. *Cell Syst.* **9**, 49–63 (2019).
54. Turcotte, M., Garcia-Ojalvo, J. . & Süel, G. . M. . A genetic timer through noise-induced stabilization of an unstable state. *Proc. Natl. Acad. Sci. USA* **105**, 15732–15737 (2008).
55. Perez-Carrasco, R., Guerrero, P., Briscoe, J. & Page, K. M. Intrinsic noise profoundly alters the dynamics and steady state of morphogen-controlled bistable genetic switches. *PLoS Comput. Biol.* **12**, e1005154 (2016).
56. Salvi, J. D., Maoiléidigh, D. Ó. & Hudspeth, A. Identification of bifurcations from observations of noisy biological oscillators. *Biophys. J.* **111**, 798–812 (2016).
57. Kuehne, A. *et al.* Acute activation of oxidative pentose phosphate pathway as first-line response to oxidative stress in human skin cells. *Mol. Cell* **59**, 359–371. https://doi.org/10.1016/J.MOLCEL.2015.06.017 (2015).
58. Zhang, C.-S. *et al.* Fructose-1, 6-bisphosphate and aldolase mediate glucose sensing by AMPK. *Nature* **548**, 112–116 (2017).
59. Goulev, Y. *et al.* Nonlinear feedback drives homeostatic plasticity in H2O2 stress response. *Elife* **6**, 1–33. https://doi.org/10.7554/eLife.23971 (2017).
60. Mitchell, A., Wei, P. & Lim, W. A. Oscillatory stress stimulation uncovers an achilles' heel of the yeast MAPK signaling network. *Science* **350**, 1379–1383 (2015).
61. Young, J. W., Locke, J. C. & Elowitz, M. B. Rate of environmental change determines stress response specificity. *Proc. Natl. Acad. Sci. USA* **110**, 4140–4145 (2013).
62. Moenke, G. *et al.* Excitability in the p53 network mediates robust signaling with tunable activation thresholds in single cells. *Sci. Rep.* **7**, 46571 (2017).
63. Yang, H. W., Chung, M., Kudo, T. & Meyer, T. Competing memories of mitogen and p53 signalling control cell-cycle entry. *Nature* **549**, 404–408 (2017).
64. Pfeuty, B. A computational model for the coordination of neural progenitor self-renewal and differentiation through Hes1 dynamics. *Development* **142**, 477–485 (2015).

Acknowledgements

This work has been supported by the LABEX CEMPI (ANR-11-LABX-0007) and by the Ministry of Higher Education and Research, Hauts de France council and European Regional Development Fund (ERDF) through the Contrat de Projets Etat-Region (CPER Photonics for Society P4S).

Author contributions

B. P. and Q.T. conceived and conducted the research, J.H., D.L. and B.P. performed simulations and analyzed the model, B.P. wrote the main manuscript text. All authors reviewed the manuscript.

Competing interests

The authors declare no competing interests.

Additional information

Correspondence and requests for materials should be addressed to B.P.

Reprints and permissions information is available at www.nature.com/reprints.

iScience

CellPress
OPEN ACCESS

Article

Quantitative modeling of pentose phosphate pathway response to oxidative stress reveals a cooperative regulatory strategy

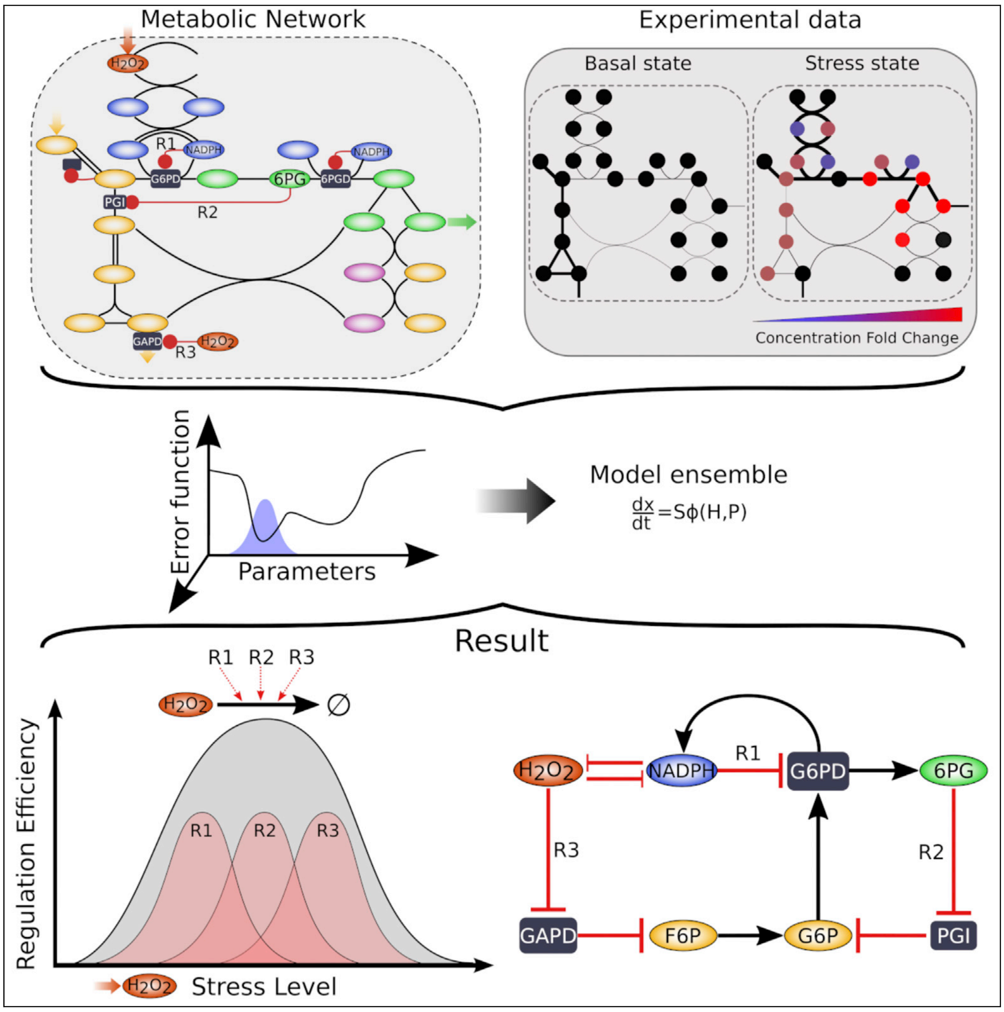

Julien Hurbain, Quentin Thommen, Francois Anquez, Benjamin Pfeuty

benjamin.pfeuty@univ-lille.fr

Highlights

Kinetic model of PP pathway is inferred from 13C-fluxomics and metabolomics data

Metabolic regulations enhance carbon flux rerouting to counteract oxidative stress

Inhibition of glycolytic enzymes and upregulation of G6PD have complementary roles

The regulatory pattern enables efficient metabolic control over a broad range of stress

Hurbain et al., iScience *25*, 104681
August 19, 2022 © 2022 The Authors.
https://doi.org/10.1016/j.isci.2022.104681

iScience

CellPress
OPEN ACCESS

Article

Quantitative modeling of pentose phosphate pathway response to oxidative stress reveals a cooperative regulatory strategy

Julien Hurbain,[1] Quentin Thommen,[2] Francois Anquez,[1] and Benjamin Pfeuty[1,3,*]

SUMMARY

Living cells use signaling and regulatory mechanisms to adapt to environmental stresses. Adaptation to oxidative stress involves the regulation of many enzymes in both glycolysis and pentose phosphate pathways (PPP), so as to support PPP-driven NADPH recycling for antioxidant defense. The underlying regulatory logic is investigated by developing a kinetic modeling approach fueled with metabolomics and ^{13}C-fluxomics datasets from human fibroblast cells. Bayesian parameter estimation and phenotypic analysis of models highlight complementary roles for several metabolite-enzyme regulations. Specifically, carbon flux rerouting into PPP involves a tight coordination between the upregulation of G6PD activity concomitant to a decreased NADPH/NADP$^+$ ratio and the differential control of downward and upward glycolytic fluxes through the joint inhibition of PGI and GAPD enzymes. Such functional interplay between distinct regulatory feedbacks promotes efficient detoxification and homeostasis response over a broad range of stress level, but can also explain paradoxical pertubation phenotypes for instance reported for 6PGD modulation in mammalian cells.

INTRODUCTION

The oxidative pentose phosphate pathway (oxPPP) is a fundamental pathway of glucose metabolism involved in nucleotide biosynthesis and redox homeostasis (Stincone et al., 2015). Its role is prominent following an oxidative stress to generate NADPH required for fueling antioxidant machinery and producing biosynthetic precursors required for repairing DNA damage. A significant increase of metabolic flux in this pathway is commonly observed in any living cells subjected to oxidative stress (Ben-Yoseph et al., 1996; Ralser et al., 2007; LaMonte et al., 2013; Kuehne et al., 2015; Christodoulou et al., 2018; Nikel et al., 2021). A common rationale for such metabolic flux rerouting relies on the acknowledged roles of NADP as a coenzyme and NADPH as a competitive inhibitor of the first oxidation reaction of the oxPPP (Warburg and Christian, 1936; Negelein and Haas, 1935; Eggleston and Krebs, 1974). The scavenging activity of glutathione antioxidant is coupled to the oxidation of NADPH into NADP$^+$, which is therefore prone to increase G6PD activity and NADPH production. However, oxidative stress has also been shown to induce the allosteric or oxidative inhibition of diverse glycolytic enzymes such as PGI (Kuehne et al., 2015; Dubreuil et al., 2020), GAPD (Ralser et al., 2007; Peralta et al., 2015), PK (Anastasiou et al., 2011), or TPI (Grüning et al., 2011, 2014). A complex pattern of regulation at the levels of both PPP and glycolysis raises the question of their coordination for efficient metabolic rerouting.

The metabolic network combining glycolytic and pentose phosphate pathways displays a complicate branching structure comprising both reversible and irreversible reactions, which obstructs intuitive understanding of multisite metabolic regulation. To investigate complex regulatory patterns, the kinetic modeling framework is often used to disentangle the respective and cooperative roles of multiple feedback regulations (Relógio et al., 2011; Pfeuty et al., 2018; Sander et al., 2019). Several kinetic models have addressed oxPPP dynamics with respect to a specific organism and experimental dataset (Thorburn and Kuchel, 1985; Schuster and Holzhütter, 1995; Kerkhoven et al., 2013). Nowadays, advanced metabolomics and fluxomics studies such as kinetic measurements of concentrations and isotopic labeling patterns provide a rich material to build increasingly reliable and comprehensive kinetic models (Miskovic et al., 2015; Foster et al., 2019; Hameri et al., 2019). Regarding the regulation of the oxidative stress response, such data are available and have already been analyzed in terms of significance and ranking of diverse

[1] CNRS, UMR 8523 - PhLAM - Physique des Lasers Atomes et Molécules, University of Lille, 59000 Lille, France

[2] CNRS, Inserm, CHU Lille, Institut Pasteur de Lille, UMR9020-U1277 - CANTHER - Cancer Heterogeneity Plasticity and Resistance to Therapies, University of Lille, 59000 Lille, France

[3] Lead contact

*Correspondence: benjamin.pfeuty@univ-lille.fr

https://doi.org/10.1016/j.isci.2022.104681

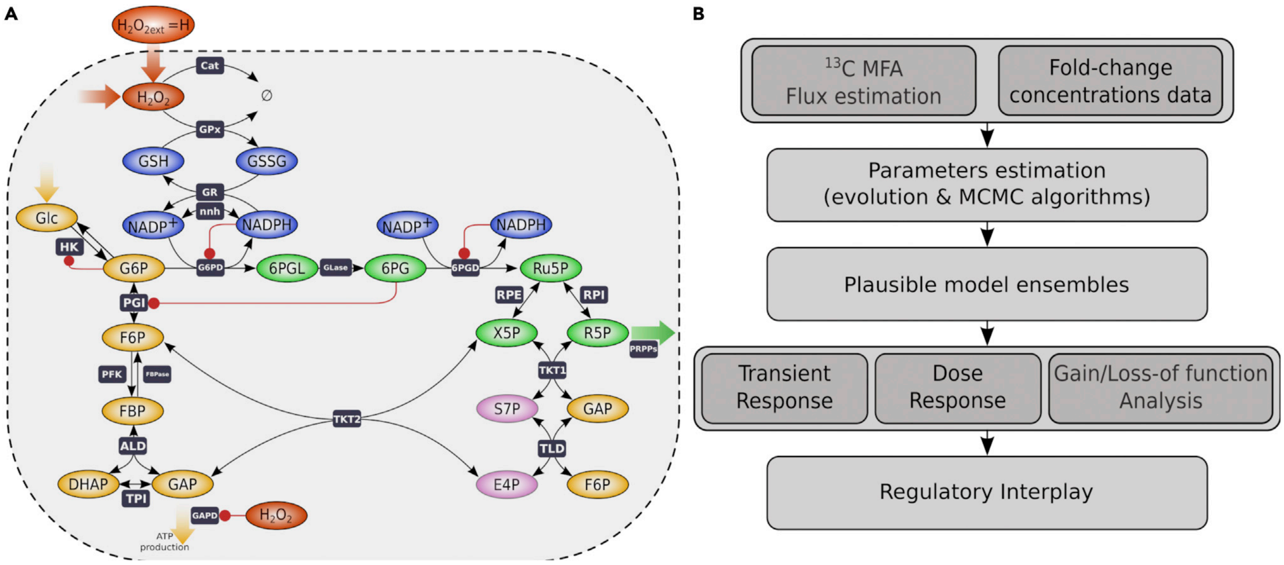

Figure 1. Modeling workflow

(A) Selected set of metabolic and regulatory pathways involved in oxidative stress response (see also Figure S1). The network comprises the glutathione, glycolytic, and pentose phosphate pathways supplemented with a selected set of allosteric and oxidative regulations (red arrows).

(B) Modeling workflow from the integration of ^{13}C fluxomics and metabolomics data (Kuehne et al., 2015) to parameter estimation of kinetic model ensemble and regulation analysis of transient response, dose response, and gain/loss-of-function phenotypes.

regulatory hypothesis (Kuehne et al., 2015, 2017; Christodoulou et al., 2018). However, questions remain about the interplay and cooperativity between those different regulatory mechanisms.

In the present study, we aim to build a class of kinetic models inferred from a comprehensive dataset associated with the oxidative stress response of neonatal human skin fibroblasts (Kuehne et al., 2015). On the one hand, the network structure of the model is chosen to fit with the available data and with the objective to understand metabolic flux rerouting for H_2O_2 detoxification. On the other hand, flux analysis from ^{13}C-labeling data and parameter estimation from flux and concentration data are based on Monte Carlo sampling methods (Saa and Nielsen, 2016; Valderrama-Bahamóndez and Fröhlich, 2019; Theorell and Nöh, 2020) so as generate a representative sample of kinetic models consistent with experimental measurement values and their uncertainties. From such model ensemble, we perform a comprehensive set of analysis regarding parameter distributions, transient dynamical responses, dose-response properties, and gain/loss-of-function phenotypes, which portrays the manner how allosteric and redox regulations contribute to the metabolic response upon oxidative stress. In particular, these analyses converge to the notion that distributed allosteric regulation is required for efficient metabolic rerouting where regulatory mechanisms display both complementary and cooperative roles.

RESULTS

Kinetic modeling of metabolic response to oxidative stress

Kinetic modeling of the early metabolic response to oxidative stress follows the conventional framework for building kinetic models of metabolic pathways (Miskovic et al., 2015; Foster et al., 2019; Hameri et al., 2019). The metabolic and regulatory network structure considered in this study is described in Figures 1A and S1 and the workflow from the integration of metabolomics and fluxomics data to model ensemble analysis is recapitulated in Figure 1B and STAR Methods. The dynamic response of a metabolic network to an oxidative stress perturbation can be described by a set of differential equations derived from the stoichiometry and enzyme-kinetic reaction rates:

$$\frac{d\vec{x}}{dt} = \mathcal{N}\,\vec{\varphi}\left(\vec{x}, S(t,H), \vec{p}\right) \qquad \text{(Equation 1)}$$

where $\vec{x} = [x_{i=1,16}]$ represents the concentrations of metabolite species i, $\mathcal{N}$ denotes the stochiometric matrix, $\vec{\varphi} = [\varphi_{j=1,23}]$ represents the reaction rates associated with enzymes j (see Table S1), $S(t,H) = H\mathcal{H}(t)$ is the Heaviside step exposure to extracellular concentrations of H_2O_2, and $\vec{p} = [p_{k=1,48}]$ represents the enzymatic or regulatory parameters (see Table S2). The steady-state equation is given by $\mathcal{N}\vec{\Phi}(\vec{X}, H, \vec{p}) = 0$ where capitalized $\vec{X}$ and $\vec{\Phi}$ denote steady-state concentration and flux vectors.

The main specificity of our class of kinetic metabolic model relates to its regulatory scheme. So far, kinetic models of oxidative stress response investigate early intracellular responses at the levels of antioxidant pathways (Adimora et al., 2010; Kembro et al., 2013; Benfeitas et al., 2014) or of glycolytic and pentose phosphate pathways (Thorburn and Kuchel, 1985; Schuster and Holzhütter, 1995; Kerkhoven et al., 2013; Christodoulou et al., 2018), leaving out the TCA cycle. The latter studies either did not include allosteric and oxidative regulations or explored all possible metabolite-enzyme regulations. In contrast, our model specifically addresses the respective roles of a subset of regulatory mechanisms that has been acknowledged to contribute to some respect to rapid metabolic adaptation to oxidative stress, namely NADPH-dependent inhibition of PPP enzymes (Yoshida and Lin, 1973; Holten et al., 1976; Christodoulou et al., 2018), 6PG-dependent inhibition of PGI (Parr, 1956; Kahana et al., 1960; Gaitonde et al., 1989; Kuehne et al., 2015; Dubreuil et al., 2020), oxidative inhibition of GAPD (Ralser et al., 2007, 2009; Peralta et al., 2015; van der Reest et al., 2018), G6P-dependent inhibition of HK, and regulation of other NADPH-consuming or producing reactions (Jeon et al., 2012; Lewis et al., 2014; Fan et al., 2014; Chen et al., 2019). Notable exceptions have been to leave out the inhibitions of PK, TPI, or PFK1 enzymes (Anastasiou et al., 2011; Grüning et al., 2011, 2014; Mullarky and Cantley, 2015) as depicted and explained in Figure S1.

Refined analysis of stress-induced flux redistribution

The stress-induced redistribution pattern of metabolic fluxes can be inferred without any knowledge about kinetic parameters. Although an expected feature of such redistribution is the increased flux in the oxidative branch of PPP, it remains unclear to which extent is such increase and whether the oxPPP flux is rather directed toward nucleotide production or toward the nonoxidative branch of the PPP. To gain a quantitative description of stress-induced redistribution of metabolic fluxes, we reanalyze ^{13}C-labeling data (Kuehne et al., 2015) using a stochastic simulation algorithm-based ^{13}C metabolic flux analysis (SSA-based ^{13}C-MFA described in STAR Methods) to simulate the isotope labeling system (Thommen et al., 2022) and a Monte Carlo sampling to determine posterior distribution of flux parameters. We obtain a distribution of all reaction fluxes (Figures 2A and S2A) associated with an accurate fit of mass isotopomer data (see Figures S2C and S2D). The size of confidence intervals associated with the estimated flux distribution determines whether the flux can be estimated accurately enough to be used as a constraint for kinetic modeling (Figure S2B).

The estimated flux distribution pattern in absence and presence of oxidative stress can be summarized for the main branches of the metabolic network as depicted in Figures 2B and 2C. The metabolic state in the unstressed condition corresponds to a glycolytic flux mode where a minor fraction (~ 20%) of glucose import flux is diverted toward oxPPP (Figure 2B). Exposure of $H = 500\ \mu M$ leads to a significant increase in oxPPP flux up to ~ 95% which is further split between nucleotide production and nonoxidative PPP (Figure 2C). It also leads to a significant reduction of about 3-fold of metabolic flux in the lower glycolytic branch below GAP. This value coincides with the fold-change reduction of PEP concentrations about 2.8 reported in the data (Kuehne et al., 2015). The decrease in PEP concentration, concomitant to that of GAPD flux, justifies the model assumption of not considering oxidative inhibition of PK and allosteric inhibition of TPI mediated by PEP (Figure S1).

In addition to the net fluxes associated with the branching architecture of the metabolic network, it is to note that some directional fluxes could be estimated in the nonoxidative PPP reactions as well as in the reversible PGI reaction, which are valuable information for kinetic model building.

Optimization and inference methods identify a plausible ensemble of kinetic models

Besides the redistribution of metabolic fluxes, oxidative stress response also induces rapid changes in metabolic concentrations below the minute timescale (Kuehne et al., 2015), which together provides a valuable dataset to estimate the parameters of kinetic models described by Equations 1 and 3. Our parameter estimation problem consists in estimating the values of 36 parameters (i.e., 12 parameters are fixed including equilibrium constants to consider thermodynamic constraints (Li et al., 2011)) from a dataset comprising 13 estimated values of fluxes and 12 measured values of concentration ratios at $t =$ 5min. The procedure combines two classes of global optimization methods, namely an evolutionary genetic

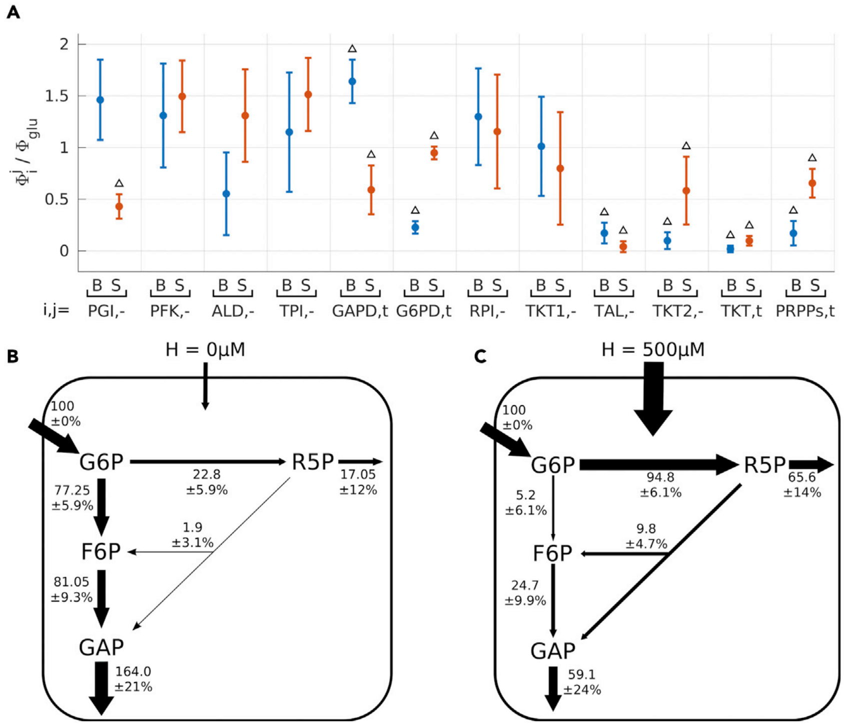

Figure 2. Stress-induced flux redistribution

(A–C) Mean and SD of the distribution of normalized flux rates obtained using stochastic stimulation algorithm (SSA) for ^{13}C-MFA (see STAR Methods details). Estimation is restricted to a set of elementary flux parameters (while other fluxes can be derived from balance equations) where the index *i* indicates the enzyme and the index *j* indicates the directionality and where estimation is performed for basal (B, blue) or stress (S, red) conditions. Triangles indicate parameter estimation that is statistically significant based on the relative size of confidence interval distribution (see Figure S2B). (B and C) Representation of the net flux rates in basal (B) and stress (C) conditions.

algorithm and a Markov Chain Monte Carlo (MCMC) algorithm, following a stepwise strategy recapitulated in Figure 3A and detailed in STAR Methods. First, the *nRMSE* (Equation 9 in STAR Methods details) of kinetic models whose parameters are randomly sampled (10^6 runs) lies with a 50% confidence interval between 2.6 and 55.4, thus confirming the need of a parameter optimization procedure to find model parameters consistent with experimental data. Second, an evolutionary genetic algorithm is used as a preliminary step to generate a sample of optimized models whose 50% confidence interval of *nRMSE* values lies between 0.8 and 3. Third, a small subset of such local optimum solutions whose $nRMSE(p) < 1$ is used as initial conditions of MCMC sampling algorithm of the parameter space. The parameter distribution obtained with large enough sampling of $\sim 10^6$ accepted steps provides an estimation for parameter uncertainty and defines a statistical ensemble of kinetic model that is called $\mathcal{P}^{opt}$ and that is analyzed in details in the following. Such statistical model ensemble is characterized with a 50% confidence interval of *nRMSE* between 0.63 and 0.86 for which the estimated distributions of fluxes and concentration ratios fall within the range of experimental uncertainties (Figures 3B and 3C) and whose R-squared values are respectively $R^2 = 0.86 \pm 0.03$ and $R^2 = 0.96 \pm 0.02$. Parameter distributions shown in Figure 3D discriminate between stiff and sloppy parameters for which 50% confidence intervals span from few percents to several order of magnitude of parameter variations. Spectral analysis of correlation matrix confirms indeed the existence of a few poorly estimated parameters generally associated with strong correlation between parameters of a same reaction (see Figures S3A and S3B). Last, a dataset about dynamic and dose-dependent concentration responses has been retained to assess the predictive capability of the plausible set of model $\mathcal{P}^{opt}$ (see Figure S3C). The dynamical and dose response are overall well predicted with, respectively, $R^2 = 0.82 \pm 0.05$ and $R^2 = 0.48 \pm 0.04$ due to sparse discrepancies such as a lower threshold of 6PG response.

In summary, the parameter estimation procedure generates a plausible set of kinetic models whose parameters show rather narrow distributions, except some parameters that have a little impact on data

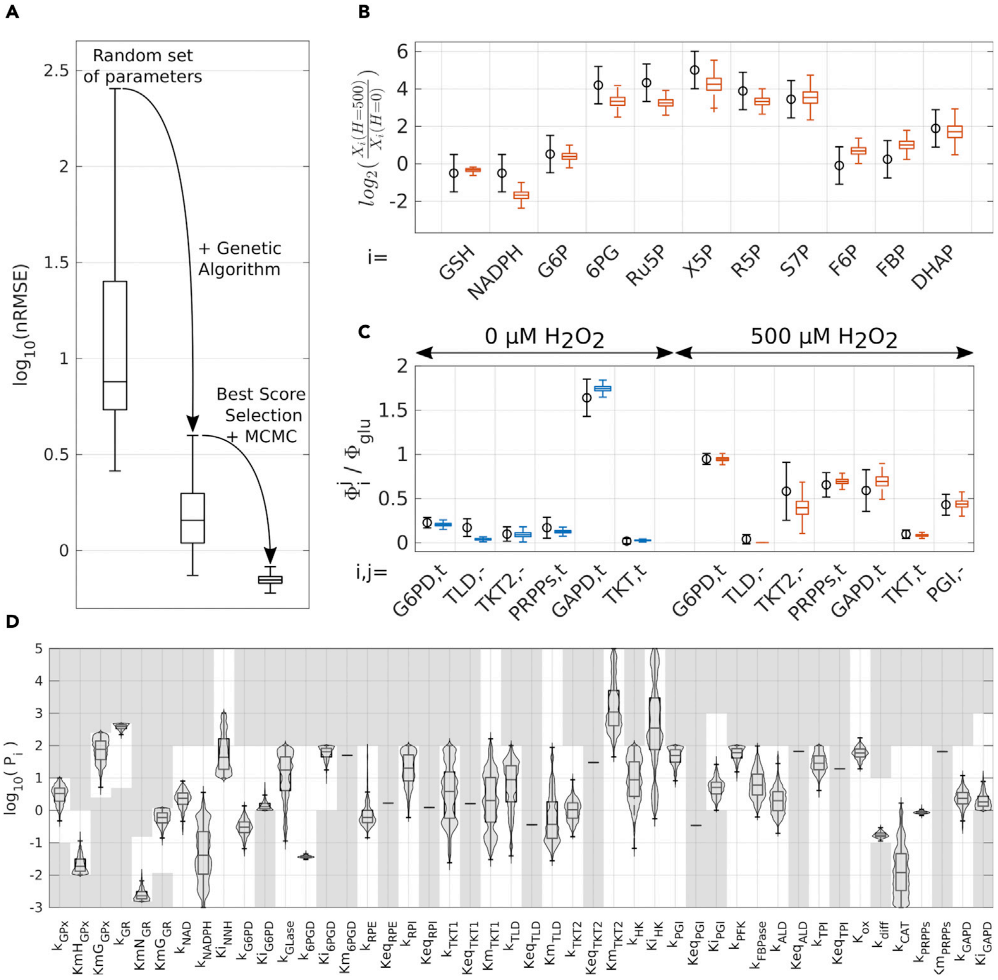

Figure 3. Model selection and parameter estimation

(A) Whisker plots associated with random parameter set (10^6), optimized parameter set using an evolutionary genetic algorithm (10^4), and parameter set ($\mathcal{P}^{opt}$) sampled with MCMC algorithm (10^6).

(B and C) Whisker plots of the concentration ratio $X_i(H = 500)/X_i(H = 0)$ for the model ensemble $\mathcal{P}^{opt}$ (red) as compared with the mean and SD of experimental values (black). (C) Whisker plots of a subset of normalized reaction fluxes $\Phi_i/\ \Phi_{GLU}$ for the model ensemble $\mathcal{P}^{opt}$ ($H = 0$ in blue and $H = 500$ μM in red) as compared with the mean and SD of estimated values (black).

(D) Violin plots of parameters for the model ensemble $\mathcal{P}^{opt}$ where the explored parameter space is represented in white (non-gray).

adjustment or that can be compensated by the change of other parameters. Importantly, most inhibitory constant parameters (Ki_{G6PD}, Ki_{GAPD} and Ki_{PGI}) show a narrow distribution, confirming the role of these regulations in shaping the metabolic response to oxidative stress. In the following, we systematically perform analysis on this model ensemble $\mathcal{P}^{opt}$ to draw a statistical picture of the regulatory properties.

Transient metabolic responses following stress display multiphasic time courses

The characteristics of the transient dynamics after oxidative stress exposure and before reaching some steady state give some preliminary insights about the respective contributions of passive and regulated metabolic responses (Figures 4 and S4). The minute time resolution in the time series dataset seemed not sufficient to identify trends arising at the second timescale (Ralser et al., 2009; Christodoulou et al., 2018). In the simulations of the model ensemble $\mathcal{P}^{opt}$, metabolites within a same metabolic module share a similar dynamic response profile (Figure 4). First, PPP metabolites display a rapid and significant monophasic increase. Second, antioxidant NADPH and GSH metabolites display a fast and significant decrease

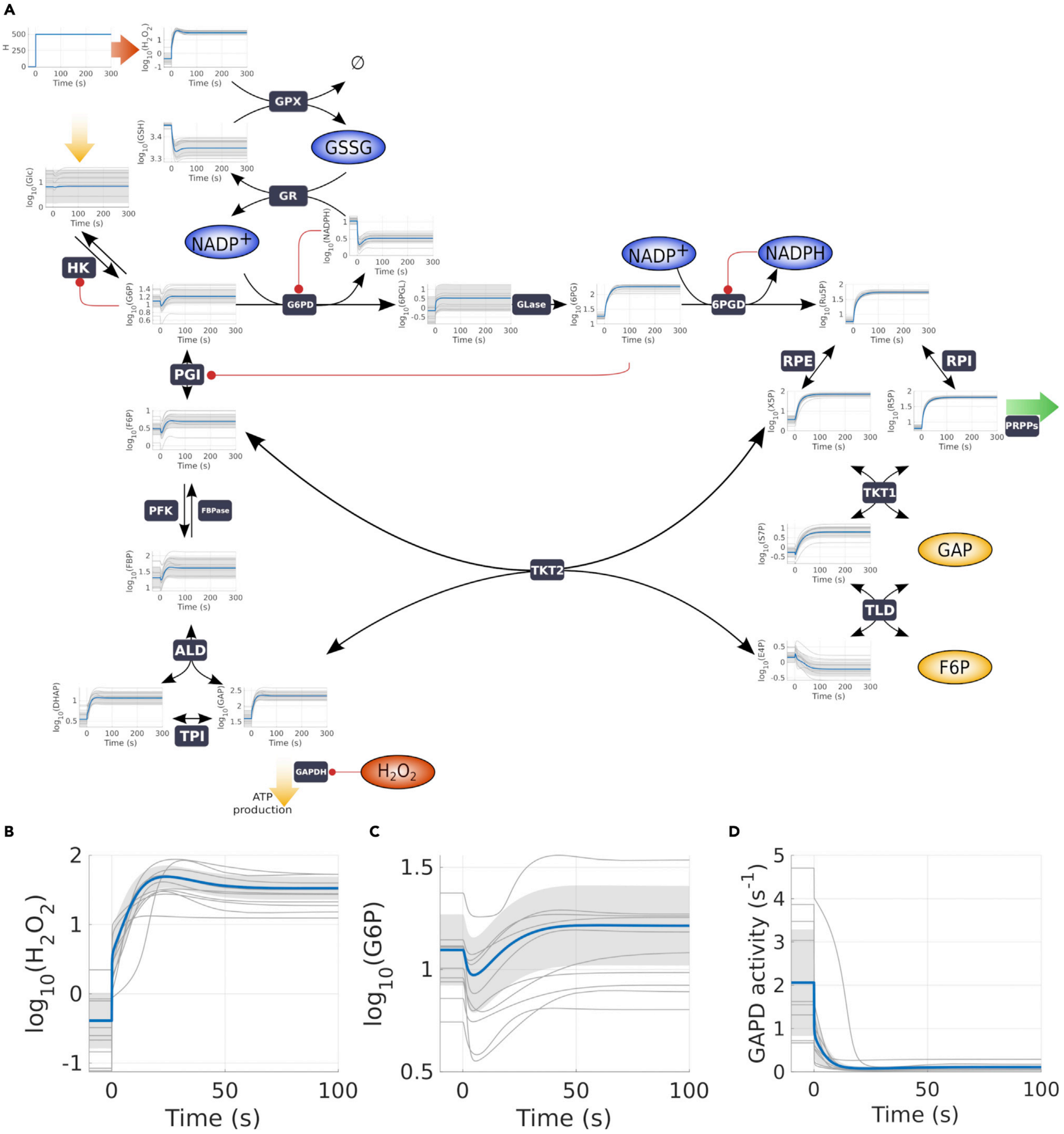

Figure 4. Transient dynamics of stress-induced metabolic responses

Temporal response of model ensemble $\mathcal{P}^{opt}$ to a step of 500μM H_2O_2 representing the mean value (blue line), a subsample of 50 trajectories (gray line) and the SD (gray shadow).

(A) Dynamic response of all metabolite species until 5 min.

(B–D) Temporal response of H_2O_2, G6P, and GAPD activity until 100 s, highlighting multiphasic and rapid adaptation responses.

followed by a slower increase. Third, glycolytic metabolites show moderate changes where a fast decrease seems followed by a slower increase. These different temporal response patterns are typically characterized with a biphasic response where a fast passive response to the perturbation is quickly followed by a slower regulated response.

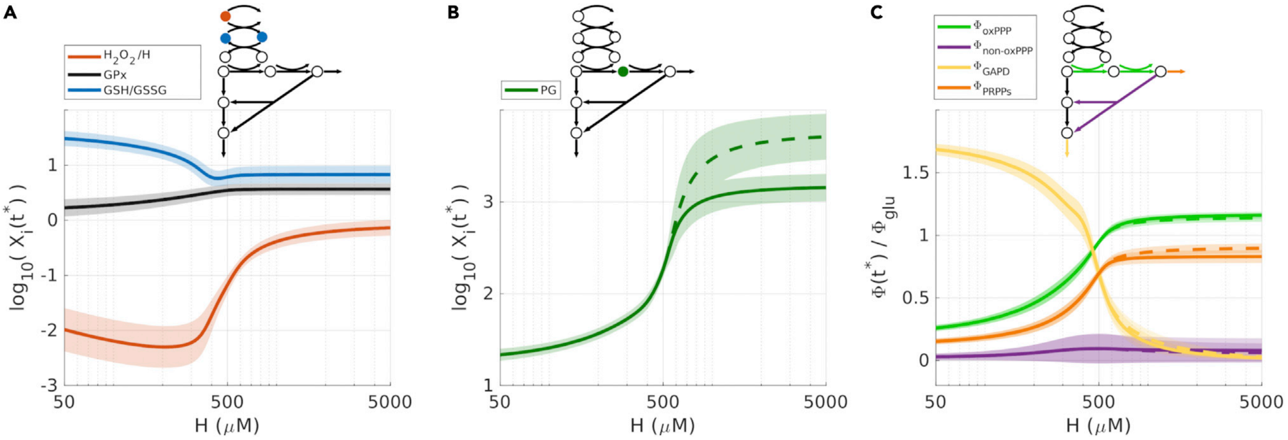

Figure 5. Dose-dependent profile of stress-induced metabolic response. Response to varying level *H* of extracellular H_2O_2 measured at 5 min (full line) and 30 min (dashed line)

(A) Dose response in the glutatione pathway of $\frac{H_2O_2}{H}$, GPx, and GSH/GSSG ratio.

(B) Dose response of 6PG metabolite (other metabolites are shown in Figure S5).

(C) Dose response of the fluxes through enzymatic reactions G6PD, TKT, GAPD, and PRPP (normalized to glucose import rate Φ_{GLU}).

The biphasic nature of the transient response is illustrated in the case of intracellular concentrations of H_2O_2 and G6P (Figures 4B and 4C). H_2O_2 shows a sharp increase about several orders of magnitude whose timescale within seconds relates to the basal degradation timescale $k_{GR} \times KmG_{GPx} \sim 10$s. The time profile of H_2O_2 later displays an overshoot in the time course where decrease of H_2O_2 mirrors the increase in GSH and NADPH, which coincides with the accumulation of glycolytic metabolites including G6P. G6P shows indeed a rapid decrease until ~ 10s before to increase again to eventually exceed its initial value (Figure 4C). The early decreasing phase of G6P dynamics coincides with an increased consumption through G6PD associated with higher $NADP^+$/NADPH levels while the late increasing phase can only be due to a decreased glycolytic flux through PGI related to the inhibition of glycolysis at the levels of GAPD or PGI. GAPD inactivation occurs indeed very rapidly within few seconds (Figure 4D), being a possible candidate for the accumulation of G6P and detoxification of H_2O_2 occurring within 10th of seconds.

In summary, the biphasic response observed in simulations of the plausible set of models distinguishes between a detoxification response in less than a second using the reservoir of GSH and NADPH and a metabolic rerouting response from few to tenths of seconds involving the inhibition of glycolysis to quickly restore high G6P levels.

Dose-response analysis identifies rate-limiting reactions

The redistribution pattern of metabolic fluxes is determined for a specific level of H_2O_2 for which ^{13}C labeling data were available. The oxPPP flux normalized to the glucose import flux, Φ_{G6PD}/Φ_{GLU}, is around 1 (Figure 2A) which is far below the maximal flux capacity associated with the full inhibitions of GAPD and PRPP enzymes (i.e., $\Phi_{G6PD}/\Phi_{GLU} \leq 6$). To explore the detoxification and flux capacity at higher stress level, we perform a dose-response analysis of the kinetic model ensemble $\mathcal{P}^{opt}$ focusing respectively on the antioxidant response, the concentration response, and the flux response (Figures 5 and S5). Simulation of the metabolic response at 5 min as function of *H* shows a transition in the detoxification response around $500\mu M$ (Figure 5A). Below this value, the detoxification activity of GPx increases with oxidative stress level thereby keeping low intracellular levels of H_2O_2 at the expense of an increased reduced state of glutathione. Above this value, GPx activity saturates such that reaction flux is bounded and cannot increase anymore to compensate for the increase in H_2O_2 production above some level. Beyond this threshold, H_2O_2 is eliminated by catalase consistently with the idea of that the rate-limiting enzymes depend on intracellular H_2O_2 concentrations (Makino et al., 2004; Ng et al., 2007). Another qualitative change of the metabolic response is observed for large enough H_2O_2 (Figure 5B). 6PG does not quickly reach a steady state and continues to slowly increase, as values differ between 5 min and 30 min. The appearance of a slower equilibration dynamics of 6PG coincides with the saturated kinetics of 6PGD enzymatic reaction associated with increased levels of 6PG below that value of Km_{6PGD}. In parallel to the concentration changes of H_2O_2 and 6PG, the dose response of metabolic fluxes displays a gradual change from a glycolytic mode to oxPPP mode up to $\Phi_{G6PD}/\Phi_{GLU} \sim 1.3 > 1$ indicating that carbon atoms can be recycled multiple times into oxPPP (Figure 5C).

In conclusion, dose-response analysis identifies distinct classes of rate-limiting mechanisms, where saturated activities of antioxidant enzymes restrain H_2O_2 detoxification for a given NADPH load while saturated activities in PPP enzymes and a leak flux through PRPPs reaction restrain the maximal production rate of NADPH.

Regulation analysis reveals complementary ranges of regulatory efficiencies

The model comprises several regulatory mechanisms likely to contribute to the metabolic flux rerouting to oxidative stress. Some of these regulations directly act at the levels of reactions producing or consuming NADPH notably in oxPPP (Ki_{G6PD}, Ki_{6PGD}, Ki_{NNH}) while others operate at the level of glycolysis (Ki_{GAPD}, Ki_{PGI} and Ki_{HK}). The distribution of estimated Ki values provides a preliminary insight for the need of regulation to reproduce experimental data. Computation of inhibitory strength X_j/Ki_j ($=1$ for enzymatic activity divided by two) over the model ensemble $\mathcal{P}^{opt}$ reveals that stress condition is associated with significant inhibition of PGI and GAPD ($X_j/Ki_j \gg 1$) but also significant disinhibition of G6PD (Figure 6A). In contrast, other inhibitory strength is either low or poorly constrained such as the feedback inhibition of HK enzyme.

A more comprehensive strategy to quantify regulatory effects consists in measuring gain of function or loss of function associated with the deletion of a single regulatory mechanism ($Ki_i \to \infty$), other things being equal. For such aim, we define a sensitivity quantity Δ measuring the impact of modulating regulatory parameters on some functional output such as intracellular H_2O_2 (Equation 10 in STAR Methods). $\Delta^{Y}_{Ki\to\infty}$ larger or lower to one indicates that deleting the regulation increases or decreases the steady-state level of Y. In Figure 6B, removal of NADPH-dependent inhibition of G6PD and H_2O_2-dependent inhibition of GAPD leads to higher H_2O_2 and lower NADPH, highlighting significant contributions of these regulations for NADPH homeostasis and H_2O_2 detoxification. Surprisingly, deleting the inhibition of PGI has a minor impact on metabolic outputs of interest, which can nevertheless be interpreted by a low net flux through PGI ($\Phi^{+}_{PGI} \sim \Phi_{PGI}{}^{-}$) for a particular stress level (Figure 2C).

To investigate whether regulation efficiency indeed depends on oxidative stress level, we evaluate the deleterious effect of removing a regulation (i.e., loss of function) as function of H (Figures 6C, 6D, and S6). The dose-dependent profile of $\Delta^{H_2O_2}_{Ki_i}(H)$ distinguishes different ranges of stress level for which each regulation Ki_i is the most efficient (Figure 6C). First, the efficiency of G6PD upregulation is the highest for low-to-moderate stress level because enzyme activity rather than G6P level is rate-limiting. Second, the efficiency of 6PG-dependent inhibition of PGI (null for $H = 500$ in Figure 6B) peaks at intermediate stress level as it requires both high enough stress for 6PG accumulation (see Figure 5B) and not-too-high stress such that the downward flux prevails over the upward flux in PGI reaction ($\Phi^{+}_{PGI} > \Phi_{PGI}{}^{-}$ or equivalently $\Phi_{G6PD}/\Phi_{GLU} < 1$) (see Figure 5C). Third, the efficiency of GAPD inhibition culminates at high oxidative stress consistently with its ability, in addition to restore G6P levels, to reverse glycolytic flux coming from the nonoxidative branch of the PPP, thus making possible a flux cycling mode where $\Phi_{G6PD}/\Phi_{GLU} > 1$.

To clarify how to reconcile the results that inactivation of GAPD starts at low intracellular oxidant levels (i.e., $H_2O_2 \sim Ki_{GAPD} \sim 2\mu M$) and GAPD inactivation is the most effective for high oxidative stress ($H > 400\mu M$), we also compute response coefficients (Equation 11 in STAR Methods) as function of stress level H (Figure 6D). The results show that the effect of Ki_{gapd} on φ_{oxPPP} is already effective for low H values but starts to increase for higher stress level. This dose-dependent effect might relate to the fact that GAPD inhibition is more prone to promote a glycolytic flux toward G6P and oxPPP flux when the carbon flux in the nonoxidative branch of PPP is already flowing from R5P to GAP (due to increased levels of R(u)5P metabolites).

Besides complementary efficiency ranges, two regulations can also combine their effect in non-trivial manners. For instance, G6PD upregulation leads to 6PG accumulation which potentializes the inhibition of PGI. Alternatively, PGI inhibition reduces G6P consumption which potentializes the upregulation of G6PD. These are second-order effects that are quantified by the computation of sensitivity factors $\Delta^{Y}_{Ki_j,Ki_k\to\infty}$ associated with the combined deletion of two regulations (Figure 6E).

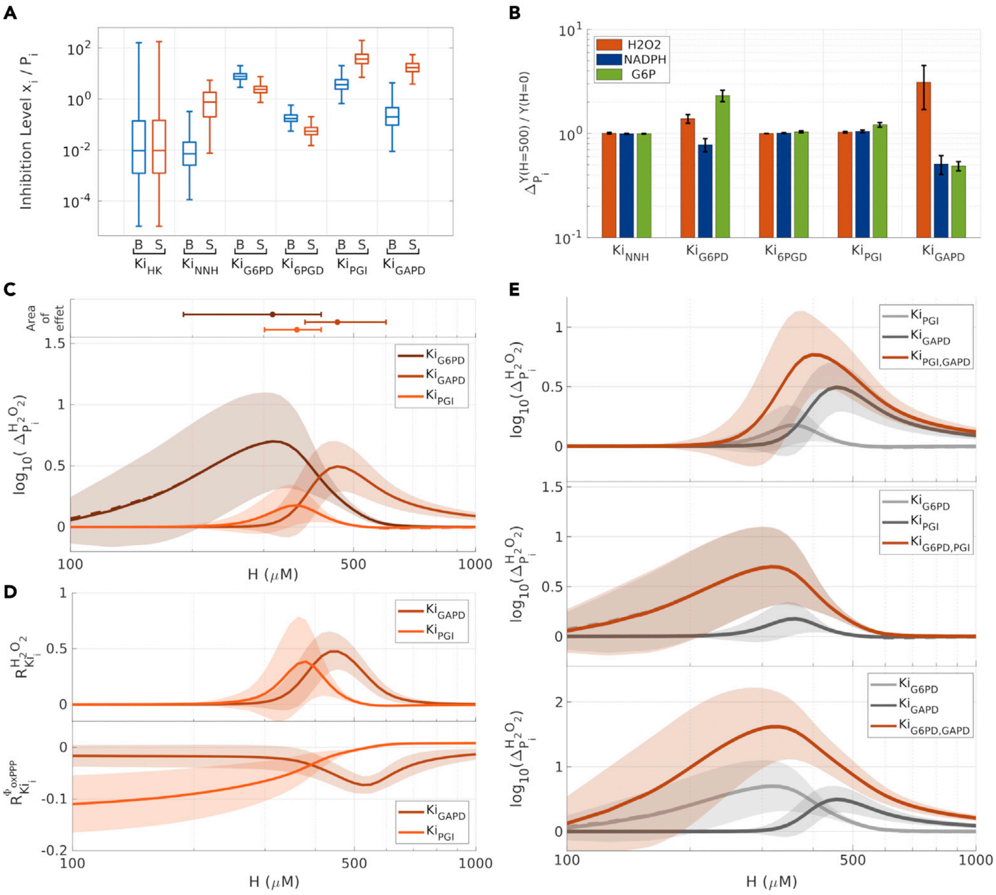

Figure 6. Regulation analysis based on gain/loss-of-function simulations

(A) Inhibitory strength X_i/Ki_j associated with the inhibition of enzyme j by metabolite i for $H = 0$ (blue) and $H = 500\mu M$ (red). $X_i/Ki_j = 1$ indicates that inhibition reduces enzymatic activity by 2-fold.

(B) Sensitivity factor $\Delta^{Y}_{P_i}(\Delta Ki_i = \infty)$ (Equation 10) of output Y with respect to several deletions of regulation Ki_i in abscisse, where the outputs Y are the metabolic responses of H_2O_2, NADPH, and G6P to oxidative stress relative to basal levels. Bars are mean values and error bars are standard deviations over the kinetic model ensemble $\mathcal{P}^{opt}$.

(C) Sensitivity factor $\Delta^{H_2O_2}_{P_i}(H, \Delta Ki_i = \infty)$ of H_2O_2 with respect to deleted regulation Ki_{GAPD}, Ki_{G6PD}, Ki_{PGI} as function of H. The dose-specific areas of regulatory effect associated with each deleted regulation ($\Delta(H)/\Delta_{max} > 0.5$) is shown upper to the panel.

(D) Response coefficients $R^{H_2O_2}_{P_i}(H)$ and $R^{\Phi_{oxPPP}}_{P_i}(H)$ (Equation 11) associated with modulated inhibition of upper and lower glycolysis Ki_{PGI} and Ki_{GAPD} as function of H.

(E) Second-order sensitivity factor $\Delta^{Y}_{P_i}$ with respect to the combined deletion of two regulations in comparison to the single deletions.

Ambivalent role of 6PGD enzyme in oxidative stress response

G6PD, 6PGD, and TKT enzymes are common targets of loss-of-function experiments to investigate oxidative stress response (Kuehne et al., 2015; Nóbrega-Pereira et al., 2016; Wan et al., 2017; Sun et al., 2019; Dubreuil et al., 2020). We therefore perform simulations of our model ensemble $\mathcal{P}^{opt}$ while varying the enzymatic activity parameter from 10-fold reduction to 10-fold increase. We record both the mean of intracellular H_2O_2, the NADPH-producing oxPPP flux, and some concentration metabolites for the model ensemble $\mathcal{P}^{opt}$ (Figure 7). Expectedly, increase (resp., decrease) of k_{G6PD} leads to a more (resp., less) efficient oxidative stress response related to subsequent change in the oxPPP flux of NADPH production (Figures 7A and 7B). In sharp contrast, modulation of k_{6PGD} leads to a more surprising and ambivalent metabolic response (Figures 7C and 7D). Depending on the level of stress and of modulation, we observe that both the increase and the decrease of k_{6PGD} can hamper the oxidative stress response, while decreasing k_{6PGD} can both weaken and improve oxidative stress response. These ambivalent phenotypes relate to the dual effect of modulating k_{6PGD} on G6PD activity itself but also on the increased level of 6PG that

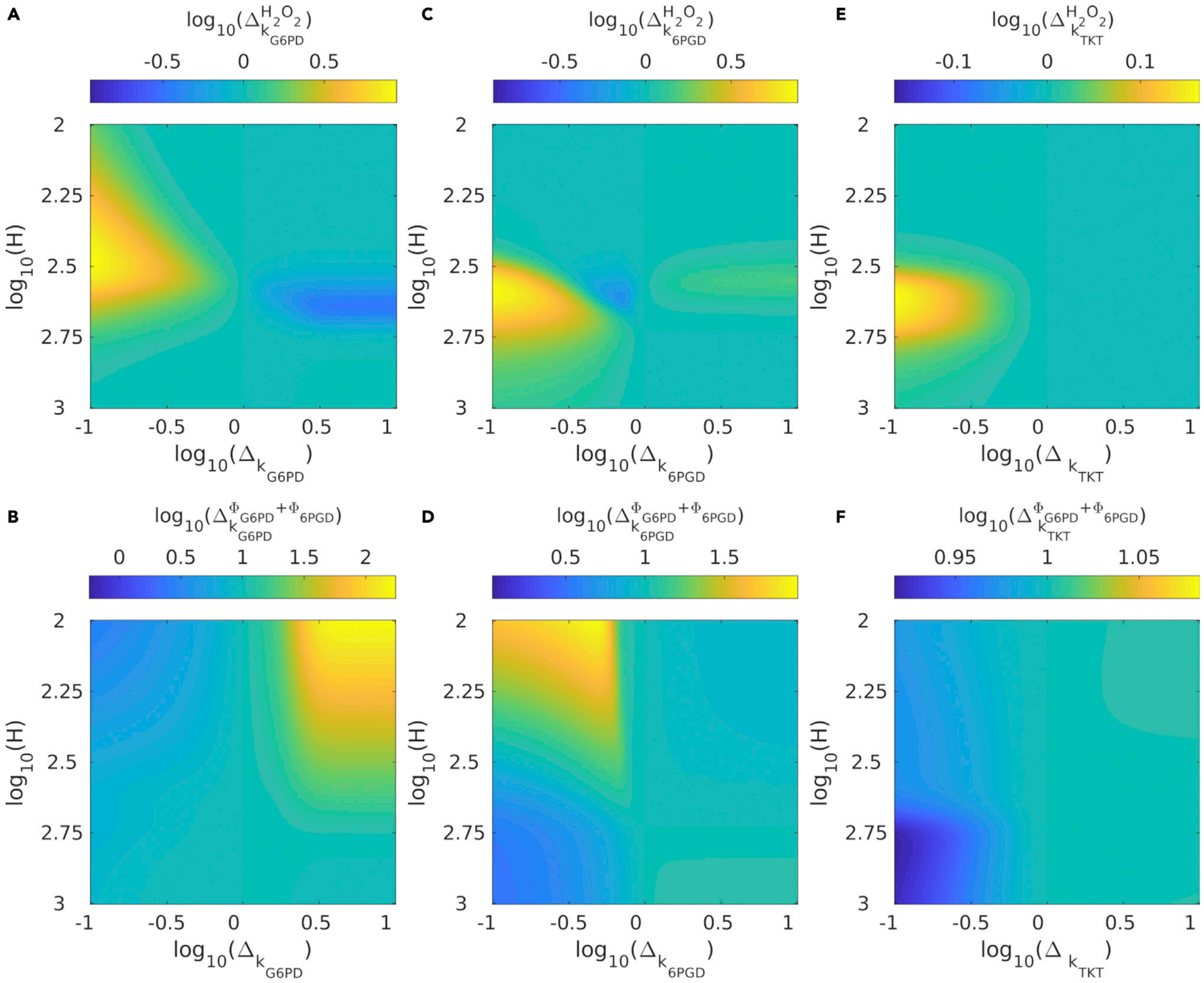

Figure 7. Gain/loss of function associated with modulated activity of PPP enzymes

Sensitivity Δ_X^Y of output Y with respect to modulation of X (Equation 10) as a function of H and the extent of parameter modulation.

(A–F) The output variable Y is either H_2O_2 (A, C, and E) or NADPH-producing flux (B, D, and F) and the modulated parameter is either k_{G6PD} (A and B), k_{6PGD} (C and D) or k_{TKT} (E and F).

inhibits PGI activity and upregulates both G6P level and G6PD flux. Specifically, reducing k_{6PGD} can lead to an imbalanced state associated with increased metabolic flux through 6PGD and decreased flux through G6PD, whose relative effect determines the occurrence of loss or gain of function. Last, the modulation of k_{TKT} has a moderate effect on flux reprogramming restricted to higher stress level (Figures 7E and 7F), consistently with the dose-dependent increase of flux in nonoxidative PPP (Figure 5C) and its crucial role for enabling a cycling flux where $\varphi_{G6PD}/\varphi_{GLU} > 1$. It is to note that some trends observed for the concentration response of glycolytic and PPP intermediates in response to modulation of k_{G6PD} and k_{TKT} (see Figure S7) are qualitatively consistent with knockdown experiments (Kuehne et al., 2015).

DISCUSSION

In this work, we use a kinetic modeling approach to investigate the interplay between several metabolic regulations in that specific functional context of oxidative stress response. Data-driven kinetic modeling framework is commonly used to identify large-scale patterns of metabolite-enzyme interactions and to investigate the role of allosteric regulation in controlling metabolic phenotypes (Grimbs et al., 2007; Link et al., 2013; Machado et al., 2015; Jahan et al., 2016; Reznik et al., 2017; Millard et al., 2017;

Christodoulou et al., 2018; Britton et al., 2020). The present study purposely focuses on a selected set of regulation proposed to contribute to the rapid and global changes of flux and concentration upon oxidative stress, resulting in PPP upregulation and NADPH recycling to support antioxidant systems (Ralser et al., 2007; Kuehne et al., 2015; Mullarky and Cantley, 2015; Stincone et al., 2015; Dick and Ralser, 2015; Christodoulou et al., 2018). By integrating metabolomics and fluxomics data, kinetic modeling reveals that the observed concentration and flux responses require the co-operation of multiple regulatory mechanisms, and that such co-operation follows a rationale of metabolic efficiency in terms of complementary and synergistic effects. Specifically, we highlight that the regulations of several PPP and glycolytic enzymes all fulfill different but coordinated roles for stress-induced carbon flux rerouting.

Using $NADP^+$ as a substrate and NADPH as a feedback inhibitor, G6PD enzyme is sensitively activated by the decrease of $NADP^+$/NADPH redox ratio associated with the oxidation of NADPH (Yoshida and Lin, 1973; Holten et al., 1976; Christodoulou et al., 2018). However, the efficiency of this sole regulatory mechanism is shown to be hampered by the concomitant decrease of G6P when oxPPP fluxes becomes of the order of downward glycolytic flux. Mechanistically, such decrease of G6P can be compensated either by a reduction of G6P consumption through PGI inhibition or an increase of G6P production through accumulation of glycolytic intermediates itself mediated by the inhibition of glycolytic enzymes below F6P. In our class of kinetic models built from a specific dataset, such inhibition is likely to be mediated by the oxidative inactivation of GAPD, but the inhibition of TPI (Grüning et al., 2011) or PFK1 (Seo and Lee, 2014) could also fulfill a similar flux rerouting role. Interestingly, inhibition of GAPD is more effective to promote oxPPP for significant stress levels coinciding with a carbon flux in the nonoxidative branch of PPP flowing from accumulated R5P to glycolytic intermediates. The inhibitory effect of a given glycolytic enzyme tightly depends on its coupling with nonoxidative PPP reactions at the level of F6P and GAP metabolites. Each regulation mechanism thus implements a specific flux rerouting strategy which results in complementary ranges of efficiency but also synergistic cooperative effects, providing altogether a flexible metabolic adaptation for diverse stress and cellular contexts. A systematic mapping between the regulation motifs and the flux control properties (Machado et al., 2015; Britton et al., 2020) is needed to refine our understanding of the role of regulation for maximizing NADPH yield over a broad range of perturbation and irrespective to the metabolic state.

Besides insights into the regulatory logic, the modeling approach could also identify the main rate-limiting processes for PPP flux increase and H_2O_2 detoxification. In the models, the maximal PPP flux generates up to 3 mol of NADPH for 1 mol of glucose due to a cycling mode where each molecule of glucose can be oxidized multiple times (Kuehne et al., 2015; Dick and Ralser, 2015; Britt et al., 2022), which is nevertheless far from the maximal yield of 12 mol of NADPH in case of complete inhibition of PRPP and GAPD enzymes. Besides the production of nucleotide precursors for DNA damage repair and of ATP for stress management, we also identify several rate-limiting reactions including GPx enzyme (Ng et al., 2007), but also 6PGD enzyme. For instance, the tight regulation of 6PGD activity is critical for a functional accumulation of G6P. Indeed, both upregulation and downregulation of 6PGD can penalize the oxidative stress response by reducing PGI activity, either too weakly for enabling glycolysis shunt at low stress and too strongly for enabling carbon recycling at high stress. Paradoxically also, the inhibition of 6PDG can both lower the maximal flux capacity for NADPH production and promote the shunt of glucose into oxPPP through the inhibition of PGI. This ambivalent effect explains the contradicting experimental observations where genetic or pharmacological inhibition of 6PGD can either promote or decrease oxidative stress response of mammalian cells depending on the context (Sun et al., 2019; Liu et al., 2019; Dubreuil et al., 2020). Knowing that AMPK, a master regulator of many metabolic processes, is itself regulated by metabolites in the oxPPP (Lin et al., 2015; Gao et al., 2019) and regulates glycolysis especially PFK1 (Wu and Wei, 2012), a better understanding of the regulated coordination between glycolysis and PPP is important for a broad range of metabolic adaptations beyond oxidative stress response.

Limitations of the study

In the present study, kinetic models have been built from a specific experimental dataset associated with neonatal human skin fibroblasts exposed to H_2O_2-supplemented medium, which questions whether unveiled regulatory patterns can be extrapolated to other types of cells and other sources of oxidative stress. Although similar metabolic responses have been observed for different mammalian cell types and oxidative stress sources (Kuehne et al., 2015; van der Reest et al., 2018; Christodoulou et al., 2019), there are also evidences of alternative metabolic adaptation strategies which restricts the generalization of our findings.

For instance, the feedback loop involving the regulation of PK and TPI glycolytic enzymes has also been shown to contribute in oxidative stress response, especially in yeast (Anastasiou et al., 2011; Grüning et al., 2011, 2014). Alternatively, oxidative stress response in some lower eukaryotic and prokaryotic organisms has been shown to involve the Entner-Doudoroff pathway (Nikel et al., 2021) or the ribose salvage pathway (Xu et al., 2013) which are both directly coupled to the PPP. Another limitation of the study inherent to any kinetic model confronted to parameter identifiability issues relates to the possible biases related to model abstractions and assumptions about the choice of reaction kinetics and of involved metabolic pathways leaving aside for instance large-scale metabolic activities and adaptations in the metabolism of ATP, NAD(H), NADP(H), or glutathione.

STAR★METHODS

Detailed methods are provided in the online version of this paper and include the following:

- KEY RESOURCES TABLE
- RESOURCE AVAILABILITY
  - ○ Lead contact
  - ○ Materials availability
  - ○ Data and code availability
- METHOD DETAILS
  - ○ SSA-based ^{13}C-MFA
  - ○ Differential equation model
  - ○ Parameter setting and estimation
  - ○ Sensitivity analysis
  - ○ Model updating procedure
- QUANTIFICATION AND STATISTICAL ANALYSIS
  - ○ Monte Carlo Markov Chain (MCMC) method
  - ○ R-squared

SUPPLEMENTAL INFORMATION

Supplemental information can be found online at https://doi.org/10.1016/j.isci.2022.104681.

ACKNOWLEDGMENTS

This work has been supported by the Labex CEMPI (ANR-11-LABX-0007) and Hauts de France council through the funding of the Cancer-RaPTOx project via the STIR 2021 program.

AUTHOR CONTRIBUTIONS

Conceptualization, J.H., Q.T., F.A., and B.P.; Methodology, J.H., Q.T., and B.P.; Formal analysis, J.H.; Investigation, J.H. and B.P.; Writing – Original Draft, J.H. and B.P.; Writing – Review & Editing, J.H., Q.T., F.A., and B.P.; Visualization, J.H.; Supervision, B.P.; Fund Acquisition, Q.T., F.A., and B.P.

DECLARATION OF INTERESTS

The authors declare no competing interests.

Received: February 24, 2022
Revised: May 12, 2022
Accepted: June 23, 2022
Published: August 19, 2022

REFERENCES

Adimora, N.J., Jones, D.P., and Kemp, M.L. (2010). A model of redox kinetics implicates the thiol proteome in cellular hydrogen peroxide responses. Antioxid. Redox Signal. *13*, 731–743. https://doi.org/10.1089/ars.2009.2968.

Anastasiou, D., Poulogiannis, G., Asara, J.M., Boxer, M.B., Jiang, J., Shen, M., Bellinger, G., Sasaki, A.T., Locasale, J.W., Auld, D.S., et al. (2011). Inhibition of pyruvate kinase M2 by reactive oxygen species contributes to cellular antioxidant responses. Science *334*, 1278–1283. https://doi.org/10.1126/science.1211485.

Beck, J.L., and Au, S.-K. (2002). Bayesian updating of structural models and reliability using Markov chain Monte Carlo simulation. J. Eng. Mech. *128*, 380–391. https://doi.org/10.1061/(asce)0733-9399(2002)128:4(380).

Benfeitas, R., Selvaggio, G., Antunes, F., Coelho, P.M., and Salvador, A. (2014). Hydrogen peroxide metabolism and sensing in human erythrocytes: a validated kinetic model and reappraisal of the role of peroxiredoxin II. Free Radic. Biol. Med. *74*, 35–49. https://doi.org/10.1016/j.freeradbiomed.2014.06.007.

Ben-Yoseph, O., Boxer, P.A., and Ross, B.D. (1996). Assessment of the role of the glutathione and pentose phosphate pathways in the protection of primary cerebrocortical cultures from oxidative stress. J. Neurochem. *66*, 2329–2337. https://doi.org/10.1046/j.1471-4159.1996.66062329.x.

Britt, E.C., Lika, J., Giese, M.A., Schoen, T.J., Seim, G.L., Huang, Z., Lee, P.Y., Huttenlocher, A., and Fan, J. (2022). Switching to the cyclic pentose phosphate pathway powers the oxidative burst in activated neutrophils. Nat. Metab. *4*, 389–403. https://doi.org/10.1038/s42255-022-00550-8.

Britton, S., Alber, M., and Cannon, W.R. (2020). Enzyme activities predicted by metabolite concentrations and solvent capacity in the cell. J. R. Soc. Interface *17*, 20200656. https://doi.org/10.1098/rsif.2020.0656.

Chen, L., Zhang, Z., Hoshino, A., Zheng, H.D., Morley, M., Arany, Z., and Rabinowitz, J.D. (2019). NADPH production by the oxidative pentose-phosphate pathway supports folate metabolism. Nat. Metab. *1*, 404–415. https://doi.org/10.1038/s42255-019-0043-x.

Christodoulou, D., Link, H., Fuhrer, T., Kochanowski, K., Gerosa, L., and Sauer, U. (2018). Reserve flux capacity in the pentose phosphate pathway enables escherichia coli's rapid response to oxidative stress. Cell Syst. *6*, 569–578.e7. https://doi.org/10.1016/j.cels.2018.04.009.

Christodoulou, D., Kuehne, A., Estermann, A., Fuhrer, T., Lang, P., and Sauer, U. (2019). Reserve flux capacity in the pentose phosphate pathway by NADPH binding is conserved across kingdoms. iScience *19*, 1133–1144. https://doi.org/10.1016/j.isci.2019.08.047.

Dick, T., and Ralser, M. (2015). Metabolic remodeling in times of stress: who shoots faster than his shadow? Mol. Cell *59*, 519–521. https://doi.org/10.1016/j.molcel.2015.08.002.

Dubreuil, M.M., Morgens, D.W., Okumoto, K., Honsho, M., Contrepois, K., Lee-McMullen, B., Traber, G.M., Sood, R.S., Dixon, S.J., Snyder, M.P., et al. (2020). Systematic identification of regulators of oxidative stress reveals non-canonical roles for peroxisomal import and the pentose phosphate pathway. Cell Rep. *30*, 1417–1433.e7. https://doi.org/10.1016/j.celrep.2020.01.013.

Eggleston, L.V., and Krebs, H.A. (1974). Regulation of the pentose phosphate cycle. Biochem. J. *138*, 425–435. https://doi.org/10.1042/bj1380425.

Fan, J., Ye, J., Kamphorst, J.J., Shlomi, T., Thompson, C.B., and Rabinowitz, J.D. (2014). Quantitative flux analysis reveals folate-dependent NADPH production. Nature *510*, 298–302. https://doi.org/10.1038/nature13236.

Foster, C.J., Gopalakrishnan, S., Antoniewicz, M.R., and Maranas, C.D. (2019). From Escherichia coli mutant 13C labeling data to a core kinetic model: a kinetic model parameterization pipeline. PLoS Comput. Biol. *15*, e1007319. https://doi.org/10.1371/journal.pcbi.1007319.

Gaitonde, M.K., Murray, E., and Cunningham, V.J. (1989). Effect of 6–phosphogluconate on phosphoglucose isomerase in rat brain in vitro and in vivo. J. Neurochem. *52*, 1348–1352. https://doi.org/10.1111/j.1471-4159.1989.tb09178.x.

Gao, X., Zhao, L., Liu, S., Li, Y., Xia, S., Chen, D., Wang, M., Wu, S., Dai, Q., Vu, H., et al. (2019). γ-6-phosphogluconolactone, a byproduct of the oxidative pentose phosphate pathway, contributes to AMPK activation through inhibition of PP2A. Mol. Cell *76*, 857–871.e9. https://doi.org/10.1016/j.molcel.2019.09.007.

Grimbs, S., Selbig, J., Bulik, S., Holzhütter, H., and Steuer, R. (2007). The stability and robustness of metabolic states: identifying stabilizing sites in metabolic networks. Mol. Syst. Biol. *3*, 146. https://doi.org/10.1038/msb4100186.

Grüning, N.M., Rinnerthaler, M., Bluemlein, K., Mülleder, M., Wamelink, M., Lehrach, H., Jakobs, C., Breitenbach, M., and Ralser, M. (2011). Pyruvate kinase triggers a metabolic feedback loop that controls redox metabolism in respiring cells. Cell Metabol. *14*, 415–427. https://doi.org/10.1016/j.cmet.2011.06.017.

Grüning, N.M., Du, D., Keller, M.A., Luisi, B.F., and Ralser, M. (2014). Inhibition of triosephosphate isomerase by phosphoenolpyruvate in the feedback-regulation of glycolysis. Open Biol. *4*, 130232. https://doi.org/10.1098/rsob.130232.

Hameri, T., Fengos, G., Ataman, M., Miskovic, L., and Hatzimanikatis, V. (2019). Kinetic models of metabolism that consider alternative steady-state solutions of intracellular fluxes and concentrations. Metab. Eng. *52*, 29–41. https://doi.org/10.1016/j.ymben.2018.10.005.

Holten, D., Procsal, D., and Chang, H.L. (1976). Regulation of pentose phosphate pathway dehydrogenases by NADP$^+$/NADPH ratios. Biochem. Biophys. Res. Commun. *68*, 436–441. https://doi.org/10.1016/0006-291x(76)91164-5.

Jahan, N., Maeda, K., Matsuoka, Y., Sugimoto, Y., and Kurata, H. (2016). Development of an accurate kinetic model for the central carbon metabolism of Escherichia coli. Microb. Cell Factories *15*, 112. https://doi.org/10.1186/s12934-016-0511-x.

Jeon, S.-M., Chandel, N.S., and Hay, N. (2012). AMPK regulates NADPH homeostasis to promote tumour cell survival during energy stress. Nature *485*, 661–665. https://doi.org/10.1038/nature11066.

Kahana, S.E., Lowry, O.H., Schulz, D.W., Passonneau, J.V., and Crawford, E.J. (1960). The kinetics of phosphoglucoisomerase. J. Biol. Chem. *235*, 2178–2184. https://doi.org/10.1016/s0021-9258(18)64594-6.

Kembro, J., Aon, M., Winslow, R., O'Rourke, B., and Cortassa, S. (2013). Integrating mitochondrial energetics, redox and ROS metabolic networks: a two-compartment model. Biophys. J. *104*, 332–343. https://doi.org/10.1016/j.bpj.2012.11.3808.

Kerkhoven, E.J., Achcar, F., Alibu, V.P., Burchmore, R.J., Gilbert, I.H., Trybiło, M., Driessen, N.N., Gilbert, D., Breitling, R., Bakker, B.M., and Barrett, M.P. (2013). Handling uncertainty in dynamic models: the pentose phosphate pathway in trypanosoma brucei. PLoS Comput. Biol. *9*, e1003371. https://doi.org/10.1371/journal.pcbi.1003371.

Kuehne, A., Emmert, H., Soehle, J., Winnefeld, M., Fischer, F., Wenck, H., Gallinat, S., Terstegen, L., Lucius, R., Hildebrand, J., and Zamboni, N. (2015). Acute activation of oxidative pentose phosphate pathway as first-line response to oxidative stress in human skin cells. Mol. Cell *59*, 359–371. https://doi.org/10.1016/j.molcel.2015.06.017.

Kuehne, A., Mayr, U., Sévin, D.C., Claassen, M., and Zamboni, N. (2017). Metabolic network segmentation: a probabilistic graphical modeling approach to identify the sites and sequential order of metabolic regulation from non-targeted metabolomics data. PLoS Comput. Biol. *13*, e1005577. https://doi.org/10.1371/journal.pcbi.1005577.

LaMonte, G., Tang, X., Chen, J.L.Y., Wu, J., Ding, C.K.C., Keenan, M.M., Sangokoya, C., Kung, H.N., Ilkayeva, O., Boros, L.G., et al. (2013). Acidosis induces reprogramming of cellular metabolism to mitigate oxidative stress. Cancer Metabol. *1*, 23. https://doi.org/10.1186/2049-3002-1-23.

Lewis, C., Parker, S., Fiske, B., McCloskey, D., Gui, D., Green, C., Vokes, N., Feist, A., Vander Heiden, M., and Metallo, C. (2014). Tracing compartmentalized nadph metabolism in the cytosol and mitochondria of mammalian cells. Mol. Cell *55*, 253–263. https://doi.org/10.1016/j.molcel.2014.05.008.

Li, X., Wu, F., Qi, F., and Beard, D.A. (2011). A database of thermodynamic properties of the reactions of glycolysis, the tricarboxylic acid cycle, and the pentose phosphate pathway. Database *2011*, bar005. https://doi.org/10.1093/database/bar005.

Lin, R., Elf, S., Shan, C., Kang, H.B., Ji, Q., Zhou, L., Hitosugi, T., Zhang, L., Zhang, S., Seo, J.H., et al. (2015). 6-Phosphogluconate dehydrogenase links oxidative PPP, lipogenesis and tumour growth by inhibiting LKB1–AMPK signalling. Nat. Cell Biol. *17*, 1484–1496. https://doi.org/10.1038/ncb3255.

Link, H., Kochanowski, K., and Sauer, U. (2013). Systematic identification of allosteric protein-metabolite interactions that control enzyme activity in vivo. Nat. Biotechnol. *31*, 357–361. https://doi.org/10.1038/nbt.2489.

Liu, R., Li, W., Tao, B., Wang, X., Yang, Z., Zhang, Y., Wang, C., Liu, R., Gao, H., Liang, J., and Yang, W. (2019). Tyrosine phosphorylation activates 6-phosphogluconate dehydrogenase and promotes tumor growth and radiation resistance. Nat. Commun. *10*, 991. https://doi.org/10.1038/s41467-019-08921-8.

Machado, D., Herrgård, M.J., and Rocha, I. (2015). Modeling the contribution of allosteric regulation for flux control in the central carbon metabolism of e. coli. Front. Bioeng. Biotechnol. *3*, 154. https://doi.org/10.3389/fbioe.2015.00154.

Makino, N., Sasaki, K., Hashida, K., and Sakakura, Y. (2004). A metabolic model describing the H2O2 elimination by mammalian cells including H2O2 permeation through cytoplasmic and peroxisomal membranes: comparison with experimental data. Biochim. Biophys. Acta *1673*, 149–159. https://doi.org/10.1016/j.bbagen.2004.04.011.

Millard, P., Smallbone, K., and Mendes, P. (2017). Metabolic regulation is sufficient for global and robust coordination of glucose uptake, catabolism, energy production and growth in escherichia coli. PLoS Comput. Biol. *13*, e1005396. https://doi.org/10.1371/journal.pcbi.1005396.

Miskovic, L., Tokic, M., Fengos, G., and Hatzimanikatis, V. (2015). Rites of passage: requirements and standards for building kinetic models of metabolic phenotypes. Curr. Opin. Biotechnol. *36*, 146–153. https://doi.org/10.1016/j.copbio.2015.08.019.

Mullarky, E., and Cantley, L.C. (2015). Diverting glycolysis to combat oxidative stress. Innov. Med. 3–23. https://doi.org/10.1007/978-4-431-55651-0_1.

Negelein, E., and Haas, E. (1935). Uber die wirkungsweise des zweischenferments. Biochem. Z. *282*, 206–220.

Ng, C.F., Schafer, F.Q., Buettner, G.R., and Rodgers, V.G.J. (2007). The rate of cellular hydrogen peroxide removal shows dependency on GSH: mathematical insight into in vivo H2O2 and GPx concentrations. Free Radic. Res. *41*, 1201–1211. https://doi.org/10.1080/10715760701625075.

Nikel, P.I., Fuhrer, T., Chavarría, M., Sánchez-Pascuala, A., Sauer, U., and de Lorenzo, V. (2021). Reconfiguration of metabolic fluxes in pseudomonas putida as a response to sub-lethal oxidative stress. ISME J. *15*, 1751–1766. https://doi.org/10.1038/s41396-020-00884-9.

Nóbrega-Pereira, S., Fernandez-Marcos, P.J., Brioche, T., Gomez-Cabrera, M.C., Salvador-Pascual, A., Flores, J.M., Viña, J., and Serrano, M. (2016). G6PD protects from oxidative damage and improves healthspan in mice. Nat. Commun. *7*, 10894. https://doi.org/10.1038/ncomms10894.

Parr, C.W. (1956). Inhibition of phosphoglucose isomerase. Nature *178*, 1401. https://doi.org/10.1038/1781401a0.

Peralta, D., Bronowska, A.K., Morgan, B., Dóka, É., Van Laer, K., Nagy, P., Gräter, F., and Dick, T.P. (2015). A proton relay enhances H2O2 sensitivity of GAPDH to facilitate metabolic adaptation. Nat. Chem. Biol. *11*, 156–163. https://doi.org/10.1038/nchembio.1720.

Pfeuty, B., and Thommen, Q. (2016). Adaptive benefits of storage strategy and dual ampk/tor signaling in metabolic stress response. PLoS One *11*, e0160247. https://doi.org/10.1371/journal.pone.0160247.

Pfeuty, B., Kress, C., and Pain, B. (2018). Network features and dynamical landscape of naive and primed pluripotency. Biophys. J. *114*, 237–248. https://doi.org/10.1016/j.bpj.2017.10.033.

Ralser, M., Wamelink, M.M., Kowald, A., Gerisch, B., Heeren, G., Struys, E.A., Klipp, E., Jakobs, C., Breitenbach, M., Lehrach, H., and Krobitsch, S. (2007). Dynamic rerouting of the carbohydrate flux is key to counteracting oxidative stress. J. Biol. *6*, 10. https://doi.org/10.1186/jbiol61.

Ralser, M., Wamelink, M.M.C., Latkolik, S., Jansen, E.E.W., Lehrach, H., and Jakobs, C. (2009). Metabolic reconfiguration precedes transcriptional regulation in the antioxidant response. Nat. Biotechnol. *27*, 604–605. https://doi.org/10.1038/nbt0709-604.

Relógio, A., Westermark, P.O., Wallach, T., Schellenberg, K., Kramer, A., and Herzel, H. (2011). Tuning the mammalian circadian clock: robust synergy of two loops. PLoS Comput. Biol. *7*, e1002309. https://doi.org/10.1371/journal.pcbi.1002309.

Reznik, E., Christodoulou, D., Goldford, J.E., Briars, E., Sauer, U., Segrè, D., and Noor, E. (2017). Genome-scale architecture of small molecule regulatory networks and the fundamental trade-off between regulation and enzymatic activity. Cell Rep. *20*, 2666–2677. https://doi.org/10.1016/j.celrep.2017.08.066.

Rohwer, J., Hanekom, A., Crous, C., Snoep, J., and Hofmeyr, J.H. (2006). Evaluation of a simplified generic bi-substrate rate equation for computational systems biology. IET Syst. Biol. *153*, 338. https://doi.org/10.1049/ip-syb:20060026.

Saa, P.A., and Nielsen, L.K. (2016). Construction of feasible and accurate kinetic models of metabolism: a Bayesian approach. Sci. Rep. *6*, 29635. https://doi.org/10.1038/srep29635.

Sander, T., Farke, N., Diehl, C., Kuntz, M., Glatter, T., and Link, H. (2019). Allosteric feedback inhibition enables robust amino acid biosynthesis in E. coli by enforcing enzyme overabundance. Cell Syst. *8*, 66–75.e8. https://doi.org/10.1016/j.cels.2018.12.005.

Schuster, R., and Holzhütter, H.-G. (1995). Use of mathematical models for predicting the metabolic effect of large-scale enzyme activity alterations: application to enzyme deficiencies of red blood cells. Eur. J. Biochem. *229*, 403–418. https://doi.org/10.1111/j.1432-1033.1995.0403k.x.

Seo, M., and Lee, Y.-H. (2014). Pfkfb3 regulates oxidative stress homeostasis via its s-glutathionylation in cancer. J. Mol. Biol. *426*, 830–842. https://doi.org/10.1016/j.jmb.2013.11.021.

Stincone, A., Prigione, A., Cramer, T., Wamelink, M.M.C., Campbell, K., Cheung, E., Olin-Sandoval, V., Grüning, N., Krüger, A., Tauqeer Alam, M., et al. (2015). The return of metabolism: biochemistry and physiology of the pentose phosphate pathway. Biol. Rev. *90*, 927–963. https://doi.org/10.1111/brv.12140.

Sun, Y., Bandi, M., Lofton, T., Smith, M., Bristow, C.A., Carugo, A., Rogers, N., Leonard, P., Chang, Q., Mullinax, R., et al. (2019). Functional genomics reveals synthetic lethality between phosphogluconate dehydrogenase and oxidative phosphorylation. Cell Rep. *26*, 469–482.e5. https://doi.org/10.1016/j.celrep.2018.12.043.

Theorell, A., and Nöh, K. (2020). Reversible jump MCMC for multi-model inference in metabolic flux analysis. Bioinformatics *36*, 232–240. https://doi.org/10.1093/bioinformatics/btz500.

Thommen, Q., Hurbain, J., and Pfeuty, B. (2022). Stochastic simulation algorithm for isotope labeling metabolic networks. Preprint at arXiv. 2201.00663. https://doi.org/10.48550/arXiv.2201.00663.

Thorburn, D.R., and Kuchel, P.W. (1985). Regulation of the human-erythrocyte hexose-monophosphate shunt under conditions of oxidative stress: a study using NMR spectroscopy, a kinetic isotope effect, a reconstituted system and computer simulation. Eur. J. Biochem. *150*, 371–380. https://doi.org/10.1111/j.1432-1033.1985.tb09030.x.

Valderrama-Bahamóndez, G.I., and Fröhlich, H. (2019). MCMC techniques for parameter estimation of ODE based models in systems biology. Front. Appl. Math. Stat. *5*, 1–10.

van der Reest, J., Lilla, S., Zheng, L., Zanivan, S., and Gottlieb, E. (2018). Proteome-wide analysis of cysteine oxidation reveals metabolic sensitivity to redox stress. Nat. Commun. *9*, 1581. https://doi.org/10.1038/s41467-018-04003-3.

Wan, N., DeLorenzo, D.M., He, L., You, L., Immethun, C.M., Wang, G., Baidoo, E.E.K., Hollinshead, W., Keasling, J.D., Moon, T.S., and Tang, Y.J. (2017). Cyanobacterial carbon metabolism: fluxome plasticity and oxygen dependence. Biotechnol. Bioeng. *114*, 1593–1602. https://doi.org/10.1002/bit.26287.

Warburg, O., and Christian, W. (1936). Pyridin, der wasserstoffübertragende Bestandteil von Gärungsfermenten. Helv. Chim. Acta *19*, E79–E88. https://doi.org/10.1002/hlca.193601901199.

Wu, S.-B., and Wei, Y.-H. (2012). AMPK-mediated increase of glycolysis as an adaptive response to oxidative stress in human cells: implication of the cell survival in mitochondrial diseases. Biochim. Biophys. Acta *1822*, 233–247. https://doi.org/10.1016/j.bbadis.2011.09.014.

Xu, Y., Létisse, F., Absalan, F., Lu, W., Kuznetsova, E., Brown, G., Caudy, A.A., Yakunin, A.F., Broach, J.R., and Rabinowitz, J.D. (2013). Nucleotide degradation and ribose salvage in yeast. Mol. Syst. Biol. *9*, 665. https://doi.org/10.1038/msb.2013.21.

Yoshida, A., and Lin, M. (1973). Regulation of glucose-6-phosphate dehydrogenase activity in red blood cells from hemolytic and nonhemolytic variant subjects. Blood *41*, 877–891. https://doi.org/10.1182/blood.v41.6.877.877.

STAR★METHODS

KEY RESOURCES TABLE

REAGENT or RESOURCE	SOURCE	IDENTIFIER
Deposited data		
Target experimental data	https://doi.org/10.1016/j.molcel.2015.06.017	Figure 2; Tables S1 and S5
Matlab code and simulation data	https://doi.org/10.5281/zenodo.6656078 https://github.com/JHurb/HurbainPaper_Algorithm/tree/v1.0.0	JHurb/HurbainPaper_Algorithm-v1.0.0.zip
SBML model	http://www.ebi.ac.uk/biomodels/MODEL2204220001	MODEL2204220001
Software and algorithms		
Matlab	https://www.mathworks.com/products/matlab.html	R2018a
SSA 13CMFA	arXiv:2201.00663v1	

RESOURCE AVAILABILITY

Lead contact

Further information and requests for resources should be directed to and will be fulfilled by the Lead Contact, Benjamin Pfeuty (benjamin.pfeuty@univ-lille.fr).

Materials availability

This study did not generate new unique reagents.

Data and code availability

- Data have been deposited at Zenodo and are publicly available as of the date of publication
- All original code has been deposited at Zenodo and is publicly available as of the date of publication. A SBML version of the model has also been deposited in the BioModels database as MODEL2204220001. DOIs and URLs are listed in the key resources table.
- Any additional information required to reanalyze the data reported in this paper is available from the lead contact upon request.

METHOD DETAILS

SSA-based ^{13}C-MFA

Stochastic simulation algorithm (SSA) for ^{13}C-based metabolic flux analysis (^{13}C-MFA) is a direct method for the forward simulation problem to compute the dynamics and steady state of (mass) isotopomer distribution in isotopic labeling networks (Thommen et al., 2022). From a given flux distribution $\vec{\varphi}$ and initial labeling state, SSA computes the temporal evolution of isotopomer numbers which are pooled to obtain the mass isotopomer distribution $m_{i,j}$ of species j. The sample size parameter of the algorithm is $\Omega = 200$. From the experimental values $m^k_{i,j,exp}$ measured for n_i mass isotopomer, n_j species j in n_k labeling conditions (Kuehne et al., 2015), SSA is performed iteratively using a MCMC sampling method based on a random walk Metropolis algorithm (see section quantification and statistical analysis) for obtaining the posterior distribution of flux parameters. In such flux estimation procedure, the root mean square error function is given by:

$$RMSE(\vec{\varphi}) = \sqrt{\frac{1}{N_m}\sum_{i,j,k}\left(m^k_{i,j,sim}(\vec{\varphi},t) - m^k_{i,j,exp}(t)\right)^2}, \qquad \text{(Equation 2)}$$

where the measurement time is $t = 10$min and the number of experiments is $N_m = n_i n_j n_k = 84$ ($n_i = 3$, $n_j = 7$, $n_k = 4$).

Differential equation model

The temporal behavior of the metabolic network is described by a differential equation system:

$$d[H_2O_2]/dt = \varphi_{Ox} - \varphi_{Cat} - \varphi_{GPx} \tag{Equation 3a}$$

$$d[GSH]/dt = 2\varphi_{GR} - 2\varphi_{GPx} \tag{Equation 3b}$$

$$d[NADPH]/dt = \varphi_{G6PD} + \varphi_{6PGD} + \varphi_{NNH} - \varphi_{NHN} - \varphi_{GR} \tag{Equation 3c}$$

$$d[G6P]/dt = \varphi_{HK} - \varphi_{G6PD} - \varphi_{PGI} \tag{Equation 3d}$$

$$d[6PGL]/dt = \varphi_{G6PD} - \varphi_{6PGL} \tag{Equation 3e}$$

$$d[6PG]/dt = \varphi_{6PGL} - \varphi_{6PGD} \tag{Equation 3f}$$

$$d[Ru5P]/dt = \varphi_{6PGD} - \varphi_{RPI} - \varphi_{RPE} \tag{Equation 3g}$$

$$d[X5P]/dt = \varphi_{RPE} - \varphi_{TKT1} - \varphi_{TKT2} \tag{Equation 3h}$$

$$d[R5P]/dt = \varphi_{RPI} - \varphi_{TKT1} - \varphi_{PRPP} \tag{Equation 3i}$$

$$d[S7P]/dt = \varphi_{TKT1} - \varphi_{TLD} \tag{Equation 3j}$$

$$d[E4P]/dt = \varphi_{TLD} - \varphi_{TKT2} \tag{Equation 3k}$$

$$d[GLC]/dt = \varphi_{GLU} - \varphi_{HK} \tag{Equation 3l}$$

$$d[F6P]/dt = \varphi_{PGI} - \varphi_{PFK} + \varphi_{TAL} + \varphi_{TKT2} \tag{Equation 3m}$$

$$d[FBP]/dt = \varphi_{PFK} - \varphi_{ALD} \tag{Equation 3n}$$

$$d[DHAP]/dt = \varphi_{ALD} - \varphi_{TPI} \tag{Equation 3o}$$

$$d[GAP]/dt = \varphi_{ALD} + \varphi_{TKT1} - \varphi_{TAL} + \varphi_{TKT2} + \varphi_{TPI} - \varphi_{GAPD} \tag{Equation 3p}$$

For reversible reactions, we also introduce directional fluxes satisfying the relation $\varphi_j = \varphi_j^+ - \varphi_j^-$ where, by convention, the + direction goes from G6P to GAP in glycolysis and from R5P to GAP in nonoxidative PPP. Note that φ_{PFK} represents the net flux of the two reactions between F6P and FBP, where φ_{PFK}^+ corresponds to the PFK1 reaction and φ_{PFK}^- corresponds to the FBPase reaction.

List of abbreviations for metabolites and enzymes

Glc, intracellular glucose; G6P, glucose-6-phosphate; F6P, fructose-6-phosphate; FBP, fructose-1,6-bisphosphate; ALD, fructose 1,6 bisphosphate aldolase; DHAP, dihydroxyacetone phosphate; GAP, glyceraldehyde-3-phosphate; PEP, phosphoenolpyruvate; 6PG, 6-phosphogluconate; 6PGL, 6-phosphogluconolactone; X5P, xylulose 5-phosphate; R5P, ribose 5-phosphate; TPI, triosephosphate isomerase; Ru5P, ribulose 5-phosphate; OX, oxidative stress E4P, erythrose-4-phosphate; S7P, sedoheptulose 7-phosphate; PEP, phosphoenolpyruvate; GT, total glutathione; NT, total NADP; Cat, catalase GR, glutathione reductase; GPx, glutathione peroxydase; Prx, peroxiredoxin; Trx, thioredoxin; HK, hexokinase; G6PD, G6P dehydrogenase; 6PGD, 6PG dehydrogenase; GLase, 6-phosphogluconolactonase; PRPP, phosphoribosyl pyrophosphate; PGI, phosphoglucose isomerase; PFK, phosphofructokinase (type 1); FBPase, fructose-1,6-bisphosphatase; GAPD, GAP dehydrogenase; PK, pyruvate kinase; TLD, transaldolase; TKT(1/2), transketolase (type 1/2); NNH, conversion from NADP$^+$ to NADPH; NHN, conversion from NADPH to NADP$^+$.

Enzyme-kinetic reaction rates

Reaction rates $\varphi(\bullet)$ can be described by diverse kinetic laws (e.g., mass action, Michaelis-Menten, Hill, Monod-Wyman-Changeux…). In the present work, we mainly use the generalized mass action kinetics, eventually associated with inhibition:

$$MA(m,n):\ \varphi(S, P, I, k_i, Keq_i, Ki_i) = k_i\left(\prod_{j=1,m} S_j - (Keq_i)^{-1}\prod_{j=1,n} P_j\right)(1 + I/Ki_i)^{-1} \tag{Equation 4}$$

where m and n are the number of substrates and products.

However in the context of oxidative stress response, the significant increase of some metabolite concentrations may require to take into account saturation constants that appear due to the formation of intermediate complexes. A generalization of the uni-uni Michaelis–Menten equation can also be used for irreversible and reversible uni/bi-substrate reaction kinetics (Rohwer et al., 2006):

$$MM(m,0): \varphi(S,P,k_i,Km_i) = \frac{k_i \prod_j S_j}{\prod_j \left(1 + S_j / Km_{sj,i}\right)} \qquad \text{(Equation 5)}$$

$$MM(m,n): \varphi\left(S,P,k_i,Keq_i,Km_i\right) = \frac{k_i\left(\prod_j S_j - \left(Keq_i\right)^{-1} \prod_j P_j\right)}{\prod_j \left(1 + S_j / Km_{sj,i} + P_j / Km_{pj,i}\right)} \qquad \text{(Equation 6)}$$

where $j = 1$ for unisubstrate reactions and $j = 1,2$ for bisubstrate reactions, and where the denominator contains numerous terms for each substrates and products. In some bisubstrate reactions, the assumption that $S \ll K_m$ is made so as to reducing the number of terms and parameter in denominator. Specifically, Michaelis constants are considered only for 6PG, H_2O_2, GSSG and GSH and in nonoxidative PPP reactions. For GPx and GR reactions, the saturation terms follow a common scheme based on experimental data (Benfeitas et al., 2014). A minimal description of saturation in nonoxidative PPP reactions consists in keeping only product terms (which prevails in case where S_i / Km_i larger than one) and assumes a same Michaelis constant for substrates and products.

The oxidative stress-dependent inhibition of NADPH consumption related to putative biosynthetic shutdown (Fan et al., 2014) is modeled as an effective rate constant $k_{NADPH} / \left(1 + \frac{[H_2O_2]}{Ki_{NNH}}\right)$. As well, a simplified description of the oxidative inhibition of GADP enzyme considers a two-state enzyme (non-oxidized and oxidized) where the back-and-forth transition rates depend on the concentration of H_2O_2 and GSH, respectively:

$$d[GAPD]/dt = f_1([GSH])([GAPD_{TOT}] - [GAPD]) - f_2([H_2 0_2])[GAPD] \qquad \text{(Equation 7)}$$

which becomes following quasi-steady-state approximation and linear approximation of regulatory functions f_1 and f_2:

$$\frac{[GAPD]}{GAPD_{TOT}} = \frac{1}{1 + f_2 / f_1} \approx \left(1 + \frac{[H_2O_2][GT]}{[GSH] Ki_{GAPD}}\right)^{-1} \qquad \text{(Equation 8)}$$

from which we derive the expression of φ_{GAPD} given in Table S1. The reaction kinetic law associated to each enzymatic reaction $\varphi_j(\bullet)$ is recapitulated in Table S1.

Parameter setting and estimation

Model includes 48 parameters including kinetic constants k_i, equilibrium constants Keq_i, Michaelis (saturation) constants Km_i, inhibitory constants Ki_i, where i denotes the enzyme, but also conserved quantities $[NT]$ and $[GT]$. To restrict and ease the parameter estimation process, parameters are bounded within a restricted range of realistic values as it is often assumed (Christodoulou et al., 2018). An exception is that 8 equilibrium constant values Keq_i have been fixed based on estimated physiological standard free energy of corresponding reactions (Li et al., 2011). In addition, two saturation constants Km_i and the conserved quantities $[GT] = 2[GSSG] + [GSH]$ and $[NT] = [NADPH] + [NADP^+]$ have also been fixed based on typical values (Benfeitas et al., 2014) and the modeling requirement to reduce parameter space and to constraint parameter estimation. A specific model of index j is denoted as $\vec{p}^{\,j}$ and a set k of model $j = 1, N_k$ is denoted $\mathcal{P}^k$.

Given a parameter space $\mathcal{P}$ where parameter values are restricted by upper and lower bounds (listed in Table S2), the parameter estimation problem consists in scoring parameter set $\vec{p} \in \mathcal{P}$ by using a normalized root mean square error (nRMSE) :

$$nRMSE\left(\vec{p} \in \mathcal{P}\right) = \sqrt{\frac{1}{N_R + N_\Phi}\left(\sum_{i=1,N_R}\left(\frac{FC_{i,sim}\left(\vec{p}\right) - FC_{i,exp}}{\Delta FC_{i,exp}}\right)^2 + \sum_{i=1,N_\varphi}\left(\frac{\Phi_{i,sim}\left(\vec{p}\right) - \Phi_{i,exp}}{\Delta \Phi_{i,exp}}\right)^2\right)}, \qquad \text{(Equation 9)}$$

where $FC_i = log_2\left(\frac{X_i(H = 500)}{X_i(H = 0)}\right)$ are concentration ratios in log scale and Φ_i are the estimated fluxes of reaction i in basal condition and in stress condition. Experimental data consists in $N_R = 12$ and $N_\Phi = 13$ values of concentration ratio FC_i and estimated fluxes Φ_i with a typical standard deviation $\Delta FC_i = 1$ and $\Delta\Phi_i$ that is estimated from ^{13}C-MFA.

This error function is used first with a population-based metaheuristic algorithm called evolution strategy to quickly explore and sample local solutions (Pfeuty and Thommen, 2016). Starting with a pool of $N_I = 20$ parameter vectors of random values (bounded uniform distribution), the algorithm involves three steps: (i) a reproduction step where a parent is randomly selected to be duplicated without applying any fitness criterion at this stage, and to generate N_I offspring; (ii) a mutation step where the parameters of each offspring are modified with a probability p_m through multiplication by a factor 10^r, where $r \in [-a_m, a_m]$ is a random number of uniform distribution; (iii) a selection step where the nRMSE of the N_I offspring are evaluated, and only the N_I highest-fitness individuals in the pool of $2N_I$ parameter sets (parents and offspring) are selected to generate the parents of the next generation. Finally, the optimization process terminates after a maximal number of generations ($N_G = 10^4$) where a local minimum of $nRMSE(\vec{p})$ is usually reached. This evolution is repeated for a broad set of random initial conditions to obtain a first set of optimized models, some of which satisfies the plausibility criteria $nRMSE < 1$. The lowest-nRMSE model $\vec{p}^1$ is used as an initial condition of the MCMC algorithm (see section quantification and statistical analysis) used to sample a posterior probabilistic distribution of parameters. After a transient, a sample of 10^6 accepted values are recorded to converge to a representative model ensemble associated to quasi-stationary distributions, while a random subsample of 10^5 models is used for the statistical analysis of model behaviors.

Sensitivity analysis

Sensitivity quantities are defined to evaluate the effect of parameter changes on stress response behaviors. A model ensemble is defined by a set of model $\vec{p}^{j=1,n_M}$. For a given kinetic model of parameter values $\vec{p}^j$, a parameter p_i^j is multiplied by a factor Δp_i. A sensitivity factor that informs about the impact of a given parameter p_i on the output state variable Y in response to a stress level H is given by:

$$\Delta_{p_i}^Y(H, \Delta p_i) = \frac{Y(H, \vec{q}^j)}{Y(H, \vec{p}^j)}, \qquad \text{(Equation 10)}$$

where $q_i^j = \Delta p_i p_i^j$. The choice of parameter p_i and variation Δp_i are selected (i) to evaluate the impact of a regulatory mechanism (i.e., p_i are inhibitory parameters Ki_i and $\Delta p_i = \infty$) and (ii) to mimmic overexpression or knockdown experiments (i.e., p_i are enzymatic activity rates k_i and $0.1 < \Delta p_i < 10$). Another class of sensitivity quantities are response coefficients:

$$R_{p_i}^Y(H) = \frac{\partial \ln Y(H)}{\partial \ln p_i}, \qquad \text{(Equation 11)}$$

The relation between both sensitivity quantities is given by $R_{p_i}^Y(H) = \lim_{\Delta p_i \to 1}\left[\left(\Delta_{p_i}^Y(H, \Delta p_i) - 1\right)/(\Delta p_i - 1)\right]$.

Model updating procedure

From a methodological perspective, the modeling approach relies on a systematic procedure for model inference and parameter estimation, which deliberately considers more parameters than data to provide the possibility to update the probability distribution as additional data becomes available or as additional mechanistic hypothesis are tested. MCMC method is very well adapted for such model updating procedure (Beck and Au, 2002). Specifically, MCMC sampling can be restarted from a given parameter distribution with a modification of the score function and of the sample space. By testing the predictive capacity of the model on dataset that are not included in the model inference procedure, we could indeed identify sparse phenotypes poorly described by the model. An example of model improvement would be to add the corresponding dataset into the monte-carlo sampling procedure which might slightly shift the parameter set of solution to be consistent with these new dataset.

QUANTIFICATION AND STATISTICAL ANALYSIS

Monte Carlo Markov Chain (MCMC) method

Monte Carlo Markov Chain (MCMC) method is used for estimating the distribution of (i) metabolic flux from ^{13}C labeling data and (ii) kinetic model parameters from concentration data and flux estimation. These two computational problems are both defined by a set of n_p parameters $\vec{\theta}$, a set of n_d data values $\vec{y}$ and a root mean square error $r(\vec{\theta}, \vec{y})$ measuring the difference between data predicted by the parameters and the actual data (see Equations 2 and 9). MCMC simulation methods use Monte Carlo sampling techniques to build Markov chains that converge to the posterior distribution of parameters θ associated to data Y. For both problems, we consider a bounded uniform distribution for the prior. For sampling, a Metropolis-Hasting algorithm is used to generate the random walk Markov chain based on (i) a Gaussian jumping distribution and (ii) an acceptance rate function α that is the ratio of likelihood associated to the next parameter state and actual parameter state. Typically, the likelihood function can be written based on the expected or assumed distribution of observed data, as $\mathcal{L}(Y,\theta) = (2\pi\sigma)^{-n/2}\exp\left(-\frac{n\,r^2}{2\sigma^2}\right)$. Specifically, we use the acceptance rate $\alpha = \min\left(1, \exp\left(-\frac{r_{i+1}^2 - r_i^2}{2\sigma^2}\right)\right)$ where the variances of jumping distribution and likelihood function σ are chosen to provide reasonable acceptance rate ($>10\%$) and convergence rate. a.

R-squared

Although R-squared is commonly used to assess the goodness-of-fit for a regression model, this quantity can be applied, in addition to RMSE, to assess the fitting and prediction score for the ordinary differential equation models without requiring knowledge about experimental uncertainties:

$$R^2\left(\vec{p} \in \mathcal{P}\right) = 1 - \frac{\sum_{i=1,N_Y}\left(Y_{i,sim}\left(\vec{p}\right) - Y_{i,exp}\right)^2}{\sum_{i=1,N_Y}\left(\overline{Y}_{i,exp} - Y_{i,exp}\right)^2} \qquad \text{(Equation 12)}$$

where $\overline{Y}_{i,exp} = \frac{1}{N_Y}\sum_{i=1,N_Y} Y_{i,exp}$ and Y represents some measurement such as fold-change concentrations.

iScience, Volume *25*

Supplemental information

Quantitative modeling of pentose phosphate pathway response to oxidative stress reveals a cooperative regulatory strategy

Julien Hurbain, Quentin Thommen, Francois Anquez, and Benjamin Pfeuty

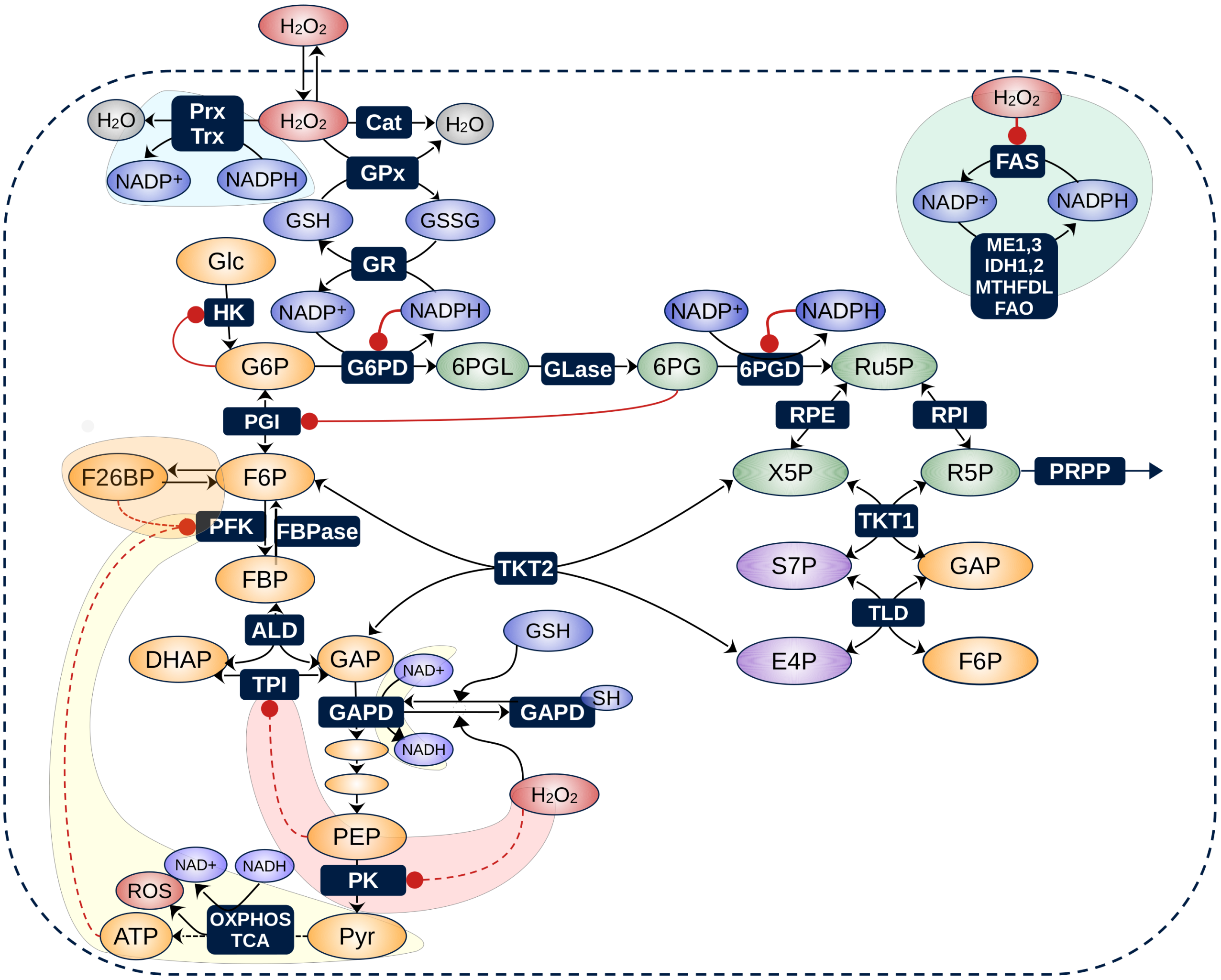

Figure S1: Overview of metabolic pathways and metabolite-enzyme interactions involved in oxidative stress response, related to Figure 1. Metabolic pathways are organized around (i) the antioxidant system (blue metabolites), (ii) the oxidative and non-oxidative pentose phosphate pathway (green and violet metabolites) and (iii) the glycolytic pathway (yellow metabolites). Arrows toward enzymes indicate the allosteric and oxidative regulations potentially involved in rapid metabolic adaptations and flux rerouting to manage oxidative stress. Colored areas correspond to metabolic and regulatory pathways that have not been incorporated in the model or that have been described in a simplified manner. *Red area*: feedback mechanism mediated by the coordination of oxidative inhibition of PK (Anastasiou *et al.*, 2011) and PEP-dependent allosteric inhibition of TPI (Grüning *et al.*, 2011, 2014) is not considered since the considered dataset shows a 2.8-decrease of PEP (Table S5 of (Kuehne *et al.*, 2015)), suggesting weak or negligible inhibition of PK enzyme. *Yellow area*: feedback mechanisms mediated by the regulation of oxidative phosphorylation (OXPHOS) generating ROS, ATP or NAD$^+$ where ROS can contribute to oxidative stress, ATP regulates PFK1 glycolytic reaction and NAD$^+$ regulates GAPD activity. These feedback are not considered due to (i) the lack of available experimental data about fluxes in the TCA and concentrations of NAD(H) and (ii) the low variations of ADP/ATP and AMP/ATP ratios less than 2 fold reported in Table S5 of (Kuehne *et al.*, 2015). *Orange area*: Interconversion between F6P and F26BP is neglected due to the absence of concentration data and 13C labeling data about F26BP. *Blue area*: intracellular detoxification of H_2O_2 is mediated by several antioxidant reactions involving catalases and two thiol-based peroxidases (Prx and GPx). For the latter, the model is restricted to gluthathione-dependent antioxidant system, keeping in mind that NADPH is the electron donor in both systems suggesting strong similarities. *Green area*: besides gluthatione pathways and PPP, the many other reactions involved in NADPH consumption and production (e.g., malic enzymes, IDH, fatty acid synthesis and oxidation, folate cycle) are pooled in effective reactions called NHN and NNH respectively. Abbreviations: TCA, tricarboxylic acid cycle; OXPHOS, oxidative phosphorylation; ROS, reactive oxygen species; FAO,FAS, fatty acid oxidation/synthesis; For other abbreviations, see STAR Methods.

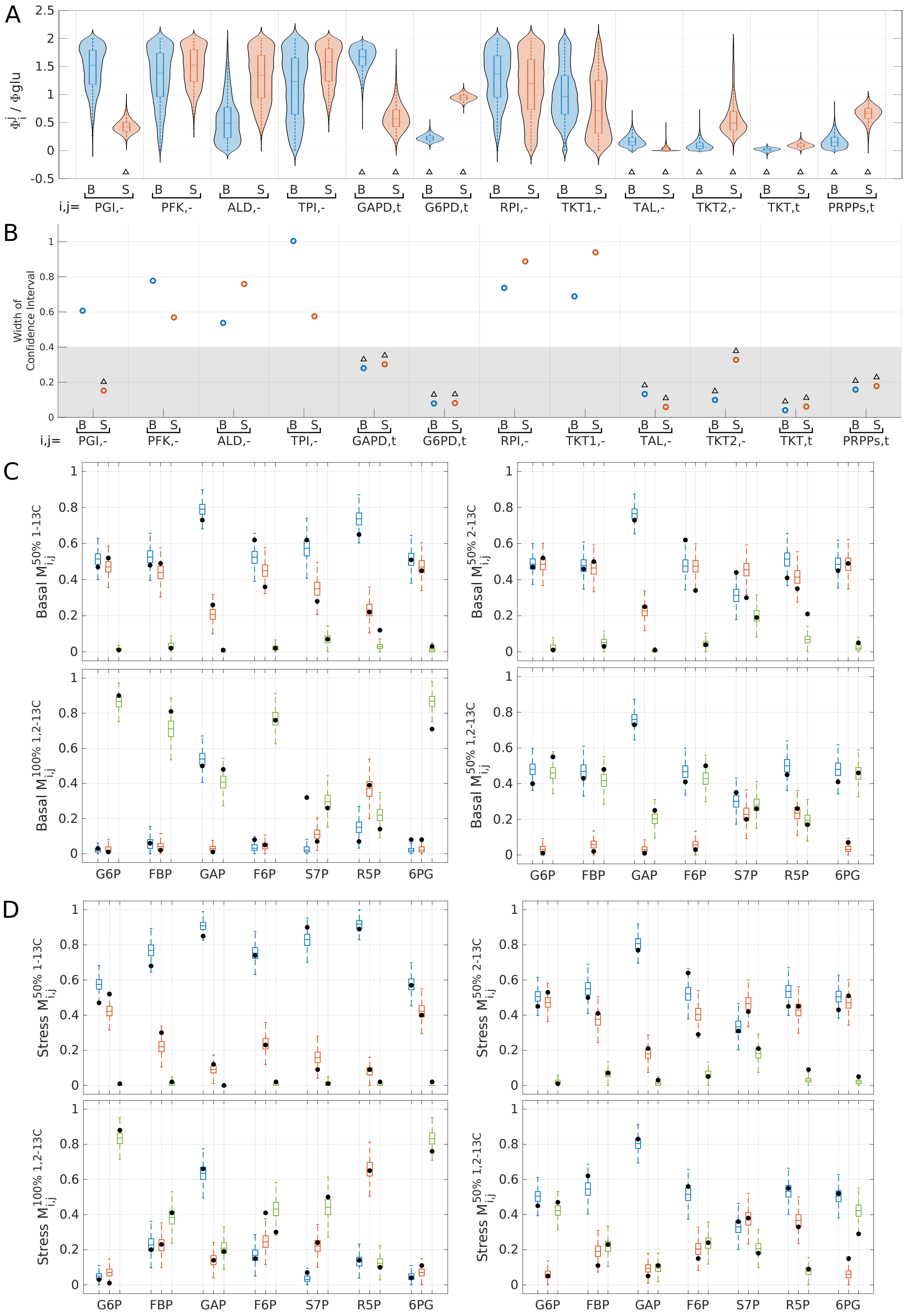

Figure S2: Metabolic flux analysis from 13C labeling data, related to Figure 2. (A) Violin plot of the estimated flux distribution obtained from MCMC sampling of SSA simulation of the labeled isotopic systems. Blue and red indicate basal and stress conditions. (B) 50% confidence intervals of flux distributions where the threshold 0.4 (gray area) determines the subset of fluxes (indicated by triangles) whose estimation is accurate enough to be used for the model fitting procedure. (C,D) Box plots of $M_{i,j}$ obtained from MCMC sampling of SSA simulation of the labeled isotopic systems in four labeling conditions as compared with experimental values (black circles) in absence (C) and presence (D) of oxidative stress respectively. Color code represents $m0$ (blue), $m1$ (red) and $m2$ (blue) respectively.

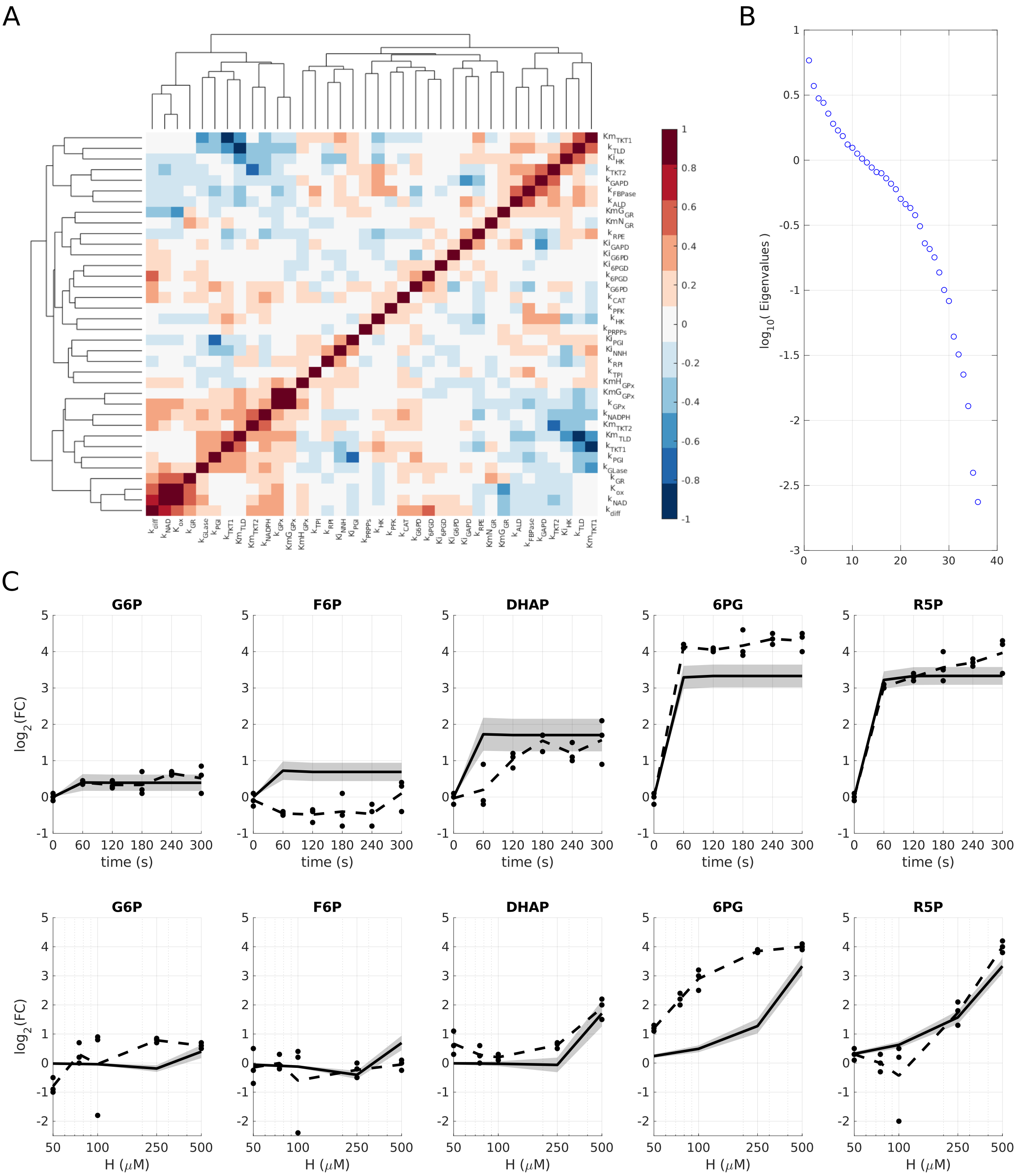

Figure S3: Parameter distribution and predictive capabilities of kinetic model ensemble, related to Figure 3. (A) Reordered correlation matrix heatmap and accompanying dendrogram for the estimated kinetic parameter p_i^j of the adjusted model ensemble $\vec{p}^j \in \mathcal{P}^{opt}$. (B) Ranked eigenvalues of the correlation matrix. The 5 highest eigenvalues contributes to 50% of the variance (i.e., 50% of the variance can be captured by four linear combinations of parameters). (C) Prediction of the model ensemble $\mathcal{P}^{opt}$ compared to some experimental data that were not purposedly used as target dataset in the nRMSE score function in the parameter estimation procedure. Fold-change (FC) of metabolite concentrations after stress versus before stress exposure as function of time (up panels) and extracellular H_2O_2 concentration (down panels). Model results (full line) is compared to data points and averaged measurements (dashed mline) (Kuehne *et al.*, 2015). Goodness-of-fit is evaluated by computing the distribution of R-squared over the model ensemble. The predicted R-squared values associated to time series data is $R^2 = 0.82 \pm 0.05$. The predicted R-squared value associated to dose-response data is $R^2 = 0.48 \pm 0.04$. Predicted R-squared values are lower than adjusted R-squared values computed in Figure 3 (associated to t = 5min and $H = 500\mu$M), but remains significantly high. The lower predicted R-squared value for dose-response data is due to the disagreement observed for the 6PG increase at $H < 250\mu$M.

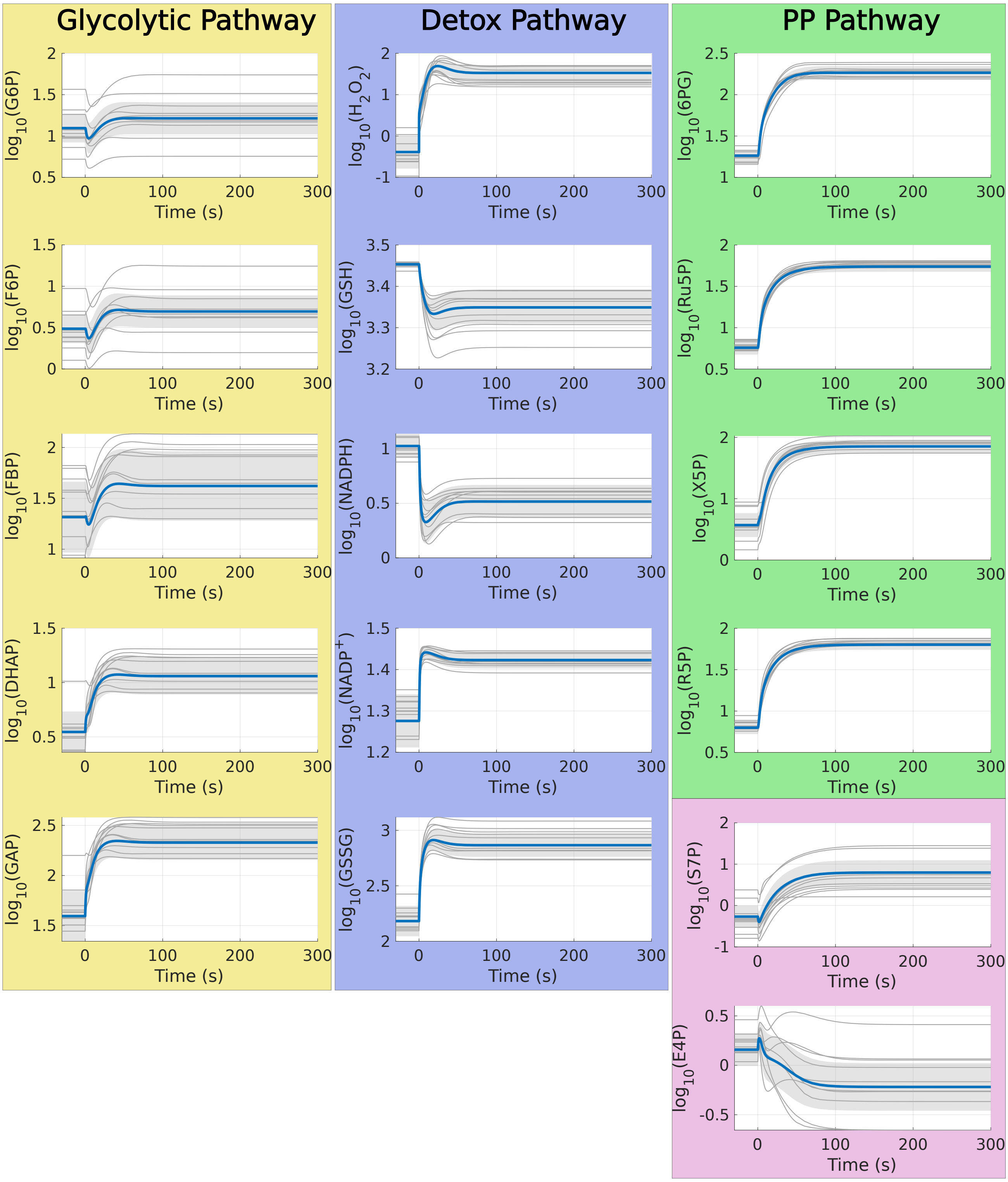

Figure S4: Dynamic response of metabolite concentrations in glycolytic, gluthathione and pentose phosphate pathways, related to Figure 4. The concentration axis uses a log-10 scale and units are μM. Blue line is the mean trajectory and gray lines are trajectories associated to a random subsample of $\mathcal{P}^{opt}$.

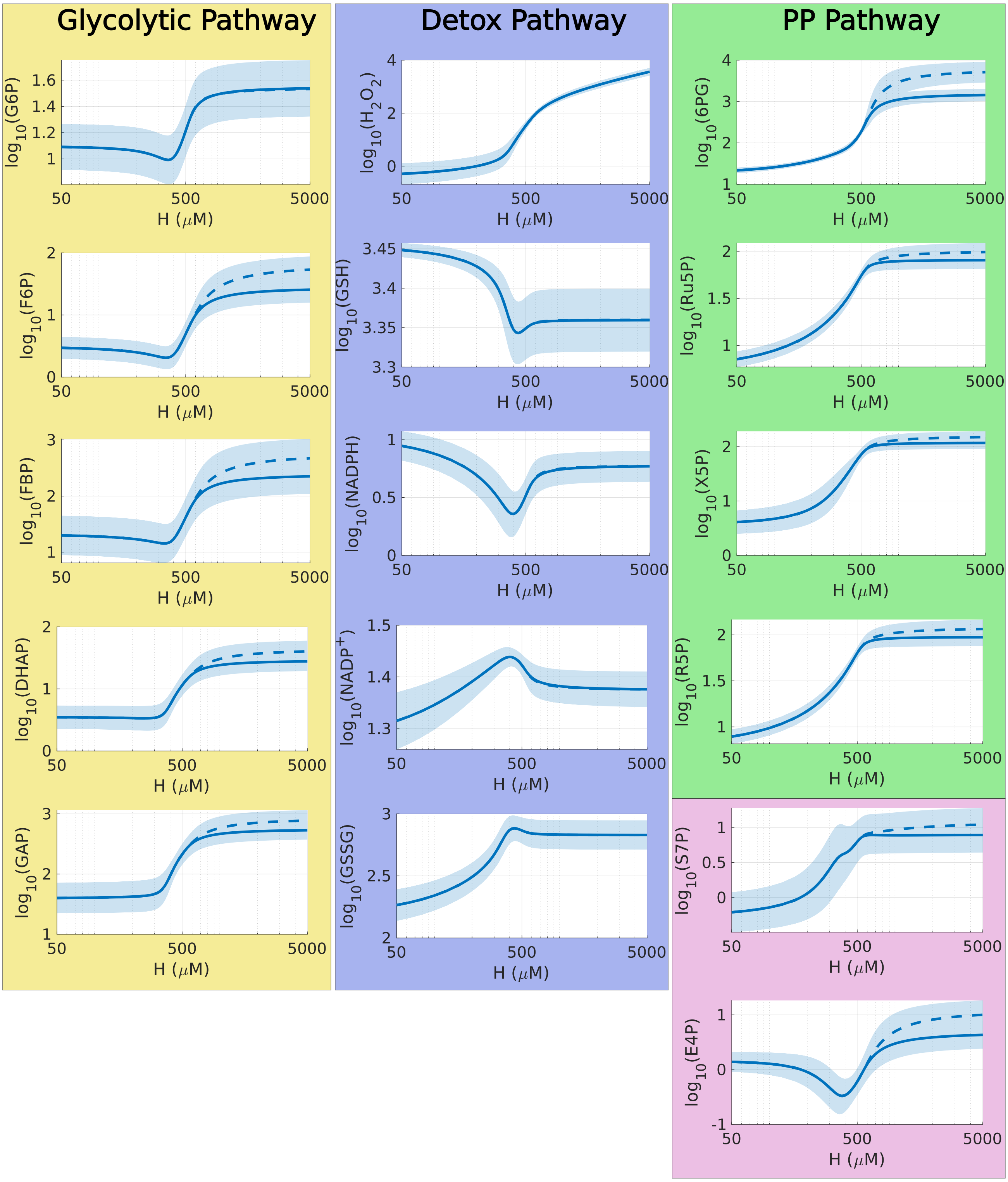

Figure S5: Dose-dependent response of metabolite concentrations in glycolytic, gluthathione and pentose phosphate pathways, related to Figure 5. The concentration axis uses a log-10 scale and units are μM. Blue line is the mean dose response curve $t = 5$min (full line) and $t = 30$min (dashed line).

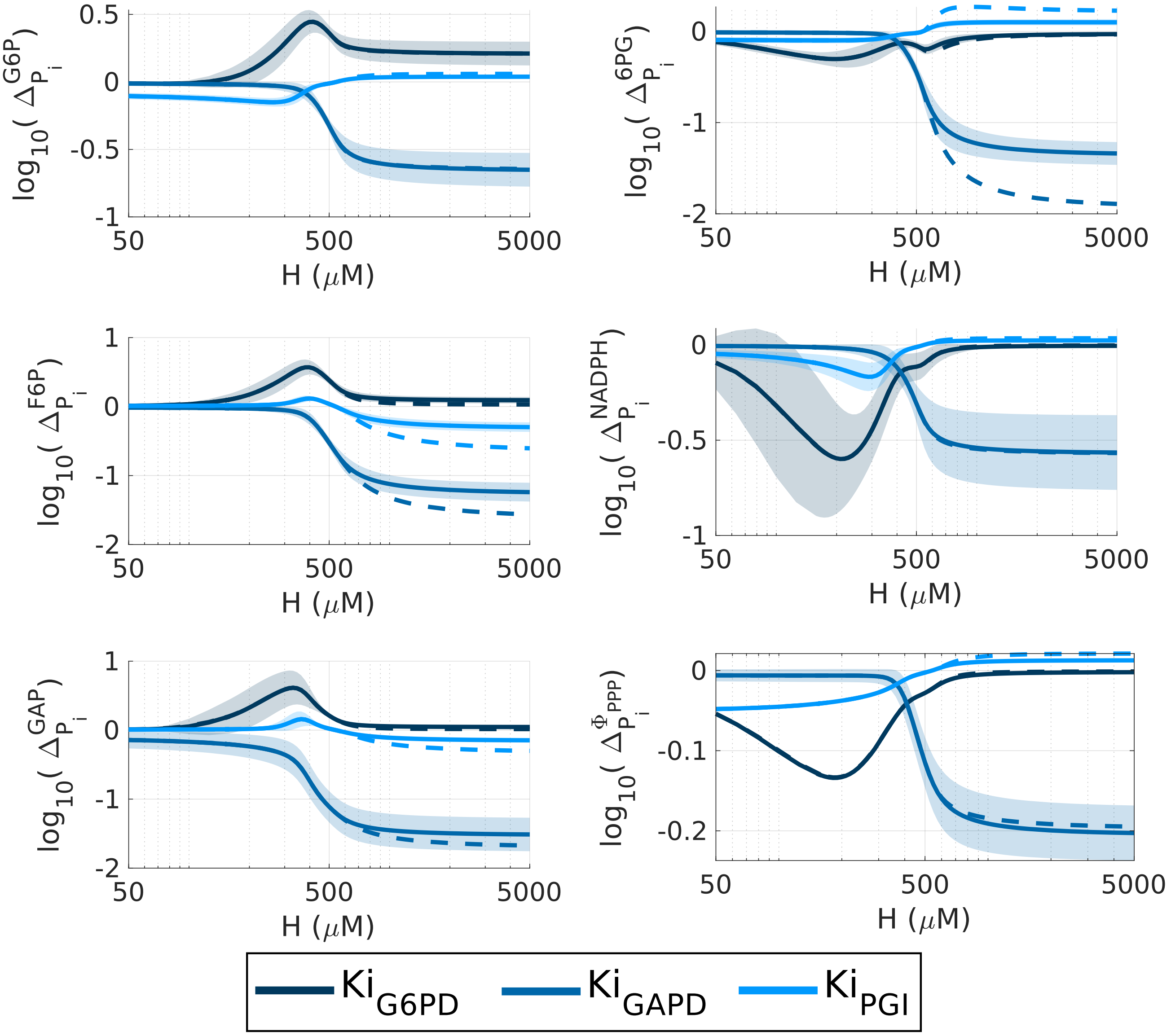

Figure S6: Metabolic responses associated to deleted regulations, related to figure 6. The sensitivity quantity is computed for deleted regulation where inhibitory constant $p_i \to \infty$ and is represented with a log-10 scale. $\log_{10}(\Delta) = 0$ indicates an absence of effect. An opposite response of glycolytic metabolites G6P, F6P and GAP (positive versus negative) is observed between the deletion of PPP enzyme inhibition (Ki_{G6PD}) versus deletion of glycolytic enzyme inhibition (Ki_{PGI}, Ki_{GAPD}). This property suggests a cooperation between the upregulation of PPP enzyme and the increase of G6P mediated by the inhibition of glycolytic enzyme inhibition for improving flux rerouting efficiency toward oxPPP.

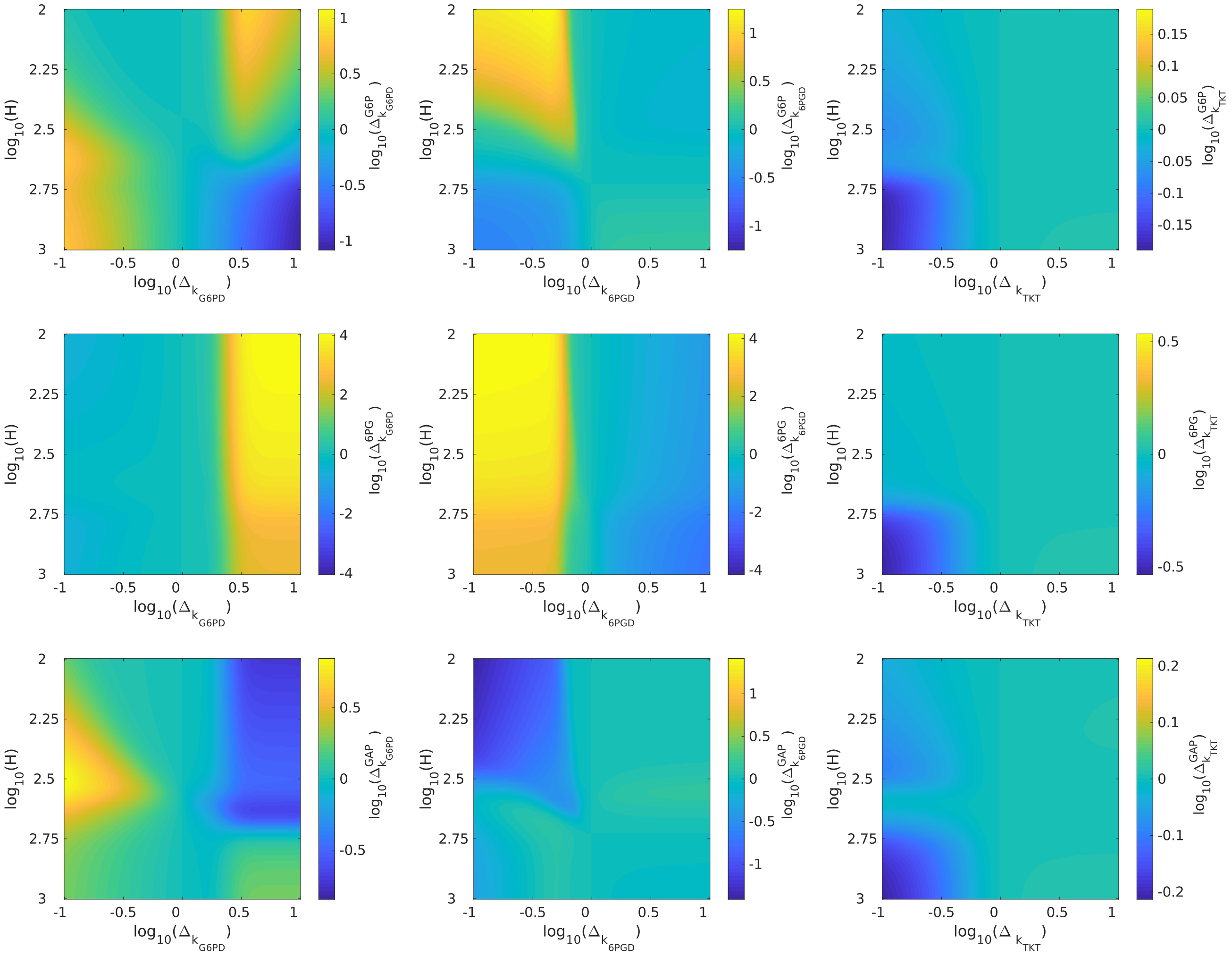

Figure S7: Metabolic responses depending enzymatic perturbation and oxidative stress level, related to Figure 7. This figure focuses on the effect of modulating the activity of key enzymes (k_i) on the concentration response to oxidative stress, which relates to experiments shown in Figure 3 of (Kuehne *et al.*, 2015) that shows the influence of G6PD/TKT/TAL-knockdown. Comparison should however be taken carefully as transfection with siRNA is made before treatment and such perturbation can lead to metabolic adaptations of the basal unstressed state itself. Downregulation of k_{G6PD} shows increased G6P and GAP and decreased 6PG (consistently with experimental data.) Downregulation of k_{TKT} shows decreased G6P, GAP and G6P (consistently experimental data except for 6PG). Downregulation of k_{6PGD} (that is not tested in experiments) shows an opposite qualitative response to that of k_{G6PD}, confirming the counterintuitive phenotype of perturbing $6PGD$.

Reaction	Law	Rate equation
ϕ_{OX}	T	$k_{OX} + k_{diff}([H_2O_2]_{ext} - [H_2O_2])$
ϕ_{CAT}	MA(1,0)	$k_{CAT}[H_2O_2]$
ϕ_{GPx}	MM(2,0)	$k_{GPx}[H_2O_2][GSH]/(\frac{[GSH]}{KmG_{GPx}} + \frac{[H_2O_2]}{KmH_{GPx}})$
ϕ_{GR}	MM(2,0)	$k_{GR}[NADPH][GSSG]/(1 + \frac{[GSSG]}{KmG_{GR}} + \frac{[NADPH]}{KmN_{GR}})$
ϕ_{NNH}	MA(1,0)	$k_{NAD}[NADP^+]$
ϕ_{NHN}	MA(1,0)+CI	$k_{NADPH}[NADPH]/(1 + \frac{[H_2O_2]}{Ki_{NNH}})$
ϕ_{G6PD}	MA(2,0)+CI	$k_{G6PD}[G6P][NADP^+]/(1 + \frac{[NADPH]}{Ki_{G6PD}})$
ϕ_{6PGL}	MA(1,0)	$k_{GLase}[6PGL]$
ϕ_{6PGD}	MM(2,0)+CI	$k_{6PGD}[6PG][NADP^+]/(1 + \frac{[NADPH]}{Ki_{6PGD}} + \frac{[6PG]}{Km_{6PGD}})$
ϕ_{RPI}	MA(1,1)	$k_{RPE}([Ru5P] - \frac{[X5P]}{Keq_{RPE}})$
ϕ_{RPE}	MA(1,1)	$k_{RPI}([Ru5P] - \frac{[R5P]}{Keq_{RPI}})$
ϕ_{PRPP}	MM(1,0)	$k_{PRPP}[R5P]/(1 + \frac{[R5P]}{Km_{PRPP}})$
ϕ_{TKT1}	MM(2,2)	$k_{TKT1}([R5P][X5P] - \frac{[GAP][S7P]}{Keq_{TKT1}})/(1 + \frac{([R5P][X5P]}{Km_{TKT1}} + \frac{[GAP][S7P])}{Km_{TKT1}})$
ϕ_{TLD}	MM(2,2)	$k_{TLD}([GAP][S7P] - \frac{[F6P][E4P]}{Keq_{TLD}})/(1 + \frac{([GAP][S7P]}{Km_{TLD}} + \frac{[F6P][E4P])}{Km_{TLD}})$
ϕ_{TKT2}	MM(2,2)	$k_{TKT2}([E4P][X5P] - \frac{[F6P][GAP]}{Keq_{TKT2}})/(1 + \frac{([E4P][X5P]}{Km_{TKT2}} + \frac{[F6P][GAP]}{Km_{TKT2}})$
ϕ_{HK}	MA(1,0)+CI	$k_{HK}[GLC]/(1 + \frac{[G6P]}{Ki_{HK}})$
ϕ_{PGI}	MA(1,1)+CI	$k_{PGI}([G6P] - \frac{[F6P]}{Keq_{PGI}})/(1 + \frac{[6PG]}{Ki_{PGI}})$
ϕ_{PFK}	MA(1,0)	$k_{PFK}[F6P] - k_{FBPase}[FBP]$
ϕ_{ALD}	MA(1,2)	$k_{ALD}([FBP] - \frac{[DHAP][GAP]}{Keq_{ALD}})$
ϕ_{TPI}	MA(1,1)	$k_{TPI}([DHAP] - \frac{[GAP]}{Keq_{TPI}})$
ϕ_{GAPD}	MA(1,0)+CI	$k_{GAPD}[GAP]/(1 + \frac{[H_2O_2][GT]}{Ki_{GAPD}}[GSH])$

Table S1: Reaction table, related to STAR Methods. CI, MM(.,.) and MA(.,.) are the reaction kinetic laws defined in STAR methods Eqs 4-6. T indicates diffusive transport.

Parameter	Value	Range	References
k_{GPx}	1s^{-1}	$[10^{-1}; 10^{1}]$	(Benfeitas *et al.*, 2014)
KmH_{GPx}	0.04μM	$[10^{-1}; 10^{1}]$	(Benfeitas *et al.*, 2014)
KmG_{GPx}	9.72μM	$[10^{-1}; 10^{1}]$	(Benfeitas *et al.*, 2014)
k_{GR}	49s^{-1}	$[10^{-1}; 10^{1}]$	(Benfeitas *et al.*, 2014)
KmN_{GR}	8.5μM	$[10^{-1}; 10^{1}]$	(Benfeitas *et al.*, 2014)
KmG_{GR}	65μM	$[10^{-1}; 10^{1}]$	(Benfeitas *et al.*, 2014)
Ki_{G6PD}	10μM	$[10^{-1}; 10^{1}]$	(Yoshida and Lin, 1973; Kuehne *et al.*, 2015)
Ki_{6PGD}	10μM	$[10^{-1}; 10^{1}]$	(Yoshida and Lin, 1973; Holten *et al.*, 1976)
Ki_{PGI}	100μM	$[10^{-2}; 10^{1}]$	(Kuehne *et al.*, 2015)
Ki_{GAPD}	100μM	$[10^{-2}; 10^{1}]$	(Peralta *et al.*, 2015)
Ki_{NNH}	100μM	$[10^{-1}; 10^{1}]$	
Km_{6PGD}	50μM		(Ceyhan *et al.*, 2005; Liu *et al.*, 2019)
Km_{PRPP}	65μM		(Hove-Jensen *et al.*, 2017)
Keq_{RPE}	1.68		(Li *et al.*, 2011)
Keq_{RPI}	1.23		(Li *et al.*, 2011)
Keq_{TKT1}	1.62		(Li *et al.*, 2011)
Keq_{TLD}	0.36		(Li *et al.*, 2011)
Keq_{TKT2}	30		(Li *et al.*, 2011)
Keq_{PGI}	0.34		(Li *et al.*, 2011)
Keq_{ALD}	66μM		(Li *et al.*, 2011)
Keq_{TPI}	19.2		(Li *et al.*, 2011)
k_{diff}	1s^{-1}	$[10^{-1}; 10^{1}]$	(Benfeitas *et al.*, 2014)
Φ_{glu}	40μM.s^{-1}		
$[NT]$	30μM		(Benfeitas *et al.*, 2014)
$[GT]$	3mM		(Benfeitas *et al.*, 2014)
k_i	1s^{-1}	$[10^{-4}; 10^{1}]$	

Table S2: Parameter space and values, related to STAR Methods. Range defines the range of variation around the indicated value. Blank range indicates fixed value. Some values (e.g., Km or Ki, not Keq) are approximated to rounded or averaged values from experimental measurements. References can be found in the main manuscript.

Stochastic simulation algorithm for isotope-based dynamic flux analysis

Quentin Thommen,[1] Julien Hurbain,[2] and Benjamin Pfeuty[2]
[1]Univ. Lille, CNRS, Inserm, CHU Lille, Institut Pasteur de Lille, UMR9020-U1277 - CANTHER - Cancer Heterogeneity Plasticity and Resistance to Therapies, F-59000
[2]Univ. Lille, CNRS, UMR 8523 - PhLAM - Physique des Lasers Atomes et Molécules, F-59000 Lille, France

(*Electronic mail: quentin.thommen@univ-lille.fr)

(Dated: 11 February 2022)

Carbon isotope labeling method is a standard metabolic engineering tool for flux quantification in living cells. To cope with the high dimensionality of isotope labeling systems, diverse algorithms have been developed to reduce the number of variables or operations in metabolic flux analysis (MFA), but lacks generalizability to non-stationary metabolic conditions. In this study, we present a stochastic simulation algorithm (SSA) derived from the chemical master equation of the isotope labeling system. This algorithm allows to compute the time evolution of isotopomer concentrations in non-stationary conditions, with the valuable property that computational time does not scale with the number of isotopomers. The efficiency and limitations of the algorithm is benchmarked for the forward and inverse problems of 13C-DMFA in the pentose phosphate pathways. Overall, SSA constitute an alternative class to deterministic approaches for metabolic flux analysis that is well adapted to comprehensive dataset including parallel labeling experiments, and whose limitations associated to the sampling size can be overcome by using Monte Carlo sampling approaches.

Keywords: Metabolic flux analysis, Flux balance analysis, Metabolism, Metabolic network model, Stable-isotope tracers, Systems biology

1. INTRODUCTION

Isotope tracing experiments have been developed to quantify fluxes in biochemical networks (Stephanopoulos, 1999). A typical carbon-13 labeling experiment metabolizes a labeled substrate, such as [1- 13C]glucose, tracks the propagation of the label on metabolites by nuclear magnetic resonance (NMR) or mass spectrometry (MS) methods and estimates metabolic fluxes by various methods including 13C-MFA (Niedenführ, Wiechert, and Nöh, 2015; Allen and Young, 2020; Antoniewicz, 2021). Despite its limitations, 13C-MFA remains the gold standard method in metabolic engineering for accurate and precise quantification of fluxes in living cells (Crown and Antoniewicz, 2013). Currently, the most efficient algorithms are all based on an advanced decomposition method using elementary metabolic units (EMUs) developed in 2007 by Antoniewicz et al (Antoniewicz, Kelleher, and Stephanopoulos, 2007). Nevertheless, one of the limitations of the classical metabolic flux analysis (MFA) method is the requirement of a metabolic isotopic steady state. Flux analysis methods that focus on estimating non-stationary metabolic fluxes are referred to as dynamic MFA (DMFA) (Leighty and Antoniewicz, 2011), or 13C dynamic MFA methods (13C-DMFA) methods (Antoniewicz, 2015a). Despite pioneering works (Antoniewicz *et al.*, 2007; Wahl, Nöh, and Wiechert, 2008) initiated more than one decade ago, little progress has been made since (Antoniewicz, 2021). Current computational methods use a deterministic modeling framework by solving EMU balance rate equations where dynamic flux parameters are modeled with B-splines (Quek *et al.*, 2020; Ohno *et al.*, 2020). Computational tractability of such method depends on the EMU system size that can be very large due to the interplay of elaborated labeling protocols (Lewis *et al.*, 2014; Antoniewicz, 2015b; Jacobson *et al.*, 2019; Dong *et al.*, 2019; Allen and Young, 2020) and complex bibi reactions (Selivanov *et al.*, 2004).

In this paper, we present a different class of method that simulates isotope propagation in non-stationary metabolic systems by a Stochastic Simulation Algorithm (SSA). We test the method in the metabolic subsystem comprising glycolytic and PPP pathways where complex carbon rearrangements occur due to bibi reactions in the nonoxidative PPP and where 13C labeling have been extensively applied to infer metabolic flux (Kuehne *et al.*, 2015; Bouzier-Sore and Bolaños, 2015; Creek *et al.*, 2015; Diaz-Moralli *et al.*, 2016; Lee *et al.*, 2019). The main idea is to represent the population of isotopomers of a chemical species by a sample of finite size, proportional to the species concentration, and to use the standard rules of stochastic chemical kinetics to propagate the marker. When a reaction occurs, the isotopomers associated to the reactants are randomly selected in the corresponding samples, the rearrangement is performed, and the products are added to the corresponding samples. The algorithm somehow mimics the discrete and stochastic processes of enzymatic reactions as it occurs in cells, but remains restricted to a small sample of metabolite species for the sake of computational efficiency. At each time step, the samples represent the population of the isotopomers of each variable from which one can compute mass isotopomer distribution for comparing with experimental data. The proposed algorithm is simple to implement, fast, visual, and above all its computation time depends very little on the chain length, which makes it an algorithm also adapted

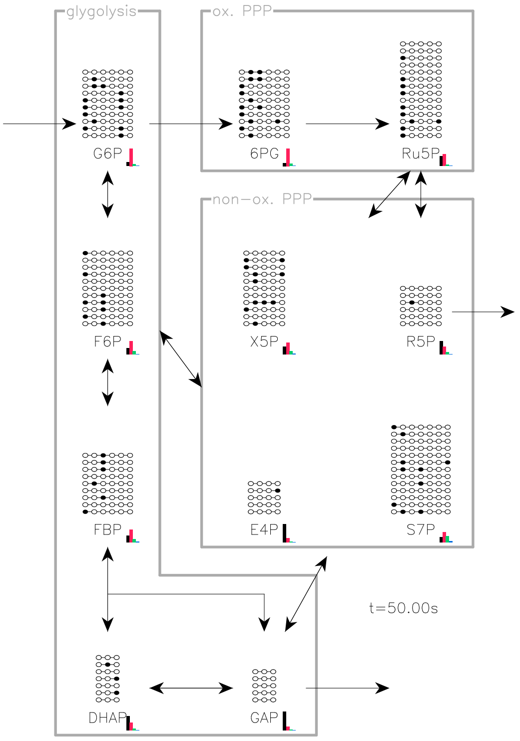

FIG. 1. Atom rearrangements in metabolic reactions. The upper glycolytic pathway supplemented by the pentose phosphate pathway provides an example of isotope labeling network. For each chemical species (G6P, F6P, FBP, DHAP, GAP 6PG, Ru5P, X5P, R5P, E4P, S7P) subsamples of the isotopomer samples are displayed as a chain of unlabeled (open circle) and labeled carbons (close circle). The number of displayed carbons chains is proportional to the species concentration. Mass isopotomer histogram is also displayed (m+0 in black, m+1 in red, m+2 in green, and m+3 in blue). The Figure illustrates the configuration 50 s after the labeling introduction that also corresponds to the perturbation of the metabolic system. The associated video provides a full dynamical picture.

to parallel labeling (13C, 2H, 15N, 18O, etc).

2. RESULTS

2.1. Stochastic Simulation Algorithm (SSA)

The propagation of labeled atoms through a biochemical network is here described by a sampling approach. The representation of the isotopomer distribution of each chemical species in the network is computed using a finite sample size proportional to its concentration. A user defined parameter Ω corresponds to a reference concentration. For example, a value of $\Omega = 1000$ c/μM indicates that a concentration of 1 μM is represented by 1000 copies of the chemical species, each copy corresponding to a different isotopomer.

The fluxes of chemical reactions are determined by mathematical functions that can be either linked to the species concentrations in the framework of chemical kinetics, or described by phenomenological functions depending on time, or by constant functions in the case of stationary flux condition. The flux value determines the time interval between two occurrences of the corresponding chemical reactions. When one occurs, the reactants are taken randomly from the corresponding samples, the rearrangement of the atoms is done according to the reaction's rule, and the products are added to the corresponding samples. In this way, the labeling propagates through the chemical reaction network; at a given date, the sample of each species is populated with different isotopomers and represents the isotopomer distribution.

Such rules are formalized within the framework of the chemical master equation once two new tools are defined, the isotopomer index and addressing operators (sec. 3.1). Chemical master equation describes the temporal evolution of the isotopomer fraction. From the chemical master equation, one can derive both a deterministic simulation algorithm (DSA) (see Sec. 3.2) and a stochastic simulation algorithm (SSA) (see Sec. 3.3). The DSA is not an efficient algorithm since it has as many variables as possible isotopomer, it is a "brute force" algorithm serving here as a control for the SSA outputs.

An example of stochastic simulation is given in Figure 1 and for the upper glycolytic pathway combined with the pentose phosphate pathway. To determine the fluxes, the mass action law is here used with unitary kinetic parameters (Table 1). At the initial time, the metabolic system is fed with labeled glucose (50% of [1-13 C]glucose and 50% of [2-13 C]glucose in (Kuehne *et al.*, 2015)), and at the same time, is perturbed by a two-fold increase of the glucose intake rate. If $\Omega = 100$ c/μM is used for SSA, the Figure 1 (and the corresponding video) only represents one element out of 20 from each sample, for the sake of visualization.

The Figure 2 represents the evolution of the concentration and mass isotopomer obtained with the SSA (point) and the DSA (continuous line), thus depicting the accurate trends of isotopomer trajectories generated with SSA. The stochastic fluctuations of the mass isotopomers induced by the SSA are only due to the random selection of the reagents in the sample. The variance of these fluctuations is thus equal to the Ω profile and the mass isotopomer concentration. The determination is thus all the more precise as the mass isotopomers are abundant. It is thus possible to reduce these fluctuations in two different ways, either by increasing the value of Ω, or by proceeding to a temporal smoothing of the stochastic evolution.

2.2. SSA Computational Performance

SSA computation time depends on both the number of chemical reactions and the execution time of each reaction. As an example, the computation cost necessary to simulate data of the Figure 1 corresponds to 224 463 reactions carried out in 62 ms for the SSA, and 2892 right-hand-side evaluation in 2100 ms for the DSA (advanced Runge-Kutta-Fehlberg method is used) using a Intel(R) Core(TM) i5-6300U CPU at 2.40GHz without parallelization. In the SSA, the number of chemical reaction occurrences can be approximated by the

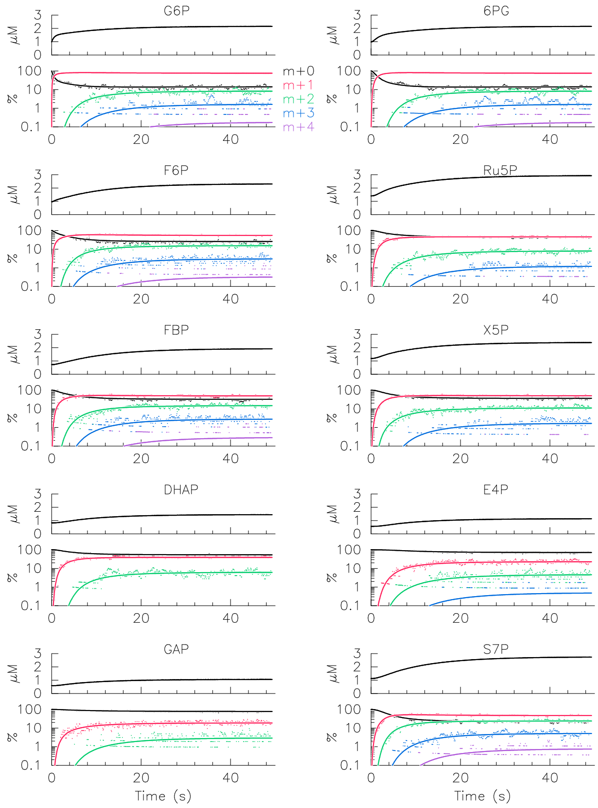

FIG. 2. Concentration and mass isotopomer dynamics in nonstationary conditions. Stochastic trajectories computed with SSA (dots) are compared with deterministic trajectories computed with DSA for control (solid lines), and corresponds to calculation presented in Figure 1 (same network, same condition). For each chemical species, the upper plot displays the concentration in μM whereas the bottom plot displays the mass isotopomers in percent (m+0 in black, m+1 in red, m+2 in green, and m+3 in blue, m+4 violet).

product $T\,v\,\Omega\,N$ where N is the number of chemical reactions in the network, v the typical flux values and T the time interval. The number of reactions does not depend on the number of isotopomer per species or, equivalently, on the chain length representing the chemical species. The time to perform a reaction depends only slightly on the chain length l thus almost not depend on the number of isotopomer. In our implementation, the computation time for one reaction varies as $1+l/15$; so when l goes from 6 to 18 (e.g., C6 to C6H12), the computation time increase by less than 60% whereas the number of isotopomer is multiplied by $2^{12} = 4096$. This is why the SSA algorithm is well adapted to cross-labeling, *e.g.* hydrogen carbon, leading to longer chain lengths and thus to a higher combinatoriality.

2.3. SSA-13C DMFA

To further test the SSA, we implemented it in a 13C-DMFA procedure. A general scheme of the procedure is shown in Figure 3. A series of measurements concerning metabolite concentrations and mass isotopomer distributions (MID) with known associated experimental errors is the target of an optimization procedure. The aim is to fit these data with a kinetic model based on mass action laws used for Figure 1 (Table 1). The flux dynamics therefore depend on the kinetic parameters of the reaction laws. Instead of a kinetic model, we could also use the stochiometric model supplemented with parameterized time functions to describe the flux. The parameter space of the model is then explored to identify the sets of parameters consistent with the target experimental data, taking into account the existing uncertainties (see (Valderrama-Bahamóndez and Fröhlich, 2019) for a review of standard method). Once the exploration is completed, the dynamics of metabolic fluxes are computed for each selected parameter set, which can be represented as a confidence region for flux trajectories.

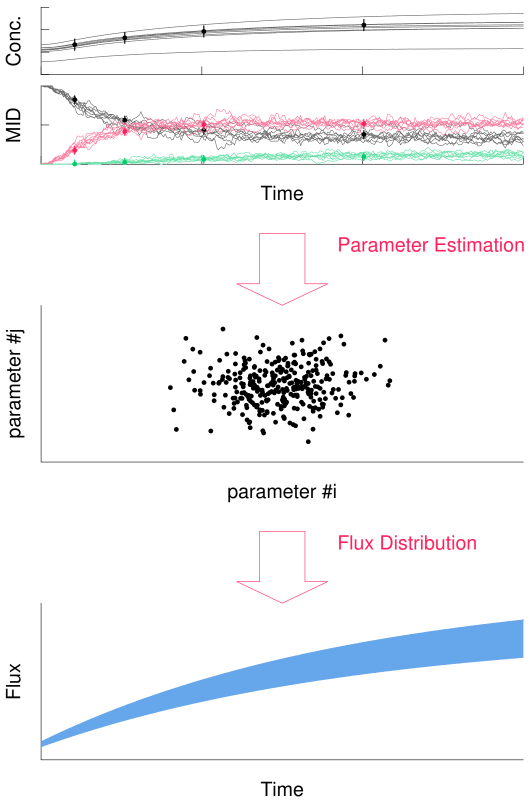

FIG. 3. 13C-DMFA generic workflow using SSA. Metabolite concentration as well as mass isotopomer distribution (MID) are the targets of parameter estimation procedure. Parameter sensitivity analysis provides a list of points in the parameter space that accurately describes targets. The range of flux dynamics is then computed from the parameter value distribution.

Here, target datasets were generated for concentrations and mass isotopomers from the DSA at $2, 5, 10, 20, 30, 40$s in the same condition as in Figure 2. Then the SSA, with $\Omega = 200$ here, is used to compute the fitness score from target dataset and kinetic parameter set. Two classes of experimental measurements are considered. In a first strategy, only the mass

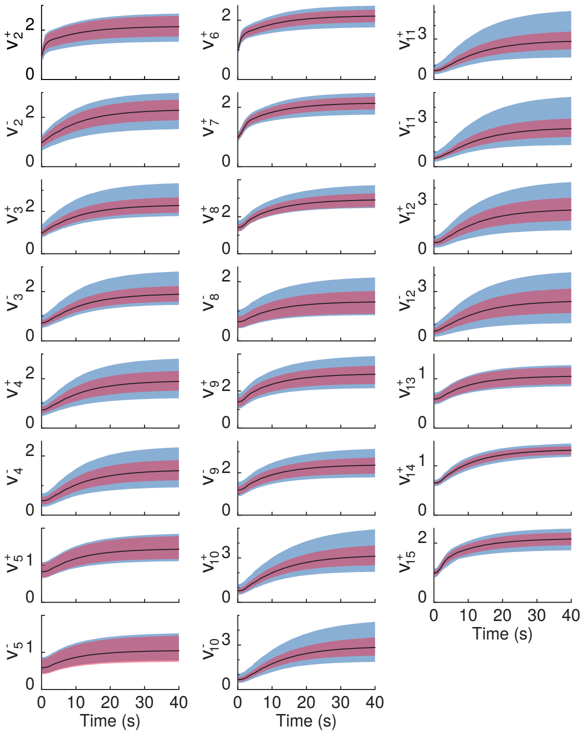

FIG. 4. Directional flux areas compatible with mass isotopomer targeting. The areas are filled with a color code. Blue areas correspond fit strategy 1; red, to fit strategy 2. Solid black lines correspond to the exact solution.

isotopomers $m+0\ldots m+3$ are targeted with an error of 5% (no data provided for the concentrations). In a second strategy, concentration data are also included and targeted with an error of 0.25 μM. These errors mimic typical experimental and measurement uncertainties. A parameter set is here kept and said to be consistent with target dataset for a chi-square per degree of freedom (i.e., fitness score) remains below unity. Here, a parameter sensitivity analysis computes the parameter ranges, one by one, to illustrate the procedure; the input flux is assumed to be known. For each strategy, the selected parameter sets are finally used to compute the dispersion of the reaction fluxes. As expected, the areas of flux trajectories comprise the exact solution and are reduced when adding concentration data (Figure 4).

3. THEORY

3.1. Chemical master equation model for isotopic labeling networks

In a network of (bio)chemical reactions, the temporal evolution of the state probabilities is described by the chemical master equation (CME) through a general formalism (Gillespie, 1992). Deterministic kinetic rate equations, on the one hand, can be derived from the first moments of the probability distribution and allow for a thorough analysis of the network dynamics by various analytical techniques (Thompson and Stewart, 2002). The probabilistic features of the dynamics such as bimodal distributions or coefficients of variation, on the other hand, can be investigated with stochastic implementation of the CME through well-established stochastic simulation algorithms (Gillespie, 1977, 2001).

3.1.1. Isotopomer index and addressing operators

A chemical reaction network such as the one depicted in Figure 1 is defined by K reactions between M chemical species whose concentrations are denoted by S_m with $m \in [1,M]$. The labeling states of the species S_m is an ordered sequence $(s_{m,1}, s_{m,2}, \ldots, s_{m,l_m})$ of length denoted l_m made of elements $s_{m,i} \in [0, q-1]$. The species S_m has therefore $L_m = q^{l_m}$ different labeling states or positional isotopomer indexed by $n_m = \sum_{i=1}^{l_m} s_{m,i}\, q^{i-1}$, also noted $n_m = (s_{m,1}, s_{m,2}, \ldots, s_{m,l_m})_q$ and called the isotopomer index. A similar approach restricted to $q = 2$ has already been introduced to describe isotopomer distribution vectors (Schmidt *et al.*, 1997). In the case 13C-labeling, each carbon may be in two different states (*i.e.*, $q = 2$) and the sequence $(0,0,1,0,0,0,0)$ for S7P indicates that 13C label is in third carbon position and corresponds to the labeling state number 4, the S7P species has therefore 2^7 different labeling states.

If the permutation rule is known, one can define addressing operators that compute the isotopomer index of the products from the isotopomer index of the reactants, and *vice versa* for each reaction of the network. The addressing operator forms an alternative to atom mapping matrices defined by Zupke *et al.* (Zupke and Stephanopoulos, 1994). In the case of the reaction mediated by transaldolase (reaction number 11 in Table 1), the addressing operators

$$\sigma_{\mathrm{F6P}}(n_{\mathrm{S7P}}, n_{\mathrm{GAP}}) = (s_{a,1}, s_{a,2}, s_{a,3}, s_{b,1}, s_{b,2}, s_{b,3})_q \qquad (1)$$
$$\sigma_{\mathrm{E4P}}(n_{\mathrm{S7P}}, n_{\mathrm{GAP}}) = (s_{a,4}, s_{a,5}, s_{a,6}, s_{a,7})_q, \qquad (2)$$

compute the product index from reactant index $n_{\mathrm{S7P}} = (s_{a,1}, \ldots, s_{a,7})_q$ and $n_{\mathrm{GAP}} = (s_{b,1}, s_{b,2}, s_{b,3})_q$. In the same manner,

$$\sigma_{\mathrm{S7P}}(n_{\mathrm{F6P}}, n_{\mathrm{E4P}}) = (s_{c,1}, s_{c,2}, s_{c,3}, s_{d,1}, s_{d,2}, s_{d,3}, s_{d,4})_q \qquad (3)$$
$$\sigma_{\mathrm{GAP}}(n_{\mathrm{F6P}}, n_{\mathrm{E4P}}) = (s_{c,4}, s_{c,5}, s_{c,6})_q \qquad (4)$$

compute the reactant index from product index $n_{\mathrm{F6P}} = (s_{c,1}, \ldots, s_{c,6})_q$ and $n_{\mathrm{E4P}} = (s_{d,1}, \ldots, s_{d,4})_q$. Therefore, in the context of a 13C labeling ($q = 2$), the reaction between a doubly labeled S7P (1000100) and a simply labeled GAP (001) – *i.e.* $n_{\mathrm{S7P}} = 17$ and $n_{\mathrm{GAP}} = 4$ – produces an F6P (100001) and an E4P (0100) – *i.e.* $n_{\mathrm{F6P}} = 33$ and $n_{\mathrm{E4P}} = 2$.

3.1.2. Chemical master equation description

The chemical master equation (CME) is a general and accurate formalism to describe the stochastic dynamics in (bio)chemical reaction networks (Gillespie, 2000). This formalism can be easily extended to also describe the stochastic dynamics of labeling states of chemical species. With above notations for isotopomer index and addressing operators, the probabilistic dynamics in isotope labeling network can naturally be described in the CME framework. The chemical species with the largest number of isotopomers determines the size N of the state space ($N = 2^7$ in the example used in Figure 1). The state of the whole system is therefore described by a $M \times N$ integer matrix ω: $\omega_{m,n}$ indicating the number of mth species in the nth labeling state. The total number of the mth species is noted $\Omega S_m = \sum_n \omega_{m,n}$ where Ω is a volume (involved as a scaling factor) and S_m is a concentration. The probability that the internal sequence of the mth species corresponds to the nth isotopomer is denoted $\rho_{m,n} = \omega_{m,n} / \Omega S_m$. The formalism of the CME describes the temporal evolution of the probability of the system to be in the state ω, noted $\mathscr{P}_\omega(t)$.

The chemical reactions that define the network are characterized by both a concentration-dependent flux of reagents v_k with $k \in [0,K]$ and a permutation rule between the position of labeled atoms of reactants and products. Reactions are distinguished depending on their input, output, or internal position in the network. For instance, the network depicted in Figure 1 has one input reaction, 3 output reactions and 11 internal reactions. As seen latter on, input reactions always require a particular consideration since the reactant is not modified. For keeping notations simple, we restrict to Bi Bi reactions of the type $A+B \to C+D$ where A,B,C,D are either chemical species or empty sets. In this case, the CME reads,

$$\begin{aligned}\frac{d}{dt}\mathscr{P}_\omega(t) = &\sum_{k=1}^{K_n} \Omega\, v_k\,(S) \sum_{n,n'} \left[\mathbb{E}^+_{a_k,n}\,\mathbb{E}^+_{b_k,n'}\,\mathbb{E}^-_{c_k,\sigma_{c_k}(n,n')}\,\mathbb{E}^-_{d_k,\sigma_{d_k}(n,n')} - 1\right] \rho_{a_k,n}\,\rho_{b_k,n'}\,\mathscr{P}_\omega(t) \\ &+ \sum_{k=K_n+1}^{K_n+K_i} \Omega\, v_k\,(S) \sum_n I_{c_k,n}(t)\ \left[\mathbb{E}^-_{c_k,n} - 1\right]\ \mathscr{P}_\omega(t)\end{aligned} \tag{5}$$

The integers a_k,b_k,c_k,d_k correspond to the indices of the species A,B,C,D of the kth reaction of type $A+B \to C+D$, the integer being null in the case of an empty set. The writing uses scale operators $\mathbb{E}^\pm_{m,n}$ (Van Kampen, 1992) :

$$\mathbb{E}^\pm_{m,n}\,\rho_{m_1,n_1}\,\rho_{m_2,n_2}\,\mathscr{P}_\omega(t) = \left[\rho_{m_1,n_1} \pm \frac{\delta_{m,m_1}\delta_{n,n_1}}{\Omega S_{m_1}}\right]\left[\rho_{m_2,n_2} \pm \frac{\delta_{m,m_2}\delta_{n,n_2}}{\Omega S_{m_2}}\right]\mathscr{P}_{\omega \pm \mathbf{E}_{m,n}}(t) \tag{6}$$

where $\mathbf{E}_{m,n}$ is a matrix of the canonical base (only the element at the intersection of row m and column n is non-zero and is unity), and $\delta_{i,j}$ the Kronecker symbol (unity if indexes are equal, zero either). The K_n first reactions concern internal and output reactions whereas the remaining K_I concerns input reactions ($\emptyset \to C$). In this later case, $I_{c_k,n}$ is the fixed probability to have an isotopomer n of the input species c_k.

3.2. Derived Deterministic Simulation Algorithm (DSA)

The CME (Eq. 5) can be approximated in the large size limit $\Omega \to \infty$ by deterministic rate equation dynamics. The probability of each internal sequence is denoted by $\rho_{m,n}$ such that $S_{m,n} = S_m\,\rho_{m,n}$ describes the concentration of nth-isotopomer of the mth species. The time evolution of isotopomer concentrations is governed by the distribution rules specific to each reaction and is formalized mathematically by a permutation of the concatenated internal sequence between the reagents and the products. The deterministic system evolves according to the ordinary differential equations,

$$\frac{d}{dt}S_{m,n} = \sum_{k=1}^{K} N_{m,k}\ v_k(S)\ \Phi^k_{m,n}(\rho)\,, \tag{7}$$

where N denotes the stoichiometry matrix, v_k $k \in [0,K]$ the concentration-dependent flux of reagents, and $\Phi^k_{m,n}(\rho)$ the flux fraction describing the permutation rules of chemical reaction satisfying $\sum_n \Phi^k_{m,n}(\rho) = 1$. Algorithm to simulate Eq. 7 with standard Runge-Kutta-Fehlberg method of order 5 with adaptive step is called Deterministic Simulation Algorithm (DSA).

Let us first consider the internal reactions restricted to Bi Bi reactions of the form $A+B \to C+D$. The reaction is characterized by the reordering of atom position defining addressing operations of the products according to the indices of the reagents. The operator $\sigma_A(n_c,n_d)$ gives the isotopomer index of the A species that produce C and D of isotopomer index n_c and n_d, respectively. In that case, the reaction index k is omitted and the flux fraction reads,

$$\Phi_{a,n_a}(\rho) = \rho_{a,n_a} \tag{8}$$

$$\Phi_{b,n_b}(\rho) = \rho_{b,n_b} \tag{9}$$

$$\Phi_{c,n_c}(\rho) = \sum_{n_d=0}^{L_d-1} \rho_{a,\sigma_A(n_c,n_d)}\, \rho_{b,\sigma_B(n_c,n_d)} \tag{10}$$

$$\Phi_{d,n_d}(\rho) = \sum_{n_c=0}^{L_c-1} \rho_{a,\sigma_A(n_c,n_d)}\, \rho_{b,\sigma_B(n_c,n_d)} \tag{11}$$

where L_c and L_d are the number of isotopomers of C and D species. If B is an empty set then $\rho_{b,x} = 1$, and if D is an empty set Eq. (11) is useless. If the reaction is an output reaction, then C and D are empty sets, $\Phi_{a,n_a}(\rho)$ and $\Phi_{b,n_b}(\rho)$ are computed with the same rules as internal reactions. As mentioned, the input reactions must be treated separately since the reactants are not variables but parameters. We consider here input reactions of simple form $\emptyset \to C$ and we note I_n the probability of synthesis of the species C in the state n, thus $\Phi_{c,n_c}(\rho) = I_n$ in this case.

Alternatively, the dynamical system (Eq. 7) can also be written as

$$\frac{d}{dt} S_m = \sum_{k=1}^{K} N_{m,k}\, v_k(S) \quad m \in [0, M] \tag{12}$$

$$S_m \frac{d}{dt} \rho_{m,n} = \sum_{k=1}^{K} N_{m,k}\, v_k(S) \left(\Phi^k_{m,n}(\rho) - \rho_{m,n} \right) \tag{13}$$

The first equation describes the time evolution of species concentrations while the second equation describes the time evolution of the fraction of different isotopomers. This additional equation highlights the key role of the concentrations S_m in the timescale of changes in isotopomer distribution: higher concentration values lead to slower evolution of isotopomer distributions.

The permutation rules defined in Φ may be easily extended to more complex reactions. In the framework developed here, they only depend on the permutation relations and not on the mathematical forms of concentration-dependent flux, because we assume that the internal modification does not impact the reaction rate. If the construction rules are simple to establish and to implement in a numerical code, the computation time of the flux vector of the dynamic system (the right-hand side term of Eq. 7) increases significantly with the length of the sequences and the number of isotopomers, because of the many summations of terms. Moreover, this implementation computes the evolution of all possible isotopomers while the experimental labeling used nowadays generates only a small subset of the possible isotopomers (Metallo, Walther, and Stephanopoulos, 2009). The deterministic system therefore requires a large number of unnecessary calculations even with an optimized implementation. It nevertheless serves as a useful benchmark to check the relative accuracy and efficiency of other methods.

3.3. Derived Stochastic Simulation Algorithm (SSA)

The CME is in fact a continuous-time approximation of discrete time stochastic processes. Stochastic algorithms are often used to simulate the molecular dynamics in chemical reaction networks and capture the statistical and temporal features of fluctuations. In the case of the above CME (Eq. 5), time evolution of isotopomer distribution can also be simulated by a stochastic Monte-Carlo algorithm based on the next reaction methods (Gibson and Bruck, 2000), here called Stochastic Simulation Algorithm (SSA). Each chemical species is represented by a finite sample of isotopomers (Figure 1) where the sampling size is proportional to the concentration of the corresponding chemical species.

The sample size of the variable m is ΩS_m where Ω is a volume. The occurrence of a chemical reaction is determined by the standard next reaction methods that we have adapted, SSA is summarized as:

Init: Compute the reaction time for all reactions

$$\tau_k = \frac{1}{\Omega\, v_k(S)} \tag{14}$$

Step 1: Find the smallest reaction time $\tau_{k'} = \min(\tau_k)$ and do reaction k' by randomly picking the reagents from their samples and synthesizing the products following the permutation rule of the reaction;

Step 2: Increment time t by $\tau_{k'}$ and compute a next time for reaction k;

Step 3: Adjust the set of reaction times to account for sample size variation induced by reaction k'

$$\tau_k \leftarrow \frac{v_{k,\text{old}}}{v_{k,\text{new}}} (\tau_k - t) + t$$

and iterate to Step 1

In this sequential process, each stochastic occurrence of a chemical reaction induces discrete changes in the number of species and of isotopomers associated to each chemical species, which results in stochastic fluctuations of both species concentrations and isotopomer distribution.

Contrary to the common use of stochastic simulation algorithms for chemical reaction networks, the Ω value does not have to represent the real number of molecules for a reference concentration because the algorithm considers mainly the propagation of marked atoms and not the stochastic fluctuations of the chemical reactions linked to the finite number of copies. In the context of metabolic networks, fluctuation of the reaction times τ_k are indeed rarely relevant. Because of the high copy number of metabolites, numerous reactions occur and fluctuations of the reaction times τ_k do not induce much concentration fluctuations. If, however, one wished to decline this algorithm to study the stochastic fluctuation of the chemical reactions, it would be enough to use the relation $\tau_k = \frac{1}{\Omega\, v_k(S)} \log\left(\frac{1}{U_k}\right)$ with independent uniform random deviates U_k in $[0,1]$ for the reaction time computations. In the latter case, a realistic estimate for the Ω parameter value must be used.

4. METHODS

4.1. Code availability and computer simulation

Both methods, SSA and DSA, were implemented with the same highest level of optimization, using low-level bit-manipulation tools to implement addressing operators in a Fortran code (compiled with gfortran and optimization flag “-O3”). Simulations were run on a standard laptop with an Intel(R) Core(TM) i5-6300U CPU at 2.40GHz. No paralellization were used. The fortran code is available in github
`https://github.com/Qthommen/Stochastic-method-for-isotope-labeling-systems.git`

4.2. Goodness of Fit

The chi-square per degree of freedom $\chi^2_\nu = \frac{1}{n-p}\sum_{i=1}^{n}\frac{(y_i - y_i^*)^2}{\sigma_i^2}$ is used a goodness of fit criterion. n is the number of targets; p, the number of parameters; y_i et y_i^* the computations and tagets; σ_i^2 the variance. The fit is accepted $\chi^2_\nu < 1$.

4.3. Metabolic Network

Table 1 lists the chemical reactions and carbon rearrangements of the upper part of the increased glycolysis of the pentose phosphate pathway (Figure 1). To illustrate the dynamics of the propagation of the labeled carbons and for the sake of simplicity, the reaction rate used corresponds to the mass action law with a kinetic parameter of unit value.

reac nb	chemical reaction	reaction speed	parameter values
1	GLU (abcde) $\longrightarrow$ G6P (abcde)	$v_{G6P} = k_1$	$k_1 = 1 \rightarrow 2\ \mu$M/s
2	G6P (abcdef) $\rightleftharpoons$ F6P (abcdef)	$v_2 = k_2^+[G6P] - k_2^-[F6P]$	$k_2^+ = k_2^- = 1$/s
3	F6P (abcdef) $\rightleftharpoons$ FBP (abcdef)	$v_3 = k_3^+[F6P] - k_3^-[FBP]$	$k_3^+ = k_3^- = 1$ /s
4	FBP (acbdef) $\rightleftharpoons$ DHAP (cba) + GAP (def)	$v_4 = k_4^+[FBP] - k_4^-[DHAP][GAP]$	$k_4^+ = 1$/s; $k_4^- = 1/\mu$M/s
5	DHAP (abc) $\rightleftharpoons$ GAP (abc)	$v_5 = k_5^+[DHAP] - k_5^-[GAP]$	$k_5^+ = k_5^- = 1$ /s
6	G6P (abcdef) $\longrightarrow$ 6PG (abcdef)	$v_6 = k_6[G6P]$	$k_6 = 1$/s
7	6PG (abcdef) $\longrightarrow$ CO2 (a) + Ru5 (bcdef)	$v_7 = k_7[6PG]$	$k_7 = 1$/s
8	Ru5 (abcde) $\rightleftharpoons$ R5P (abcde)	$v_8 = k_8^+[Ru5] - k_8^-[R5P]$	$k_8^+ = k_8^- = 1$ /s
9	Ru5 (abcde) $\rightleftharpoons$ X5P (abcde)	$v_9 = k_9^+[Ru5] - k_9^-[X5P]$	$k_9^+ = k_9^- = 1$ /s
10	X5P (abcde) + R5P (ABCDE) $\rightleftharpoons$ S7P (abABCDE) + GAP (cde)	$v_{10} = k_{10}^+[X5P][R5P] - k_{10}^-[S7P][GAP]$	$k_{10}^+ = k_{10}^- = 1\ /\mu$M/s
11	S7P (abcdefg) + GAP (ABC) $\rightleftharpoons$ F6P (abcABC) + E4P (defg)	$v_{11} = k_{11}^+[S7P][GAP] - k_{11}^-[F6P][E4P]$	$k_{11}^+ = k_{11}^- = 1\ /\mu$M/s
12	X5P (abcde) + E4P (ABCD) $\rightleftharpoons$ F6P (abABCD) + GAP (cde)	$v_{12} = k_{12}^+[X5P][E4P] - k_{12}^-[F6P][GAP]$	$k_{12}^+ = k_{12}^- = 1\ /\mu$M/s
13	GAP (abc) $\longrightarrow$	$v_{13} = k_{13}[GAP]$	$k_{13} = 1$ /s
14	R5P (abcde) $\longrightarrow$	$v_{14} = k_{14}[R5P]$	$k_{14} = 1$ /s
15	CO2 (a) $\longrightarrow$	$v_{15} = k_{15}[CO2]$	$k_{15} = 1$ /s

TABLE I. List of chemical reactions and reaction speed used to simulate the 13C propagation through the upper glycolytic pathways supplemented by the pentose phosphate pathway displayed in Figure 1

5. DISCUSSION

In this study, we propose a stochastic algorithm to emulate the propagation of labeled atoms in a nonstationary metabolic system. This algorithm derives from the chemical master equation which is the most comprehensive framework for describing chemical reaction network dynamics. The efficiency of the algorithm has been applied to 13C-DMFA of the illustrative case of the pentose phosphate pathways for which 13C-labeling and concentration time series data has been synthesized. One of the main computational advantages of the proposed method lies in the very weak dependence of the computation time on the length of the marking chain and thus the number of isotopomer. Deterministic methods exhibit by construction a number of variables and a computation time that both rapidly increase with the combinatoriality associated to the power-law dependence with the chain length. SSA is therefore well adapted to the study of parallel labeling, combining for instance carbon and hydrogen labeling (Lewis *et al.*, 2014; Antoniewicz, 2015b; Jacobson *et al.*, 2019; Dong *et al.*, 2019). Moreover, a simulation that mimics the stochastic and discrete nature of metabolic reaction processes provides a more accurate and comprehensive picture relating the propagation of labeling with the dynamics of isotopomer and metabolite concentrations. Finally, this rigorous and straightforward method requires no tinkering or approximations depending on the resolution of the experimental measurements or the nature of the metabolic process, as it calculates all isotopomers at no additional cost and natively handles both stationary and non-stationary conditions. In other words, the SSA method can be used interchangeably or simultaneously for 13C-MFA (Hurbain *et al.*, 2022), 13C-NMFA or 13C-DMFA. Because problem-dependent reduction or solving techniques are not used, the implementation does not require any particular software and can simply be done in any programming language, as it is the case for chemical kinetics modeling (see Code availability).

Estimation of metabolic flux dynamics from 13C labeling and metabolomics data can be done either by inverse kinetic model modeling (Wahl, Nöh, and Wiechert, 2008; Baxter *et al.*, 2007) or by considering flux function (Antoniewicz *et al.*, 2007; Leighty and Antoniewicz, 2011; Schumacher and Wahl, 2015; Quek *et al.*, 2020). The preference of latter methods have been motivated by the lack of information about intracellular enzyme kinetics, but also the computational cost of deterministic simulation of kinetic models comprising isotopomer variables. Thanks to the computational efficiency of SSA for simulating isotopomer dynamics, inverse kinetic modeling integrating 13C labeling data become an achievable goal. However, SSA can still be used with flux function as well, for instance with constant function in case of stationary metabolic condition (*e.g.*, 13C-MFA and 13C-NMFA) (Hurbain *et al.*, 2022). To summarize, a SSA-based 13C-DMFA method would require (1) defining a stoichiometry model, (2) defining kinetic laws or flux functions, (3) using an optimization method to estimate the parameters of reaction laws or flux functions, (4) using a Monte-Carlo method to evaluate the distribution of such parameters, (5) adjust iteratively the model (stoichiometry or kinetic structure) to optimize tradeoff between a good fit and a narrow parameter distributions. The last step corresponds to the well-known problem of model selection (Mangan *et al.*, 2017). It is, however, to keep in mind that overparametrization is not a issue as long as one focuses on the estimation of flux trajectories. If, on the other hand, the 13C-DMFA is used for dynamic control purposes (Hartline *et al.*, 2021), the parameterization of flux functions will be of great importance, and it will be necessary to model the chemical kinetics as precisely as possible.

The only delicate issue associated to this method is associated to the appropriate choice of the sample size Ω. Ω must be large enough to ensure that the level of fluctuations in isotopomer concentration are below the experimental uncertainties. At the same time, computational time scales linearly with Ω motivating to keep its value as low as possible. The parameter Ω thus needs to be adjusted to a typical value (typically $100-1000$) to optimize the tradeoff between simulation uncertainties (below experimental uncertainties) and computational efficiency. For such system size, the residual fluctuations of isotopomer concentration leads to a narrow distribution of error score for a same parameter set, which is not an issue when using Monte Carlo sampling algorithm used for metabolic flux analysis (Theorell *et al.*, 2017; Valderrama-Bahamóndez and Fröhlich, 2019; Heinonen *et al.*, 2019; Theorell and Nöh, 2020). For a given value Ω, a temporal averaging procedure may be added to narrow the distribution of mass isotopomer concentrations for given Ω, allowing to use lower Ω values. Another limitation relates to the high number of reactions which depends on the absolute value of directional fluxes, not of net fluxes. This limitation can be largely compensated by the property that the number of operations (*e.g.*, computational time) does not depend on isotopomer number per metabolites.

ACKNOWLEDGEMENTS

The authors thank Darka Labavic for the fruitful discussions.

FUNDING

This work has been supported by the LABEX CEMPI (ANR-11-LABX-0007) and by the Ministry of Higher Education and Research, Hauts de France council and European Regional Development Fund (ERDF) through the Contrat de Projets Etat-Region (CPER Photonics for Society P4S and CPER Cancer 2015-2020).

Allen, D. K. and Young, J. D., "Tracing metabolic flux through time and space with isotope labeling experiments," Current opinion in biotechnology **64**, 92–100 (2020).

Antoniewicz, M. R., "Methods and advances in metabolic flux analysis: a mini-review," Journal of industrial microbiology and biotechnology **42**, 317–325 (2015a).

Antoniewicz, M. R., "Parallel labeling experiments for pathway elucidation and 13c metabolic flux analysis," Current opinion in biotechnology **36**, 91–97 (2015b).

Antoniewicz, M. R., “A guide to metabolic flux analysis in metabolic engineering: methods, tools and applications,” Metabolic engineering **63**, 2–12 (2021).

Antoniewicz, M. R., Kelleher, J. K., and Stephanopoulos, G., “Elementary metabolite units (EMU): a novel framework for modeling isotopic distributions,” Metabolic engineering **9**, 68–86 (2007).

Antoniewicz, M. R., Kraynie, D. F., Laffend, L. A., González-Lergier, J., Kelleher, J. K., and Stephanopoulos, G., “Metabolic flux analysis in a nonstationary system: fed-batch fermentation of a high yielding strain of E. coli producing 1, 3-propanediol,” Metabolic engineering **9**, 277–292 (2007).

Baxter, C., Liu, J., Fernie, A., and Sweetlove, L., “Determination of metabolic fluxes in a non-steady-state system,” Phytochemistry **68**, 2313–2319 (2007).

Bouzier-Sore, A.-K. and Bolaños, J. P., “Uncertainties in pentose-phosphate pathway flux assessment underestimate its contribution to neuronal glucose consumption: relevance for neurodegeneration and aging,” Frontiers in Aging Neuroscience **7**, 89 (2015).

Creek, D. J., Mazet, M., Achcar, F., Anderson, J., Kim, D.-H., Kamour, R., Morand, P., Millerioux, Y., Biran, M., Kerkhoven, E. J., *et al.*, “Probing the metabolic network in bloodstream-form trypanosoma brucei using untargeted metabolomics with stable isotope labelled glucose,” PLoS pathogens **11**, e1004689 (2015).

Crown, S. B. and Antoniewicz, M. R., “Parallel labeling experiments and metabolic flux analysis: Past, present and future methodologies,” Metabolic engineering **16**, 21–32 (2013).

Diaz-Moralli, S., Aguilar, E., Marin, S., Coy, J. F., Dewerchin, M., Antoniewicz, M. R., Meca-Cortés, O., Notebaert, L., Ghesquière, B., Eelen, G., *et al.*, “A key role for transketolase-like 1 in tumor metabolic reprogramming,” Oncotarget **7**, 51875 (2016).

Dong, W., Moon, S. J., Kelleher, J. K., and Stephanopoulos, G., “Dissecting mammalian cell metabolism through 13C-and 2H-isotope tracing: Interpretations at the molecular and systems levels,” Industrial & Engineering Chemistry Research **59**, 2593–2610 (2019).

Gibson, M. A. and Bruck, J., “Efficient exact stochastic simulation of chemical systems with many species and many channels,” The journal of physical chemistry A **104**, 1876–1889 (2000).

Gillespie, D. T., “Exact stochastic simulation of coupled chemical reactions,” The journal of physical chemistry **81**, 2340–2361 (1977).

Gillespie, D. T., “A rigorous derivation of the chemical master equation,” Physica A: Statistical Mechanics and its Applications **188**, 404–425 (1992).

Gillespie, D. T., “The chemical langevin equation,” The Journal of Chemical Physics **113**, 297–306 (2000).

Gillespie, D. T., “Approximate accelerated stochastic simulation of chemically reacting systems,” The Journal of chemical physics **115**, 1716–1733 (2001).

Hartline, C. J., Schmitz, A. C., Han, Y., and Zhang, F., “Dynamic control in metabolic engineering: Theories, tools, and applications,” Metabolic engineering **63**, 126–140 (2021).

Heinonen, M., Osmala, M., Mannerström, H., Wallenius, J., Kaski, S., Rousu, J., and Lähdesmäki, H., “Bayesian metabolic flux analysis reveals intracellular flux couplings,” Bioinformatics **35**, i548–i557 (2019).

Hurbain, J., Thommen, Q., Anquez, F., and Pfeuty, B., “Quantitative modeling of pentose phosphate pathway response to oxidative stress reveals a cooperative regulatory strategy,” bioRxiv (2022), 10.1101/2022.02.04.478659.

Jacobson, T. B., Adamczyk, P. A., Stevenson, D. M., Regner, M., Ralph, J., Reed, J. L., and Amador-Noguez, D., “2H and 13C metabolic flux analysis elucidates in vivo thermodynamics of the ed pathway in zymomonas mobilis,” Metabolic engineering **54**, 301–316 (2019).

Kuehne, A., Emmert, H., Soehle, J., Winnefeld, M., Fischer, F., Wenck, H., Gallinat, S., Terstegen, L., Lucius, R., Hildebrand, J., *et al.*, “Acute activation of oxidative pentose phosphate pathway as first-line response to oxidative stress in human skin cells,” Molecular cell **59**, 359–371 (2015).

Lee, M. H., Malloy, C. R., Corbin, I. R., Li, J., and Jin, E. S., “Assessing the pentose phosphate pathway using [2, 3-13c2] glucose,” NMR in Biomedicine **32**, e4096 (2019).

Leighty, R. W. and Antoniewicz, M. R., “Dynamic metabolic flux analysis (DMFA): a framework for determining fluxes at metabolic non-steady state,” Metabolic engineering **13**, 745–755 (2011).

Lewis, C. A., Parker, S. J., Fiske, B. P., McCloskey, D., Gui, D. Y., Green, C. R., Vokes, N. I., Feist, A. M., Vander Heiden, M. G., and Metallo, C. M., “Tracing compartmentalized nadph metabolism in the cytosol and mitochondria of mammalian cells,” Molecular cell **55**, 253–263 (2014).

Mangan, N. M., Kutz, J. N., Brunton, S. L., and Proctor, J. L., “Model selection for dynamical systems via sparse regression and information criteria,” Proceedings of the Royal Society A: Mathematical, Physical and Engineering Sciences **473**, 20170009 (2017).

Metallo, C. M., Walther, J. L., and Stephanopoulos, G., “Evaluation of 13C isotopic tracers for metabolic flux analysis in mammalian cells,” Journal of biotechnology **144**, 167–174 (2009).

Niedenführ, S., Wiechert, W., and Nöh, K., “How to measure metabolic fluxes: a taxonomic guide for 13c fluxomics,” Current opinion in biotechnology **34**, 82–90 (2015).

Ohno, S., Quek, L.-E., Krycer, J. R., Yugi, K., Hirayama, A., Ikeda, S., Shoji, F., Suzuki, K., Soga, T., James, D. E., *et al.*, “Kinetic trans-omic analysis reveals key regulatory mechanisms for insulin-regulated glucose metabolism in adipocytes,” Iscience **23**, 101479 (2020).

Quek, L.-E., Krycer, J. R., Ohno, S., Yugi, K., Fazakerley, D. J., Scalzo, R., Elkington, S. D., Dai, Z., Hirayama, A., Ikeda, S., *et al.*, “Dynamic 13C flux analysis captures the reorganization of adipocyte glucose metabolism in response to insulin,” Iscience **23**, 100855 (2020).

Schmidt, K., Carlsen, M., Nielsen, J., and Villadsen, J., “Modeling isotopomer distributions in biochemical networks using isotopomer mapping matrices,” Biotechnology and bioengineering **55**, 831–840 (1997).

Schumacher, R. and Wahl, S. A., “Effective estimation of dynamic metabolic fluxes using 13c labeling and piecewise affine approximation: from theory to practical applicability,” Metabolites **5**, 697–719 (2015).

Selivanov, V. A., Puigjaner, J., Sillero, A., Centelles, J. J., Ramos-Montoya, A., Lee, P. W.-N., and Cascante, M., “An optimized algorithm for flux estimation from isotopomer distribution in glucose metabolites,” Bioinformatics **20**, 3387–3397 (2004).

Stephanopoulos, G., “Metabolic fluxes and metabolic engineering,” Metabolic engineering **1**, 1–11 (1999).

Theorell, A., Leweke, S., Wiechert, W., and Nöh, K., “To be certain about the uncertainty: Bayesian statistics for 13c metabolic flux analysis,” Biotechnology and bioengineering **114**, 2668–2684 (2017).

Theorell, A. and Nöh, K., “Reversible jump MCMC for multi-model inference in metabolic flux analysis,” Bioinformatics **36**, 232–240 (2020).

Thompson, J. M. T. and Stewart, H. B., *Nonlinear dynamics and chaos* (John Wiley & Sons, 2002).

Valderrama-Bahamóndez, G. I. and Fröhlich, H., “Mcmc techniques for parameter estimation of ode based models in systems biology,” Frontiers in Applied Mathematics and Statistics **5**, 55 (2019).

Van Kampen, N. G., *Stochastic processes in physics and chemistry*, Vol. 1 (Elsevier, 1992).

Wahl, S. A., Nöh, K., and Wiechert, W., “13 c labeling experiments at metabolic nonstationary conditions: an exploratory study,” Bmc Bioinformatics **9**, 1–18 (2008).

Zupke, C. and Stephanopoulos, G., “Modeling of isotope distributions and intracellular fluxes in metabolic networks using atom mapping matrixes,” Biotechnology Progress **10**, 489–498 (1994).

Abstract

Living cells such as mammalian cells in particular, are continuously exposed to multiple and varied types of stress. These stresses can perturb the cellular homeostasis and induce damages on the cellular components which could induce several types of diseases. It is particularly the case for a change of cellular redox state called oxidative stress induced by an excessive production or insufficient consumption of reactive oxygen species such as hydrogen peroxide (H_2O_2).

Cells have developed efficient defence mechanisms against oxidative stress that involve anti-oxidant systems such as glutathiones which reduce the oxidizing molecules, but also metabolic pathways such as Pentose Phosphate Pathway (PPP) and glycolysis. These metabolic pathways are known to reroute the carbon flux resources from the glycolysis toward the PPP which induces high $NADPH$ recycling that is required for efficient detoxification rate of the anti-oxidant systems. It remains however unclear how regulatory mechanisms (i) contribute to such reallocation of metabolic flux resources during oxidative stress and (ii) give rise to observed adaptation profiles of intracellular H_2O_2 concentrations.

In the thesis, the role of regulations in the metabolic response to oxidative stress is addressed using a comprehensive kinetic modeling framework. First, a model is built from a set of metabolomics and ^{13}C labeling data, using conventional parameter estimation methods but also a novel metabolic flux analysis techniques based on a stochastic simulation algorithm. Systematic analysis of the model reveals that many metabolic inhibitions, especially on $G6PD$, PGI and $GAPD$, can favour flux rerouting for $NADPH$ production. In particular, we show that all these regulations work in a dose-dependent and complementary manner, which explains some paradoxes and controversies, and is consistent with observed adaptation phenotypes. A more phenomenological model has also been developed to show how such adaptation phenotype could contribute to cell-fate heterogeneity, such as fractional killing, as a long-term outcome of oxidative stress.

Keywords : Cell, oxidative stress, mathematical modeling, metabolic regulations, adaptation.